THE PLANT SOIL INTERFACE: NICKEL BIOAVAILABILITY AND THE MECHANISMS OF PLANT HYPERACCUMULATION

by

David H. McNear Jr.

A dissertation submitted to the Faculty of the University of Delaware in partial
fulfillment of the requirements for the degree of Doctor of Philosophy in Plant and
Soil Sciences

Winter 2006

UMI Number: 3205442

ProQuest Information and Learning Company
300 North Zeeb Road
P.O. Box 1346
Ann Arbor, MI 48106-1346

THE PLANT SOIL INTERFACE: NICKEL BIOAVAILABILITY AND THE MECHANISMS OF PLANT HYPERACCUMULATION

by

David H. McNear Jr.

Approved: ____
Donald L. Sparks, Ph.D.
Chair of the Department of Plant and Soil Sciences

Approved: ____
Robin Morgan, PhD.
Dean of the College of Agriculture and Natural Resources

Approved: ____
Conrado M. Gempesaw II, Ph.D.
Vice Provost for Academic Programs and Planning

I certify that I have read this dissertation and that in my opinion it meets the academic and professional standard required by the University as a dissertation for the degree of Doctor of Philosophy.

Signed: ____

Donald L. Sparks, Ph.D.
Professor in charge of dissertation

I certify that I have read this dissertation and that in my opinion it meets the academic and professional standard required by the University as a dissertation for the degree of Doctor of Philosophy.

Signed: ____

Rufus L. Chaney, Ph.D.
Member of dissertation committee

I certify that I have read this dissertation and that in my opinion it meets the academic and professional standard required by the University as a dissertation for the degree of Doctor of Philosophy

Signed: ____

D. Janine Sherrier, Ph.D.
Member of dissertation committee

I certify that I have read this dissertation and that in my opinion it meets the academic and professional standard required by the University as a dissertation for the degree of Doctor of Philosophy

Signed: ____

Steve Sutton, Ph.D.
Member of dissertation committee

ACKNOWLEDGMENTS

Like for most, this has been a long journey….14 years to be exact (post- high school). But the journey started long before that. It started with my family… early morning fishing and hunting trips with my dad, Thanksgivings in the mountains at my aunt’s. It was there that I gained an appreciation for nature and through those experiences that I decided to dedicate myself to preserving the environment we live in. This journey, however, would not have been possible had it not been for the myriad of people who have helped guide me along the way.

There was a time that I was considering taking a much more “typical” path. I thought I would work for a while, save some money, perhaps buy a car and then go to college. My father had the foresight to quell these thoughts and strongly encouraged me to start college immediately. This was one of the first distinct “nudgings” to keep me on the path and I am truly grateful for him and Sue’s generosity along the way. One constant throughout my journey was the unending support, encouragement, confidence (and all the other superlatives I can’t think of at the moment) that my Mom and Dan have provided. They were always there to offer advice and encouragement, to help move me in and out of (and clean) the multiple apartments and houses that I went through as a student, fixing the car(s), keeping me fed and clothed, etc. etc. They provided the essential “infrastructure” that made getting my degree’s possible. I hope they know how important their unceasing confidence in me was to my achieving this goal. Another "nudging" came from my M.S. advisor Jon Chorover. I would like to take this opportunity to thank Jon. He had the confidence in me and the vision to offer my name when Dr. Sparks approached him to inquire about potential PhD students. Thank you for keeping me on the path.

I thank my PhD advisor Dr. Sparks for accepting Jon's recommendation. You have built an amazing environment for the development of young scientists into world-class researchers; the ranks among which I am humbled to be a very small part of. I truly do appreciate the academic freedom and endless opportunities that came with being a part of the Sparks Environmental Soil Chemistry group. Dr. Sparks' commitment to promoting the careers of his student's, the breadth of his scientific knowledge and perhaps more importantly his academic integrity are truly admirable traits.

I would also like to thank the members of my dissertation committee. Dr. Rufus L. Chaney (USDA-ARS Beltsville) was instrumental for not only making available the materials for my research project but also for offering his tremendous knowledge of the literature and his candid advice. Special thanks go to Dr. Steve Sutton (University of Chicago, APS-GSECARS) who helped teach me about the ins-and-outs of X-ray tomography and put up with my unending questions during the preparation of our manuscript. It was fun working with Steve; he is patient and kind in a very fatherly way and I hope I to get to work with him more in the future. Lastly, I would like to thank Dr. Janine Sherrier, my future *boss*. Janine was generous with her time, fielding the numerous questions I had while getting initiated into the world of plants, and confident in my training to offer me a position in her lab to further pursue the fascinating interaction between plants and soils.

Because of the multi-technique, multidisciplinary approaches taken in completing this dissertation, there numerous people to thank from the laboratories used in and outside of UD. Thanks to Matthew Marcus and Sirine Fakra for their help and support while running at ALS 10.3.2. Thanks to the folks at the APS GSECARS BM and ID beamlines, Steve Sutton, Matt Newville and Mark Rivers. Thanks to Ken Livi at John's Hopkins for help with EPMA data collection and analysis. Thanks to Kirk Czymmek and Debbie Powell at the DBI for help with confocal and FE-SEM data collection.

I also need to acknowledge the supporting members of the Sparks Soil Chemistry group. I send a sincere thanks to Amy Broadhurst for keeping me registered, paid and the myriad of other things that I was oblivious to. I congratulate here on completing her degree and wish her lots of luck in the future. Not enough thanks can go out to Jerry Hendricks. Jerry is an integral component to the proper functioning of the group not only for his coordination of the lab or support on beamtrips, but also for managing and mediating the various conflicts that can arise from putting so many *strong-personalitied* people in one place. He has earned his Uncle Jerry moniker. Outside of the lab, I consider Jerry (and Barbara) good friends and thank them for helping me de-focus and smell the roses once in a while.

I would also like to acknowledge all of my fellow students and friends most of whom I got the opportunity to work with and get to know while here at UD. Maarten, Markus, Stefan, Derek and Yuji when I first arrived at UD and Kristin, Laura, Jeff, Ted, Mike, Kristian, Ryan, Jen, Brandon, Masayuki, Saengdao, Gautier. I wish you all the best of luck.

Last, but certainly not least, I want to thank my wife Maria. Our time at Delaware has been permeated by many firsts. We got married, bought our first house, first new car and conceived our first child. It has been a wonderful ride thus far and I sincerely appreciate and love you for all the support, encouragement and confidence you have given me throughout these years. I look forward to what's to come. I can't finish without thanking our mutts, Chloe and Lila. During the final and long days of writing this dissertation the dogs kept me company at the office; their unconditional affection (and Chloe's unceasing whining at cats and squirrels) kept me company and the walks around the farm they continually prodded me for kept me sane.

TABLE OF CONTENTS

LIST OF TABLES

LIST OF FIGURES

Words to live by:

“Use what talent you possess: the woods would be very silent if no birds sang except those that sang best.”

-Henry Van Dyke -
American short-story writer, poet and essayist

"The worst part is not in making a mistake but in trying to justify it, instead of using it as a heaven-sent warning of our mindlessness or our ignorance."

- Santiago Ramón y Cajal -
Spanish Histologist and Nobel Prize in Medicine, 1906

“We abuse land because we regard it as a commodity belonging to us. When we see land as a community to which we belong, we may begin to use it with love and respect.“

- Aldo Leopold -
Scientist, conservationist, writer and father of wildlife ecology

“To waste and destroy our natural resources, to skin and exhaust the land instead of using it so as to increase its usefulness, will result in undermining in the days of our children the very prosperity which we ought by right to hand down to them.”

- Theodore Roosevelt -
Twenty-sixth president of the United States, 1901-1909

“Never, never, never give up.”

- Winston Churchill
Author, soldier, journalist, politician and Nobel Prize winner, 1953

ABSTRACT

Industrial processes, such as base metal smelting and refining, often result in the widespread distribution of heavy metals and acid forming compounds into the surrounding environment. The impact of this deposition on the neighboring ecosystems can be devastating, leading, in some cases, to perturbation or loss of ecological viability, which depends primarily on the amount, concentration and type of metal species. In order to restore the productivity of these lands, remediation practices aimed at reducing soil metal concentrations or minimizing their mobility and bioavailability are necessary. The cost associated with conventional (i.e. excavation and disposal) remediation methods can be prohibitively expensive (> \$3 million ha^{-1}), and therefore, alternative methods must be examined.

In this research, a variety of macroscopic, microscopic and cutting-edge spectroscopic tools were used to investigate the influence of in-situ chemical treatment (i.e., liming) and soil type (Welland Loam vs. Quarry Muck) on the speciation of nickel (Ni) in soils surrounding an historic Ni refinery in Port Colborne, Ontario Canada. In addition, Ni speciation and compartmentalization were determined in the Kotodesh cultivar of the Ni hyperaccumulator *Alyssum murale* (Waldst. & Kit.) to ascertain the biochemical mechanism used by *A. murale* to remove Ni and explore its potential as an alternative remediation method from these soils. In doing so, the

development and implementation of novel synchrotron-based microtomographic methods were shown to be very effective at determining the location and concentration of metals within and throughout unaltered *A. murale* tissues.

Chemical treatment and soil type had a pronounced influence on the type of metal species formed in the refinery-enriched soils. Monitoring the dissolution of Ni from potential soil Ni species by pH 4 HNO_3 using a stirred-flow technique, showed that 100% and 79% of NiO and NiS compared to 62% and 57% of the Ni Al-LDH and α-$Ni(OH)_2$ remained after the 8-hr experiment. Making the soils calcareous with the addition of 33-88 Mt ha^{-1} dolomitic limestone was effective at reducing Ni mobility. In both the unlimed muck and mineral soils, roughly 2% of the total Ni was released throughout the duration of the 8 hour experiment compared to 0.1% for the treated soils.

Conventional sequential extraction methods were ineffective at accurately determining the Ni speciation in both muck and loam untreated field soils as well as a highly enriched forested muck soil. Examining the solids remaining after each sequential extraction step using synchrotron based X-ray absorption fine structure spectroscopy (XAFS) revealed that NiO persisted through each extraction step, compromising the identification of other Ni species. Scanning electron microscopy (SEM) confirmed the presence of NiO particles in all of the extracted residuals from the muck soils, but not the loam. Efficient removal of Ni from the muck soil may have been compromised by the high organic content of the soils, or the high initial Ni loading compared to the loam soil (~5000 mg kg^{-1} vs. 22,000 mg kg^{-1}). Sequential extraction was able to show that a significant amount (>90%) of the Ni in both the soils can be considered immobile. However, in the highly enriched forest soil there is a much larger mobile fraction (~15%) likely due to its lower CEC and pH and high Ni loading.

Direct determination of the soil Ni speciation using synchrotron based micro X-ray fluorescence (μ-SXRF) and micro X-ray absorption fine structure (μ-XAFS) spectroscopic analyses showed for the first time that Ni Al-LDH phases form in anthropogenically enriched field soils. The Ni Al-LDH species formed in both the treated and untreated mineral soils, with a tendency towards more stable (e g. aged-LDH and phyllosilicate) Ni species in the treated soil; their formation likely aided by the solubilization of Si with increasing pH. In the muck soils, Ni-organic complexes (namely fulvic acid) dominated the speciation in both treated and untreated soils, with stronger complexes forming under the excess lime (i.e. higher pH) treatments.

A multi-technique investigation of the speciation and compartmentalization of Ni in the Ni hyperaccumulator *A. murale* grown in both the untreated Welland and Quarry muck Ni enriched soils showed that 58% of the Ni in A. murale leaf tissues is complexed by strong ligands (predominantly malate) with the remaining 38% either weakly complexed with non-specific ligands or present as free hydrated Ni (Ni(aq)). Histidine was identified in the leaf veins using μ-XAFS and in sap extracts using attenuated total reflectance Fourier transform infrared (ATR-FTIR) spectroscopy. Manganese was also found in the basal compartments of the leaf trichomes in the +2 oxidation state (possibly as MnO) and chemically segregated from Ni.

Finally, synchrotron based fluorescence and absorption edge computed microtomographies (CMT) was shown to be well suited for determining the compartmentalization and concentration of metals in hyperaccumulating plant tissues. Fluorescence CMT of in-tact leaf, stem and root samples revealed that Ni concentrated in stem and leaf dermal tissues and, together with Mn, in distinct concentrations associated with the Ca rich trichomes on the *A. murale* leaf surface. Metal enrichment was also observed within the vascular system of the finer roots, stem and leaves, but absent from the coarser root, which had a well correlated metal coating. Absorption edge CMT showed the three-dimensional distribution of the highest metal concentrations and verified that epidermal localization and Ni and Mn co-localization at the trichome base are phenomena that occurred throughout the entire leaf and may contribute significantly to metal detoxification and storage. Ni was also observed in the leaf tips, possibly resulting from release of excess Ni with guttation fluids.

In summary, this research shows the necessity of using multi-scale, multi-technique approaches for deciphering metal speciation in heterogeneous samples. In particular, the use of micro synchrotron based techniques (i.e., μ-SXRF and μ-XAFS) were instrumental in demonstrating for the first time, that secondary precipitates of Ni (i.e. Ni Al LDH) can form in field soils, enhanced by limestone additions, which have a pronounced influence on metal mobility and bioavailability. In addition, we determined the Ni speciation in *A. murale* tissues and demonstrate a novel tomographic technique for determining Ni compartmentalization in the tissues of metal hyperaccumulating plants which enhance our understanding of metal hyperaccumulation.

Chapter 1

THE PLANT/SOIL/METAL INTERFACE

1.1 Introduction

Enrichment of soils with geogenically or anthropogenically deposited heavy metals can have a pronounced influence on the health and viability of natural, agricultural and urban ecosystems. Naturally occurring serpentine or ultramafic soils containing high concentrations of Co, Cr and Ni can be found on every continent, with the largest distribution in Canada. Anthropogenic inputs of heavy metals, on the other hand, particularly since the industrial revolution, have resulted in the widespread enrichment of soils primarily around population centers. Examples include mercury (Hg) deposition from burning of coal, or possibly the most pronounced example being lead (Pb), resulting from its use as an “anti-knock” fuel additive in gasoline. Applications of soil amendments, biosolids in particular, and the use of plant protection chemicals in agricultural fields (e.g. $Pb_5OH(AsO_4)_3$), together with the by-products of industrial mining and metal processing, have also been important sources of pollutants such as Co, Cr, Cu and Ni.

In order to develop remediation strategies that are not only effective at stabilizing or removing the contaminants, but also economically feasible, it is necessary to assess the fate of the enriched metal. In some cases, the area of metal enrichment is well defined and requires only containment or removal of the contaminated soil. However, when enrichment results from aerial deposition, as a byproduct of metal refineries or smelters for example, the affected area can be on the order of tens to hundreds of square kilometers. Such widespread enrichment makes conventional remediation strategies (i.e. excavation and disposal) impossible and necessitates an alternative. The alternatives can range from in-situ stabilization through the addition of amendments such as lime or organic matter to targeted degradation with metal specific plants (Geebelen et al, 2002; Vangronsveld et al, 2000; Mench et al, 2003). Scientists, when looking at the effectiveness of these remediation alternatives, have often only focused on the metal-soil or metal-plant interactions alone, neglecting the influence that soil metal speciation has on the mechanisms of metal uptake, or conversely, on the effect that plants have on the soil metal speciation. In order to more effectively predict the fate of metals in the environment it is necessary to not only look at isolated components of the soil/metal/plant model, but to examine the interaction of each of these components. To accomplish this, a multidisciplinary, multitechnique approach to identifying and characterizing the components of soil/metal/plant interactions is needed.

This chapter is a compilation of research findings covering the basic concepts of metal sequestration, transformation and mobility in soils, and how activities at the soil/water/root interface (i.e. rhizopshere) influence these processes. A brief review of the techniques available for exploring these reactions are discussed primarily the use of cutting-edge synchrotron based techniques. Finally, the chapter summarizes the reasons and justification for this research concerning the enrichment of soils around a Ni refinery in Port Colborne, Ontario Canada.

1.2 Metal Sequestration in Soils

The soil environment is an intricate mixture of organic, inorganic and biological materials, each intimately interacting with the other, resulting in a highly dynamic and complex system. Adding to their complexity, soils are open to the environment and thus influenced and formed by the flux of materials and energy from atmospheric, biological, geological and hydrological compartments. It is the flux of materials and energy among each of these compartments that governs the reactivity, mobility and bioavailability of plant nutrients as well as contaminants in soils and which lends credence to this treatise on heavy metal reactivity in the soil environment.

The processes having the most influence on metal reactivity in the soil environment are those that occur between the soil solution and the various inorganic, organic and biological components. The soil solution is mostly water which is discontinuous, containing solutes (metal ions, plant nutrients etc.) that, because of different pore space distributions and locations, can vary in concentration (Brady and Weil 2002). The soil solution is the medium from which plants and other organisms obtain life sustaining ions, and thus the reactions controlling the ion content of the soil solution will have a large impact on the fertility and arability of the land.

There are several physical and chemical processes occurring at the soil-solution interface that govern how much of a metal is retained on a soil constituent surface and present in solution. Included in these are the pH and ionic strength of the soil solution, the type and amount of clay minerals, type and amount of metal, the reaction time and the organic matter content.

1.2.1 pH – The Master Variable

The parameter with the most influence on soil solution ion content is pH. The pH of a soil is determined by measuring the concentration of H^+ ions in solution (active acidity) with an excess of H^+ compared to OH^- ions resulting in a lower pH and the reverse a higher pH (as described by the relationship: $pH = -\log[H^+]$). The chemical reactions controlling the H^+ concentration and thus the soil solution pH include mineral weathering reactions, carbonic acid dissociation and acid-base reactions of soil humus and aluminum hydroxy polymers/monomers (Sposito 1989). Paramount among these, are the reactions involving Al. In the early 20th century great debates revolved around whether it was H or Al that had the greatest control on soil acidity. It was later verified by N.T. Coleman and C.I. Rich that indeed, both exchangeable and non-exchangeable forms of Al have the greatest influence on soil solution pH (Sparks 2001). The influence of Al over the soil solution pH is due to its ability to hydrolyze in dilute solutions with low OH/Al ratios (Sparks 2003).

Hydrolysis of Al forming monomeric species produces H^+ ions which then act to reduce the soil solution pH, the magnitude of which depends on the amount of Al in solution. However, soil solution pH measurements only account for the amount of H^+ ions resulting from aluminum hydrolysis or dissociation from exchange sites. A soil also has 'reserve acidity', which refers to the number of exchange sites within the soil occupied by Al^{3+} cations which contribute to the soil solution H^+ ion concentration

As soil pH relates to metal bioavailability, it generally stands that as the pH of a system is decreased more metals (e.g. Mn, Fe and Al) are released to the soil solution because of proton competition for exchange sites of clay minerals or organic matter, or through proton promoted dissolution of soil minerals. The release of metals can be detrimental to plant and microorganism viability. Conversely, as the pH increases, the soil retains more base saturating cations (i.e., non-hydrolyzing exchangeable bases such as Mg, Ca, and K) which may lead to nutrient deficiency. Increase in pH can also induce metal complexation or precipitation (section 1.2.3) which can also account for nutrient or metal sequestration.

Climate can have a pronounced influence on soil pH. For example, soils of the humid tropics (e g. Oxisols) are highly weathered because of the higher temperatures and amount of rainfall and thus are leached of their base saturating cations (e.g. Ca, Mg, Na) resulting in a typical pH range of 5-7. The reverse is true for soil in arid regions which retain their base-saturating cation and thus have a pH ranging from 7-9.

1.2.2 Surface Charge and Metal Adsorption

Adsorption refers to the attachment or accumulation of a material at the solution – surface interface (Sparks 2003). Adsorption does not include three dimensional growth of precipitates (even if they occur at a surface), diffusion, or polymerization; the former two phenomena of which will be discussed later in this chapter. The substance in solution that has the potential to be adsorbed is called the *adsorptive*. The solid surface which it may attach to is termed the *adsorbent*. Once the substance is adsorbed it is referred to as the *adsorbate* and collectively as an *adsorption complex*. If the mechanism of substance attachment is unknown (i.e. either adsorption, precipitation or polymerization) then the process is generically referred to as *sorption*, in which case *sorptive*, *sorbent* and *sorbate* refer to the substance in solution, the solid surface and the substance on the solid surface, respectively.

Soil constituents can have both positive and negative charge, with the latter being the most prevalent under normal environmental conditions. Soil constituents gain their negative charge from either isomorphic substitution of a cation of lower charge for a cation of higher charge (e.g. Mg^{2+} for Al^{3+}) in the tetrahedral or octahedral layer of 2:1 silicate clays (e.g. smectite) or through broken bonds on the edges of 1:1 clays (e.g. kaolinite), metal oxides (e.g. goethite) or organic colloids. The charge arising from isomorphic substitution is considered permanent or constant and not affected by pH. The charge on 1:1 clays or metal oxides however, is highly pH dependent and results largely from the protination and deprotination of –OH groups at the broken edge. The negatively charged sites are called surface functional groups. Surface functional groups are charged molecular units that protrude from a surface of organic and inorganic substrates into the surrounding soil solution (Sposito 1989). Adsorption of metals at a surface occurs through both physical and chemical interactions with surface functional groups. In general adsorption can be characterized as non-specific (outer-sphere and diffuse ion interactions) or specific (inner-sphere, chemisorption).

Adsorption of metals by outer-sphere complexation or through association with the diffuse-ion swarm adjacent to the particle surface are considered non-specific because they rely mostly on electrostatic interactions with the surface and depend on the electronic configuration of the surface functional group or the solvated metal (Sposito, 1989). Outer-sphere complexation describes a situation where a water molecule is located between the metal cation and the surface functional group. A metal adsorbed in the diffuse-ion swarm is not associated with a specific surface functional group, but instead, the solvated metal is free to “float” about the surface, satisfying charge in a delocalized manner. Each of these adsorption mechanisms are typically considered “weak” and influenced by ionic strength and in some cases pH. Therefore, the metal is retained in a form that is exchangeable with other cations and thus subject to removal by plants and microbes or by leaching. The exchange of one cation for another is called “cation exchange”. The amount of exchange sites present in a soil can be loosely defined as the Cation Exchange Capacity (CEC) and, as the term implies, is a measure of the capacity of a soil to retain cations. The components contributing to CEC, as mentioned earlier, are organic matter, clay minerals and oxides of Al, Fe and Mn.

Contrary to outer-sphere complexes, inner-sphere complexes involve direct interaction of the metal cation with the surface functional group through ionic or covalent bonding. Consequently, specific adsorption depends on the electronic configuration of both the metal and the surface functional group. Inner-sphere complexes are monodentate or bidentate if bound to one or two surface functional groups, respectively. Bidendate complexes can be either mononuclear or binuclear depending on the coordination of the surface functional group within the adsorbent. Metals forming inner-sphere complexes are considered non-exchangeable and thus are less available for uptake by plants and microbes and less susceptible to leaching than metals adsorb via outer-sphere complexation. Additionally, inner-sphere complexation is typically independent of ionic strength and as the pH is raised the metals become increasingly non-exchangeable (McBride, 1994).

The sorption of metals, regardless of the mechanism, plays a vital role in determining their availability and mobility in soils. In the following sections, the evolution of surface charge on both organic and inorganic soil constituents will be discussed further, along with how these constituents and their charge influences metal retention and mobility.

1.2.2.1 Soil Organic Matter - Metal interactions

Soil organic matter (SOM) has a marked influence on a soil's ability to retain metals. Soil organic matter or humus includes the total organic content of soils (with the exception of unaltered, identifiable plant material and biomass) and is composed of plant, microbial and animal residues and exudates at various stages of decomposition (Sparks 2003). The structure of SOM, unlike soil minerals, is not uniform making the study of its chemical properties difficult. As such, SOM is typically fractionated into three components -fulvic, humic acid, and humin-, based on differences in their solubility in acid or alkali solutions. Fulvic acid is soluble in both acid and alkali solutions, humic acid is only soluble in an alkali solution while humin is soluble in neither. Fulvic acid differs from humic acid because it has a slightly higher O/C ratio, total acidity, and carboxylic functional group and sulfur contents. Humin is similar to humic acid, but has higher polysaccharide content and is less aromatic (Sparks 2003). As described by Sposito (1989) humic and fulvic acids exhibit four characteristics that strongly influence their chemical reactivity in soils: polyfunctionality, macromolecular charge, hydrophilicity and structural lability. With respect to polyfunctionality, the surface functional groups that exhibit the most influence on metal retention are the carboxyl (COOH) and phenolic OH (aromatic ring-OH) groups. The charge of the surface functional group is dependent on the pH of the soil solution and thus the charge on organic matter is considered variable or pH dependent. The complexation of metals with organic matter has traditionally been studied by determining conditional metal stability constants and complexation capacities (Xia et al., 1997).

Metal stability constants provide a measure of a metal's affinity for a ligand and a relative assessment of a metal's availability and mobility (Sparks 2003). However, these values tell little about the coordination environment of the metal –ligand complex and thus provide only limited information on the type of adsorption complex that is forming. Techniques such as nuclear magnetic resonance (NMR), Fourier transform infrared (FTIR) and electron paramagnetic resonance (EPR) spectroscopies provide more direct information about the metal-ligand chemical environment. However, interpretation of the results from these techniques can be complicated, with some techniques requiring well defined systems (not necessarily easy when dealing with SOM), and in the case of EPR, a metal which is paramagnetic (a limitation when trying to study Ni or Zn).

Xia et al. 1997) were the first to use extended x-ray absorption fine structure (XAFS) and x-ray absorption near edge structure spectroscopy (XANES) to study the coordination chemistry of the first row transition metals complexed with soil and aquatic humic substances. They found that Ni and Co formed an inner-sphere complex, coordinated with six oxygen atoms (i.e. octahedral coordination) in the first shell and two carbon atoms in the second shell with average bond distances of 2.09 and 2.94 Å, respectively. Strathmann and Myneni 2004) using both XAFS and attenuated total reflectance (ATR) FTIR, investigated the coordination of Ni(II) with structurally similar carboxylic acids and soil fulvic acid. They found that the strength of the Ni-carboxylate complex that formed depended on the structure of the carboxylic acid (mono or polycarboxylates), with Ni forming weak complexes with the monocarboxylates and stronger, chelates, with the polycarboxylates. They concluded that the Ni(II) complexes with soil fulvic acid were inner sphere and complexation occurred with one or more carboxylate groups. In general, the maximum amount of metal that can be complexed by soil organic matter is roughly equal to the number of carboxylic functional groups (Stevenson 1994).

Further advances in analytical techniques will shed more light on the interaction of metals with soil organic matter. One such technique that shows promise is soft x-ray microscopy combined with carbon near edge x-ray absorption fine structure spectroscopy (NEXAFS) (Nachtegaal et al. 2003). Utilizing this technique, functional groups can be “imaged” and shifts in spectral intensity and position can be used to predict the coordination environment of the metal as well as its affinity for SOM functional groups.

1.2.2.2 Soil Mineral-Metal Interactions

The primary surface functional groups on inorganic soil components which can interact with metals are: the plane of oxygen atoms at the surface of 2:1 clays and edge/surface hydroxyls (Sparks, 2002). Isomorphic substitution occurs in both primary and secondary clay minerals; however, only in the 2:1 layer silicates does it have a marked impact on the surface charge (Sposito, 1989). Isomorphic substitution occurs during mineral formation when an ion of similar radius is substituted for either Si^{4+} in the tetrahedral sheet (with Al^{3+} or Fe^{3+}) or for Al^{3+} in the octahedral sheet (with Fe^{3+}, Mg^{2+}, Zn^{2+}, Fe^{2+}) of 2:1 layer silicates. The deficit in charge arising from isomorphic substitution manifests itself through the hexagonal cavities in the plane of oxygen atoms associated with the silica tetrahedra (a.k.a. the siloxane surface). These siloxane cavities are constructed from six corner-sharing silica tetrahedra with a diameter of approximately 0.26nm (Sposito, 1989). The charge at this cavity, and accordingly, the strength of the complex that can be formed is dictated by whether isomorphic substitution has occurred in the underlying octahedral or tetrahedral layer as well as the proximity of the substitution to the cavity. As a rule of thumb, the most reactive siloxane cavity will result from substitution within the tetrahedral layer followed by octahedral substitution. Charge of this variety is considered permanent and not affected by soil solution pH.

Surface and edge hydroxyl groups, as the name implies, occur on the basal plane as well as at the broken edges of primary and secondary clay minerals, amorphous materials (i.e. repeating crystalline structure with diameter <3nm) and metal (Fe, Al, Mn) oxides, hydroxides and oxyhydroxides. The reactivity of surface hydroxyl groups depends on how they are coordinated with the metal in the underlying matrix. On metal oxides, such as goethite (α-FeOOH), there are four surface functional groups. A, B and C-type surface functional groups are composed of hydroxyls that are bound to 1, 3 and 2 Fe(III) ions, respectively. Only the A-type site is reactive and is both a proton acceptor and proton donor (amphoteric) and thus reactive over a wide range of pHs. The fourth type of surface functional group is the Lewis acid site. In the case of Geothite, the Lewis acid site occurs where water is chemisorbed to an Fe(III) ion (the Lewis acid). In clay minerals such as kaolinite there are Lewis acid sites in which a water molecule is chemisorbed to Al(III) at the broken mineral edge. The chemisorbed water at both of these sites is positively charged and thus very reactive, rapidly undergoing ligand exchange (i.e. anion for —OH_2^+) with anions, forming tightly bound inner-sphere complexes. The surface, through dissociated chemisorption, can also become hydroxylated and thus reactive towards metal cations in solution. In addition, there are singly coordinated OH groups associated with Al (aluminol; >Al—OH) and Si (silanol; >Si—OH) at broken mineral edges. The *silanol* group consists of a hydroxylated oxygen bound to silica at the broken edge of the tetrahedral sheet. Similarly, the *aluminol* group is a hydroxylated oxygen bound to aluminum at the broken edge of the octahedral sheet. In terms of reactivity, the aluminol groups chemisorb metals better than the silanol groups based on the difference in the metal valence (Si(IV) vs. Al(III)) to coordination number ratio (McBride, 1994). The reactivity of all of these groups is strongly dependent on the pH and as such they are considered variably charged.

To evaluate the type of adsorption mechanism that is occurring, adsorption isotherms and models are traditionally used. The caveat of these experiments is that they cannot definitively determine the adsorption mechanism, but only provide an initial assessment to later be proven by more direct methods such as x-ray spectroscopy.

1.2.3 Precipitation

Precipitation generally refers to the formation of an *insoluble* solid from the reaction of ionic compounds in solution (Ebbing 1993). In bulk solution, the thermodynamic probability of precipitation can be determined by the saturation index (SI) which relates the ion activity product (IAP) and the solubility product constant (Ksp) as described by the following equation: SI= log (IAP/Ksp). The IAP is the *measured* activity (i.e. reactivity per unit vol.) of ions in solution that comprise a solid phased at any given time, and the Ksp is the *calculated* solubility constants for the reactants and products at *equilibrium* (assuming a pure solid and infinitely dilute solution). The distinction between the IAP and the Ksp is subtle, and the expressions look virtually identical. The important difference is that the IAP is an actual measure of the ion activity in solution, while the Ksp is based on equilibrium values; a condition rarely reached in soils. Regardless, the SI can be used to evaluate if a system is oversaturated with respect to the mineral solid phase (i.e. IAP > Ksp, or SI >1) in which case precipitation is expected to occur, undersaturated with respect to the solid phase (i.e. IAP <Ksp or SI < 1) in which case dissolution is expected to occur, or in equilibrium with respect to the solid phase in which case the system remains as is. The SI is useful for predicting if precipitation is likely to occur in bulk solution; however, it doesn't indicated if, or when it will form, nor does it take into account the presence of a solid phase (such as a mineral surface). The presence of a charged mineral surface can lower the energy barrier (activation energy) necessary for precipitation to occur and thus may induce precipitate formation even when the SI indicates the system is undersaturated. Surface induced precipitation can be further favored when the structure of the mineral surface is similar to that of the forming precipitate (i.e. steric compatibility).

Many studies in the past 10yrs have focused on defining the conditions favorable for transition metal (Cr, Ni, Co, Cu, and Zn) surface precipitate formation in lab conditions utilizing pure materials, fixed metal concentrations and a range of pH values (Fendorf et al. 1994; Scheidegger et al. 1997; O'Day et al. 1994; Scheidegger et al. 1997a; Towle et al. 1997; Xia et al. 1997; Cheah et al. 1998; Schlegel et al. 2001; Ford and Sparks 2000; Trainor et al. 2000). Characterization of the surface precipitate reveals that depending on the reaction conditions, a metal hydroxide, hydrotalcite like mixed metal layer double hydroxide (LDH) or a phyllosilicate is formed (Thompson et al. 1999; Manceau et al. 1999; Ford et al. 1999; Scheinost et al. 1999). Research from the Environmental Soil Chemistry Group of Dr. Donald Sparks on Ni and Zn has shown that with surface precipitate formation, the metal complex becomes more stable and resistant to weathering, which is indicated by a reduction in dissolvable metals (Scheckel et al. 2000; Scheckel and Sparks 2001). The increased stability has been attributed to either transition of the mixed layer double hydroxide to a more stable neo-formed phyllosilicate phase via interlayer silication (on aluminum bearing clays such as pyrophyllite) or to Ostwald ripening (on non-aluminum bearing minerals such as talc) (Ford et al. 1999; Morse and Casey 1998). A recent study by Peltier et al. (2005), found that the identity of the interlayer anion can also have an influence on the stability of the LDH phase formed. They compared their results for SO_4^{2-} and NO_3^--interlayered LDH to that of a CO_3^{2-}-interlayerd LDH (Allada et al. 2002; Allada et al. 2005) and found that it was more stable than SO_4^{2-} followed by NO_3^-. Substitution of Si for CO_3^{2-} in the interlayer resulted in an even more stable phase, confirming the earlier findings of Ford et al (1999). They also noted that the Ni-LDH phases are thermodynamically favored over $Ni(OH)_2$ precipitates when aluminum bearing clays are present, especially at pH values ≥ 6.5, and serve as precursors to the formation of more stable Ni-phyllosilicate phases.

With confirmation of surface metal precipitate formation for a number of the transition metals, the research has moved toward how other components such as organic coatings, biofilms and type of clay or oxide, influence their formation (Scheidegger et al. 1997; Scheckel and Sparks 2000; Nachtegaal and Sparks 2003, Yamaguchi et al. 2001; Roberts et al. 1999; Elzinga and Sparks 1999). From these studies it is clear that regardless of the conditions, surface precipitates seem to form at concentrations well below monolayer coverage and at pHs undersaturated according to the available thermodynamic stability constants for the metal hydroxide.

There is clearly a need to move outside of the pure laboratory systems and begin to assess whether surface metal precipitates form in natural systems and what impact they have on metal mobility and bioavailability. There is growing evidence of Zn Al-LDH formation in anthropogenically enriched field soils facilitated, in large part, by the use of synchrotron based micro-spectroscopy. Roberts et al. 2002) for example using μ-EXAFS and μ-SXRF among other techniques, were able to quantitatively speciate Zn in a heavily impacted smelter soil Similarly, Nachtegaal et al. (2005) recently showed that the majority of Zn in soils surrounding a Zn smelting facility in Belgium was comprised of Zn-LDH or phyllosilicate precursor phases. Interestingly, they noted that, unlike in the laboratory model systems, the Zn Al-LDH phases formed in soils appear to be less stable with decreasing pH

To date, there is still little evidence that Ni Al-LDH species form in natural soil systems. Roberts et. al. (1999) using bulk XAFS looked at a pH 7.5 whole soil spiked with 3mM nickel (as $NiNO_3$) and found what appeared to be the presence of a nickel LDH precipitate after 24hrs of reaction. These findings lend credence to the possibility of surface precipitate formation within field soils containing a multitude of competitive sorbents. However, there are still no studies reporting on the presence of Ni Al-LDH phases in anthropogenically enriched field soils.

.

1.2.4 Diffusion

Soil minerals and organic matter are composed of both macropores (>2nm) and micropores (<2nm) into which metals can become entrained, especially during the long contact times experienced in natural systems (Sparks et al., 1999). Entrapment of metal ions in mineral pores can occur via diffusion; which is a broad term describing the physical process involved in the removal of ions from the solution surrounding a mineral. Driving diffusion is a continuum of processes. Within the soil solution, ions are adsorbed from the thin film closest to the soil particle creating a gradient in ion concentrations from the bulk solution (high) to the soil particle surface (low). The gradient creates a motive force for the movement of ions toward the particle. As the metal ion moves toward the particle, it has to traverse the thin, ion depleted film (film diffusion) at the particle surface, before (if not being adsorbed) entering and moving about or along the individual particle pores (intra-particle diffusion), moving in pores between particles or moving within the particle matrix (inter-particle diffusion). Affecting this rate are the type of metal, the porosity of the mineral, and the availability of surface functional groups.

Diffusionary processes can have a pronounced effect on how fast a metal ion is removed from the soil solution or released from the particle; congruently influencing the metal's mobility and bioavailability. For example, Axe and Trivedi (2002) determined that 50, 40 and 90% of Sr, Cd and Zn sorption in HAO, HFO and HMO coatings resulted from diffusion into the microporous structure; noting that the diffusion is related to the species and sorbent characteristics. Metal coatings are ubiquitous in soil and aquatic systems. They are typically very porous, with high surface areas and high affinities for metal cations and thus are an effective sponge for metal cations. Strawn et al. (1998) found that Pb sorption and desorption at the aluminum oxide – water interface was biphasic with 75% of the Pb being removed from solution within 15 min followed by a slower sorption step that, among other possibilities, was attributed to diffusion through micropores.

1.3 Plant Soil Interface

To this point, only the physical and chemical mechanisms of metal retention, mobility and bioavailability have been considered. However, soils are not abiotic, but instead are teaming with microbes, macro-invertebrates and plant roots, each having a distinct influence on metal cycling. The rhizosphere was first defined by Hans Hiltner in 1904 as the zone of soil in which exudates from plant roots can have an influence on the activities of microorganism (Pinton et al. 2001). The thickness of the rhizosphere is not clearly delineated but depends strongly on the amount of root exudate produced and its subsequent utilization. Setting this zone apart from the bulk soil are differences in chemical, biochemical and biological processes. Most of the research since Hiltner's time has focused on the beneficial (e.g., mycorrhiza) and detrimental (e.g., nematodes) root interactions. However, with the increasing popularity of phytoremediation, some focus has turned to the mechanisms by which plants are able to remove and store large amounts of metals from soils enriched from a variety of sources.

1.3.1 Hyperaccumulators Defined

There are a number of journal articles, reviews and books on the identification and distribution of hyperaccumulating plants on ultramafic (Serpentine) and Calamine soils throughout the world (Baker and Brooks 1989; Baker et al. 2000; Brooks and Radford 1978; Brooks et al. 1990; Jaffre 1992; Morrey et al. 1992; Brooks 1998). By definition, a hyperaccumulator is a plant that is capable of removing metal from its surroundings and transporting it from the roots to the shoots, where it is stored at concentrations exceeding 1,000 μg g^{-1} dry matter (Brooks et al. 1977). These criteria hold for Ni, Co, Cu, Pb and Se, whereas Zn and Mn have a threshold of 10,000 μg g^{-1} and Cd 100 μg g^{-1} respectively (McGrath et al. 2002). Hyperaccumulators are additionally characterized by a shoot to root metal ratio >1 unlike non-hyperaccumulators which capture or preclude metals at the roots (Baker 1981). To date there have been over 400 hyperaccumulator species identified with the majority (~300) of the species hyperaccumulating Ni.

There are several hypotheses for plants having the ability to hyperaccumulate metals. Boyd and Martens 1992) summarized these as 1) tolerance mechanisms (Baker 1981), 2) disposal of metal from the plant (Severne 1974) , 3) drought resistance (Whiting et al. 2003), 4) interference with neighboring plants (Boyd and Jaffre 2001), 5) inadvertent uptake and 6) defense against herbivores (Martens and Boyd 1994; Martens and Boyd 2002; Pollard and Baker 1997; Jiang et al. 2005;Davis and Boyd 2000;Jhee et al. 1999; Huitson and Macnair 2003) . Most studies have focused on the anti-herbivory hypothesis for metal accumulation. It is more than likely, however, that more than one of these hypotheses is responsible for metal hyperaccumulation. For example, plants may isolate metals to the dermal tissues as a means of tolerating high soil metal concentrations while minimizing disruption of photosynthetic processes, which then has a corollary benefit of inhibiting herbivory from insects that feed via rasping of the dermal tissues. Regardless of why these plants have developed the ability to hyperaccumulate metals, their use provides a unique, natural opportunity for remediation of anthropogenically enriched soils or for an economic use of marginal, geogenically enriched lands.

1.3.2 Phytoremediation – Types and Potential Economic Returns

Phytoremediation is a general term referring to the use of plants to remediate soils, wastes and waters. Chaney 1983 was the first to describe the process of using plants to remove metals from enriched soils. Since this time phytoremediation has been divided into many sub-disciplines, reflecting the diversity of contaminants and the physiological function of the plants. Included under this broad definition are phytostabilization, phytoimmobilization, phytodegradation, phytovolatilization and phytoextraction. Phytostabilization and immobilization rely on plants that are metal tolerant to either prevent erosion loss of metals (mechanical stabilization) or enhance soil chemical processes that promote the adsorption or precipitation of the metals. The latter three technologies rely on hyperaccumulator plants to remove contaminants from the soil and either degrade (organics), volatilize (volatile organics, Hg or Se) or accumulate (metals) the contaminant in or from their above ground tissues. There are many examples in the literature of field scale applications of these technologies (Vangronsveld et al. 1995; Alcantara et al. 2001; Dushenkov et al. 1999; Kling 1997;O'Keeffe et al. 1996; Olson et al. 2001; Mench et al. 2003), and still more to come as the utility of phytoremediation technologies are fully realized. The focus of this dissertation will be placed on the phytoextraction of metals from anthropogenically and geogenically enriched soils.

Saxena et al. 1999 estimated that, using conventional remediation technologies (i.e. dig-and-dump) it would cost in excess of US$ 7.1 billon in the US alone to clean up metal enriched soils. Conventional remediation strategies are not only expensive, they are applicable only to relatively small, highly concentrated areas of enrichment, and rarely is there ever any economic return. Phytoextraction, however, may provide the opportunity for not only the removal of metals from vast areas of metal enrichment (such as aerial deposition from refining and smelting activities), but also the potential for economic return via phytomining.

Phytomining is a form of phytoextraction in which the above ground, metal containing plant biomass is harvested, incinerated for energy and the ash refined (Chaney, 1983). In order for phytomining to be economical, there are several plant traits that are necessary which include 1) high biomass production or, 2) a bioconcentration factor >1 (plant shoot metal concentration / topsoil metal concentration), 3) harvestability, and 4) metal tolerance mechanisms (Li et al. 2003). Li et al. (2003) point out that no natural metal hyperaccumulating plants retain all of these qualities. Therefore, research efforts have divided into two "camps" with the focus of each to create a plant that retains all of these qualities. The first camp is using conventional plant breeding and agronomic (i.e. fertilization, selective breeding etc.) methods to enhance natural high biomass producing hyperaccumulator ecotypes. The second camp is attempting to elucidate the underlying biochemical mechanisms using modern molecular genetic approaches in hopes of transferring these mechanisms to higher biomass producing plants (examples: As -Dhankher et al. 2002; Hg - Heaton et al. 1998; Se -Terry et al. 2003). Of these two approaches, the former has a higher potential for success in the short term because there is still very little known about the genetic mechanism of metal hyperaccumulation or hypertolerance.

Ultimately, in order for phytomining to be profitable, an adequate metal yield must be achieved per unit area of land. The necessary yield depends on the target metal and the world metal price. Several researchers have assessed the feasibility of using various natural hyperaccumulating species for phytomining of Zn, Cd and more recently Ni. As mentioned earlier, Chaney (1983) was the first to provide a practical description of the use of hyperaccumulators to remediate soils. Brooks et al (2001) compared *Berkheya coddii* Roessler and *Alyssum bertononii* for phytomining of Ni and found that *B. coddii* was able to achieve 110 kg Ni/ha worth about $579 based on Ni prices at the time. They estimated that planting of a *B. coddii* crop would generate more money per hectare than a crop of wheat, allowing revenue to be generated on land that would otherwise be impossible to farm, conventionally mine or remediate. Several other examples exist in the literature (Robinson et al. 1997; Robinson et al. 1999-wheat and Ni on serpentine; Anderson et al. 1999; Chaney et al. 1999; Boominathan et al. 2004; Mohan 2005; Robinson et al. 1997).

1.3.3 Metal Acquisition Strategies

While the use of plants for phytoremediation is promising, there is still little known about the mechanism plants use to extract metals from soils. Plants acquire ions from the soil solution and thus the soil chemical and physical mechanisms (adsorption, desorption, precipitation etc.) controlling ion content of the soil solution should have a significant influence on plant metal availability. For example, lowering soil pH can result in the release of metal cations into the soil solution (e.g. Al) which may be detrimental to plant growth, and conversely, raising the pH can result in nutrient deficiencies. However, just because an ion is in soil solution doesn't necessarily translate into an immediate uptake by the plant and conversely, just because an ion is strongly bound to soil particles doesn't mean it can't be taken up. Marschner 1995 pointed out that ion uptake by plants is characterized by selectivity, accumulation and genotype.

For example, there are many studies that use chemical extractants such as EDTA, DTPA or metal salts to remove metals from soils and related the removed fraction to plant accumulated metals (Misra and Pande, 1974; Haq et al, 1980). In most of these studies there is good correlation between the results, with the reagent-extracted metal representing the most labile metal pool, which intrinsically should be the most plant available species. However, in a study using *Alyssum murale* and nickel contaminated soil (the same as those used in this study), Kukier et al. (2004) found what appeared to be a counterintuitive accumulation of Ni with increasing soil pH. As the pH was raised in these systems, the plant Ni content increased. This is opposite to findings that Kukier and Chaney (2000) had for 11 agronomic crops grown on the same soils. Li et al. 1997) pointed out several possibilities for the counterintuitive pH response including: 1) *A. murale* adapted to growing in serpentine Ni rich soils with pH ranging from 6-8.5 and thus the transport channels operate more efficiently at higher pH, 2) competition with other solubilized ions, 3) organic pool labialization, 4) low Fe and Mn oxide content in the soils which, if present, would more effectively bind metals at higher pH, and 5) more efficient root exudate activity.

Regarding root exudates, few studies have examined the exudation of organic compounds (e.g. organic acids) into the rhizosphere as a potential mechanism for metal solublization and uptake. However there is little evidence that this mechanism is important in Ni hyperaccumulation. Salt et al (2000) found that the rate of Ni uptake was the same for the Ni hyperaccumulating *T. goesingense* and the non accumulator *T. arvense* suggesting that the process responsible for excessive uptake in *T. goesingense* is not an active process (i.e., facilitated by root exudates and specific membrane transporters), but instead a result of increased Ni tolerance. Similarly, Zhao et al. 2001 found that root exudates collected from *Thlaspi caerulescens* were ineffective at mobilizing or increasing the uptake of Cd, Cu, Zn or Fe in wheat or canola. Some researches have suggested that histidine plays a role in enhancing Ni uptake (Kramer et al. 1996). However, histidine-bound Ni is also found in non-accumulators and thus this is most likely not a specific response of hyperaccumulators for acquiring excessive amounts of Ni. Further research is still needed to verify the role of root exudates (if any) on increased metal acquisition in hyperaccumulators.

Once at the root, metals enter the apoplastic space where they can be bound to negatively charged cation exchange sites. Non-specific adsorption at exchange sites within the apoplastic space is effective at holding cations close to active transport sites in the plasma membrane which has been shown to indirectly enhance ion uptake (Marschner, 1995). On the contrary, some metals such as Cu can form stronger complexes within the apoplasm, accounting for the high total content of these metals within some plant roots (Marschner, 1995).

Essentially, the roots (specifically the cell wall, plasma membrane and tonoplast) of plants act as mediators, excluding the uptake of some ions while promoting the acquisition or release of others. Active uptake mechanisms have been demonstrated for many nutrient cations including $Fe, SO_4^{2-}, Cl^-, NO_3^-$, Ca^{2+} and K^+. The primary *modus operandi* occurs via an electrical potential gradient across the plasma membrane created by membrane bound proton pumps (H^+—ATPase) which are stimulated by differences in symplastic or cytosolic ion concentrations. The ions are then shuttled along the electronic potential gradient in a process mediated by membrane bound proteins or enzymes. The efflux or influx of amino acids and sugars are driven by the same proton-pump created electrical potential gradient. Ion uptake, however, isn't always an active process. Metal ions can also move into the cyctoplasm through pores in the plasma membrane via diffusion from areas of higher concentration (e.g., symplasm) to areas of lower concentration (within the cytoplasm)

(Marschner, 1995). In addition, ion channels provide another passive mechanism for ion movement into the cell.

As it pertains to metal transport and hyperaccumulation, membrane transporters (i.e., proteins or enzymes) have been genetically isolated for metals which have essential roles in plant metabolism (e.g. Fe and chlorophyll; Zn-enzymes). Isolation of metal transporters have been identified primarily through functional complementation in yeast strains for Zn (Assuncao et al. 2001; Pence et al. 2000; Kim et al. 2004; Lasat et al. 2000) and Fe (Eide et al. 1996; Thomine et al. 2003). There is little evidence of a specific membrane bound transporter for Ni.

As a final note, it is generally thought that microorganisms do not play a significant role in increasing the uptake of metals from the rhizosphere. However, Abou-Shanab et al. 2003; Abou-Shanab et al. 2003 found that Rhizobacterium in the rhizosphere of A. murale were effective at solublizing Ni and thus enhancing uptake. Additional research is necessary to confirm or dispel the role of microbes in metal acquisition.

1.3.4 Metal Transport and Compartmentalization

Several researchers have focused on deciphering the biochemical mechanisms plants use to tolerate high metal concentrations in their above ground tissue. The proposed species involved in metal transport and storage within the plant include organic and amino acids (Sarret et al. 2002; Salt et al. 1999; Kramer et al. 1996; Kramer et al. 1997; Sagner et al. 1998; Persans et al. 1999; Homer, 1991; Baker et al.

1983; Kerkeb and Kramer 2003; Lee et al. 1977; Vergnano and Gabbrielli 1987; Pelosi et al. 1976; Lee, 1978) and/or metallothioneins (MT) which include enzymes (transpeptidase), phytochelatins (numerous) and cysteine-rich proteins (Polette et al. 2000; Garcia-Hernandez et al. 1998).

In most of these studies, the primary mechanism of metal transport and tolerance appears to be complexation to organic acids with the most prominent being citrate, malate, malonate and histidine. No evidence is available to infer that phytochelatins are involved in the hyperaccumulation of Ni. Phytochelatin production is an energy intensive process, and one that the plant would most likely avoid using unless sufficiently stressed, preferring instead to use readily available organic and amino acids.

Once transported to the shoots, plants have adapted a variety of ways in which to cope with the increased metal concentrations, depending upon metal variety and plant species. Heath et al. 1997 found that the location of Ni in *Thlaspi montanum* to be in the subsidiary cells surrounding the guard cells but not in the guard cells themselves. Frey et al. 2000 found a similar exclusion of Zn from the guard and subsidiary cells in the leaves of *Thlasi caerulescens*, also noting that while a majority of Zn was in the vacuoles of the epidermal cells, there was also Zn in the cell wall and mesophyll. Looking at three nickel hyperaccumulators, *Alyssum lesbiacum*, *A. bertolonii* and *T. goesingense*, Kupper et al. 2001 found nickel to be preferentially located in the epidermal cells of the leaves and stems, most likely in the vacuoles, with a second peak within the boundary cells between the vascular bundle and the cortical parenchyma of the stems. They also noted the absence of nickel from the calcium rich trichomes on the leaf surface with minor amounts at the base. Kupper et al. 2000 observed a similar appearance of concentrated metal at the base of the trichome when looking at the accumulation of Zn in the Zn hyperaccumulator *Arabidopsis halleri*. However, they concluded from that study that a majority of the Zn was found in the mesophyll cells compared to the epidermal cells. This result is contradictory to the pattern of Zn accumulation observed by Kupper et al. 1999 in a similar study of Zn in *T.i caerulescens*, where, as in previous studies, epidermal vacuole localization was the primary mechanism. They did note, however, that the epidermal cells were small compared to the mesophyll cells, which may account for their apparent low metal concentrations. Kramer et al. 1997), examining *Alyssum lesbiacum* by nuclear microscopy using μ-PIXE (photo ionization X-ray emission), found Ni to be concentrated predominantly in the trichomes on the surface of the leaf. This pattern, however, was not seen in other studies with the exception of the regions of concentrated Zn and Ni observed in the basal cells of the trichome. This discrepancy is most likely the result of differing sample preparations (shock freezing vs. chemical substitution and freezing) and/or technique (SEM-EDAX vs. NM μ-PIXE).

Summarizing these studies, it is clear that in most hyperaccumulating plants metals accumulate within the vacuole of the epidermal cells and are absent from the guard and subsidiary cells within the stomatal complex. However, there is variability among species, with some observing non-typical accumulations within the mesophyll, the cells between the cortical parenchyma and vascular bundle, and at the base of the trichome.

1.4 Multidisciplinary, Multitechnique Approaches To Investigate the Plant-Soil Interface.

The research contained in this dissertation relies on the use of multiple chemical and physical techniques to ascertain the behavior of Ni in both plant and soil systems. These techniques include: total metal analysis, sequential extraction, ion chromatography (IC), scanning electron microscopy (SEM), attenuated total reflectance, Fourier transform infrared spectroscopy (ATR-FTIR), x-ray absorption fine structure spectroscopy (XAFS), synchrotron based x-ray fluorescence (SXRF) and absorption edge and fluorescence computed microtomographies (CMT). An abundance of research has been dedicated to the refinement of each of these techniques individually, however the application of them together to assess the chemical behavior of Ni in the soil and plant systems studied in this dissertation reflects the author's philosophy that "multi-component systems require multi-technique approaches". The most important of the techniques used have been those based on synchrotron radiation because they provide a direct measure of the metal speciation within a variety of organic and inorganic systems with very little necessary sample pretreatment.

1.4.1 Synchrotron X-ray Spectroscopy

As alluded to earlier, bulk- XAFS techniques only provide an idea of the average speciation of a metal over a few cubic millimeters. In such a case, high Z elements, when coordinated to the central absorbing atom, tend to dominate the spectra, making detection of minor but potentially significant species impossible (Manceau et al, 2000). As such, it is difficult to interpret the spectra from bulk techniques since they may be comprised of several minor species, making fitting the data accurately difficult if not impossible. With increasing instrumental sensitivity and spatial resolution of synchrotron-based techniques, together with enlarging reference databases, it is likely that the previous shortcomings can be surmounted. Manceau et al (2002) have outlined a procedure on using synchrotron-based techniques to properly ascertain metal speciation within soil samples. By using bulk XAFS, it is possible to find the compositionally dominant species within the sample, and then using micro-spectroscopic tools such as μ-XAFS, μ-SXRF, μ-XRD and μ-tomography minor yet potentially more reactive components can be detected. A typical μ-XAFS experiment (Fig. 1) begins by first collecting X-ray fluorescence elemental maps from which metal correlations can be observed. From these maps, regions of interest (i.e., hotspots) are selected and further probed using the microfocused X-ray beam. Analysis of XAFS spectra collected from multi-component systems cannot rely on traditional fitting procedures in which the spectra are broken down into individual atomic shells. Therefore, to determine the species present within a mixed system, a dataset of spectra from multiple spots throughout a sample are

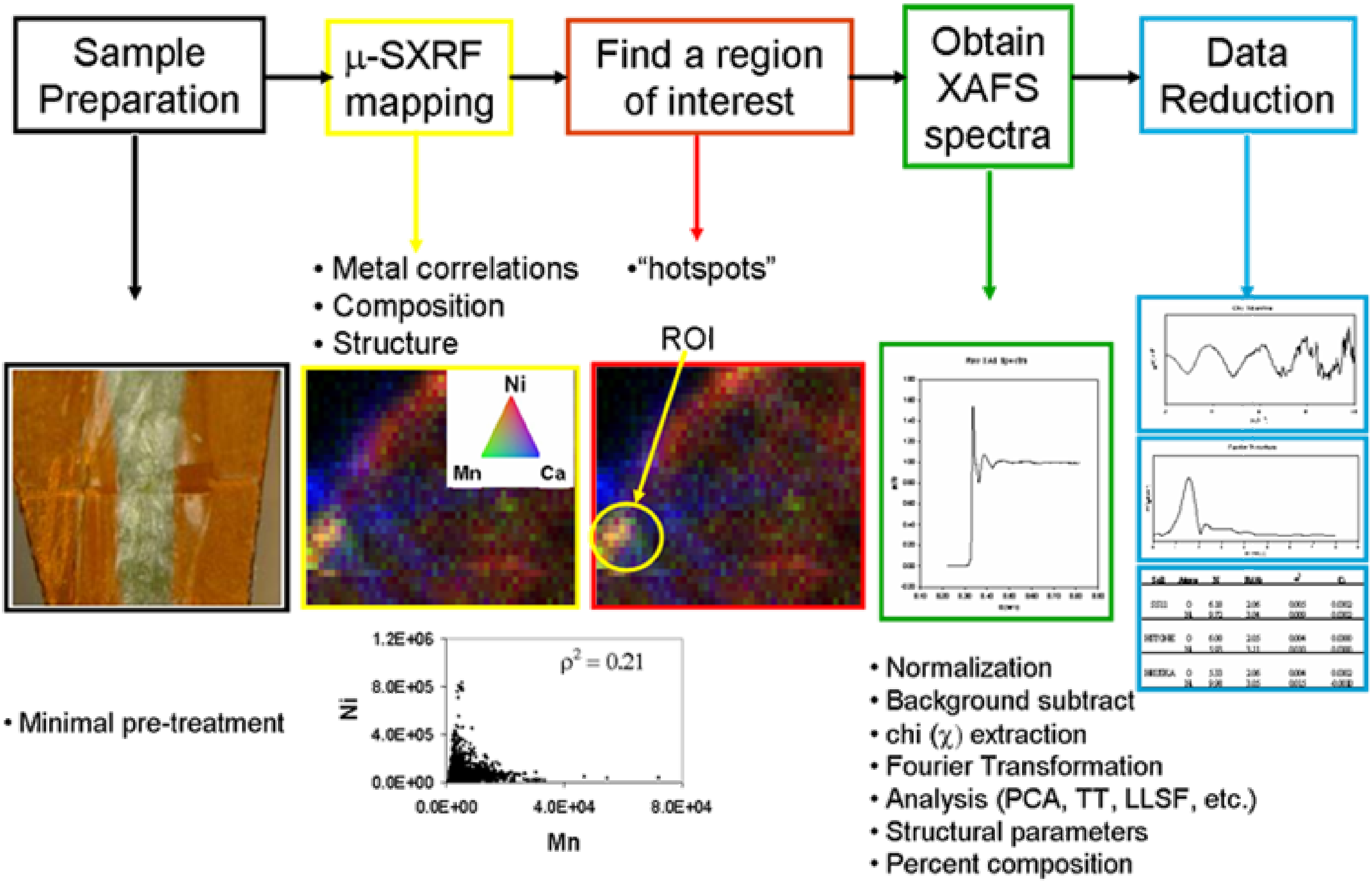

Sample Preparation

μ-SXRF mapping

Find a region of interest

Obtain XAFS spectra

Data Reduction

- Metal correlations
- Composition
- Structure

- “hotspots”

ROI

- Minimal pre-treatment

- Normalization
- Background subtract
- chi (χ) extraction
- Fourier Transformation
- Analysis (PCA, TT, LLSF, etc.)
- Structural parameters
- Percent composition

analyzed statistically using principal component analysis (PCA). The PCA technique determines if the data set can be described as weighted sums of a smaller number of components, which would be the case if each spot in the dataset is comprised of a smaller number of distinct compounds. Target transformation (TT) is then used to identify the components by taking a spectrum of a known reference compound and mathematically removing from the spectrum anything that does not look like the principle components identified by PCA. If minimal information has to be removed from the known reference spectrum, then one can conclude it is most likely present in the sample. After the contributing standard phases are identified, linear least squares fitting (LLSF) is used to determine the number of components and amount (%) of each standard species within the individual sample spectra making up the dataset. The accuracy of this fitting approach is dependent upon the data quality, the completeness of the standards data set, and the range over which the data were fit. Additional and more thorough discussions on μ-XAFS applications and methods of data collection and analysis for contaminants in heterogeneous systems can be found in Bertsch and Hunter (2001) and Manceau et al. (2002).

1.5 Research Justification

1.5.1 Port Colborne: A Metal Refining Legacy

The International Nickel Company (INCO) in Port Colborne, Ontario, Canada operated a Ni refining operation on the shore of Lake Erie for almost 70 years (1918-1984). During this period, the refinery went through five distinct operating phases, distinguishable by the type of ore and the refining process used (Jacques Whitford Environmental 2001c). From 1918 to 1930, impure copper-nickel sulphide was refined using the Orford Process, a pyrometallurgical method which uses sodium sulfate to separate Ni from copper. From 1931 to 1938, the Orford process was replaced with reverberatory-type furnaces in which nickel sulphide was converted to nickel oxide and then further processed using electro-refining to produce Ni metal. From 1939 to 1959 a nickel-sulfide concentrate was first sintered to “aggregate fine particulates”, and to drive off SO_2, and then refined using both reverberatory furnaces and electrolyte baths to produce Ni metal. From 1960 to 1979 both NiO and NiS mattes were refined using electrolyte baths and electro-refining. In 1984, Ni refining ceased.

During its operational life, 7 billion pounds of electrolytic Ni were produced. While emissions were not monitored, it is estimated that 18,000 tones of Ni was emitted by the refinery, 97% occurring before 1960, and the majority (11,466 tones) occurring between 1939 and 1959 (Jacques Whitford Environmental 2001c). Particulate emissions during this time would have likely included nickel subsulfide, nickel carbonate, nickel hydroxides, nickel oxide, nickel sulfate and nickel metal. The emission emanated from two stacks that, in their original construction were 350 feet, but were raised to nearly 500 feet in the 1930’s and used until nickel operations ceased (Conrad 2001).

The combination of stack height and unmonitored emission resulted in the enrichment of soils throughout the Port Colborne area (Figure 1.2). Twenty-nine square kilometers of soils contain Ni concentrations in excess of the Canadian

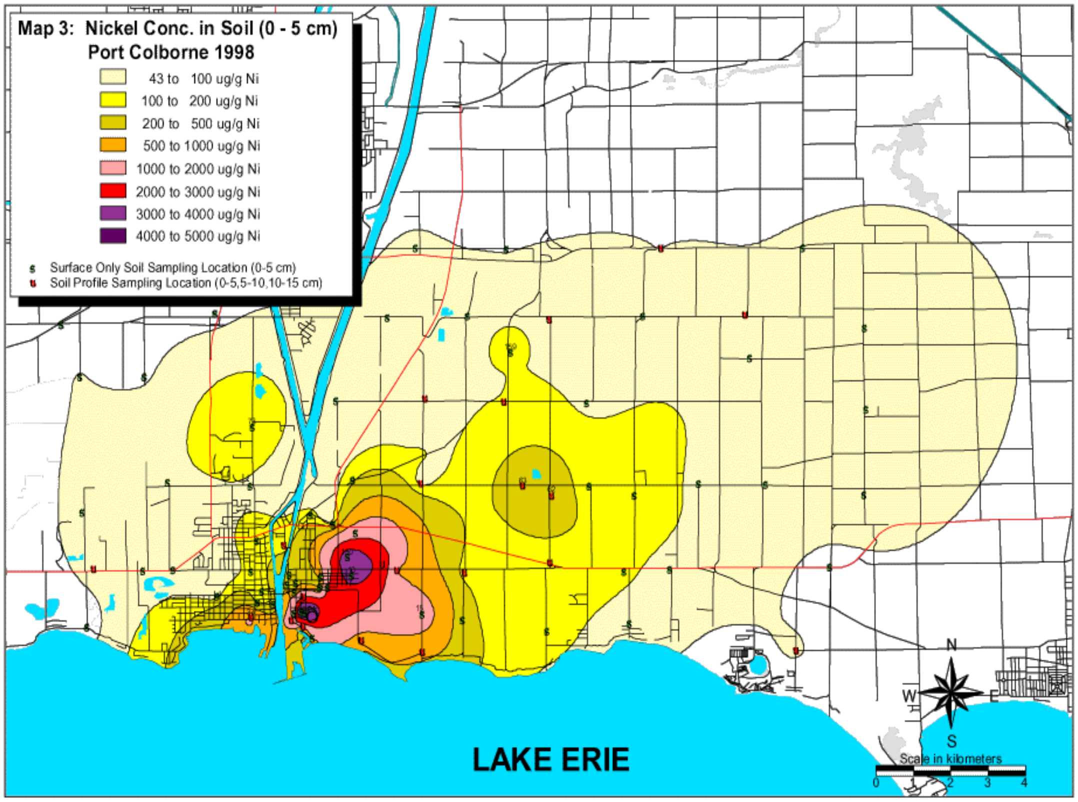

Figure 1.2: Ni concentration in the top 0-5 cm of soil surrounding the nickel refinery in Port Colborne, Ontario Canada. The isotherm encompassing the beige area represents 345km^2 exceeding 45 mg/kg Ni. The area in yellow (~29 km^2) exceeds the Canadian Ministry of the Environment (MOE) phytotoxicity threshold and thus requires cleanup.

Ministry of the Environment (MOE) phytotoxicity based action level of 200 μg /g. Estimated clean up costs using traditional methods (dig-and-dump) would cost upwards of US$ 8.7 billion (2900 ha @ $3 million/ha).

The need to find an alternative method of managing the vast area of soil enrichment around this site provides the social and economic impetus behind this research. The scientific motivation comes from the desire to understand how the different soil types and treatment have influenced the Ni speciation and what impact this speciation has on the bioavailability of Ni. Specifically, our interests are in determining if the degradation of aerially deposited Ni has resulted in the formation of more stable nickel phases (i.e. surface precipitate) as well as the biochemical mechanisms responsible for excess Ni accumulation in *Alyssum murale* 'Kotodesh'.

1.6 Research Objectives

The three primary objectives of the research can be summarized as follow:

1. Determine the influence of soil type and remediation on the speciation and bioavailability of Ni in refinery impacted soils,

This objective will be addressed in Chapter 2 where we used chemical, microscopic and spectroscopic tools to evaluate Ni speciation in field soils collected form test plots established by Dr. Rufus Chaney (Agronomist, USDA-ARS Beltseville) adjacent to the Ni refinery in Port Colborne. The chemical techniques include total elemental analysis, sequential extraction and a stirred-flow method to assess Ni dissolution. These methods provide an initial idea of the relative chemical forms of Ni present as well their persistence. Electron microscopy was used to assess the morphology of Ni within the soils as well as any associations with lighter elements (e.g. Si, Al) undetectable by X-ray spectroscopy. The use of bulk and micro-synchrotron X-ray spectroscopy (both μ-SXRF and μ-EXAFS) were used to obtain direct chemical and spatial information on the distribution and elemental associations of Ni species in the various soils. Principal component analysis and linear least squares fitting was then be used to quantify the Ni speciation within the samples.

2. To determine the biochemical mechanism of Ni transport and storage in the Ni hyperaccumulator *Alyssum murale* 'Kotodesh'.

This objective will be addressed in Chapter 3 where synchrotron based X-ray fluorescence and extended X-ray absorption fine structure spectroscopy, ion chromatography and attenuated total reflectance Fourier transform infrared spectroscopy were used to determine what chemical form *A. murale* uses to store and transport Ni. *Alyssum murale* was chosen because it is one of the only plants shown to be an effective and commercially viable phytoremediation and phytomining technology for the remediation of vast areas of enriched soils (Chaney et al. 1999; Li et al. 2003; Li et al. 2003).

3. To determine where Ni is stored in *Alyssum murale* 'Kotodesh' using novel synchrotron-based X-ray computed micro-tomography

In Chapter 4 synchrotron based computed microtomographies were used to assess and quantify the distribution of Ni in root stem and leaf tissues. This work was published in Environmental Science and Technology 2005: 39(7), 2210-2218. This objective arose from a desire to find a more direct, *in vivo* method of determining how hyperaccumulating plants store metals within selected living plant tissues. Current methods (e.g. SEM) require that the sample be fixed (e.g., shock frozen and freeze-dried) and fractured prior to analysis, which may alter the metal distribution or speciation. We have attempted to "get around" the fixation limitation by using absorption edge tomography which is effective at determining the amount and three-dimensional distribution of the highest metal concentrations throughout hydrated leaf and stem tissues.

1.8 References

Abou-Shanab RA, Angle JS, Delorme TA, Chaney RL, van Berkum P, Moawad H, Ghanem K, Ghozlan HA (2003) Rhizobacterial effects on nickel extraction from soil and uptake by *Alyssum murale*. New Phytologist 158: 219-224

Abou-Shanab RI, Delorme TA, Angle JS, Chaney RL, Ghanem K, Moawad H, Ghozlan HA (2003) Phenotypic characterization of microbes in the rhizosphere of *Alyssum murale*. International Journal of Phytoremediation 5: 367-379

Alcantara E, Barra R, Benlloch M, Ginhas A, Jorrin JV, Lopez JA, Lora A, Ojeda MA, Puig M, Pujadas A, Requejo R, Romera J, Ruso J, Sancho ED, Shilev SI, Tena M (2001) Phytoremediation of a metal contaminated area in Southern Spain. Minerva Biotecnologica 13: 33-35

Allada RK, Navrotsky A, Berbeco HT, Casey WH (2002) Thermochemistry and aqueous solubilities of hydrotalcite-like solids. Science 296: 721-723

Allada RK, Navrotsky A, Boerio-Goates J (2005) Thermochemistry of hydrotalcite-like phases in the MgO-Al_2O_3-CO_2-H_2O system: A determination of enthalpy, entropy and free energy of hydrotalcite-like solids. American Mineralogist 90: 329-355

Anderson CWN, Brooks RR, Chiarucci A, LaCoste CJ, Leblanc M, Robinson BH, Simcock R, Stewart RB (1999) Phytomining for nickel, thallium and gold. Journal of Geochemical Exploration 67: 407-415

Assuncao AGL, Martins PD, De Folter S, Vooijs R, Schat H, Aarts MGM (2001) Elevated expression of metal transporter genes in three accessions of the metal hyperaccumulator Thlaspi caerulescens. Plant Cell and Environment 24: 217-226

Baker AJM (1981) Accumulators and excluders - strategies in the response of plants to heavy metals. Journal of Plant Nutrition 3: 643-654

Baker AJM, Brooks RR (1989) Terrestrial higher plants which hyperaccumulate metal elements: A review of their distribution, ecology, and phytochemistry. Biorecovery: 81-126

Baker AJM, McGrath SP, Reeves RR, Smith JAC (2000) Metal hyperaccumulator plants: A review of the ecology and physiology of a biological resource for phytoremediation of metal-polluted soils. In: Terry N, Banuelos G, Vangronsveld J (ed) Phytoremediation of contamined soil and water, Lewis Publisher,Boca Raton, pp 85-107

Baker EN, Baker HM, Anderson BF, Reeves RD (1983) Chelation of nickel(II) by citrate. The crystal structure of a nickel-citrate complex, $K_2[Ni(C_6H_5O_7)(H_2O)_2]_{2.4}H_2O$. Inorganica Chimica Acta 78: 281-285

Boominathan R, Saha-Chaudhury NM, Sahajwalla V, Doran PM (2004) Production of nickel bio-ore from hyperaccumulator plant biomass: Applications in phytomining. Biotechnology and Bioengineering 86: 243-250

Boyd RS, Jaffre T (2001) Phytoenrichment of soil Ni content by Sebertia acuminata in New Caledonia and the concept of elemental allelopathy. South African Journal of Science 97: 535-538

Boyd RS, Martens SN (1992) The Raison d'etre for metal hyperaccumulation by plants. In: Baker AJM, Proctor J, Reeves RD (ed) The Vegetation of Ultramafic (Serpentine) Soils, Intercept Ltd.,Andover, Hampshire, U.K., pp 279-289

Brady NC, Weil RR (2002) The Nature and Property of Soils. 13th edition. Prentice Hall, New York

Brooks RR (1998) Plants That Hyperaccumulate Heavy Metals: Their Role in Archaeology, Microbioloy, Mineral Exploration, Phytomining and Phytoremediation. CAB International, Wallingford

Brooks RR, Lee J, Reeves RD, Jaffre T (1977) Detection of nickeliferous rocks by analysis of herbarium specimens of indicator plants. J. Geochem. Explor. 7: 49-57

Brooks RR, Radford CC (1978) Nickel Accumulation by European Species of Genus Alyssum. Proceedings of the Royal Society of London Series B-Biological Sciences 200: 217-224

Brooks RR, Reeves RD, Baker AJM, Rizzo JA, Diaz-Ferreira H (1990) The Brazilian serpentine plant expedition (BRASPEX) - April/May 1988. National Geographic Research 6: 205-219

Chaney R (1983) Plant uptake of inorganic waste constituents. In: Parr JF, Marsh PB, Kla JM (ed) Land treatment of hazardous wastes, Noyes Data Corp,Park Ridge, NJ, pp 50-76

Chaney R, Angle J, Baker A, Li Y (1999) Method for phytomining of nickel, cobalt, and other metals from soil. US Patent No. 5,944,872 issued Aug 31, 1999 (Continuation in part of US Patent 5,711,784), issued Jan. 27, 1998

Cheah SF, Brown GE, Parks GA (1998) XAFS spectroscopy study of Cu(II) sorption on amorphous SiO_2 and gamma-Al_2O_3: Effect of substrate and time on sorption complexes. Journal of Colloid and Interface Science 208: 110-128

Conrad B (2001) Wilfred Robert Pearson vs. INCO Limited. Ontario Superior Court of Justice 12023/01: 1

Davis MA, Boyd RS (2000) Dynamics of Ni-based defense and organic defenses in the Ni hyperaccumulator, *Streptanthus polygaloides* (Brassicaceae). New Phytologist 146: 211-217

Dhankher OP, Li YJ, Rosen BP, Shi J, Salt D, Senecoff JF, Sashti NA, Meagher RB (2002) Engineering tolerance and hyperaccumulation of arsenic in plants by combining arsenate reductase and gamma-glutamylcysteine synthetase expression. Nature Biotechnology 20: 1140-1145

Dushenkov S, Mikheev A, Prokhnevsky A, Ruchko M, Sorochinsky B (1999) Phytoremediation of radiocesium-contaminated soil in the vicinity of Chernobyl, Ukraine. Environmental Science & Technology 33: 469-475

Ebbing DD (1993) General Chemistry. 4th edition. Haughton Mifflin Co., Boston

Eide D, Broderius M, Fett JP, Guerinot ML (1996) A novel iron-regulated metal transporter from plants identified by functional expression in yeast. Proc Natl Acad Sci USA 93: 5624-5628

Elzinga EJ, Sparks DL (1999) Nickel sorption mechanisms in a pyrophyllite-montmorillonite mixture. Journal of Colloid and Interface Science 213: 506-512

Fendorf SE, Sparks DL, Lamble GM, Kelley MJ (1994) Applications of X-Ray absorption fine structure spectroscopy to soils. Soil Science Society of America Journal 58: 1583-1595

Ford RG, Scheinost AC, Scheckel KG, Sparks DL (1999) The link between clay mineral weathering and the stabilization of Ni surface precipitates. Environmental Science & Technology 33: 3140-3144

Ford RG, Sparks DL (2000) The nature of Zn precipitates formed in the presence of pyrophyllite. Environmental Science & Technology 34: 2479-2483

Frey B, Keller C, Zierold K, Schulin R (2000) Distribution of Zn in functionally different leaf epidermal cells of the hyperaccumulator Thlaspi caerulescens. Plant Cell and Environment 23: 675-687

Garcia-Hernandez M, Murphy A, Taiz L (1998) Metallothioneins 1 and 2 have distinct but overlapping expression patterns in Arabidopsis. Plant Physiology 118: 387-397

Heath SM, Southworth D, Dallura JA (1997) Localization of nickel in epidermal subsidiary cells of leaves of *Thlaspi montanum* var siskiyouense (Brassicaceae) using energy-dispersive x-ray microanalysis. Int. J. Plant Sci. 158: 184-188

Heaton ACP, Rugh CL, Wang NJ, Meagher RB (1998) Phytoremediation of mercury- and methylmercury-polluted soils using genetically engineered plants. Journal of Soil Contamination 7: 497-509

Huitson SB, Macnair MR (2003) Does zinc protect the zinc hyperaccumulator Arabidopsis halleri from herbivory by snails? New Phytologist 159: 453-459

Jacques Whitford Environmental L (2001c) Draft report on potential CoC identification using emission inventories and dispersion modelling of Inco and Algoma operations. JWEL Project No. Omt34648. November 23, 2001

Jaffre T (1992) Floristic and ecological diversity of the vegetation on ultramafic rocks in New Caledonia. In: Baker AJM, Proctor J, Reeves RD (ed) The Vegetation of Ultramafic (Serpentine) Soils, Inercept,Andover, Hampshire, U.K., pp 101-107

Jhee EM, Dandridge KL, Christy Jr. AM, Pollard JA (1999) Selective herbivory on low-zinc phenotypes of the hyperaccumulator *Thlaspi caerulescens* (Brassicaceae). Chemoecology 9: 93-95

Jiang RF, Ma DY, Zhao FJ, McGrath SP (2005) Cadmium hyperaccumulation protects *Thlaspi caerulescens* from leaf feeding damage by thrips (*Frankliniella occidentalis*). New Phytologist *167*: 805-814

Kerkeb L, Kramer U (2003) The role of free histidine in xylem loading of nickel in *Alyssum lesbiacum* and *Brassica juncea*. Plant Physiology 131: 716-724

Kim D, Gustin JL, Lahner B, Persans MW, Baek D, Yun D-J, Salt DE (2004) The plant CDF family member TgMTP1 from the Ni/Zn hyperaccumulator Thlaspi goesingense acts to enhance efflux of Zn at the plasma membrane when expressed in Saccharomyces cerevisiae. The Plant Journal 39: 237-251

Kling J (1997) Phytoremediation of organics moving rapidly into field trials. Environmental Science & Technology 31: A129-A129

Kramer U, Cotter-Howells JD, Charnock JM, Baker AJM, Smith JAC (1996) Free histidine as a metal chelator in plants that accumulate nickel. Nature 379: 635-638

Kramer U, Grime GW, Smith JAC, Hawes CR, Baker AJM (1997) Micro-PIXE as a technique for studying nickel localization in leaves of the hyperaccumulator plant *Alyssum lesbiacum*. Nucl. Instrum. Methods Phys. Res., Sect. B 130: 346-350

Kramer U, Smith RD, Wenzel WW, Raskin I, Salt DE (1997) The role of metal transport and tolerance in nickel hyperaccumulation by *Thlaspi goesingense Halacsy*. Plant Physiology 115: 1641-1650

Kupper H, Lombi E, Zhao FJ, McGrath SP (2000) Cellular compartmentation of cadmium and zinc in relation to other elements in the hyperaccumulator *Arabidopsis halleri*. Planta 212: 75-84

Kupper H, Lombi E, Zhao FJ, Wieshammer G, McGrath SP (2001) Cellular compartmentation of nickel in the hyperaccumulators *Alyssum lesbiacum*, *Alyssum bertolonii* and *Thlaspi goesingense*. Journal of Experimental Botany 52: 2291-2300

Kupper H, Zhao FJ, McGrath SP (1999) Cellular compartmentation of zinc in leaves of the hyperaccumulator *Thlaspi caerulescens*. Plant Physiology 119: 305-311

Lasat MM, Pence NS, Garvin DF, Ebbs SD, Kochian LV (2000) Molecular physiology of zinc transport in the Zn hyperaccumulator *Thlaspi caerulescens*. Journal of Experimental Botany 51: 71-79

Lee J, Reeves RD, Brooks RR, Jaffre T (1977) Isolation and identification of a citrato-complex of nickel from nickel-accumulating plants. Phytochemistry 16: 1503-1505

Li Y-M, Chaney RL, Brewer EP, Angle JS, Nelkin J (1997) Phytoextraction of Nickel and cobalt by hyperaccumulator alyssum species grown on nickel-contaminated soils. Environ Sci Technol 37: 1463-1468

Li Y-M, Chaney RL, Brewer EP, Angle JS, Nelkin J (2003) Phytoextraction of nickel and cobalt by hyperaccumulator *Alyssum* species grown on nickel-contaminated soils. Environ. Sci. Technol. 37: 1463-1468

Li Y-M, Chaney RL, Brewer EP, Roseberg R, Angle JS, Baker AJM, Reeves R, Nelkin J (2003) Development of a technology for commercial phytoextraction of nickel: economic and technical considerations. Plant and Soil 249: 107-115

Manceau A, Schlegel M, Nagy KL, Charlet L (1999) Evidence for the formation of trioctahedral clay upon sorption of Co^{2+} on quartz. Journal of Colloid and Interface Science 220: 181-197

Marschner H (1995) Mineral Nutrition of Higher Plants. Second. Academic Press, San Diego, CA, U.S.A.

Martens SN, Boyd RS (1994) The ecological significance of nickel hyperaccumulation - a plant-chemical defense. Oecologia 98: 379-384

Martens SN, Boyd RS (2002) The defensive role of Ni hyperaccumulation by plants: A field experiment. American Journal of Botany 89: 998-1003

McGrath SP, Zhao FJ, Lombi E (2002) Phytoremediation of metals, metalloids, and radionuclides. Advances in Agronomy 75: 1-56

Mench M, Bussiere S, Boisson J, Castaing E, Vangronsveld J, Ruttens A, De Koe T, Bleeker P, Assuncao A, Manceau A (2003) Progress in remediation and revegetation of the barren Jales gold mine spoil after in situ treatments. Plant and Soil 249: 187-202

Mohan BS (2005) Phytomining of gold. Current Science 88: 1021-1022

Morrey DR, Balkwill K, Balkwill M-J, Williamson S (1992) A review of some studies of the serpentine flora of Southern Africa. In: Baker AJM, Proctor J, Reeves RD (ed) The Vegetation of Ultramafic (Serpentine) Soils, Intercept Ltd.,Andover, Hampshire, U.K., pp 147-157

Morse JW, Casey WH (1998) Ostwald processes and mineral paragenesis in sediments. American Journal of Science 288: 537-560

Nachtegaal M, Jacobsen CJ, Sparks DL (2003) X-ray microscopy and C1SNEXAFS studies of 3D metal interactions with humic acid. Abstracts of Papers of the American Chemical Society 225: U931-U931

Nachtegaal M, Sparks DL (2003) Nickel sequestration in a kaolinite-humic acid complex. Environmental Science & Technology 37: 529-534

O'Day PA, Parks GA, Brown GE (1994) Molecular structure and binding sites of cobalt(II) surface complexes on kaolinite from X-ray absorption spectroscopy. Clays and Clay Minerals 42: 337-355

O'Keeffe B, Horn S, Cope V, Lavoie K, OKeeffe D (1996) Phytoremediation of metal finishing wastes. An on-site study using the water hyacinth (Eichhornia crassipes). Abstracts of Papers of the American Chemical Society 212: 111-Agro

Olson PE, Flechter JS, Philp PR (2001) Natural attenuation/phytoremediation in the vadose zone of a former industrial sludge basin. Environmental Science and Pollution Research 8: 243-249

Pelosi P, Fiorentini R, Galoppini C (1976) On the nature of nickel compounds in Alyssum bertolonii. Agr. Biol. Chem 40: 1641-1642

Pence NS, Larsen PB, Ebbs SD, Letham DLD, Lasat MM, Garvin DF, Eide D, Kochian LV (2000) The molecular physiology of heavy metal transport in the Zn/Cd hyperaccumulator Thlaspi caerulescens. Proceedings of the National Academy of Sciences of the United States of America 97: 4956-4960

Persans MW, Yan XG, Patnoe JMML, Kramer U, Salt DE (1999) Molecular dissection of the role of histidine in nickel hyperaccumulation in Thlaspi goesingense (Halacsy). Plant Physiology 121: 1117-1126

Pinton R, Varanini Z, Nannipieri P (2001) The rhizosphere as a site of biochemical interactions among soil components, plants and microorganisms. In: Pinton R, Varanini Z, Nannipieri P (ed) The Rhizosphere: biochemistry and organic substances at the soil-plant interface, Marcel Dekker, Inc.,New York, pp 424

Polette LA, Gardea-Torresdey JL, Chianelli RR, George GN, Pickering IJ, Arenas J (2000) XAS and microscopy studies of the uptake and bio-transformation of copper in Larrea tridentata (creosote bush). Microchemical Journal 65: 227-236

Pollard AJ, Baker AJM (1997) Deterrence of herbivory by zinc hyperaccumulation in *Thlaspi caerulescens* (Brassicaceae). New Phytologist 135: 655-658

Roberts DR, Scheidegger AM, Sparks DL (1999) Kinetics of mixed Ni-Al precipitate formation on a soil clay fraction. Environmental Science & Technology 33: 3749-3754

Roberts DR, Scheinost AC, Sparks DL (2002) Zinc speciation in a smelter-contaminated soil profile using bulk and microspectroscopic techniques. Environmental Science & Technology 36: 1742-1750

Robinson BH, Brooks RR, Clothier BE (1999) Soil Amendments Affecting Nickel and Cobalt Uptake by Berkheya coddii: Potential Use for Phytomining and Phytoremediation. Annals of Botany 84: 689-694

Robinson BH, Brooks RR, Howes AW, Kirkman JH, Gregg PEH (1997) The potential of the high-biomass nickel hyperaccumulator Berkheya coddii for phytoremediation and phytomining. Journal of Geochemical Exploration 60: 115-126

Sagner S, Kneer R, Wanner G, Cosson JP, Deus-Neumann B, Zenk MH (1998) Hyperaccumulation, complexation and distribution of nickel in *Sebertia acuminata*. Phytochemistry 47: 339-347

Salt DE, Prince RC, Baker AJM, Raskin I, Pickering IJ (1999) Zinc ligands in the metal hyperaccumulator *Thlaspi caerulescens* as determined using x-ray absorption spectroscopy. Environmental Science & Technology 33: 713-717

Sarret G, Saumitou-Laprade P, Bert V, Proux O, Hazemann JL, Traverse AS, Marcus MA, Manceau A (2002) Forms of zinc accumulated in the hyperaccumulator Arabidopsis halleri. Plant Physiology 130: 1815-1826

Saxena PK, KrishnaRaj S, Dan T, Perras MR, Vettakkorumakankav NN (1999) Phytoremediation of Heavy Metal Contamination and Polluted Soils. In: Prasad MNV, Hagemeyer J (ed) Heavy Metal Stress in Plants: From Molecules to Ecosystems, Springer,Berlin, pp 402

Scheckel KG, Scheinost AC, Ford RG, Sparks DL (2000) Stability of layered Ni hydroxide surface precipitates - A dissolution kinetics study. Geochimica Et Cosmochimica Acta 64: 2727-2735

Scheckel KG, Sparks DL (2000) Kinetics of the formation and dissolution of Ni precipitates in a gibbsite/amorphous silica mixture. Journal of Colloid and Interface Science 229: 222-229

Scheckel KG, Sparks DL (2001) Dissolution kinetics of nickel surface precipitates on clay mineral and oxide surfaces. Soil Science Society of America Journal 65: 685-694

Scheidegger AM, Lamble GM, Sparks DL (1997) Monitoring the growth of secondary precipitates upon metal sorption on clay minerals and aluminum oxides using X-ray absorption fine structure (XAFS) spectroscopy. Abstracts of Papers of the American Chemical Society 213: 69-GEOC

Scheidegger AM, Lamble GM, Sparks DL (1997a) Spectroscopic Evidence for the Formation of Mixed-Cation Hydroxide Phases upon Metal Sorption on Clays and Aluminum Oxides. Journal of Colloid and Interface Science 186: 118-128

Scheinost AC, Ford RG, Sparks DL (1999) The role of Al in the formation of secondary Ni precipitates on pyrophyllite, gibbsite, talc, and amorphous silica: A DRS study. Geochimica Et Cosmochimica Acta 63: 3193-3203

Schlegel ML, Manceau A, Charlet L, Chateigner D, Hazemann JL (2001) Sorption of metal ions on clay minerals. III. Nucleation and epitaxial growth of Zn phyllosilicate on the edges of hectorite. Geochimica Et Cosmochimica Acta 65: 4155-4170

Severne BC (1974) Nickel accumulation by Hybanthus floribundus. Nature 248: 807-808

Sparks DL (2001) Elucidating the fundamental chemistry of soils: Past and recent achievements and future frontiers. Geoderma 100: 303-319

Sparks DL (2003) Environmental Soil Chemistry. 2nd edition. Academic Press, New York

Sposito G (1989) The Chemistry of Soils. Oxford University Press, New York

Stevenson FJ (1994) Humus Chemistry: Genesis, Composition, Reactions. 2nd edition. John Wiley & Son Inc., New York

Strathmann TJ, Myneni SCB (2004) Speciation of aqueous Ni(II)-carboxylate and Ni(II)-fulvic acid solutions: Combined ATR-FTIR and XAFS analysis. Geochimica et Cosmochimica Acta 68: 3441-3458

Terry N, Sambukumar SV, LeDuc DL (2003) Biotechnological approaches for enhancing phytoremediation of heavy metals and metalloids. Acta Biotechnologica 23: 281-288

Thomine S, Lelievre F, Debarbieux E, Schroeder JI, Barbier-Brygoo H (2003) AtNRAMP3, a multispecific vacuolar metal transporter involved in plant responses to iron deficiency. The Plant Journal 34: 685-695

Thompson HA, Parks GA, Brown GE (1999) Dynamic interactions of dissolution, surface adsorption, and precipitation in an aging cobalt(II)-clay-water system. Geochimica Et Cosmochimica Acta 63: 1767-1779

Towle SN, Bargar JR, Brown GE, Parks GA (1997) Surface precipitation of Co(II)(aq) on Al_2O_3. Journal of Colloid and Interface Science 187: 62-82

Trainor TP, Brown GE, Parks GA (2000) Adsorption and precipitation of aqueous Zn(II) on alumina powders. Journal of Colloid and Interface Science 231: 359-372

Vangronsveld J, Vanassche F, Clijsters H (1995) Reclamation of a bare industrial-area contaminated by nonferrous metals - in-situ metal immobilization and revegetation. Environmental Pollution 87: 51-59

Vergnano O, Gabbrielli R (1987) The response of plants to heavy metals:Organic acid production. Giornale Botanico Italiano 121: 209-212

Whiting SN, Neumann PM, Baker AJM (2003) Nickel and zinc hyperaccumulation by Alyssum murale and Thlaspi caerulescens (Brassicaceae) do not enhance survival and whole-plant growth under drought stress. Plant Cell and Environment 26: 351-360

Xia K, Bleam W, Helmke PA (1997) Studies of the nature of binding sites of first row transition elements bound to aquatic and soil humic substances using X-ray absorption spectroscopy. 61: 2223-2235

Xia K, Mehadi A, Taylor RW, Bleam WF (1997) X-ray absorption and electron paramagnetic resonance studies of Cu(II) sorbed to silica: Surface-induced precipitation at low surface coverages. Journal of Colloid and Interface Science 185: 252-257

Yamaguchi NU, Scheinost AC, Sparks DL (2001) Surface-induced nickel hydroxide precipitation in the presence of citrate and salicylate. Soil Science Society of America Journal 65: 729-736

Zhao FJ, Hamon RE, McLaughlin MJ (2001) Root exudates of the hyperaccumulator Thlaspi caerulescens do not enhance metal mobilization. New Phytologist 151: 613-620

Chapter 2

SOIL TYPE AND CHEMICAL TREATEMENT EFFECTS ON NI SPECIATION IN REFINERY ENRICHED SOILS: A MULTI-TECHNIQUE INVESTIGATION

2.1 ABSTRACT

Aerial deposition of Ni from a refinery in Port Colborne, Onatrio Canada has resulted in the enrichment of $29km^2$ of land with Ni concentrations exceeding 200mg/kg. The Canadian Ministry of the Environment has established the latter value as a phytotoxicity threshold above which remedial action is required. Several studies on these soils have shown that making the soils calcareous was effective at reducing the DTPA or $SrNO_3$ extractable Ni fraction and subsequently alleviating Ni phytotoxicity symptoms in vegetable crops grown in the vicinity of the refinery. Conversely, limestone additions resulted in the increased uptake of Ni in the Ni hyperaccumulator Alyssum murale ‘Kotodesh’; a plant whose use was proposed as an alternative or concomitant method of remediation for this area. None of the previous studies have directly assessed the speciation of Ni in the soils around the refinery, or what role soil type and lime treatments play in altering the soil Ni speciation. Therefore, the objectives of this paper are to examine the influence of soil type and

treatment on the speciation of Ni in a Welland loam and Quarry muck soil and relate these findings to Ni mobility and bioavailability.

The speciation and mobility of Ni was assessed using conventional and cutting-edge techniques. Stirred-flow dissolution experiments using pH 4 HNO_3 showed that Ni release from the treated Quarry Muck and Welland Loam soils was reduced (~0.10%) relative to the untreated soils (~2.0%). Sequential chemical extractions of the unlimed Welland Loam and Quarry Muck field soils found that ~2-3% of the Ni was associated with the exchangeable ($MgCl_2$-extractable) fraction. A significant amount of Ni was associated with the metal oxide fraction, where > 50% of was removed from both soils. A considerable amount of the Ni was un-recover in the muck soils demonstrating that sequential chemical extractions may not be effective for soils with large amounts of organic matter. By combining the oxide, residual and un-recovered fractions, >90% of the Ni can be considered non-mobile. However, in the highly enriched forested muck soil a large amount of Ni (~22%) was removed with the first two extraction steps. The lower CEC and high Ni loading of these soils may result in a larger mobile fraction. Using both bulk-XAFS and SEM-EDX showed that the NiO particles persisted throughout each of the extraction steps; a testament to their insolubility even when reacted with the harshest of extractants. The persistence of these particles compromised the detection of other Ni species. Further, electron probe microanalysis (EMPA) showed that the NiO particles are approximately spherical, are associated with no other metals, and range from 5-50μm in diameter. Synchrotron micro X-ray absorption fine structure and X-ray fluorescence spectroscopy's showed that Ni Al-LDH phases were present in both the treated and untreated mineral soils, with a tendency towards more stable (e g. aged-LDH and phyllosilicate) Ni species in the treated soil, possibly aided by the solubilization of Si with increasing pH. In the muck soils, Ni-organic complexes (namely fulvic acid) dominated the speciation in both treated and untreated soils.

The results reported herein show that both soil type and treatment have a pronounce effect on the speciation of Ni in the soils surrounding the Port Colborne refinery. We demonstrate for the first time that Ni Al-LDH phase can form in anthropogenically enriched mineral field soils at circumneutral pH, and can lead to a reduction in Ni mobility. In the organic soils Ni is strongly complexed by soil organic matter; a property enhanced with liming. In both systems liming was effective at reducing Ni mobility by both the formation and secondary precipitates and strong complexation with soil organic matter.

2.2 INTRODUCTION

Nickel (Ni) comprises roughly 0.016% of the Earth's crust, making it the 24th most abundant metal (Burkin, 1987). Once regarded as a waste product in the copper smelting process (known as "devils copper" or "kupfernickel" from which it bears its name), Ni now has many uses with the most prominent being as a component (in concert with Cr, Nb, Mo, Ti) in stainless steel (Bacon et al. 2002). Acquisition of Ni involves beneficiation of the metal from both laterite (i.e. oxide) and sulphide ores, with most coming from the latter because of the lower energy requirements necessary for extraction. Removing and concentrating metals has primarily relied on pyrometallurgical processes in which the impurities in the ore are "cooked off" leaving behind an enriched matte (Nriagu 1996). During this process acid forming compounds (e.g. SO_2, Cl, etc.) as well as particulates of varying composition and morphology are produced and, prior to adequate emission standards, released into the environment (Hoflich et al. 2000). As a result, vast areas of soil enrichment and, in some cases, the complete perturbation of the ecosystem surrounding metal processing facilities have occurred.

The operation of a Nickel refinery in Port Colborne, Ontario, Canada from 1918 to 1984 has resulted, through aerial deposition, in the enrichment of roughly 345km^2 of soils with greater than 45 mg/kg Ni. As reported by several researchers (Frank et al. 1982; Bisessar 1989; Temple and Bisessar 1981), farms in the immediate vicinity of the refinery have soil Ni concentrations ranging from 600- to 10,000-mg/kg which resulted in a reduction in vegetable crop yields (the primary activity on the muck soils surrounding the facility). As such, the Canadian Ministry of the Environment (MOE) established a phytotoxicity based guideline of 200 mg/kg above which remediation is deemed necessary (Kuja et al. 1999). An estimated 29km^2 surrounding the facility are above the established remediation guideline. The large area of enriched soils makes remediation by conventional methods (i.e. excavation and disposal) impractical because of the associated high costs (> US$3millon/hectare) (McGrath, 1995). As an alternative, in-situ stabilization, in which amendments are added to the soil in an effort to promote long-term sequestration of the metal/s, may be more practical, especially if the objective is to simply alleviate Ni phytotoxicity.

Several researchers have found that liming of Port Colborne soils is effective at alleviating the symptoms of Ni phytotoxicity. Bisessar (1989) found that increasing the soil pH with $Ca(OH)_2$ was effective at reducing the phytoavailable Ni fraction (i.e., ammonium acetate extractable) and thus eliminating Ni toxicity in celery grown in the Ni enriched muck soils. Kukier and Chaney (2001) found a similar reduction in phytoavailable ($SrNO_3$ and DTPA extractable) Ni for oat, wheat and red beat grown in both the mineral and muck soils amended with dolomitic limestone. Similarly, Kukier and Chaney (2004) found that soil liming was effective at alleviating Ni toxicity in 11 agronomically important crops grown in the mineral soils. As a long-term solution, they proposed making the soils calcareous (i.e. addition of excess lime) to buffer the acidifying potential of agronomic fertilizers and acid rain.

Research on remediation of large areas of metal deposition has focused on *in-situ* immobilization in which materials are added to the soil to enhance sequestration of the metal, subsequently reducing its mobility and bioavailability. A promising alternative to in-situ methods is the use of specialized metal accumulating plants (hyperaccumulators) which are able to remove and concentrate metals in their shoots. The Ni hyperaccumulating plant *Alyssum murale* 'Kotodesh' has been evaluated for use in phytomining of Ni from the soils surrounding the Port Colborne refinery. In phytomining, the plants are harvested, the dry-matter incinerated for energy and the remaining ash refined to recover the entrained metals (Li et al. 2003). While investigating the effect of pH on nickel phytoextraction efficiency, they found a counterintuitive response of increased Ni uptake with increased pH. In most cases, increasing soil pH results in less plant available metal as it becomes less labile (as the previous studies with vegetable crops showed). The pH response of *A. murale* may provide a unique opportunity to combine in-situ stabilization methods (i.e. limestone additions) with phytomining.

For phytoremediation to be effective, it is necessary for the plant to extract enough metal to make recovery economical, and more importantly, not to simply dilute the metal into several more tons of metal enriched plant biomass than the original amount of contaminated soil. With both in-situ stabilization and phytoremediation, the speciation of the metal in the soils is of utmost importance, as it determines how effective the additive is at sequestering the metal, and dictates how bioavailable the metal is for uptake by plants.

The use of synchrotron radiation techniques has revolutionized the way we investigate metal speciation in environmental systems. Using synchrotron X-rays, the speciation of metal in a sample can be directly assessed, because it requires no sample treatment. The first synchrotron methods relied on bulk-XAFS, which used a relatively large beam size (i.e., mm^2). Because natural samples are heterogeneous, bulk-XAFS methods are only capable of determining the average speciation within the mm^2 of sample analyzed. Because of this, investigations into metal speciation in environmental systems were limited to single sorbent, single sorbate systems. However, with the development of better optics, we are now able to focus the X-ray beam down to square microns (μm^2) and thus probe within heterogeneous systems. With this ability, special care must be taken to assure that the data collected are representative of the speciation in the whole system. Several statistical approaches have been used to limit the potential subjectivity imposed by this type of analysis. Among them, principle component analysis and linear least squares fitting have been the most successful. Manceau et al. (2002) have outlined a procedure for using synchrotron-based techniques to properly ascertain metal speciation within soil samples. By using bulk XAFS, it is possible to find the compositionally dominant species within the sample, and then using micro-spectroscopic tools such as μ-XAFS, μ-SXRF and μ-XRD minor yet potentially more reactive components can be detected. There are an increasing number of examples in the literature where this approach has been used (Sarret et al. 2002; Voegelin et al. 2005, Nachtegaal et al. 2005).

While synchrotron techniques have moved us a long way in understanding the mechanisms of metal sequestration in soils, their use is complimentary to conventional techniques. For example, total metal analyses provide information on the overall spatial distribution of metals on a larger scale, allowing one to focus remediation efforts where they are most needed. Sequential extractions, while inherently operationally defined, can provide an indication of the metal's relative recalcitrance in a system as well as its relative mobility and bioavailability. In addition, if used in concert with other techniques (e g., SEM or XAFS), sequential extraction analysis can 'reveal' species that would have otherwise been masked by more concentrated phases.

To evaluate the effectiveness of soil treatments on Ni mobility and plant availability in Port Colborne soils, the previous studies (Frank et al. 1982; Kukier and Chaney 2000; Kukier and Chaney 2001; Kukier and Chaney 2004) used chemical extractants (i.e., $Sr(NO)_3$, DTPA, Ammonium Acetate). None, however, has looked directly at the change in chemical speciation of Ni within their soils affected by remediation or soil type. As such, the objective of this study is investigate the influence of past in situ remediation efforts (liming) and soil type (organic vs. mineral) on the speciation of Ni and evaluate how the speciation has impacted Ni mobility and bioavailability.

2.3 MATERIALS AND METHODS

2.3.1 Soil Collection, Characterization and Sample Preparation

Soils were collected in November 2002 from field plots maintained by the United State Department of Agriculture (USDA) on land located adjacent to a historic Ni refinery near the town of Port Colborne, Ontario, Canada. The research plots were established in 1999 to explore the ameliorative effects of liming on Ni toxicity to selected crop plants as well as the phytoextraction potential of the Ni hyperaccumulator *Alyssum murale*. In 1999, selected sites received a dolomitic lime treatment of 88 dry metric tons/ha, followed by another treatment of 33 Mt/ha in the spring of 2000. Soils are of the Welland (Typic Epiquoll; Canadian classification, Orthic Humic Gleysol) and Quarry muck (Terric Haplohemist; Canadian classification, Terric Mesisol) series. Sites were selected based on soil type (organic or mineral) and treatment (limed or unlimed) from which several representative sub-samples were collected from the plow-layer (upper 20 cm) from each plot and then homogenized in 20gal Rubbermaid ™ tubs. Soils were sieved moist past a 2mm sieve and then stored for future analysis.

The fraction of sand, silt and clay was determined using the Bouyoucos Hydrometer method. Pretreatment of the soil to remove soluble salts and carbonates, organic matter, and metal oxides followed by wet settling and centrifugation was conducted to isolate the <2μm fraction for X-ray analysis (Lavkulic.LM and Wiens 1970). Mineralogical composition of the < 2μm fraction was determined by X-ray diffraction. The pH of the air-dried soils was determined using a soil to deionized water ratio of 1:2 with a 1 hour equilibration time. Soil organic matter content was determined using the loss-on-ignition (LOI) method. The cation exchange capacity (CEC) of each soil was determined using the Compulsive Exchange Method (Sumner and Miller 1996). Free iron and aluminum oxide content of the soils was determined using the sodium-citrate-bicarbonate-dithionite method (Mehra and Jackson 1960). Total metal contents of the soil samples were determined using a microwave assisted acid (HNO_3 and HCl) digestion (US Environmental Protection Agency 1995 Method 3051). The soils were analyzed for total Ni, Cd, Co, Cu, Fe, Pb, and Zn content via Inductively Coupled Plasma Atomic Emission Spectrometry (ICP-OES).

2.3.2 Stirred-Flow Dissolution Studies

A stirred-flow reactor similar to that described by Strawn and Sparks (2000) was employed to study the dissolution of Ni from limed and unlimed Welland loam and Quarry muck soils as well as α-$Ni(OH)_2$, Ni/Al-LDH, NiS_2 and NiO reference materials. Nitric acid (HNO_3, pH 4) was used as a dissolution agent to mimic natural weathering processes as would occur via acid rain, fertilizer additions or root exudates in the rhizosphere.

The stirred-flow reactor consists of a 7.5 ml chamber which is positioned on top of a stir plate where effective mixing (400rpm) is provided via a stir bar in the reaction chamber. The flow of desorbing solution, supplied at a constant flow by a peristaltic pump, enters the bottom side of the chamber, is mixed thoroughly, and then exits through the top. To prevent loss of the material within the reaction chamber, a 25mm diameter, 0.22 μm filter is inserted at the top prior to the outlet. The solution leaving the reaction chamber is then sent to a fraction collector where the samples are deposited in 18ml HDPE test tubes. The desorbing solution flow rate was no greater than 0.8 ml/min (48ml/hr) in order to ensure a proper residence time within the mixing chamber and to minimize re-adsorption of Ni onto the soil. Samples were collected every 5 min for the first hour and every 10 min thereafter for a total of 8 hrs. Based on preliminary studies, 8 hrs was sufficient time for the reaction to reach an apparent steady-state in Ni dissolution. Twelve, 4 ml samples were generated in the first hour followed by 42, 8 ml samples for the remaining 7 hours, resulting in a total of 54 samples per dissolution experiment. Supernatants were analyzed for Ni content using ICP-OES. Data are presented as chamber volumes (CV) versus the concentration (mg/L) of Ni being released from the reaction chamber. Chamber volumes were calculated by multiplying the flow rate by the time and dividing by the volume of the chamber. Expressing the data in this way allows for the comparison of data from experiments performed across different flow rates. Therefore, differences in the data obtained can be attributed to surface reactions and not a product of flow rate.

2.3.3 Sequential Extractions

Selective chemical extractions were performed on the unlimed muck and mineral field soils as well as a forested muck soils. These soils represent the most enriched soils in this study and were analyze as an initial assessment of the Ni speciation in the Lake Plane soils. The selective extraction method followed a variation of the protocol outlined by Tessier et al (1979) (Table 1), which permits quantitative analysis of Ni and other metals associated with the following "operationally defined" soil phases: (i) exchangeable, (ii) carbonate, (iii) iron-manganese oxide, (iv) organic and (v) residual. The variation of the method appears in the last step, where EPA method 3050b (microwave assisted HNO_3/HCl) digest was used to determine the residual Ni fraction. Selective extractions were performed on 0.50 grams of soil in Nalgene™ polypropylene co-polymer 50 ml centrifuge tubes. Between each successive extraction, separation of the reagent and soil solid was effected by centrifugation for 30 min at 10,000 rpm (7796 RCF) using a Sorvall Superspeed RC5C+ centrifuge (Sorvall Insturuments-Dupont Company, Newton, CT).

Supernatants were stored in 60 ml high density polyethylene (HDPE) bottles and refrigerated until analysis for metal content. Removal of entrained solutions (i.e., wash) was carried out once between each extraction step by adding 8ml deionized water and shaking for 30 min, followed by centrifugation at 10,000 rpm (7796 RCF). All shaking steps were performed at high speed on a flat bed shaker. All glassware used was acid washed in 10 % HCl and rinsed three times in distilled water followed by three times in deionized water. All reagents used were analytical or trace metal grade. Deionized water used in preparing stock solutions was obtained from a Millipore Milli-Q UV Plus system.

Sequential extraction began with five replicates to allow for the sacrifice of a sample after each step. The sacrificed samples were then analyzed microscopically and spectroscopically for changes in soil structure and Ni speciation. After the wash step, the pellets from the sacrificed samples were shock frozen in liquid nitrogen and freeze dried at -34°C for > 24 hours. Samples were attached to an adhesive carbon disk and examined using a Hitachi S-4700 field emission scanning electron microscope (FE-SEM) equipped with an Oxford INCA energy-dispersive spectrometer (EDS). Samples for examination via XAS, were mounted in the well of a Perspecs sample holder and sealed with Kapton ™ tape for examination at beamline X-11A at the National Synchrotron Light Source, Brookhaven National Lab, Upton, New York. XAS data analysis proceeded as described in section 2.3.5 below.

Table 2.1: Reagents and methods used for removing specified target phases in the sequential extraction procedure (after Tessier et al., 1979)

EXTRACTANT	TARGET PHASE	PROCEDURE
1M $MgCl_2$ (pH 7)	exchangeable	add 8 mL; shake for1 hour
		Milli-Q Wash
1M NaOAc (pH 5 w/ HOAc)	carbonate	add 8 mL; shake for 5 hours
		Milli-Q Wash
1M NH_3OH HCl (in 20% HOAc)	Fe-Mn Oxides	add 20 mL and place in 96°C water bath for 6 hours w/ occasional agitation
		Milli-Q Wash
0.02 M HNO_3 + 30% H_2O_2 (at pH 2 w/ HNO_3)	organic	add 3 mL of HNO_3 + 5 mL of H_2O_2 , place in 85°C water bath for 2 hrs
		add 3 mL of H_2O_2 and soak for an additional 3 hrs
3.2 M NH_4OAc (in 20% HNO_3)		allow samples to cool, add 5 ml dilute to 20 ml shake for 30 min
		Milli-Q Wash
1 N HNO_3 & conc. HNO_3 (EPA method 3050)	residual	add 10 mL HNO_3 reflux for 30 min; add 5 mL conc. HNO_3 reflux until 5 mL or soln. remains; continue until no brown fumes are evolved

2.3.4 Electron Probe Micro-analysis (EPMA)

Portions of the treated and untreated mineral and muck were prepared for EMPA analysis by first embedding them in Scotchlight ® electrical resin after which they were thin sectioned to 30µm and mounted on pure quartz slides. Prior to analysis the thin sections were sputter coated with carbon and then examined on a JEOL JXA-8600 microprobe (John Hopkins University) with wavelength and energy dispersive detectors (WDS and EDS, respectively). Samples were first scanned manually from 50-300x using back-scattered electron (BSE) imaging to find regions of high nickel concentration after which EDS was used to generate elemental maps for Ni, O, Ca, Al, K, Mg, Fe, Cu and Si.

2.3.5 Bulk XAFS Standard Preparation, Data Collection and Characterization

A total of 33 Ni standards were generated, purchased, or compiled from previous work published by the UD environmental soil chemistry group, and were used to identify the unknown species present in the soils. Bunsenite (*green*-NiO), millerite (NiS), arupite ($Ni_3(PO_4)_2$) and $NiCO_3$ were obtained from Johnson Matthey. The minerals trevorite ($(Ni,Cu)Fe^{3+}{}_2O_4$), heazlewoodite (Ni_3S_2), godlevskite ($(Ni_{8.7},Fe_{0.3})_9S_8$), violarite ($Ni_2,Fe^{2+}S_4$), and gaspeite ($(Ni,Mg,Fe)CO_3$) were obtained from Excaliber (Peekskill, NJ). Mineral samples were prepared by grinding to a fine powder in a ceramic ball-mill or mortar and pestle. The coprecipitate α-$Ni(OH)_2$ was prepared following the methods of Gennin et. al. (1991). The β-$Ni(OH)_2$ was generated by aging the initial α-$Ni(OH)_2$ precipitate under a nitrogen atmosphere at 298K for 1 month. Fresh (i.e. no aging) Ni-Al LDH (NO_3) was acquired from Scheinost et al. (1999) and was prepared as described in Taylor (1984). The aged Ni-Al LDH was acquired from Peltier et al. (2006) and was generated by incubating an initial Ni-Al LDH (CO_3) precipitate (prepared as above) for 2 weeks at 65°C. The Ni-$Al(OH)_3$ + SiO_2, Ni-SiO_2, Ni-gibbsite, Ni-Talc, Ni-pyrophyllite and Ni-phyllosilicate were generated as described in Scheckel and Sparks (2000), Scheinost et al. (1999) and Scheidegger et al. (1997c) but were aged for 7 years at constant temperature (298K). The Ni-Humic acid standard was taken from Nachtegaal and Sparks (2003), and was generated by dissolving 5wt% HA in 0.05 M NaOH, precipitating the sample at pH 3 and then raising the pH to 7.5 and adding 3mM Ni (as $NiNO_3$). The Ni-Fulvic acid (Elliott soil fulvic acid 2S102F) standard was taken from Strathmann and Myneni (2004). After preparation, solids were washed and isolated by centrifugation and either stored in the refrigerator as wet pastes or shock frozen and freeze-dried until analysis. Aqueous organic standards were prepared as follows: Ni-aqueous, 30mM $NiSO_4$; Ni-Aconitate, 50 mM $NiSO_4$ + 150 mM aconitate; Ni-malate, 30 mM $NiSO_4$ + 300 mM malate; Ni-malonate, 30 mM $NiSO_4$ + 300 mM malonate; Ni-Citrate, 30 mM $NiSO_4$ + 120 mM citrate; Ni-oxalate, 30 mM $NiSO_4$ + 300 mM oxalate; Ni-Tartrate, 50 mM $NiSO_4$ + 500 mM tartrate; Ni-histidine, 30 mM $NiSO_4$ + 300 mM histidine; Ni-glutathione, 30 mM $NiSO_4$ + 300 mM glutathione; Ni-cystine, 30 $NiSO_4$ + 300 mM cystine; Ni-glycine, 30 mM $NiSO_4$ + 300 mM glycine. Samples were adjusted to pH 6.5 using HNO_3. ACS trace metal grade chemicals, acid washed containers and ultra-pure double-deionized (18.2Ω Millipore) water were used to generate all standards.

XAS data for standards were collected on beamline X-11A at the National Synchrotron Light Source (NSLS), Brookhaven National Laboratory, Upton, NY (unless otherwise stated). The electron beam energy was 2.5-2.8 GeV with a maximum beam current of 300 mA. The monochromator consisted of two parallel Si (111) crystals with a vertical entrance slit opening of ~0.5 mm. The beam size on the sample was maintained at 2 × 10 mm for all samples and standards. Prior to data collection, the energy was calibrated to the first inflection point on the K adsorption edge of a Ni metal foil standard ($E_o = 8.333$ keV for Ni). Solid samples were loaded into individual acrylic sample holders and sealed with Kapton™ tape. For aqueous standards, non-adhesive Kapton™ film was used to seal the sample chamber to avoid any interaction of the sample with the tape adhesive. The samples were then mounted 45^o to the incident beam and data collected at the Ni K-edge over the energy range 8183-9082 eV in fluorescence mode using a N_2/Ar (95/5%) filled Lytle Cell. To optimize the Ni signal and remove elastically scattered radiation, the fluorescence signal was filtered using a Co foil, one to two sheets of Al foil and Soller slits. Harmonic rejection was achieved by detuning the monochromator 20% of I_o. Multiple scans (≥3) were collected for each sample to improve the signal-to-noise ratio.

XAS data analyses were performed using WinXAS 3.1 (Ressler 1997). Prior to averaging, the individual spectra were background corrected and normalized.

Background subtraction was performed by fitting a linear polynomial to the pre-edge region between 150 and 50 eV below the Ni K-edge. The edge jump was normalized to unity by fitting a linear polynomial between 100 and 500 eV above the Ni K-edge. The threshold energy (E_o) was determined by selecting the root of the second derivative through the absorption edge of the differentiated spectra, and used to convert the spectra from energy to k-space (photoelectron wave vector ($Å^{-1}$)). A cubic spline function with ≤ 7 knots was then used to remove the contribution to the spectrum resulting from atomic absorption in the absence of backscattering contributions. This step generated the XAFS function (χ (k)), which was then weighted by k^3, to compensate for dampening of the XAFS amplitude with increasing k. The $k^3\chi(k)$-spectra were then Fourier transformed using a Bessel window with a smoothing parameter of 3-4 to reduce artifacts due to the finite Fourier filtering range used. This step produced radial structural functions (RSF) which were not corrected for phase shift.

The first two major shells below 3.5 $Å^{-1}$ were individually selected, back-transformed and fit using a non-linear least squares approach and theoretical scattering paths generated using ATOMS and FEFF 7.02 software packages (Zabinsky et al., 1995). The layered double hydroxide (LDH) standards were fit with an R range below 6.4 $Å^{-1}$ to include the weak backscattering contribution from Al occuring around 6.09 $Å^{-1}$ (Scheinost and Sparks 2000). Ab initio phase and amplitude functions for Ni-O, Ni-Fe, Ni-Mn, and Ni-Al were generated from the refinement of hydrotalcite where Ni, Fe, or Mn were substituted for Mg in the octahedral layer, and from the structures of Trevorite ($[(Ni,Cu)Fe^{3+}{}_2O_4]$), Heazlewoodite (Ni_3S_2), Godlevskite ($(Ni_{8.7},Fe_{0.3})_9S_8$), Violarite ($Ni_2,Fe^{2+}S_4$), and Gaspeite ($(Ni,Mg,Fe)CO_3$). The Ni-O and Ni-C (organic acids) phase and amplitude functions were generated using either nickel acetate tetrahydrate ($Ni(CH)_3COO)_2$•H2O) (Nicolai et al. 1998) or disaguabis(salicyladehydato) nickel ($Ni(sal)_2(H_2O)_2$) (Stewart et al. 1961) and Ni-N (amino acids) paths using Ni – Imidazole $(C_3H_4N_2)_6Ni(NO_3)_2$ (Santoro et al. 1969). The parameters obtained fitting the individual shells were then refined using a multi-shell fit over the entire spectra in k and R spaces. The energy shift parameters (E_o) were set equal for all paths and the root mean square disorders [RMSD (σ^2(Å^2) or the Debye-Waller factor] and bond distance (R) were set equal for those metals sharing atomic shells. The amplitude reduction factor ($S_o{}^2$) was fixed at 0.85. Errors in the bond distance (R) are estimated to be R ± 0.02 Å and R ± 0.05 Å, and errors for the coordination number (CN) are estimated to be CN ± 20% and CN ± 40%, for the first (Ni-O/S/N) and second shells (Ni-Ni/Al/Si/C), respectively based on results of other researchers investigating similar systems. These estimates are based on the fitting results and comparisons with previously published XRD and EXAFS data on similar systems (Scheidegger et al. 1998; O'Day et al. 1994).

2.3.6 μ-SXRF and μ-XAS Data Collection and Analysis

μ-EXAFS and μ-synchrotron based X-ray fluorescence (μ-SXRF) data were collected on beamline 10.3.2 (1.9 GeV and 300 mA) at the Advanced Light Source, Lawrence Berkeley National Lab (Berkeley, CA) (Marcus et al. 2004). Soils were embedded in resin (3M™ Scotchcast ™ electrical resin) and sectioned to 30μm. The soil thin sections were mounted to the sample stage aligned 45° to the incident beam. Fluorescence signals were collected using a Ge solid-state multi-element detector. To assess the spatial distribution of Ni and other elements in the samples, fluorescence maps were collected over 1000 μm^2 (coarse map) and 200 μm^2 (fine map) with a beam size of 16 x 7 μm and 5 x 5 μm and using a step size of 20 and 5 μm, respectively and an integration time of 100 ms. For mapping, the beam energy was set to 11 keV to allow for the detection of relevant elements including Ni, Fe, Co, Cu, Zn, and Mn. Using the map, data cross correlations were performed to determine element associations (e.g., Ni/Fe, Ni/Mn) within samples. The metal associations were evaluated using the Pearson's correlation coefficient(r) between the two element intensities on a per-pixel basis (Manceau et al, 2002). To determine the Ni speciation at regions of interest (ROI) in the maps, μ-XAS spectra were collected up to 500 eV above the Ni K-edge. The number of μ-XAS spectra collected at each point depended on the concentration at the ROI (i.e., number of fluorescent counts). To obtain sufficient data quality (i.e. signal-to-noise) a minimum of 1 million total integrate fluorescence counts were collected, which resulted in a minimum of 3 scans per ROI. Prior to μ-XAS data collection, the beamline energy was calibrated to the first inflection point of the Ni metal foil standard (E_o = 8.333 keV)

Analysis of XAFS spectra collected from multicomponent systems (such as soils) cannot rely on traditional fitting procedures in which atomic shells are individually selected and fit. Difficulty arises because the multiple metals in the system may have overlapping atomic shells making it difficult if not impossible to separate them. Therefore, to determine the species present within a mixed system, a dataset of spectra from multiple spots throughout a sample are analyzed statistically using principal component analysis (PCA) (Wasserman et al. 1999). The PCA technique determines if the data set can be described as weighted sums of a smaller number of components, which would be the case if each spot in the dataset is comprised of a smaller number of distinct compounds. Selection of the number of principal components was made where the empirical indicator (IND) and Eigenvalues were at their minimum (Malinowski 1977). Target transformation (TT) is then used to identify the components by taking a spectrum of a known reference compound and mathematically removing from the spectrum anything that does not look like the principle components identified by PCA. If minimal information has to be removed from the known reference spectrum, then one can conclude it is most likely present in the sample. Reference spectra are evaluated for their “goodness of fit” by the SPOIL value (Malinowski 1978). Generally, numbers < 1.5 are considered excellent, 1.5 to 3 good, 3-4.5 fair, 4.5-6 poor and >6 unacceptable. After the contributing standard phases are identified, linear least squares fitting (LLSF) is used to determine the amount (%) of each standard within the individual sample spectra making up the dataset. The fit is optimized where the normalized sum squared (NSS) value is at a minimum. A reference phase was included in the fit only if it decreased the NSS by 20% or more. The accuracy of this fitting approach is dependent upon the data quality, the completeness of the standards data set, and the range over which the data were fit (Manceau et al. 2002).

2.4 RESULTS AND DISCUSSION

2.4.1 Soil Characteristics

The physiochemical and mineralogical properties of the limed and unlimed Welland loam and Quarry muck soils can be seen in Table 2.2. Additionally, data are included from an unlimed Quarry muck soil collected from a forested area adjacent to the test plots. The forested Quarry muck soil and the Welland loam field soil represent the highest Ni loadings found in the collected soils. The high Ni concentrations in the forested soils result from the "filtering" effect of the trees, which removed and concentrated the airborne particulates in the underlying soils. The organic matter (OM) content of the Quarry Muck field soil is ten times that of the Welland Loam. However, the Welland soil possesses a substantial amount of OM compared to most soils, which is typical for soils formed in colder climates such as these Lake Plane soils. The forested muck soil has a considerably lower CEC (18.8 meq/100g) than its field counterpart (~50 meq/100g). Helling et al. (1964) and Yuan et al. (1967) have clearly shown that the CEC of a soil significantly increases as pH is increased and acidic groups (namely COOH) are deprotinated. The pH of the forest soil is ~ 5 which may account for the reduced CEC, however, with >60% OM in these soils, it is unlikely the CEC would be this low. Conversely, it is possible that the excess Ni in the forested soils caused an "anti-fungal" or "anti-bacterial" effect which

Table 2.2: Physiochemical and mineralogical properties of the limed and unlimed Quarry Muck and Welland Loam soils

	OM	Particle size Sand/Silt/Clay	CEC	pH	Ni	Co	Cu	Fe	Pb	Zn	Mineralogy of < 2mm clay fraction
Soil	-----------	%----------	meq/100g		---------------------			(mg/kg)		---------------------	
Quarry Muck											
Unlimed	71.7	51/34/15	49.2	5.8	4902	38.4	293	15908	51.9	118	Kaolinite > Montmorillonite > Mica > Geothite > Quartz
Limed	72.3		64.5	6.5	3516	59.9	426	20049	63.9	164	
Welland Loam											
Unlimed	9.8	29/35/36	18.1	7.1	4700	50.1	475	13860	64.8	181	Kaolinite > Mica > Geothite > Quartz
Limed	8.2		22.7	7.5	3468	31.5	300	13198	37.1	101	
Quarry Muck Forest Soil	64	51/34/15	18.8	5.1	22444	52.1	412	16061	62.6	170	Kaolinite > Montmorillonite > Mica > Geothite > Quartz

limited the degradation of surface litter and/or the "light" fraction, in effect reducing the production of soil humus (i.e. humification) and subsequently the CEC (Yano et al. 1998).

The Ni, Co, Cu, and Zn concentrations in all of the soils are elevated, compared to normal background concentrations, resulting from refinery and other fallout from surrounding industries. The limed Welland and Quarry Muck soils are 0.4 and 0.7 pH units above their unlimed counterparts, respectively. The unlimed Welland loam soil pH is uncharacteristically high compared to those measured by other researchers (Li et al 2003, Kukier and Chaney 2004). This may have to do with the soils being sampled from historic farm fields where pH corrections would have been made as part of normal farming practices prior to them becoming test plots.

2.4.2 Stirred Flow Dissolution Studies

To evaluate the relative solubility of important Ni species present in these soils, stirred-flow experiments were performed on reagent grade NiS, green-NiO, α-Ni(OH)$_2$ and Ni-Al LDH reference compounds (Figure 2.1). The most obvious result is the resistance of NiO followed by NiS$_2$ to dissolution by pH 4 HNO$_3$. At the completion of the 8-hr dissolution experiment, 100% and 79% of the NiO and NiS remain, respectively. In contrast, the α-Ni(OH)$_2$ and (fresh) Ni-Al LDH reference phases were characterized by an initially rapid release of Ni followed by a constant release with 57% and 62% of the total α-Ni(OH)$_2$ and *fresh* Ni Al-LDH phases,

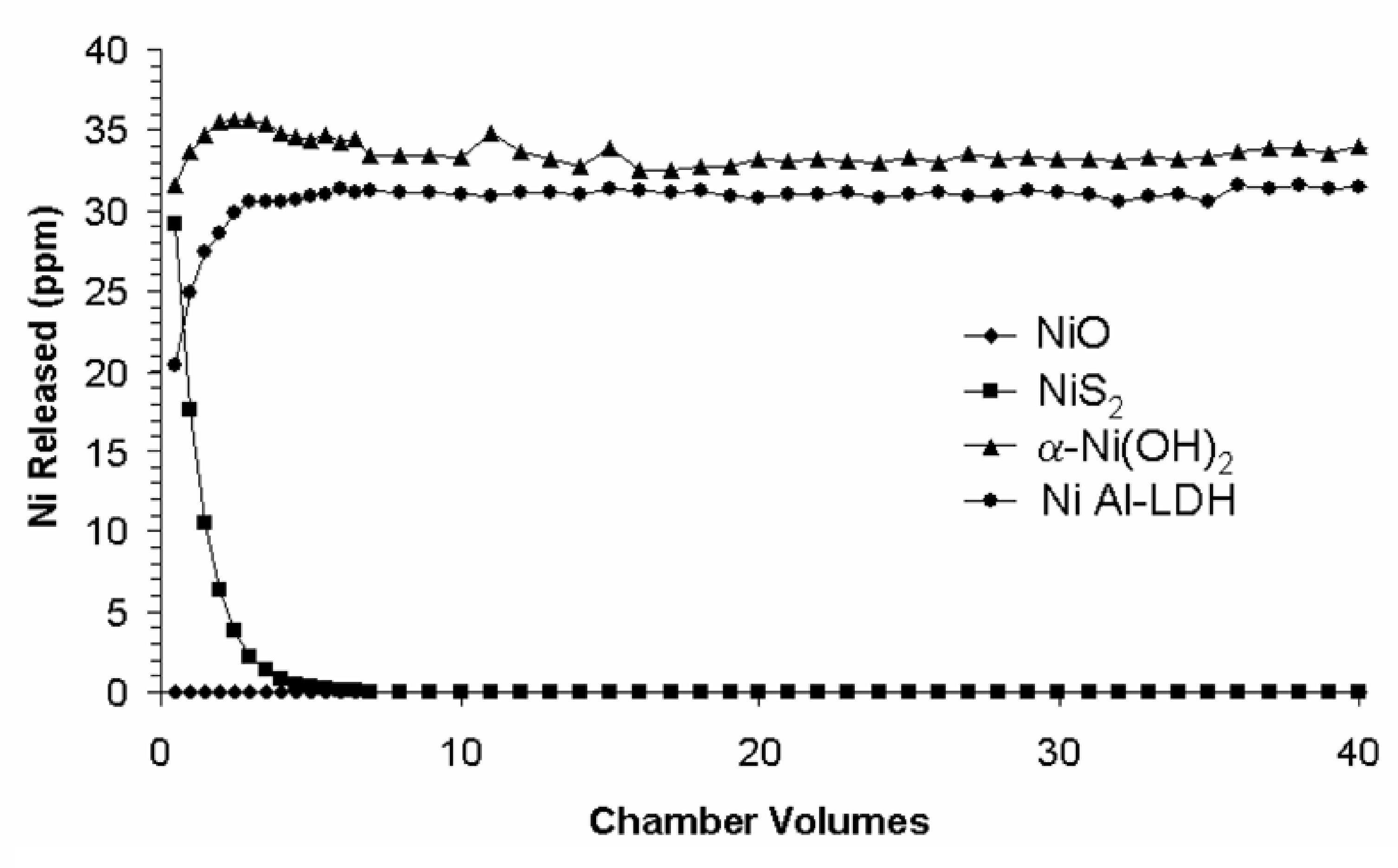

Figure 2.1: Ni release from NiS_2, $Ni(OH)_2$, *fresh*-Ni Al-LDH and NiO standards during an 8-hr stirred-flow dissolution experiment using pH 4 HNO_3

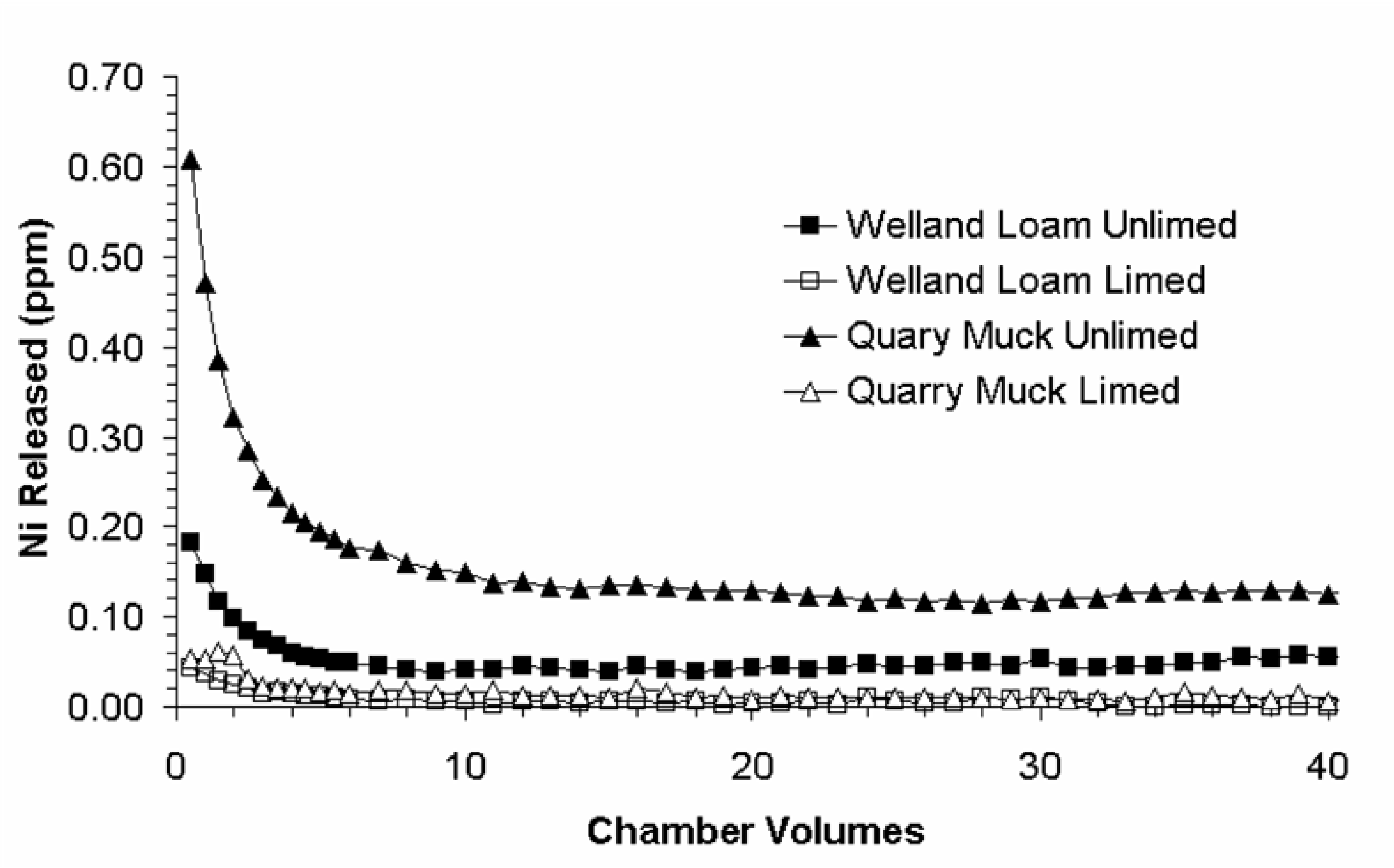

Figure 2.2: Ni release from Welland loam and Quarry muck limed and unlimed soils during an 8-hr stirred-flow dissolution experiment using pH 4 HNO_3

respectively remaining after the 8-hr experiment. The results for α-Ni(OH)$_2$ and Ni-Al LDH are similar to those of Scheckel et al. (2000) in that the α-Ni(OH)$_2$ appears to be more soluble than the LDH phase.

The results for the stirred-flow experiments using pH 4 HNO_3 as a dissolution agent are shown in Figure 2.2. The influence of lime additions on the amount of Ni released from each of the soils is evident. Of the total nickel present in the Welland loam, ~2.0% was removed from the unlimed soil compared to 0.11% from the limed soil during the duration of the 8 hr experiment. A similar trend was observed for the Quarry muck soils with ~2.3% and 0.10% Ni removal from the unlimed and limed muck soils, respectively. The reduction in Ni loss as a result of raising the pH indicates that liming may have altered the soil Ni speciation. These results corroborate findings by Kukier and Chaney (2004) who saw a similar reduction in $Sr(NO_3)_2$ extractable Ni with increasing pH.

2.4.3 Sequential Chemical Extraction

A sequential extraction (SE) procedure was used as an initial assessment of the metal species present in both soil types and, when coupled with spectroscopic and microscopic methods, to aid in the identification of species that may normally go undetected in the presence of more concentrated components. Scheinost et al. (2002) used a similar technique to speciate Zn in a smelter-impacted soil. They found that selective sequential extractions significantly improved the identification and quantification of Zn species when coupled with XAFS. Figure 2.3 shows the amount

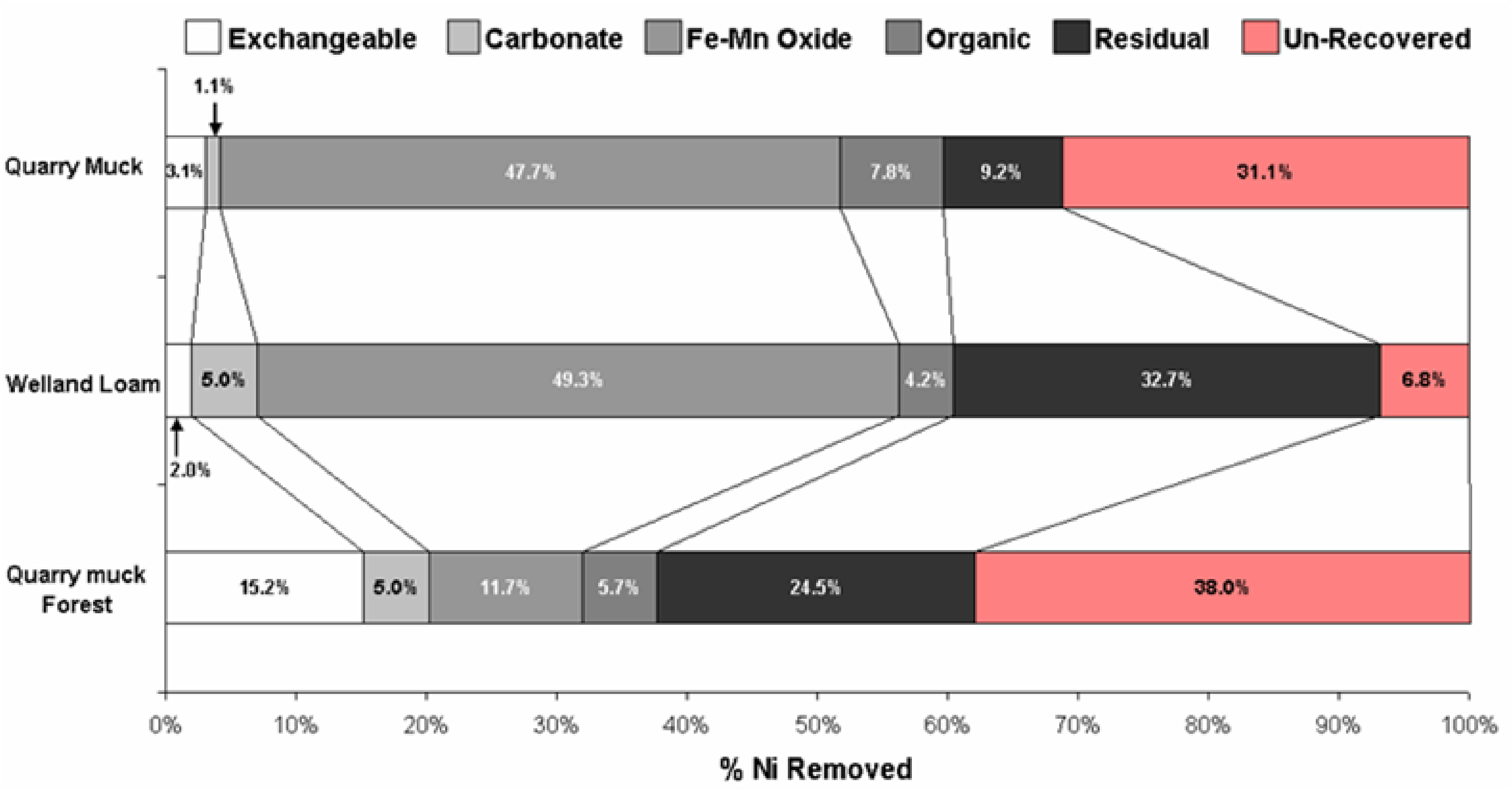

Location	Soil	Total Ni (ppm)[a]	Exchangeable	Carbonate	Oxide	Organic	Residual	Un-Recovered	Total Recovery
Field	Quarry Muck	4902	3.1%	1.1%	47.7%	7.8%	9.2%	31.1%	68.9%
	Welland Loam	4700	2.0%	5.0%	49.3%	4.2%	32.7%	6.8%	93.2%
Forest	Quarry Muck	22444	15.2%	5.0%	11.7%	5.7%	24.5%	38.0%	62.0%

[a] EPA 3050b HNO_3/HCl hot microwave digest;

Figure 2.3: Fraction of Ni associated with the operationally defined exchangeable, carbonate, oxide, organic and residual fractions from sequential extractions of Welland Loam and Quarry muck field soils and a Quarry muck forest soil

(%) of Ni associated with each of the extracted metal fractions from the Welland loam and two Quarry muck soils. The first two extraction steps (exchangeable and carbonate) accounted for an average of ~4% and 7.5% of the total Ni removed from the Quarry and Welland soils, respectively, indicating a small but accessible exchangeable Ni pool. However, in the forested muck soil ~ 22% of the Ni was removed with the first two steps. A higher Ni content of the forested soils, together with the uncharacteristically low CEC may have resulted in saturation of the exchange sites in these soils with Ni and thus a larger mobile fraction. At the pHs of the Quarry (5.8) and Welland soils (7.1), it is highly unlikely that Ni carbonate would persist and thus, we consider the carbonate extractable fraction to represent more specifically sorbed Ni (Sadiq and Enfield 1984; Sadiq and Enfield 1984). A significant amount of Ni was associated with the metal oxide fraction (typically oxides of Fe, Mn and Al) in both field soils, with over half of the Ni removed in this step. Surprisingly, there was very little Ni associated with the organic fraction of the Quarry Muck soils. In the Welland soil, a third of the metal was associated with the residual fraction compared to 9.2% and 24.5% for the Muck field and forested soils, respectively. However, total Ni recovery from the muck soils was substantially lower (~65%) than that from the Loam soils (93%). Including the un-recovered fraction with the measured residual fraction, nearly 40% of the Ni in both the muck and loam field soils is in a highly resistant form. The reduction in Ni recovery from the muck soils can be attributed to the high organic matter content which may have caused incremental losses of soluble organic bound Ni during the washing steps, inadequate removal during the organic extraction step or, interference with the chemical reagents used in the preceding or subsequent steps.

Spectroscopic and microscopic analyses were performed on the solids remaining after each extraction step from the Welland loam field soil and the Quarry muck forest soil. The raw EXAFS spectra, $k^3\chi(k)$-spectra and radial structure functions (RSF) for the muck and loam extracted solids and for comparison, Bunsenite (NiO), are shown in Figures 2.4 and 2.6, respectively. In the Quarry muck soils, the raw EXAFS and $k^3\chi(k)$-spectra show very little change from the untreated soil to the final residual fraction (Fig. 2.4). The first oscillation in the RSF occurring at $R \approx 1.6$ Å (uncorrected for phase shift) represent the first coordination shell of oxygen and remains constant in amplitude and position throughout the muck extraction series. However, the second RSF peak at ~2.5 Å grows in magnitude with each extraction step, refining the spectra to look more and more like that of the NiO reference. The structural parameters derived from non-linear least squares fitting (NLLSF) with the theoretical Ni-O and Ni-Ni scattering paths obtained from the structural refinement of Bunsenite (NiO) can be seen in Table 2.3. The first RSF peak of the whole Quarry muck soil (i.e. soil before any treatment) was best fit using ~ 6 O atoms at $R_{Ni\text{-}O} \approx 2.07$ Å indicating that Ni is in octahedral coordination. The second RSF peak was best fit using ~8 Ni atoms at $R_{Ni\text{-}Ni} \approx 2.95$ Å which agrees well with that of the NiO standard. In general there is an upward trend in the second shell coordination number (N) from 6.2 in the exchangeable residue to ~9.0 in the residual. The XAFS results show that NiO persists throughout each extraction step and is concentrated in the residual

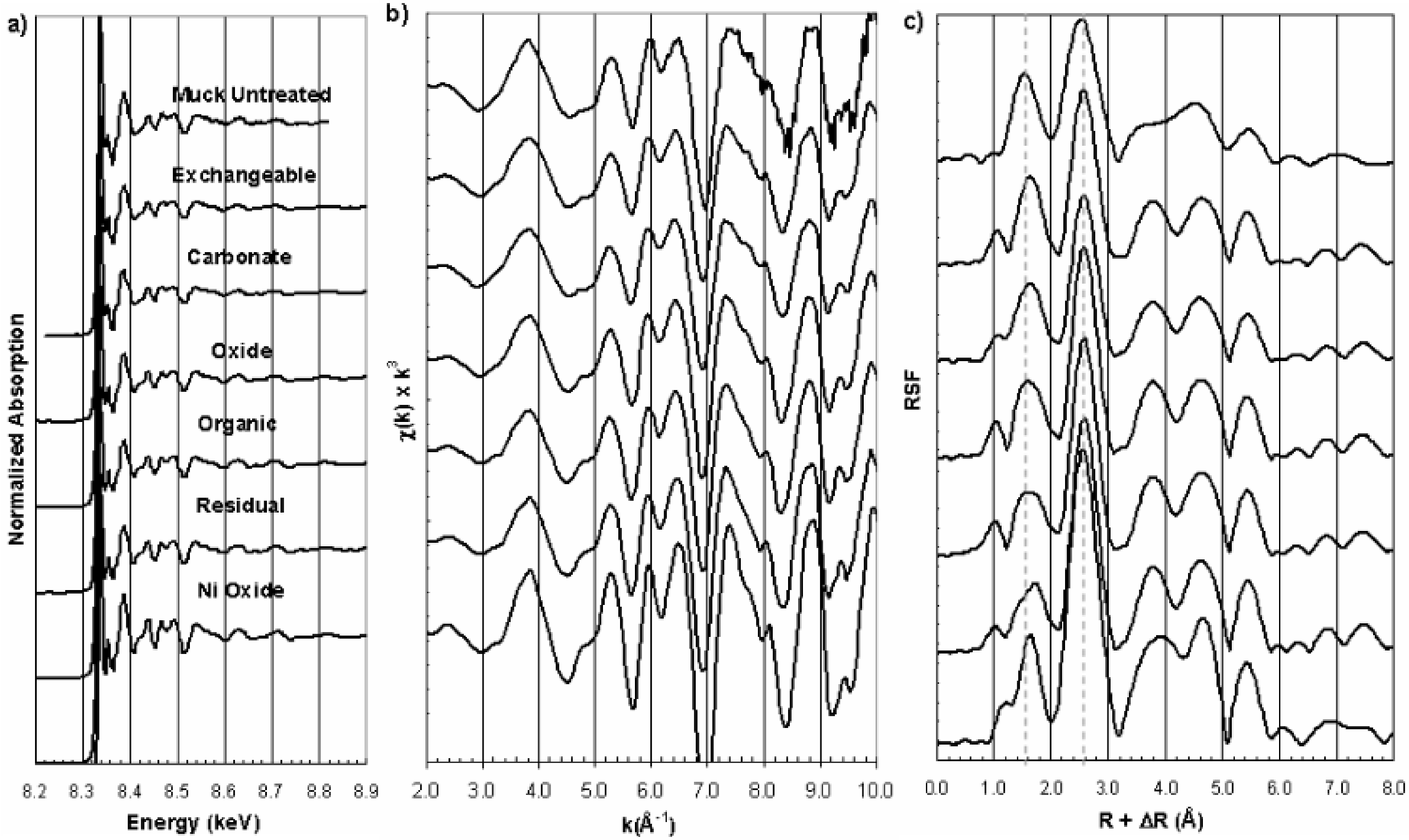

Figure 2.4: Background corrected (a), $k^3\chi(k)$-spectra (b) and radial structure function (RSF) spectra (c) of the untreated Quarry muck soil and the solids remaining after the exchangeable, carbonated, oxide, organic and residual sequential extraction steps. The NiO standard spectra is included for reference.

fraction. Scanning electron microscopic (SEM) analyses of each of the extraction residuals (Figure 2.5) confirms this result. In each of the extracted residues examined, distinct approximately spherical NiO particles were identified ranging from 3 to 10 μM. Notably, as the more soluble Ni and soil components were removed with each extraction step, the identification of NiO particles in the SEM micrographs became considerably easier.

Changes in the raw EXAFS spectra, $k^3\chi(k)$-spectra and RSF for the Welland loam extractions (Figure 2.6) are more obvious than the Quarry muck spectra. Little changes occur in the EXAFS, $k^3\chi(k)$-spectra and RSF for the first two (exchangeable and carbonate) extractions, in line with the small losses of nickel during these two steps (2.1 and 5.4% for the exchangeable and carbonate fractions, respectively). The fit results (Table 2.3) are consistent with this observation, showing Ni in 6-fold coordination with O in the first coordination shell at $R_{Ni-O} \approx 2.06$ Å and Ni in the second at $R_{Ni-Ni} \approx 2.97$ Å for both residues. However, after the oxide extraction step, pronounced spectral changes in the $k^3\chi(k)$-spectra between 6 and 7 $Å^{-1}$ and at 8 $Å^{-1}$ as well as shifts in the shell between 1 and 2 $Å^{-1}$ in the RSF from $R \approx 1.6$ $Å^{-1}$ to 1.8 $Å^{-1}$ were observed. The $N_{Ni-O/Ni}$ and $R_{Ni-O/Ni}$ were higher than those determined in previous extraction steps. The longer bond distances and high Debye-Waller factors (0.010 and 0.012 $Å^2$) indicate significant structural disorder consistent with the partial dissolution of the NiO particles. The oxide extraction step accounted for 53% of the Ni removed, a portion of which can be contributed to the partial dissolution of the NiO

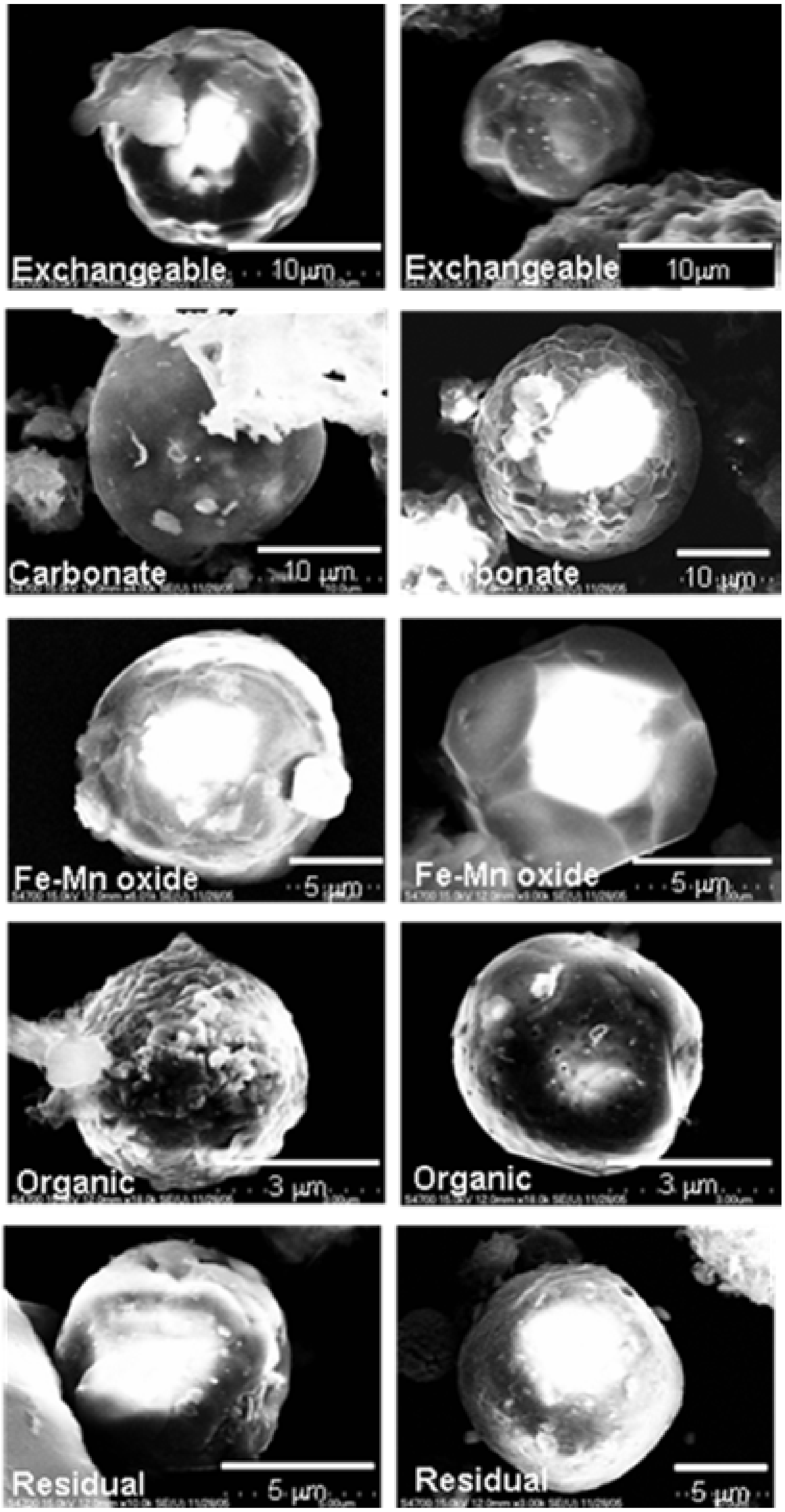

Figure 2.5: Scanning electron micrographs of the solids remaining after each selective sequential extraction step (as indicated on the micrographs) of the forested Quarry muck soil showing the approximately spherical NiO particles.

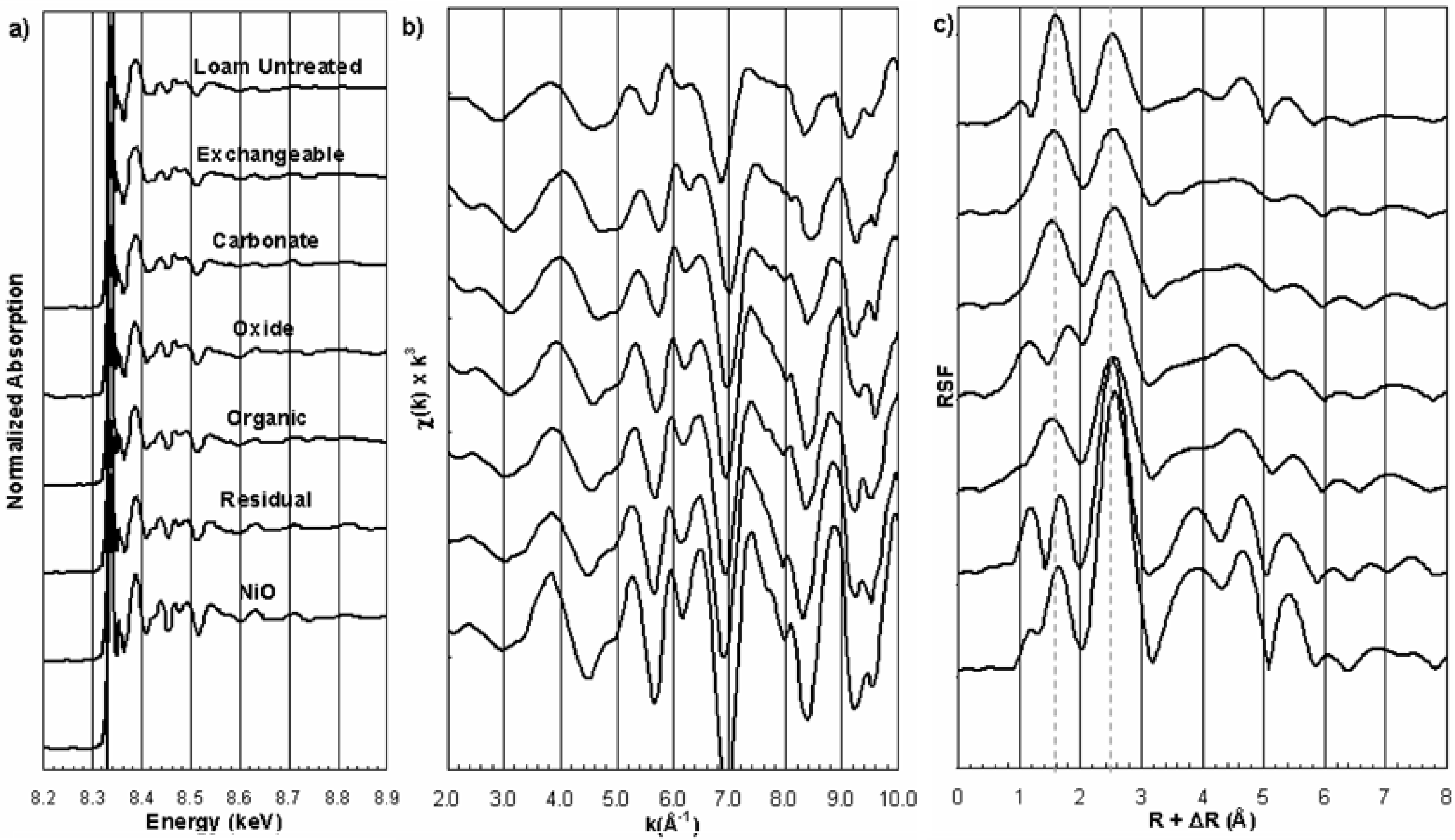

Figure 2.6: Background corrected(a), $k^3\chi(k)$-spectra (b), and radial structure function (RSF) spectra (c) of the untreated Welland loam soil and the solids remaining after the exchangeable, carbonate, oxide, organic and residual sequential extraction steps. The NiO standard spectra is included for reference.

Table 2.3: Structural parameters obtained from non-linear least squares fitting of the unaltered, exchangeable, carbonate, oxide, organic and residual sequentially extracted solid fractions from the Welland Loam and Quarry Muck soils. NiO, α-NI(OH)$_2$ and β-Ni(OH)$_2$ and Ni Al-LDH standards are included for comparison.

		First shell				**Second Shell**				
Fraction Removed	Atom	N[a]	R (Å)[b]	$\Delta\sigma^2$ (Å^2)[c]	Atom	N	R (Å)	$\Delta\sigma^2$ (Å^2)	ΔE_o (eV)[d]	X^2_{res} %
Quarry Muck										
Untreated	**O**	6.00	2.07	0.006	**Ni**	8.30	2.95	0.007	-3.17	3.72
Exchangeable	**O**	4.28	2.07	0.004	**Ni**	6.20	2.96	0.005	-3.46	6.68
Carbonate	**O**	5.10	2.07	0.007	**Ni**	7.01	2.96	0.007	-3.16	4.12
Oxide	**O**	5.02	2.07	0.006	**Ni**	8.01	2.96	0.006	-3.25	4.78
Organic	**O**	4.75	2.07	0.007	**Ni**	8.48	2.96	0.006	-3.57	4.64
Residual	**O**	4.73	2.08	0.007	**Ni**	9.13	2.96	0.006	-2.78	3.82
Welland Loam										
Untreated	**O**	6.62	2.06	0.007	**Ni**	6.26	2.96	0.007	-3.81	3.8
Exchangeable	**O**	6.00	2.07	0.007	**Ni**	6.40	2.97	0.007	-3.18	2.87
Carbonate	**O**	6.00	2.06	0.006	**Ni**	6.33	2.97	0.006	-3.31	3.26
Oxide	**O**	7.19	2.11	0.010	**Ni**	13.13	2.99	0.012	-1.11	2.9
Organic	**O**	6.23	2.06	0.009	**Ni**	9.65	2.96	0.008	-4.26	3.44
Residual	**O**	3.23	2.09	0.002	**Ni**	5.6	2.91	0.002	-10.02	14.64
References										
NiO	**O**	6.01	2.07	0.006	**Ni**	12.8	2.95	0.006	-4.16	3.89
α-Ni(OH)$_2$	**O**	5.60	2.04	0.005	**Ni**	6.15	3.10	0.006	-3.62	3.75
β-Ni(OH)$_2$	**O**	6.50	2.06	0.005	**Ni**	6.00	3.12	0.003	0.02	3.13
Ni Al-LDH	**O**	5.80	2.05	0.004	**Ni**	3.80	3.06	0.005	-2.64	11.79
					Al	1.90	3.06	0.005		

[a] Coordination number; [b] Interatomic distance; [c] Debye-Waller factor

[d] Energy shift parameters were corellated durring fitting

particles. Only a small amount of Ni was removed in the organic extraction step, and as such, little change in the spectra (Fig. 2.5) from the proceeding step was expected. However, the EXAFS, $k^3\chi(k)$-spectra and RSF resemble that of the carbonate extraction step, only with a reduction in the first shell intensity. The final step in the organic extraction (addition of 3.2 M NH_4OAc in 20% HNO_3) may have been effective at removing the weakly bound Ni from the NiO particle surface and thus the spectra is “cleaner” and the fit parameters are more consistent with those of NiO. The residual fraction RSF has a doublet peak at lower energy as was seen in the oxide residue $\chi(k)k^3$-spectra, but without the shift to higher energy. The fit was not very good as indicated by a X^2_{res}% of 14.64 and a significantly higher energy shift (-10.02 eV). Variability in these values are again an indication that the extraction step (hot HNO_3/HCl microwave digest) was effective at dissolving a portion of the NiO (as is intended) but there is still an un-recovered Ni fraction remaining in the residual. Detection of the NiO particles using SEM, was tenuous for the Welland Loam compared to the Quarry soils because of the structural similarity (approximately spherical) of many of the mineral soil constituents compared to the more linear morphology found in the highly organic muck soils. Regardless, the spectroscopic data supports the presence of NiO in each of the extraction steps and affirms the relative insolubility of the particles exposed to the harshest of extractants.

2.4.4 Electron Probe Micro-Analysis (EMPA)

Electron probe microanalysis was used to assess Ni associations with lower Z elements such as Al or Si which are undetectable via other methods employed in this research (e.g. XAFS). The backscattered electron images and associated elemental distributions for the Welland loam and Quarry muck, limed and unlimed soils can be seen in Figures 2.7(a-b) and 2.8(a-b), respectively. The most resounding feature among all of the soils and treatments is the presence of distinct approximately spherical Ni rich particles ranging from ~5- to 50μm in diameter. Hoflich et al. (2000) and Weinbruch et al. (2002) examined Ni refinery aerosols and found similar spherical morphologies with variable chemical composition differentiated chiefly by the silica and sulfur contents. In our samples, the particles are not associated with any of the elements analyzed with the exception of oxygen. This is evident in the Welland loam untreated sample (Fig 2.7b). A particle has been dissected in the microtoming process, revealing the interior of the particle. The interior has darker spots in the center and a darker shell which correlates well with the O elemental map. The particle is most likely metallic Ni which has begun to weather, forming an oxide coating on its exterior.

Diffuse Ni associations are also visible in the elemental maps of both the limed Welland loam (Fig. 2.7a) and Quarry muck (Fig. 2.8a) soils (see arrows). In the bottom left corner of the Welland loam sample, Fe, Ni and Cu are well correlated on the surface of a K, Al and Si containing particle (possibly feldspar or mica). Nickel is well correlated with Cu throughout both the limed and un-limed muck samples. The

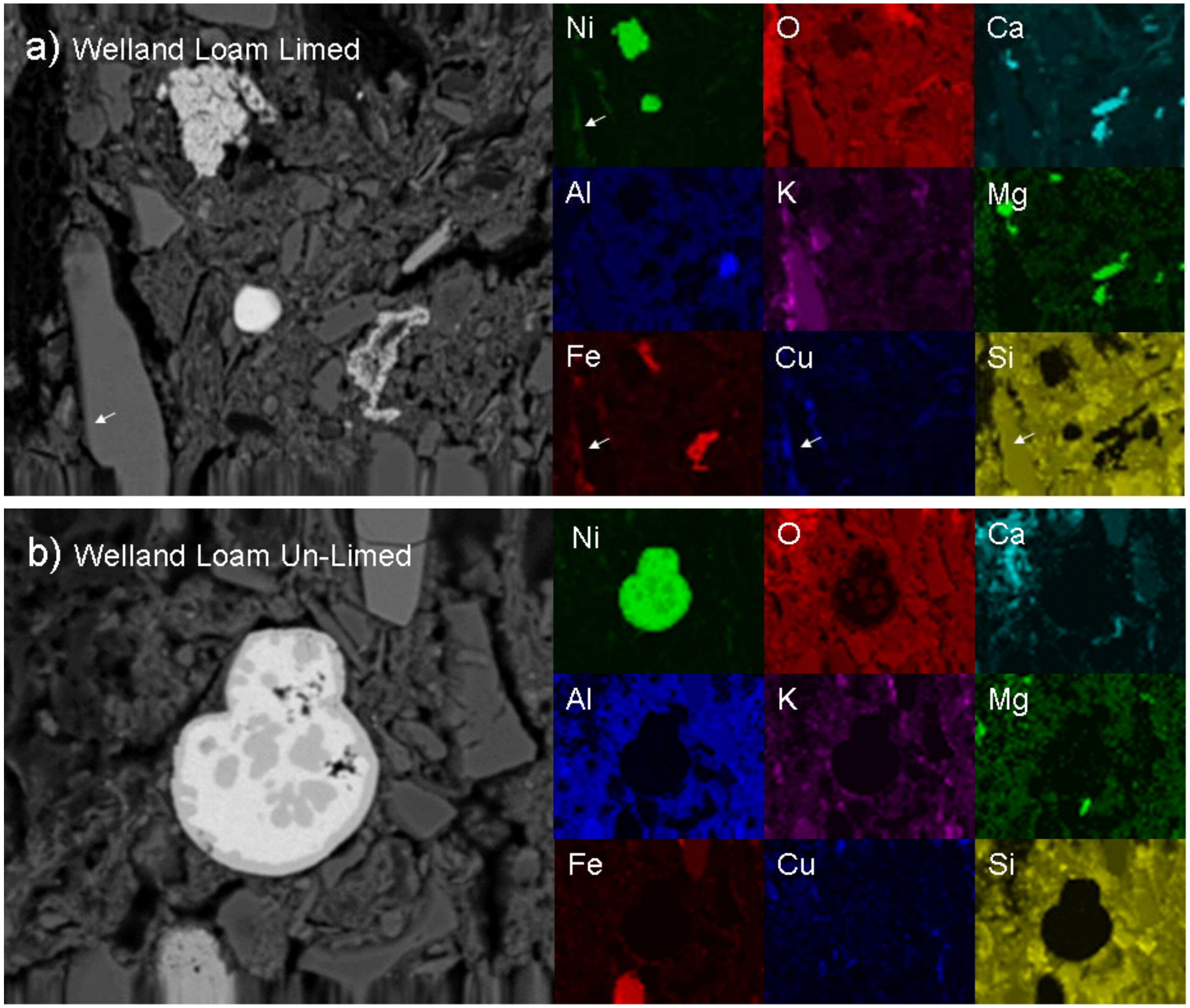

Figure 2.7: Backscatter electron image (large) and elemental distributionsmaps (small) of the limed (a) and unlimed (b) Welland loam soils.

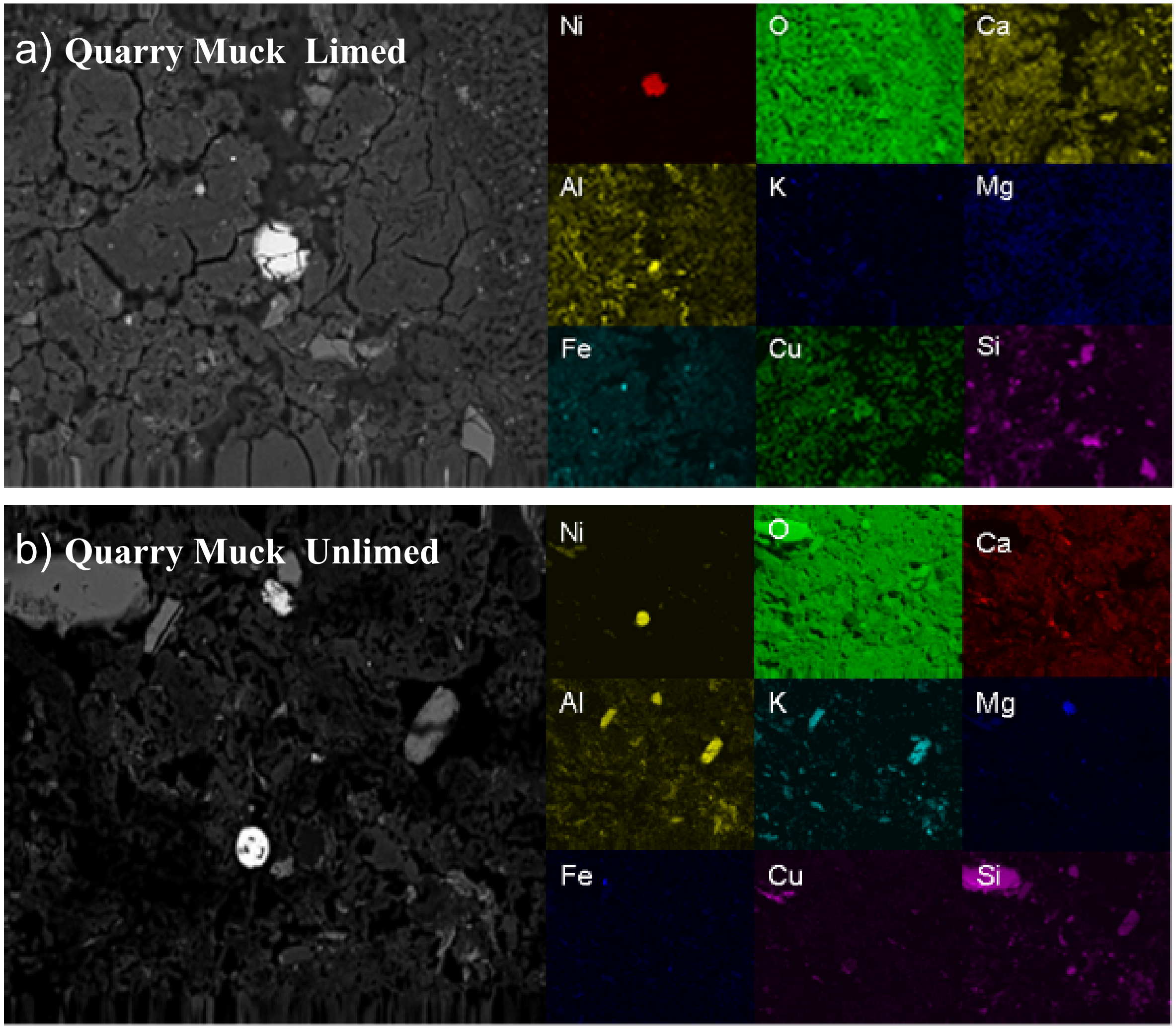

Figure 2.8: Backscattered electron image (Large) and elemental distribution maps for the limed (a) and unlimed (b) Quarry muck soils.

most obvious example of the Ni-Cu association is shown in the top left corner of the Ni and Cu elemental maps of fig. 2.8a where Ni and Cu are associated with a Si and O containing (most likely quartz) particle. Since these soils are extremely high in organic matter and Cu has a very high affinity for OM (followed by Ni), it is likely the Ni and Cu are complexed in an organic coating on the surface of the quartz particle.

2.4.5 XAFS Characterization of Standards

When using principal component and target transform analysis, it is critical to have a well characterized set of reference phases representing all of the possible metal species present within the system under investigation. Figure 2.9a and b shows the extracted $k^3\chi(k)$-spectra for some of the reference phases and Table 2.4, the structural parameters derived from non-linear least squares shell fitting. The mineral standards used include bunsenite (NiO), trevorite ($(Ni,Cu)Fe_2O_4$), heazlewoodite (Ni_3S_2), godlevskite ($(Ni,Cu)_9S_8$), Violarite (Ni_2,FeS_4), Millerite (NiS) and Gaspeite ($(Ni,Mg,Fe)CO_3$) which were identified by Weinbruch et al. (2002) using transmission and scanning electron microscopy to examine aerosols present in a refinery processing nickel sulfide ores. The coordination number and bond distances for Bunsenite compare well with those reported in the literature (Trivedi et al. 2001). Nickel is in tetrahedral coordination in the sulfur bearing minerals with average Ni-S first shell distances of 2.3 Å. Non linear least squares fits (NLLSF) for Millerite were best achieved using 4.5 S atoms at approximately 2.3 Å, which represents the average bond

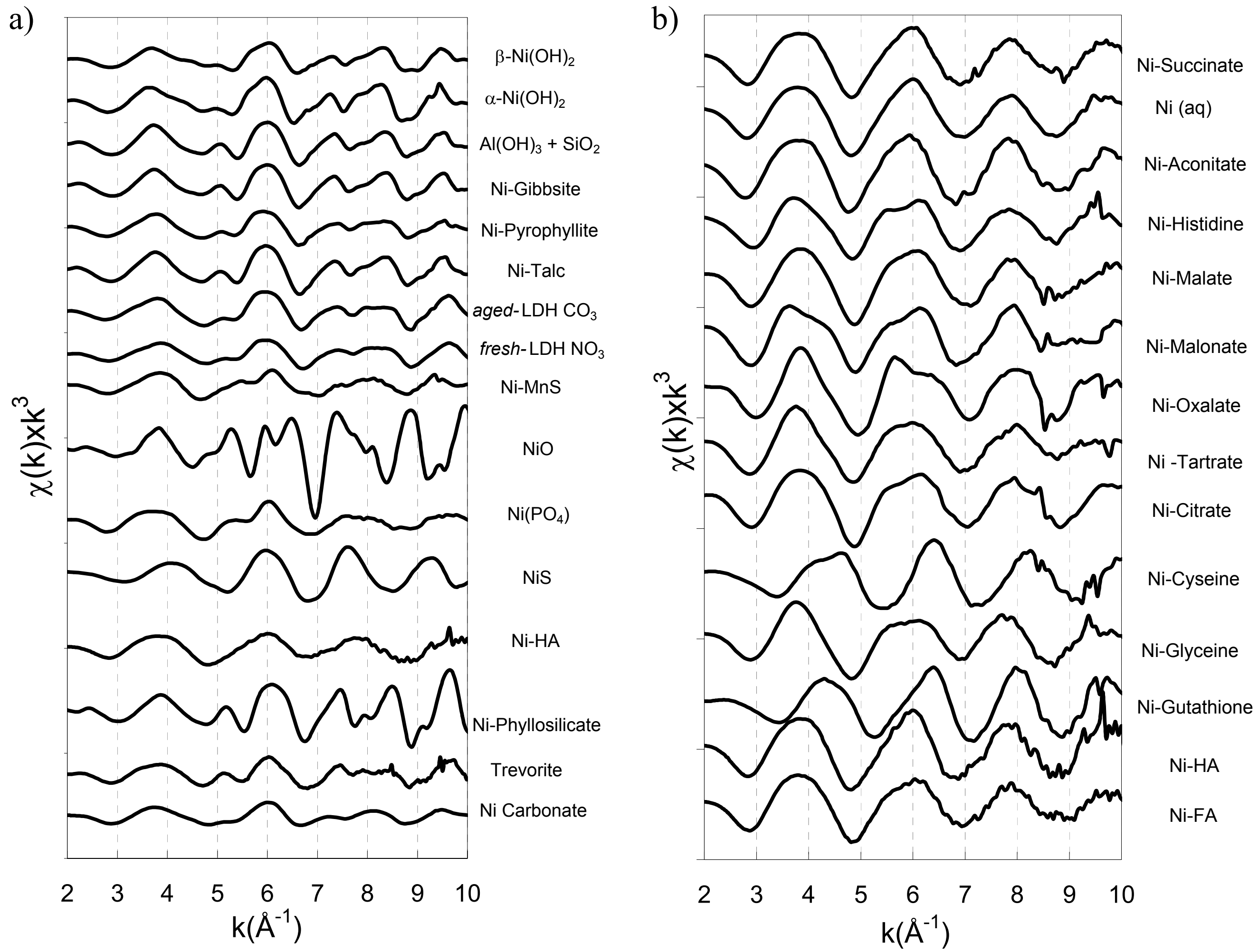

Figure 2.9: Ni-K k3 weighted c-spectra of selected mineral (a) and organic (b) reference phases used in principal component analysis and linear least squares fitting

Table 2.4: Best-fit EXAFS parameters for reference mineral and sorption/precipitate samples used in principal component analysis.

		First shell				Second Shell				
	Atom	CN	R (Å)[a]	$\Delta\sigma^2$ (Å^2)	Atom	CN	R (Å)[a]	$\Delta\sigma^2$ (Å^2)	ΔE_o (eV)	X^2_{res} %
Minerals										
Bunsenite (NiO)	**O**	6.01	2.07	0.006	**Ni**	12.80	2.95	0.006	-4.16	3.89
Trevorite [(Ni,Cu)$Fe^{3+}{}_2O_4$]	**O**	5.07	2.06	0.004	**Ni**	4.79	3.07	0.007	-2.48	2.54
					Fe	3.31	2.93	0.013		
Heazlewoodite [Ni_3S_2]	**S**	3.96	2.25	0.007	**---**				-7.95	2.00
Godlevskite [$(Ni_{8.7},Fe_{0.3})_9S_8$]	**S**	3.25	2.32	0.003	**Ni**	3.27	2.52	0.03	8.69	2.74
Violarite [Ni_2,Fe^{2+} S_4]	**S**	4.56	2.32	0.007	**---**				14.53	10.95
Millerite (NiS)	**S**	4.45	2.33	0.008	**---**				3.17	2.09
Gaspeite (Ni,Mg,Fe)CO_3	**O**	4.83	2.07	0.005	**C**	2.60	2.93	0.002	2.5	13.59
Arupite ($Ni_3(PO_4)_2$)	**O**	6.60	2.05	0.006	**---**	---	---	---	-5.88	1.46
$NiCO_3$	**O**	5.28	2.05	0.007	**Ni**	3.12	3.11	0.009	-2.43	6.08
Co-precipitates										
α-$Ni(OH)_2$	**O**	5.60	2.04	0.005	**Ni**	6.15	3.10	0.006	-3.62	3.75
β-$Ni(OH)_2$	**O**	6.50	2.06	0.004	**Ni**	6.00	3.12	0.003	0.02	3.13
Ni-Al LDH (CO_3)	**O**	6.00	2.06	0.005	**Ni**	4.28	3.07	0.006	-4.72	11.00
					Al	0.50	3.07	0.008		
Aged Ni-Al LDH (CO_3)	**O**	5.34	2.06	0.05	**Ni**	2.90	3.06	0.007	-3.7	8.37
					Al	2.00	3.06	0.005		
Fresh Ni-Al LDH (NO_3)	**O**	5.80	2.05	0.0043	**Ni**	3.80	3.06	0.005	-2.64	11.79
					Al	1.60	3.06	0.005		
Ni-$Al(OH)_3$ + SiO_2 (7yr)	**O**	7.50	2.06	0.008	**Ni**	3.60	3.08	0.005	-2.28	1.6
(i.e. Gibbsite+Quartz)					**Si**	7.60	3.30	0.008		
Ni Phylosilicate	**O**	5.60	2.06	0.003	**Ni**	3.65	3.06	0.001	-2.33	1.56
($Ni_3Si_4O_{10})OH)_2$)					**Si**	6.70	3.27	0.001		
Sorption Samples										
Ni (aq)	**O**	6.70	2.05	0.006	---	---	---	---	-4.31	1.47
Ni-Humic Acid	**O**	6.60	2.06	0.003	**C**	1.80	2.85	0.010	-2.93	2.13
Ni-Fulvic Acid	**O**	6.60	2.04	0.007	**C**	2.10	2.87	0.006	2.96	5.3
Ni-Mn S	**O**	7.70	2.05	0.009	**Mn**	4.38	3.48	0.010	-4.84	3.37
					S	0.75	2.68	0.002	10.94	
Ni-Gibbsite (7yr)	**O**	6.00	2.04	0.006	**Ni**	5.30	3.08	0.009	2.5	
					Al	0.40	3.08	0.009		
Ni-SiO_2 (7yr)	**O**	6.60	2.06	0.007	**Ni**	6.80	3.10	0.007	-1.16	7.46
Ni-Talc (7yr)	**O**	6.00	2.06	0.006	**NI**	5.70	3.09	0.008	-2.49	3.9
					Si	5.60	3.26	0.010		
Ni-Pyrophyllite (7yr)	**O**	7.80	2.05	0.008	**Ni**	6.44	3.08	0.009	-5.83	4.89
					Si	4.79	3.16	0.014		
Aqueous Organic										
Ni-Succinate	**O**	6.00	2.05	0.007		---	---	---	-0.12	2.23
Ni-Aconitate	**O**	6.50	2.05	0.006	**C**	---	---	---	-0.4	9.97
Ni-Histidine	**N/O**	6.40	2.09	0.005	**C**	5.50	2.92	0.012	-2.23	5.44
Ni-malate	**O**	6.00	2.05	0.002	**C**	3.50	2.82	0.003	1.96	6.48
Ni-malonate	**O**	5.90	2.03	0.004	**C**	3.01	2.87	0.007	-1.4	7.63
Ni-citrate	**O**	6.00	2.03	0.004	**C**	4.30	2.83	0.006	-3.52	6.76
Ni-Oxalate	**O**	6.00	2.05	0.004	**C**	4.25	2.84	0.000	-1.07	6.12
Ni-Tartrate	**O**	6.00	2.05	0.004	**C**	5.50	2.82	0.007	0.61	7.30
Ni-Glutathione	**S**	2.00	2.21	0.005	**C**	1.67	2.91	0.001	8.4	8.34
	N	4.00	2.19	0.002	**---**	**---**	**---**	**---**		
Ni-Cystine	**S**	4.59	2.15	0.007	**C**	5.43	2.93	0.007	-6.38	7.21
Ni-Glycine	**N**	7.00	2.09	0.007	**C**	4.23	2.88	0.006	3.54	5.4

[a] bond distances derived from single shell fiting and thus represent the average radial distance

CN = Coordination Number (±20% (Scheidegger et al., 1997)

R = inter-atomic distance (±0.02 Å for first shell and ± 0.05 Å for the second and third shell (Scheidegger eta al., 1997))

σ^2(Å^2) = Debye Waller factor

ΔE_o = Energy shift

(7yr) = indicates sorption/co-precipitate samples that have been incubated for 7 yrs at constant temp distance for the S atoms (@ 2.26, 2.78 and 2.36 Å) in the distorted tetragonal structure (Parise 1980). The NLLSF for the Heazlewoodite standard verifies its trigonal structure observed by Fleet (1977) with edge and point sharing tetrahedra containing Ni coordinated to 4 sulfur atoms at an average distance of 2.25 Å. The NLLSF for Godlevskite verifies its orthorhombic structure, with edge and point sharing tetrahedra and pyramids containing Ni surrounded by 4 or 5 S atoms at an average distance of 2.19 -2.32 Å and a second coordination shell of ~ 4 Ni atoms at 3.52 Å. Ni in Violarite is tetrahedrally coordinated to ~4 S atoms at 2.32 Å which agrees well with the XRD crystallographic data for this spinel mineral (Grimaldi 1964).

A variety of sorption and coprecipitate standards were generated to represent all of the possible Ni sorption complexes expected within the soils The aged (7 year) Ni-Al$(OH)_3$ + SiO_2, Ni-Talc and Ni pyrophyllite samples were best fit with ~4 Ni atoms at ~3.08Å and ~5-8 Si atoms at ~3.25Å in the second coordination shell, similar to that of Ni phyllosilicate (Scheidegger et al. 1998; Scheinost et al. 1999; Scheckel and Sparks 2000; Scheinost and Sparks 2000; Nachtegaal and Sparks 2003). Contrastingly the 7yr Ni-SiO_2 standard was best fit with ~6 Ni at 3.10 Å in the octahedral layer, similar to that of α-Ni$(OH)_2$. There is increasing evidence that mixed metal (e.g. Ni, Zn) layered double hydroxides (M^{n+}-Al LDH) form in field soils (Roberts et al. 1999; Manceau et al. 2000; Nachtegaal et al. 2005). As such several Ni-Al LDH samples and their precursors were included in the database (Ford et al. 1999). Two lab generated LDH precipitates were used; one with NO_3, and another with CO_3 occupying the interlayer space, and each with a Ni to Al ratio of ~2:1. Furthermore, the CO_3 interlayered LDH was aged at 65°C for two weeks to produce a more ordered phase as would be expected with longer aging times in the natural environment. The success of the aging process is reflected in the higher second shell Al content and the slightly lower residual error (11.37 (fresh) to 8.34 (aged)) of the fit and the $\Delta\sigma^2$ values for the second shell aluminum (0.008Å^2 (fresh) to 0.005Å^2 (aged)) for the aged sample compared to the freshly precipitated LDH. In addition, both the alpha- and beta- type hydroxides were included with α-$Ni(OH)_2$ having a characteristically shorter Ni-Ni distance (3.10 Å) compared to the beta form (3.12 Å).

Ni-humic and –fulvic acid sorption samples, as well as isolated organic and amino acid sorption standards were included in the dataset to represent the diversity of functional groups most likely present in the highly organic Quarry muck soils. The $k^3\chi(k)$-spectra of the organic and amino acid standards (Figure 2.9b) are very similar to the hexaquo-Ni standard ($Ni(H_2O)_6 \bullet NO_3$); however, there are characteristic features in the second and third oscillations which are indicative of the binding environment of Ni. Strathmann and Myneni 2004) used both FTIR and synchrotron X-ray spectroscopies to characterize the binding environment of Ni with several organic acids. They noted that longer chain organic acids, where the carboxylate functional groups are separated by one or more methylene groups form weak complexes with Ni, whereas those with shorter chains or closely packed carboxyl (COOH) groups supported by adjacent alcohol (C-OH) donor groups form stronger complexes, and in some cases, chelates. We found similar results with fits for Ni -malate, -malonate, -citrate, -oxalate and –tartrate best achieved using ~ 4-5 C atoms at ~ 2.83-2.87Å in the second coordination shell. Aconitate is similar in structure to citrate, but lacks the alcohol group at the C_3 carbon (adjacent to the carboxylic acid group) which may reduce its ability to form chelates with Ni. As such, no carbon second shell could be confidently fit. The amino acid histidine was fit with ~6 N/O atoms at 2.09 Å in the first shell and ~6 C atoms at 2.91 Å in the second shell which is indicative of inner-sphere complexation. Ni complexes with the plant/microbial antioxidant glutathione and its components were also included.

2.4.6 Synchrotron μ-SXRF and μ-XAFS

The first step in a μ-XAFS experiment is to obtain X-ray fluorescent maps over several regions within each sample from which elemental distributions and correlations can be ascertained. Fluorescence maps were collected over several regions within the Welland loam and Quarry muck limed and unlimed soils. Figure 2.10a, for example, is a map a from the un-limed Welland loam soils, in which the fluorescence signals for Ni, Fe and Mn were assigned the colors red, green and blue, respectively. The color coded fluorescence signals are then superimposed with the resulting mixing of colors representative of metal associations. The color correlation triangle in the upper left corner of the μ-SXRF map is a key to interpreting the mixing of colors in the map. For example, the equal mixing of nickel (red), iron (green) and manganese (blue) fluorescence signals would appear as a white spot on the map, while the equal mixing of iron (green) and manganese (blue) would result in cyan. Following this convention, the Ni, Fe and Mn distributions in the Welland Loam unlimed (Figure 2.10a) and limed (Figure 2.11a) soils, as well as the unlimed and limed (Figures 12a and 13a) Muck soils were assessed. Fluorescence yield from Ca, Cr, Ti, Cu, Zn and As were simultaneously collected and analyzed for their association with Ni, but no clear pattern was observed. The lack of Ni-metal associations was confirmed by cross correlating the fluorescence yield (which is proportional to the concentration) on a pixel by pixel basis for each element in the map. Therefore, we show here the maps of Ni with Fe and Mn because they are ubiquitous in soils and provide, with reasonable detail, the structure of the soil aggregates.

As was seen in the SEM micrographs, there are discrete approximately spherical Ni particles throughout all of the samples (e.g. white arrow Figure 2.10a). The Sequential extractions and EMPA analysis confirmed thatthese particles are NiO. The sequential extractions clearly showed that these particles are, for the most part, insoluble, persisting through the harshest of extractions steps. However, the removal of some Ni during both the stirred-flow experiments and the initial steps (i.e $MgCl_2$ and NaOAc extractable fractions) of the sequential extractions indicate that phases other than the insoluble NiO may exist. Therefore, μ-XAFS was used to probe around the obvious NiO spots in order to characterize the less obvious, put potentially more reactive and significant (in terms of bioavailability) Ni species.

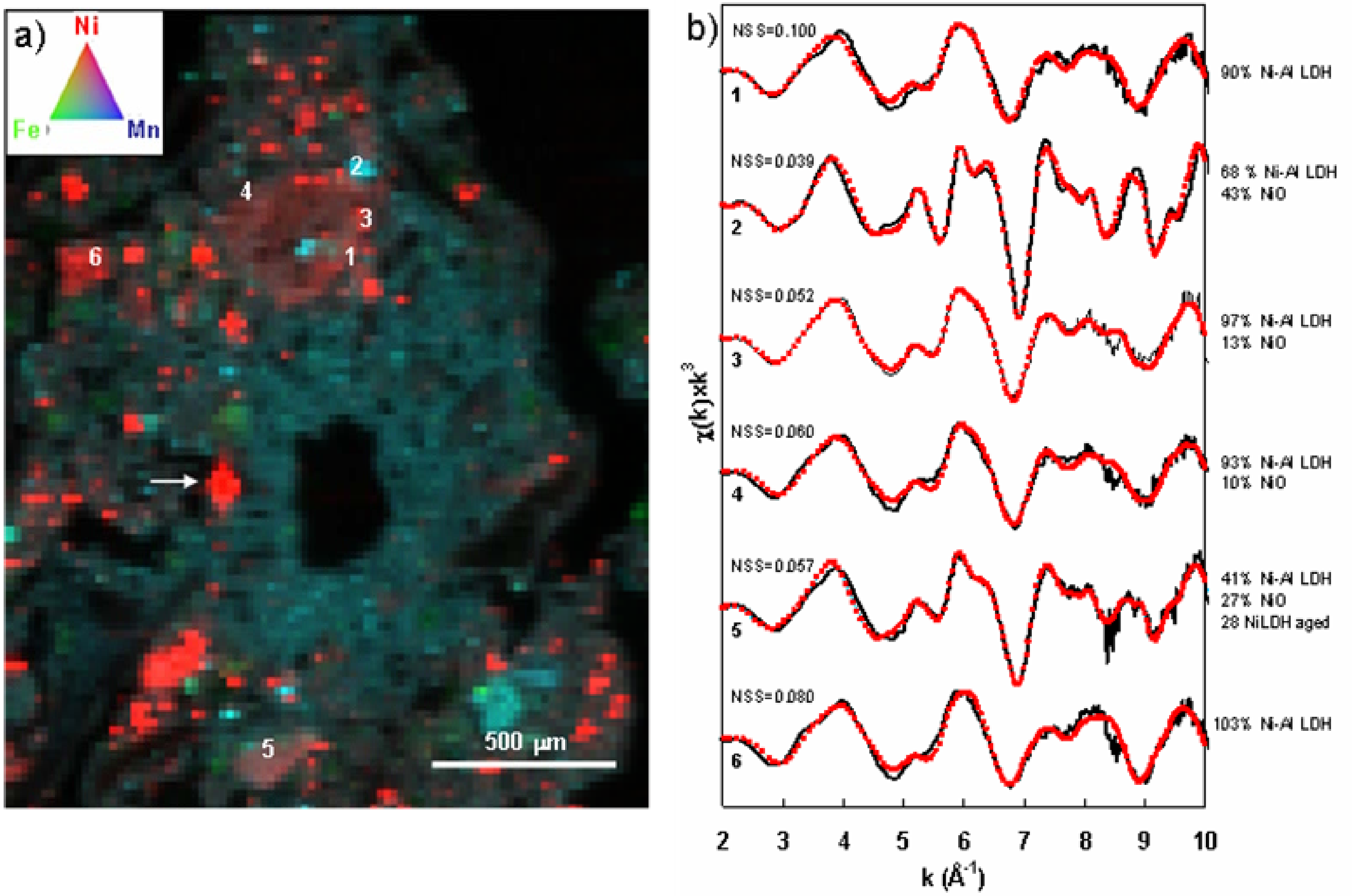

Figure 2.10: a)$_{\chi}$-SXRF tricolor map of the Welland loam unlimed soil and b)$_{\chi}$-EXAFS spectra from selected spots within the maps. Solid lines represent the k^3 weighted$_{\chi}$-spectra and the dotted red line the best fits obtained using a linear least squares fitting approach.

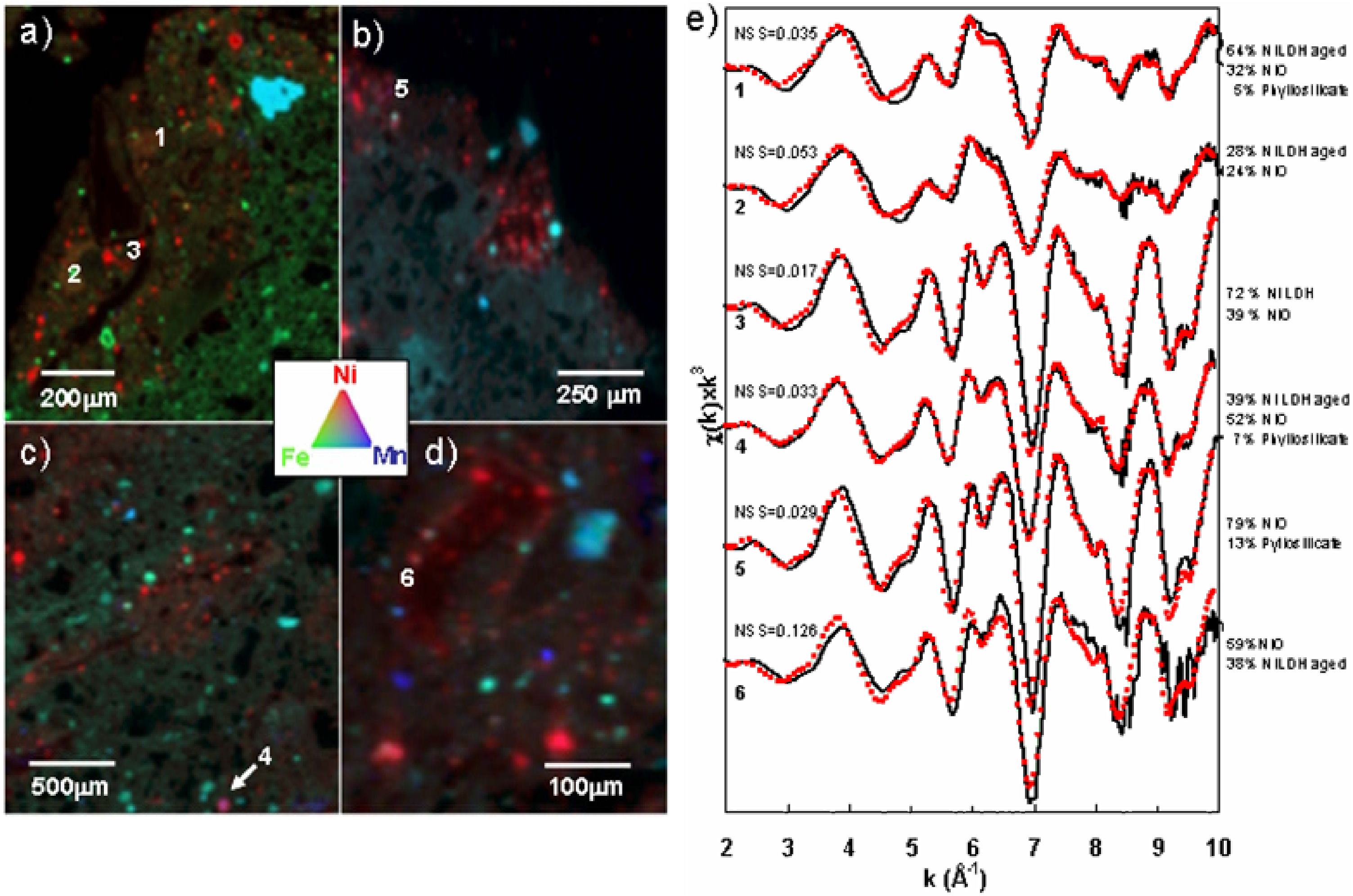

Figure 2.11: a-d) μ-SXRF tricolor map of the Welland loam Limed soil and e) μ-XAFS spectra from selected spots within the maps. Solid lines represent the k^3 weighted χ-spectra and the dotted line the best fits obtained using a linear least squares fitting approach.

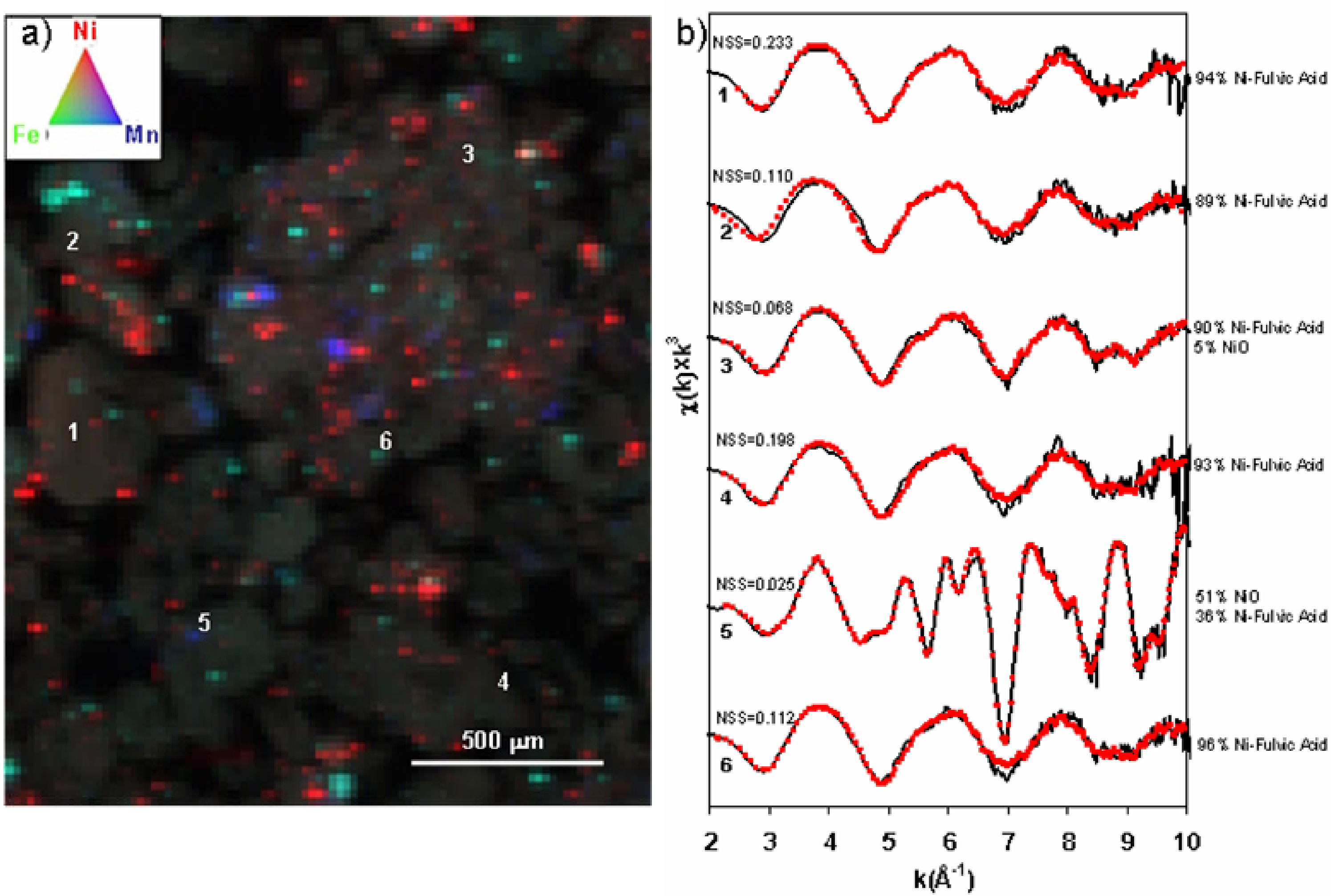

Figure 2.12: a) χ-SXRF tricolor map of the Quarry muck unlimed soil and b) χ-EXAFS spectra from selected spots within the maps (numbered 1-6). Solid lines represent the k^3 weighted χ-spectra and the dotted line the best fits obtained using a linear least squares fitting approach

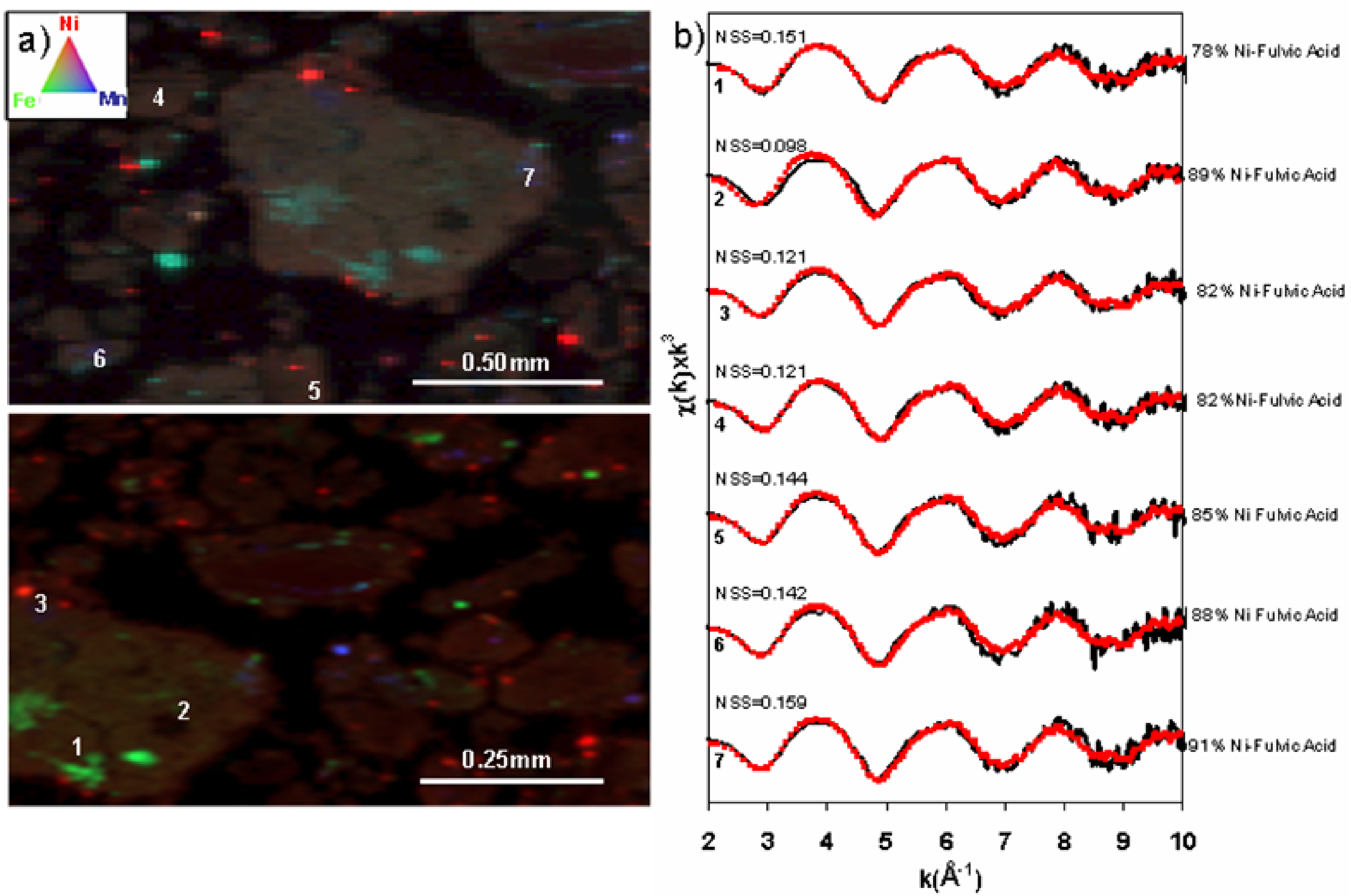

Figure 2.13 a)χ-SXRF tricolor map of the Quarry muck treated soil and b)χ-XAFS spectra from selected spots within the maps. Solid line represents the k^3 weighted χ-spectra and the dotted line the best fits obtained using a linear least squares fitting approach.

To highlight the diffuse Ni distribution, the fluorescence yield (i.e. gamma) for Ni was increased in all of the μ-SXRF maps. By doing so the diffuse regions of Ni appear in the loam soils as red "clouds" in/on/around selected soil aggregates. In the Quarry muck soils, Ni is more homogeneously distributed throughout the soil aggregates. Examples of diffuse regions of Ni can be seen in the top center of the μ-SXRF map for the un-treated Welland Loam soil (Figure 2.10a), or in the μ-SXRF map for the limed Quarry muck soils (Figure 2.13a and 2.13b). To obtain specific chemical and structural information about the binding environment of Ni in these areas, multiple μ-XAFS spectra were collected throughout each of the samples. Locations where μ-XAFS data were collected are indicated by numbers on the μ-SXRF maps which correspond to the adjacent $k^3\chi(k)$ spectra . The data presented here represent only a subset of the total spectra taken for each of the soils and treatments, but represent all of the Ni species identified. In all, 19 spectra were collected from the Quarry muck soils (7 limed + 13 unlimed) and 30 spectra from the Welland loam soils (11 limed + 19 unlimed). Included in these datasets were spectra from isolated silt and clay fractions from both untreated soils as well as bulk XAFS spectra for both treated and untreated soils. Principal component analysis was performed on the combined (Lime + Un-limed) datasets for each of the soil types. PCA indicates the datasets for both the Quarry muck and Welland loam soils are best represented by 3 unique spectral components.

Table 2.5: Target transform SPOIL values using three components for the Quarry muck and Welland loam soils

	SPOIL Value*	
	Quarry Muck	**Welland Loam**
Minerals		
Bunsenite (NiO)	**2.23**	**2.36**
Trevorite [$(Ni,Cu)Fe^{3+}{}_2O_4$]	10.88	3.85
Heazlewoodite [Ni_3S_2]	8.96	7.59
Godlevskite [$(Ni_{8.7},Fe_{0.3})_9S_8$]	14.53	7.34
Violarite [$Ni_2,Fe^{2+} S_4$]	18.59	7.54
Millerite (NiS)	12.78	6,81
Gaspeite $(Ni,Mg,Fe)CO_3$	10.11	4.46
Arupite ($Ni_3(PO_4)_2$)	6.59	5.43
$NiCO_3$	6.21	3.70
Co-precipitates		
α-$Ni(OH)_2$	10.55	5.73
β-$Ni(OH)_2$	8.73	5.19
Ni-Al LDH (CO_3)	8.79	3.18
Aged Ni-Al LDH (CO_3)	8.19	**3.00**
Fresh Ni-Al LDH (NO_3)	7.37	**1.93**
Ni-$Al(OH)_3$ + SiO_2 (7yr) (i.e. Gibbsite+Quartz)	13.10	6.34
Ni Phylosilicate ($Ni_3Si_4O_{10})OH)_2$)	16.52	**2.86**
Sorption Samples		
Ni (aq)	3.44	3.31
Ni-Humic Acid	5.00	4.44
Ni-Fulvic Acid	**2.34**	3.73
Ni-Mn S	6.25	5.06
Ni-Gibbsite (7yr)	13.25	6.17
Ni-SiO_2 (7yr)	13.01	5.69
Ni-Talc (7yr)	10.78	5.42
Ni-Pyrophyllite (7yr)	8.53	5.11
Aqueous Organic		
Ni-Aconitate	3.47	3.69
Ni-Histidine	3.71	4.34
Ni-malate	**2.53**	3.70
Ni-malonate	3.58	3.79
Ni-citrate	3.10	4.03
Ni-Oxalate	5.17	4.26
Ni-Tartrate	3.82	3.89
Ni-Glutathione	16.25	13.42
Ni-Cystine	14.25	23.49
Ni-Glycine	5.56	4.65

***SPOIL** values < 1.5 indicate an excellent fit, 1.5-3 good, 3-4.5 fair, 4.5-6 poor, and values >6 are unacceptable

To determine the most likely species represented by the principal components, target transform (TT) analysis was performed. The resulting SPOIL values for both soils can be seen in Table 2.5. The standard phases that received the lowest SPOIL values (from lowest to highest) in the Welland loam soils are: *fresh* NO_3 interlayered LDH (1.93), NiO (2.36) and Ni-phyllosilicate (2.86) and an *aged* CO_3 interlayer LDH (3.00). For the Quarry muck soils the standard phases that received the lowest SPOIL values were NiO (2.23), Ni-Fulvic Acid (2.34) and Ni-malate (2.53).

Linear least squares fits were performed to determine the proportion of each of the identified standard species in the μ-EXAFS scans. The solid lines in Figure 2.10b, 2.10e, 2.11b and 2.12c are the raw $k^3\chi(k)$-spectra and the red dotted lines the best fits using a combination of the identified reference spectra. The proportion of each of the standard phases used is located to the right of each $k^3\chi(k)$-spectra. The normalized sum square value (NSS) on the left of each spectra is a “goodness-of-fit” parameter with lower values representing a better fit. The NSS values ranged from 0.017 to 0.385 (average ≈ 0.161) and 0.025 to 0.233 (average ≈ 0.116) for the Welland Loam and Quarry muck soils respectively, indicating that the 3 components used in the LLSF adequately describe the speciation in the soils.

The results of the LLSF for spots 1-6 in the μ-SXRF map for the unlimed Welland loam soil are shown in Figure 2.10b. Spots 1-4 and 6 were fit with all or a combination of the fresh NO_3 interlayerd LDH, and NiO standards. The best fit for spot 1 was achieved using only the fresh LDH, however, the NSS value (0.100) indicates a less than ideal fit. By including reference spectra that were not identified by PCA in the LLSF, we found that Ni-malate significantly improved the fit (0.056). Malate (or malic acid) is an organic acid containing two carboxyl functional groups and most likely serves as a proxy for nickel interactions with functional groups of soil organic matter; which is probable considering these soils contain ~9% OM. We saw evidence for the Ni-OM interactions in the SEM-EDX micrographs (Figure 2.7), where Ni and Cu were well correlated in an organic coating around a quartz aggregate. The best fit for spot 5 included the aged LDH standard which we identified as a more structurally robust (i.e. well ordered) LDH compared to the freshly precipitated variety and thus indicating a more ordered precipitate phase has formed at this location. Notably, in the μ-SXRF map, the color mixing at spot 5 appears slightly more uniform than spots 1-4 and 6, and the particle more angular, which may indicate that the precipitate at this spot is present as a coating on a clay particle. Similar spots were seen in the limed loam samples (Figure 2.10), specifically spots 1, 2 and 4, which in addition to the aged LDH species, were also fit well using Ni-phyllosilicate. The $\chi(k)k^3$-spectra collected from the limed soils have more structure, with a "doublet" peak between 6.5 Å^{-1} and the deep trough at 7 Å^{-1} which are characteristics of strong backscattering from highly ordered phases such as NiO.

The average Ni distribution found using μ-XAFS in all of the spots analyzed from both the limed and un-limed Welland loam soils combined is: *fresh* Ni-Al LDH (NO_3) (56%) > aged Ni Al LDH (CO_3) (21%) ≈ NiO (20%) > Ni-phyllosilicate (1%).

The average Ni distribution in the unlimed soils is: *fresh* Ni Al LDH (NO_3) (66%) > aged Ni-Al LDH (CO_3) (15%) ≈ NiO (12%). The average distribution in the limed soils only is: *fresh* Ni-Al LDH (NO_3) (39%) ≈ NiO (33%) > *aged* Ni-Al LDH (15%) > Ni phyllosilicate (2%). Overwhelmingly, the speciation of the diffuse areas in both the limed and un-limed Welland loam soils is dominated by secondary precipitate of Al and Ni. In the limed soils we found a larger proportion of Ni in the more stable Ni LDH phases and as Ni phyllosilicate.

Fits of the bulk XAFS spectra, using the species identified in PCA, to determine the primary Ni species in the Welland Loam limed and unlimed soils can be see in Figure 2.14. The two spectra look very similar with the only difference being a small shoulder on the down side of the large peak around 8$Å^{-1}$ in the unlimed soil, which may be a contribution from the LDH and therefore accounts for the slightly higher amount of LDH. The spectra are fit well using two components, NiO and the NiAl LDH. Notably, unlike in the LLSF for the μ-XAFS spectra, the *fresh* and *aged* Ni-Al LDH were interchangeable in the fit; the subtleties of each most likely masked by the overlapping contributions in the bulk spectra. Additionally, inclusion of a Ni phyllosilicate phase did not improve the fit, further highlighting the effectiveness of μ-XAFS techniques at detecting minor components.

The results for the LLSF of the spots in the μ-SXRF map for the unlimed Quarry muck soil can be seen in Figure 2.12b. With the exception of spot 5, the spectra are strongly sinusoidal out to ~10$Å^{-1}$ with a slight split at ~ 6 $Å^{-1}$. Spots 1, 2, 4

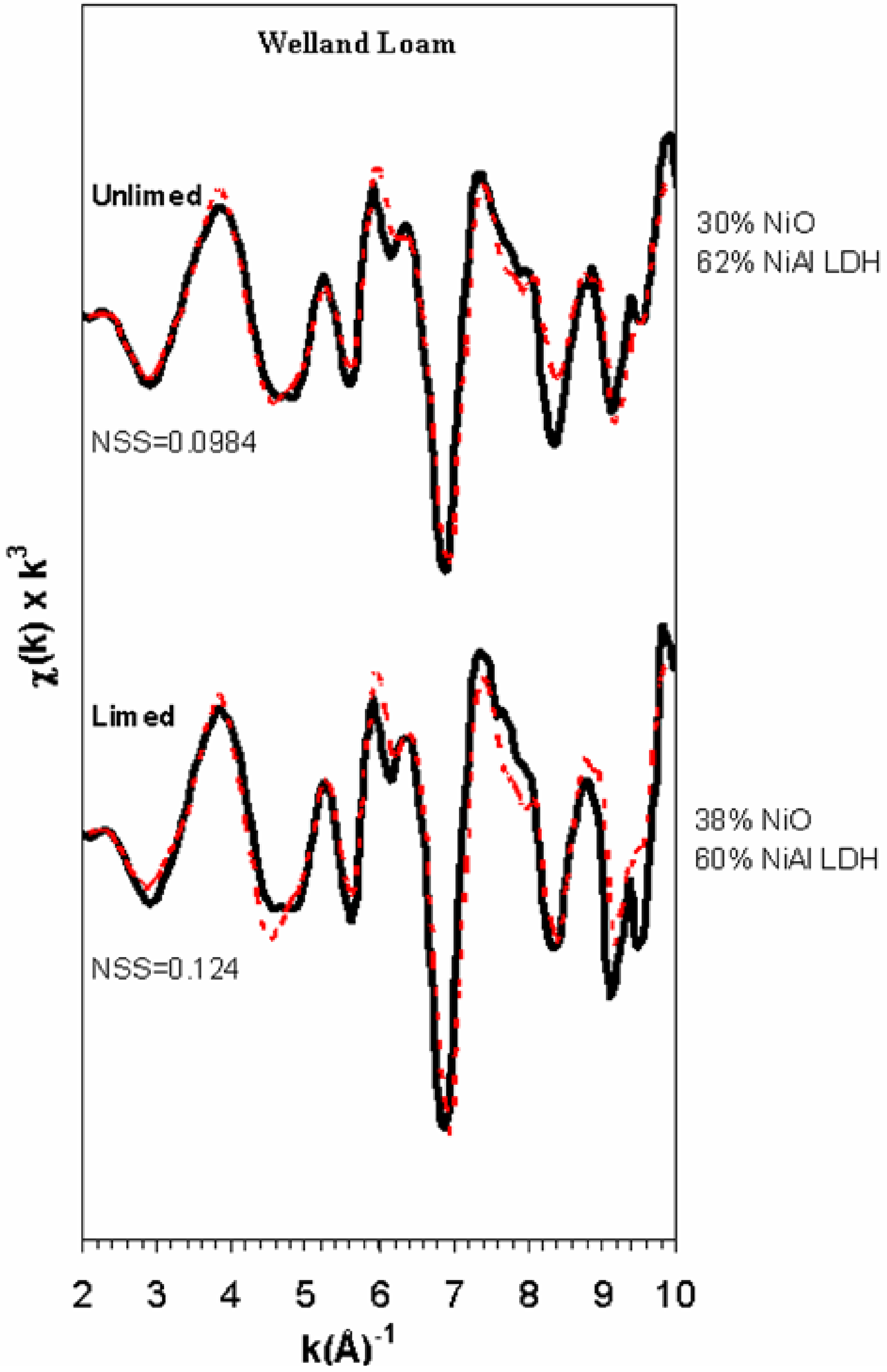

Figure 2.14: Best fits of the bulk EXAFS spectra from the limed and unlimed Welland Loam soils. Solid line represents the k^3 weighted χ-spectra and the dotted line the best fits obtained using a linear least squares fitting apporach.

and 6 were best fit using Ni-Fulvic acid only, while spots 2 and 5 contained significant amounts of NiO. In the limed soils, only the Ni-Fulvic acid standard produced the best fits. PCA indicated that there were 3 components necessary to reproduce the dataset, yet only NiO and Ni-FA provided best fits in our analysis. The most likely explanation is that fulvic acid is comprised of a mixture of functional groups (the most prominent being –COOH) each capable of sequestering Ni and other metals in a unique configuration. This FA "mixture" does a reasonable job of fitting the average coordination environment of Ni in the sites analyzed in our samples. Comparing the two treatments, we were better able to fit the sum (i.e., % total contribution of the standard to the unknown) of the spectra for the unlimed muck soils (92%) compared to the limed soils (85%). Research has shown that several factors, including pH, have a pronounced impact on the morphology of soil humic and fulvic acids which may lead to a more disordered binding environment and thus inferior fits for the unlimed soils (Myneni et al. 1999). Conversely, the functional groups partaking in the sequestration of Ni and/or the configuration of Ni binding changes with increased pH; a configuration which may not be well represented in our present standard dataset.

Fits of the bulk, limed and unlimed Quarry muck soils can be seen in Figure 2.15. Much like the Welland soils, the limed and unlimed Quarry muck spectra look similar, closely resembling the NiO spectra. The fit for the unlimed soil was very good (NSS=0.0257) compared to the limed soil (NSS = 0.102). The fit had trouble reproducing the features between 4 and 5Å^{-1} and the trough at ~8.4 Å^{-1}. These

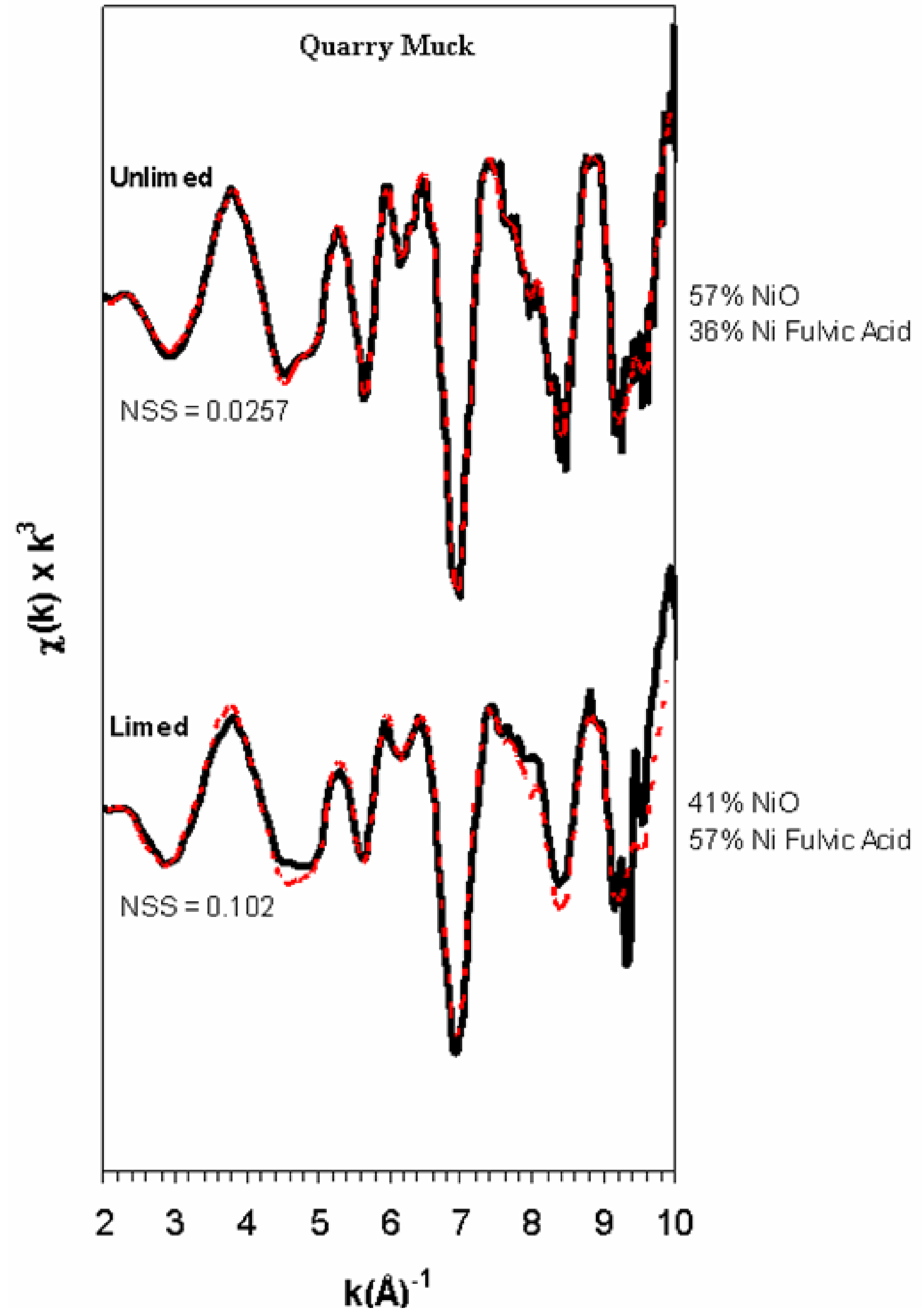

Figure 2.15: Best fits of the bulk EXAFS spectra from the limed and unlimed Quarry muck soils. Solid line represents the k^3 weighted χ-spectra and the dotted line the best fits obtained using a linear least squares fitting apporach.

features are slightly dampened compared to those in the unlimed soil, as well as the NiO standard; likely due to the increased amount of organically bound Ni.

2.5 Summary of Ni Speciation, mobility and bioavailability

The objectives of this research were to determine the effect of soil type and treatment on the speciation of Ni in Welland loam and Quarry muck soils surrounding an historic nickel refinery in Port Colborne, Ontario Canada. Using a combination of methods, we determined that NiO is the common Ni species in both the Welland loam and Quarry muck soils. Electron microscopy and μ-SXRF showed that the NiO particles have an approximately spherical morphology, are ~10 to 50 microns in diameter and are associated with no other metals. The sequential extraction revealed that ~50 % of the Ni in the muck and loam field soils was associated with the oxide fraction with a balance of the remaining Ni (~40%) found in the residual fraction. These results show that ~90% of the Ni in these soils can be considered relatively immobile. Bulk XAFS and SEM of the extraction residuals confirmed that NiO was a persistent phase (especially in the organic soils) demonstrating that either the oxide extraction step was ineffective at removing all of the NiO, or that NiO species of varying solubility are present. Identification of phase's other than NiO in the sequential extraction residues via bulk XAFS and NLLSF was compromised by the persistence of NiO.

According to the materials safety data sheets for NiO, it is considered soluble in acids, potassium cyanide and ammonium hydroxide but insoluble in both cold and hot water and caustic solutions. However, nickel solubility is highly dependent on the type of NiO which can vary with the process used to produce it as well as the mineral source from which it was derived. The most common forms of NiO are the more crystalline black NiO, which has higher oxygen content than green nickel oxide; the other common form. The wide range in NiO solubility has been shown by several researchers (Takahashi et al. 1992; Yamada et al. 1993; Takahashi et al. 1999). In these studies, it was shown that the green form of NiO was less soluble than the black form. The dissolution of Ni from the black forms was attributed to Ni carbonate impurities (~1%) which quickly dissolved upon reaction with water. Our analyses are based on the *green*-NiO standard (Johnson and Matthey), however it is uncertain whether distinguishable differences exist in the XAFS spectra from the two types of NiO. Attempts were not made here to distinguish between the types of NiO present in the Port Colborne soils. Regardless, it is very likely that any impurities that may have existed have since dissolved over the ~70yrs since their initial deposition. Additionally, based on the resistance of the NiO particles to the most aggressive of the sequential extraction steps (hot HNO_3/HCl microwave digest), they will likely remain in the soils for many years to come.

Exploring the speciation, μ-XAFS revealed that Ni- fulvic acid (FA) dominated the speciation within the Quarry muck soils. Interestingly, all of the organic acid (OA) standards used in the PCA had SPOIL values that were several orders of magnitude better than the inorganic standards (Table 2.5); ranging from 2.53 (malate) to 3.82 (tartrate). The reason for this is likely due to the fulvic acid standard being comprised of a mixture of functional groups with the most prominent being carboxylate (-COOH) which can bind Ni in a variety of configurations. If we exclude the FA standard from the LLSF we find that good fits were obtained for most sample spectra (as indicated by the NSS value) with the di- and tri-carboxylic complexes of Ni-malate and Ni-citrate. While citric and malic acids are found in the rhizosphere as exudates from plant roots or microbes, it is unlikely that these are the exact components being fit in the PCA-LLSF analysis. In a study looking for an analog for dissolved organic matter in natural waters, MacRae et al. (1999) found that the three organic acids, dipicolinic, oxalic and malonic, mimicked the copper binding properties of DOM in stream waters. Similarly, in our soils, it is likely that citric and malic acid serve as proxies for the different coordination environments encountered by Ni in the Muck soils. Interestingly, in the unlimed (pH 5.8) soils, a larger fraction of the Ni complexation could be attributed to Ni-malate, while in the treated (pH 6.5) soils we saw a higher proportion of the Ni complexed with citrate. Helling et al., (1964) and Yuan et al. (1967) have clearly shown that the CEC of a soil significantly increases with pH as acidic groups (namely COOH) are ionized. Even the small change in pH observed in our soils could result in orders of magnitude greater CEC and therefore a noticeable change in the coordination environment of Ni. Therefore, the presence of more stable Ni-OA complexes (i.e. Ni-citrate) in the limed soils gives spectroscopic evidence for the stronger binding of Ni in these soils and explains the reduction in Ni desorption in the stirred-flow studies as well as the reduction in plant available Ni in other studies on these soils (Frank et al. 1982; Kukier and Chaney 2000; Kukier and Chaney 2001)

The µ-XAFS, µ-SXRF investigation of the subsidiary phases in the loam soils found that secondary precipitates of Ni and Al were the prevalent species in both the unlimed (pH=7) and limed (pH=7.5) soils. Several studies have demonstrated that Zn LDH and phyllosilicate precursor phases can form in soil surrounding Zn smelters (Manceau et al. 2000; Nachtegaal et al. 2005; Roberts et al. 2002). There were several studies indicating that Ni Al-LDH phases can form in natural soils. Roberts et al. 1999) using bulk XAFS found that Ni Al-LDH precipitates formed in ~ 24 hours in a lab contaminated whole soil at pH 7.5. The loam soils in this study had higher pH (7-7.5) which is high enough even in the unlimed treatment to facilitate the formation of LDH phases. The presence of more "stable" LDH phases or phyllosilicates indicates a shift towards a more stable system. This probably has to do with the higher solubility of Si at higher pH values and the localized higher pH around the slowly dissolving dolomitic limestone particles. The formation of these phases almost certainly accounts for the reduction in Ni loss observed in the stirred-flow experiments.

2.6 CONCLUSIONS

This work is the first account of Ni Al-LDH phases forming in anthropogenically enriched soils. Like other accounts looking at Zn, we found that these phases can dominate the speciation of metals in soils. We have also demonstrated the utility and limitations of traditional sequential extraction procedures and how coupling these methods with direct techniques can help verify the predictions made by sequential extractions. Using this methodology, we showed that the presence of sparingly soluble phases (i.e. NiO) and highly organic soils may complicate the predicted metal associations.

The data analysis supports a model in which any soluble Ni species aerially deposited from the refinery into the Quarry muck and Welland loam soils have since been incorporated into subsidiary phases (e.g precipitates or organic complexes). The sparingly soluble NiO particles still persist in the soils and will most likely do so for many years to come. The persistence of these particles will complicate attempts to reduce Ni concentrations below the Canadian MOE requirements of 200mg/kg using phytoremediation alone, because it is unlikely that the plant is capable of accessing Ni from NiO. Interestingly, increased accumulation by *A. murale* with increasing pH indicates that the plant is capable of removing Ni from either the LDH or the organically complexed Ni in the loam or Muck soils respectively; phases typically considered unavailable to plants. It has yet to be shown how accessible these phases are to soil plant roots, or if one phase is “preferred” over another. Both Massoura et al. 2004 and Shallari et al. 2001using isotopically labeled Ni, found that the *Alyssum murale* was only able to access the labile pools of Ni in the soils they tested which is the opposite of what we seem to be finding here. They concluded that the increased accumulation of Ni in these species may not be due to the solubilization of the more resistant phase. Additional research is necessary to assess the availability of the various Ni phases present in these soils. Plant roots exude a variety of organic complexes in their attempt to acquire the necessary nutrients for growth and thus it is likely that the acidifying or organically complexing properties of these exudates could facilitate the proton or ligand promoted dissolution of Ni from these phases, making it available for uptake from soil solution.

2.7 REFERENCES

Bacon WG, Dalvi AD, Rochon BA, Selby M (2002) Nickel outlook - 2000 to 2010. Cim Bulletin 95: 47-52

Bisessar S (1989) Effects of lime on nickel uptake and toxicity in celery grown on muck soil contaminated by a nickel refinery. The Science of The Total Environment 84: 83-90

Fleet ME (1977) The crystal structure of heazlewoodite, and metallic bonds in sulfide minerals. American Mineralogist 62: 341-345

Ford RG, Scheinost AC, Scheckel KG, Sparks DL (1999) The link between clay mineral weathering and the stabilization of Ni surface precipitates. Environmental Science & Technology 33: 3140-3144

Frank R, Stonefield KI, Suda P, Potter JW (1982) Impact of nickel contamination on the production of vegetables on an organic soil, Ontario, Canada, 1980-1981. The Science of The Total Environment 26: 41-65

Grimaldi FS (1964) Greigite, the thio-spinel of iron a new mineral. American Mineralogist 49: 543-555

Hoflich BLW, Wentzel M, Ortner HM, Weinbruch S, Skogstad A, Hetland S, Thomassen Y, Chaschin VP, Nieboer E (2000) Chemical composition of individual aerosol particles from working areas in a nickel refinery. Journal of Environmental Monitoring 2: 213-217

Kuja A, Jones R, McIlveen W. Phytotoxicology soil investigation: INCO-Port Colborne 1999. Phytotoxicology and Soils Standards Section, Rep. No. SDB-031-3511-2000 Standards Development Branch, Ontario, Ministry of the Environment, Queen's Printer of Ontario: Toronto, Canada 2000

Kukier U, Chaney RL (2000) Remediating Ni-phytotoxicity of contaminated Quarry muck soil using limestone and hydrous iron oxide. Canadian Journal of Soil Science 80: 581-593

Kukier U, Chaney RL (2001) Amelioration of nickel phytotoxicity in muck and mineral soils. Journal of Environmental Quality 30: 1949-1960

Kukier U, Chaney RL (2004) In situ remediation of nickel phytotoxicity for different plant species. Journal of Plant Nutrition 27: 465-495

Lavkulic.LM, Wiens JH (1970) Comparison of Organic Matter Destruction by Hydrogen Peroxide and Sodium Hypochlorite and Its Effects on Selected Mineral Constituents. 34: 755

Li YM, Chaney R, Brewer E, Roseberg R, Angle JS, Baker A, Reeves R, Nelkin J (2003) Development of a technology for commercial phytoextraction of nickel: economic and technical considerations. Plant and Soil 249: 107-115

MacRae RK, Maest AS, Meyer JS (1999) Selection of an organic acid analogue of dissolved organic matter for use in toxicity testing. Can. J. Fish. Aquat. Sci. 56: 1484-1493

Malinowski ER (1977) Determination of the number of factors and the experimental error in a data matrix. Anal Chim Acta 49: 612-617

Malinowski ER (1978) Theory of error for target factor analysis with applications to mass spectrometry and nuclear magnetic resonance spectrometry. Anal Chim Acta 103: 354-359

Manceau A, Lanson B, Schlegel ML, Harge JC, Musso M, Eybert-Berard L, Hazemann JL, Chateigner D, Lamble GM (2000) Quantitative Zn speciation in smelter-contaminated soils by EXAFS spectroscopy. American Journal of Science 300: 289-343

Manceau A, Marcus MA, Tamura N (2002) Quantitative speciation of heavy metals in soils and sediments by synchrotron X-ray techniques. In: Fenter PA, Rivers ML, Sturchio NC, Sutton SR (ed) Applications of synchrotron radiation in low-temperature geochemistry and environmental sciences, Reviews in Minerology and Geochemistry 49, Minerological Society of America pp 341-428

Marcus MA, MacDowell AA, Celestre R, Manceau A, Miller T, Padmore HA, Sublett RE (2004) Beamline 10.3.2 at ALS: a hard X-ray microprobe for environmental and materials sciences. Journal of Synchrotron Radiation 11: 239-247

Massoura ST, Echevarria G, Leclerc-Cessac E, Morel JL (2004) Response of excluder, indicator, and hyperaccumulator plants to nickel availability in soils. Australian Journal of Soil Research 42: 933-938

Mehra OP, Jackson ML (1960) Iron oxide removal from soils and clays by dithionite-citrate-system buffered with sodium bicarbonate. Clays and Clay Minerology: 317-327

Myneni SCB, Brown J, Martinez GA, Meyer-Ilse W (1999) Imaging of humic substance macromolecular structures in water and soils. Science 286: 1335-1337

Nachtegaal M, Marcus MA, Sonke JE, Vangronsveld J, Livi KJT, van der Lelie D, Sparks DL (2005) Effects of in situ remediation on the speciation and bioavailability of zinc in a smelter contaminated soil. Geochimica Et Cosmochimica Acta 69: 4649-4664

Nachtegaal M, Sparks DL (2003) Nickel sequestration in a kaolinite-humic acid complex. Environmental Science & Technology 37: 529-534

Nicolai B, Kearley GJ, Johnson MR, Fillaux F, Suard E (1998) Crystal structure and low-temperature methyl-group dynamics of cobalt and nickel acetates. Journal of Chemical Physics 109: 9062-9074

Nriagu JO (1996) A history of global metal pollution. Science 272: 223-224

O'Day PA, Parks GA, Brown GE (1994) Molecular structure and binding sites of cobalt(II) surface complexes on kaolinite from X-ray absorption spectroscopy. Clays and Clay Minerals 42: 337-355

Parise JB (1980) Structure of hazelwoodite (Ni_3S_2). Acta Cryst B36: 1179-1180

Peltier E, Allada RK, Navrotsky A, Sparks DL (2006) Nickel solubility and precipitation in soils: a thermodynamic study. Clays and Clay Minerals In press

Ressler T (1997) WinXAS: A new software package not only for the analysis of energy-dispersive XAS data. Journal De Physique IV 7: 269-270

Roberts DR, Scheidegger AM, Sparks DL (1999) Kinetics of mixed Ni-Al precipitate formation on a soil clay fraction. Environmental Science & Technology 33: 3749-3754

Roberts DR, Scheinost AC, Sparks DL (2002) Zinc speciation in a smelter-contaminated soil profile using bulk and microspectroscopic techniques. Environmental Science & Technology 36: 1742-1750

Sadiq M, Enfield CG (1984) Solid phase formation and solution chemistry of nickel in soil 1: theoretical. Soil Science 138: 262-270

Sadiq M, Enfield CG (1984) Solid phase formation and solution chemistry of nickel in soils 2: Experimental. Soil Science 138: 335-340

Santoro A, Mighell AD, Zocchi M, Reimann CW (1969) The crystal and molecular structure of hexakis(imidazole)nickel(II) nitrate, $(C_3H_4N_2)_6Ni(NO_3)_2$. Acta Crystallographica Section B 25: 842-847

Sarret G, Saumitou-Laprade P, Bert V, Proux O, Hazemann JL, Traverse AS, Marcus MA, Manceau A (2002) Forms of zinc accumulated in the hyperaccumulator Arabidopsis halleri. Plant Physiology 130: 1815-1826

Scheckel KG, Scheinost AC, Ford RG, Sparks DL (2000) Stability of layered Ni hydroxide surface precipitates - A dissolution kinetics study. Geochimica Et Cosmochimica Acta 64: 2727-2735

Scheckel KG, Sparks DL (2000) Kinetics of the formation and dissolution of Ni precipitates in a gibbsite/amorphous silica mixture. Journal of Colloid and Interface Science 229: 222-229

Scheidegger AM, Lamble GM, Sparks DL (1997c) The kinetics of nickel sorption on pyrophyllite as monitored by x-ray absorption fine structure (XAFS) spectroscopy. Journal De Physique IV 7: 773-775

Scheidegger AM, Strawn DG, Lamble GM, Sparks DL (1998) The kinetics of mixed Ni-Al hydroxide formation on clay and aluminum oxide minerals: A time-resolved XAFS study. Geochimica Et Cosmochimica Acta 62: 2233-2245

Scheinost AC, Ford RG, Sparks DL (1999) The role of Al in the formation of secondary Ni precipitates on pyrophyllite, gibbsite, talc, and amorphous silica: A DRS study. Geochimica Et Cosmochimica Acta 63: 3193-3203

Scheinost AC, Kretzschmar R, Pfister S (2002) Combining selective sequential extractions, X-ray absorption spectroscopy, and principal component analysis for quantitative zinc speciation in soil. Environ Sci Technol 26: 5021-5028

Scheinost AC, Sparks DL (2000) Formation of layered single- and double-metal hydroxide precipitates at the mineral/water interface: A multiple-scattering XAFS analysis. Journal of Colloid and Interface Science 223: 167-178

Shallari S, Echevarria G, Schwartz C, Morel JL (2001) Availability of nickel in soils for the hyperaccumulator *Alyssum murale* Waldst. & Kit. South African Journal of Science 97: 568-570

Stewart JM, Lingafelter EC, Breazeale JD (1961) The crystal structue of Disaguabis(salicylaldehydato) nickel. Acta Cryst 14: 888

Strathmann TJ, Myneni SCB (2004) Speciation of aqueous Ni(II)-carboxylate and Ni(II)-fulvic acid solutions: Combined ATR-FTIR and XAFS analysis. Geochimica et Cosmochimica Acta 68: 3441-3458

Strawn DG, Sparks DL (2000) Effects of soil organic matter on the kinetics and mechanisms of Pb(II) sorption and desorption in soil. Soil Science Society of America Journal 64: 144-156

Sumner ME, Miller WP (1996) Cation exchange capacity and exchange coefficients. In: (ed) Methods Of Soil Analysis Part 3 Chemical Methods, Soil Science Society of America,Madison, WI, pp

Takahashi S, Oishi M, Takeda E, Kubota Y, Kikuchi T, Furuya K (1999) Physicochemical characteristics and toxicity of nickel oxide particles calcined at different temperatures. Biol Trace Elem Res 69: 161-74.

Takahashi S, Yamada M, Kondo T, Sato H, Furuya K, Tanaka I (1992) Cytotoxicity of nickel oxide particles in rat alveolar macrophages. J Toxicol Sci 17: 243-51.

Temple PJ, Bisessar S (1981) Uptake and toxicity of nickel and other metals in crops grown on soil contaminated by a nickel refinery. Journal of Plant Nutrition 3: 473-482

Trivedi P, Axe L, Tyson TA (2001) XAS studies of Ni and Zn sorbed to hydrous manganese oxide. Environmental Science & Technology 35: 4515-4521

Voegelin A, Pfister S, Scheinost AC, Marcus MA, Kretzschmar R (2005) Changes in zinc speciation in field soil after contamination with zinc oxide. Environmental Science & Technology 39: 6616-6623

Wasserman SR, Allen PG, Shuh DK, Bucher JJ, Edelstein NM (1999) EXAFS and principal component analysis: A new shell game. Journal of Synchrotron Radiation 6: 284-286

Weinbruch S, Van Aken P, Ebert M, Thomassen Y, Skogstad A, Chashchin VP, Nikonov A (2002) The heterogeneous composition of working place aerosols in a nickel refinery: a transmission and scanning electron microscope study. J Environ Monit 4: 344-350

Yamada M, Takahashi S, Sato H, Kondo T, Kikuchi T, Furuya K, Tanaka I (1993) Solubility of nickel oxide particles in various solutions and rat alveolar. Biol Trace Elem Res 36: 89-98.

Yano S, Inoue S, Nouchi R, Mogami K, Shinohara Y, Yasuda Y, Kato M, Tanase T, Kakuchi T, Mikata Y, Suzuki T, Yamamoto Y (1998) Antifungal nickel(II) complexes derived from amino sugars against pathogenic yeast, Candida albicans. Journal of Inorganic Biochemistry 69: 15-23

Chapter 3

NICKEL SPECIATION AND COMPARTMENTILIZATION IN THE NICKEL HYPERACCUMULATOR *ALYSSUM MURALE* ‘KOTODESH’

3.1 ABSTRACT

The Ni hyperaccumulator *Alyssum murale* ‘Kotodesh’ was examined to determine the internal speciation and compartmentalization of Ni, and other metals, in an effort to ascertain the mechanism used by *A. murale* to tolerate extremely high shoot Ni concentrations. Plants were grown either hydroponically or in Ni enriched soils from an area surrounding an historic Ni refinery in Port Colborne Ontario, Canada. Electron probe microanalysis (EPMA), synchrotron based computed micro - tomography and micro X-ray fluorescence revealed the Ni was concentrated in the dermal tissues of the leaf and stem as well as being entrained in the vascular tissues. Manganese, in the +2 oxidation state possibly as MnO_2, was found to preferentially accumulate in the basal compartment of the calcium rich leaf trichomes. Ni was not chemically associated with Mn at these locations, but bound solely to malate. Based on the dissimilar patterns of Ni accumulation it appears that A. murale uses different mechanism/s to detoxify Mn.

Determination of the Ni speciation in biological tissues is difficult because of the weak backscattering from second nearest neighbors such as C. Therefore, the Ni

speciation in *A. murale* was based on the following six criteria: 1) normalized sum of squares (NSS; or badness of fit) values from linear least squares fitting (LLSF), 2) Principle component analysis and non linear least squares fitting (PCA-NLLSF), 3) goodness of the NLLSF to the diagnostic features between 3 and 7 $Å^{-1}$ of the $k^3\chi(k)$-spectra 4) Ion chromatography results from crude plant extracts and 5) attenuated total reflectance Fourier transform infrared spectroscopy (ATR-FTIR) analyses of plant sap, and 6) published data on ligands in similar hyperaccumulating plants. Based on this approach we found most of the Ni in *A. murale* was complexed with malate (38%) followed by Ni(aq) (16%), Ni-tartrate (11%), histidine (5%) and malonate (4%). The balance of the Ni was associated with non-specific oxygen donor ligands (succinate, acconitate) or as the hydrated Ni(II) complex (Ni(aq)). Therefore, 58% of the Ni in the plant tissues appears to be complexed by stronger ligands, with the remaining 38% existing as either weak complexes with non-specific oxygen donor ligands or present as free hydrated Ni. ATR-FTIR analysis of the plant sap and μ-XAFS spectra from select leaf veins detected histidine. These findings support a model where transport in the xylem is facilitated by chelation of Ni by histidine (and other organic acids), after which it is transported and stored in the vacuoles of the leaf epidermal cells complexed with organic acids (malate, malonate, tartrate, succinate) or as the free aquo-Ni(II).

3.2 INTRODUCTION

The uncontrolled emissions from an historic Ni refining in Port Colborne , Ontario Canada has resulted in the enrichment of a large area of soil. The soils surrounding the metal refinery were predominantly used for vegetable crop production which, as a result of the increased soil Ni levels, experienced significant yield reductions (Temple and Bisessar 1981; Frank et al. 1982; Bisessar 1989). As a result, the Canadian Ministry of the Environment established a phytotoxicity based remediation standard of 200mg/kg above which the soils would have to be remediated. There are 29km^2 of soils that are above this level. Because of the cost associated with conventional dig-and-haul remediation methods (>$3 mil ha^{-1}) the use of the Ni hyper accumulator *Alyssum murale* 'Kotodesh' has been proposed as a means of reducing soil Ni levels below regulatory levels.

The use of specialized metal hyperaccumulating plants for phytomining, phytoextraction or phytostabilization is a promising and, in some cases, economically rewarding alternative to traditional dig-and-haul remediation methods. However, there is still little known about the biochemical or physiological mechanisms responsible for excess metal uptake and storage in these plants.

There have been many studies aimed at deciphering these mechanisms. From these, it appears that the mechanisms used by the plant depend primarily on the plant species, the chemical properties of the element being detoxified (Assuncao et al. 2003) or , in some cases, tissue type and age (Kupper et al. 2004). For Ni (and other transition metals), most studies have shown that oxygen or nitrogen donor ligands such as citrate, malate, malonate or histidine are responsible for increased metal uptake and storage. Histidine is the only plant constituent shown to increase in plant xylem in response to increased metal concentrations in the growth media (Kramer et al. 1996). There is no evidence to support that overproduction of organic acids is a specific response resulting from metal exposure. Instead, selected hyperaccumulators have been found to have a constant and unnaturally high amino acid concentration which may imply that excess metal accumulation in some species is a constitutive property. In this case, metal tolerance, perhaps as an adaptation to growing on metal rich soils, would be a sufficient explanation for increased metal uptake.

Alternatively, phytochelatins have been implicated as a tolerance mechanism in some plants. Phytochelatins (PC) are comprised of cystein, glyciene and glutamate and are used in algae and plants to detoxify excess cellular metal. PCs are readily produced in metal stressed non-hypertolerant organisms, but their production in hypertolerant species is only inducible at extremely high exogenous metal concentrations (Schat et al. 2002; Ebbs et al. 2002). Therefore, it is unlikely that they are playing a direct role in metal tolerance in hyperaccumulating plants. The exception is with As, and most notably Pteris vittata (Chinese Brake Fern), which several researchers have shown to have inducible PC production (Zhang and Cai 2003).

The objective of this research was to determine the biochemical mechanism/s of Ni transport and storage in the Ni hyperaccumulator *Alyssum murale* 'Kotodesh'. The following study used multiple techniques to characterize the ligands responsible for Ni tolerance in *A. murale*, including the application of μ-EXAFS, principal component analysis (PCA) and linear least squares fitting (LLSF). A thorough analysis of the metal species present in the plants utilizing these techniques should help in improving the efficiency of current phytoremediation technologies as well as facilitating the transfer of these traits to higher biomass, higher metal yielding plants in the future.

3.3 MATERIALS AND METHODS

3.3.1 *Alyssum murale* Propagation

The Ni hyperacumlator *Alyssum murale* 'Kotodesh' was grown in a glass house in Ni enriched soils collected from an area adjacent to an historic Ni refinery in Port Colborne, Ontario, Canada. Soils were sieved wet, mixed thoroughly and 1500 grams (dry weight) of loam soil or 800 grams (dry weight) of muck soil were placed in 1.5 liter plastic pots. Based on Mehlich III soil test analyses, the total amounts of macro- and micro-nutrients applied to each pot were: 154 mg N (as calcium nitrate), 291 mg P (as calcium phosphate and potassium phosphate), 231 mg K (as potassium phosphate), 22 mg Mg (as magnesium sulfate) and 1 mg B (as boric acid) (Siebielec et al., 2000). All fertilizers were added as solutions with the exception of calcium phosphate, which was added as a dry powder. Previous studies have shown that the Port Colborne soils develop a Mn deficiency particularly when limed to alleviate Ni phytotoxicity. (Baldwin and Johnson, 1986; Brown et al., 1997; Brown and Chaney, 1998). Therefore, $MnSO_4$ was added at a rate of 200 kg/ha of Mn to each pot

(Siebielec and Chaney, 2000). The fertilizers were mixed with the soil in plastic bags and added to the pots. The pots were watered and incubated for 7 days after which the soils were mixed again and cultivated. In addition, some plants were grown in the greenhouse aeroponically, using ¼ strength Hoagland's solution with 50µm Ni (added as $NiNO_3$) and for the Ni/Mn trichome studies 15µM Mn (added as MnSO4). The plants were subjected to light for 16 hours each day using high pressure sodium vapor lamps as artificial lighting. Day/night temperatures were set at 25ºC and 21ºC, respectively. Pots were watered as needed using reverse osmosis filtered water and saucers were used to prevent loss of the leachate.

3.3.2 Ion Selective Chromatography

Sap was extracted from plants using a pressure bomb. Portions of plant shoot were cut and the cut end inserted into the pressure bomb aperture. The pressure chamber was filled to ~15 lbs in^{-2} with N_2. A syringe with needle was then used to extract sap as it exuded from the cut end of the stem after which it was deposited in a conical bottomed PCR vial. Following ~30 -60min of extraction, the sap was either analyzed immediately, or shock frozen in liquid nitrogen and stored at -60^{o}C until analysis. Additionally, leaves were sectioned into tip, midsection and petiole and ground in 2.5 mM KH_2PO_4 at pH 2.5 (with H_3PO_4). The ground samples were then centrifuged and the supernatant retained for analysis.

Compounds in the sap were chromatographed by isocratic elution on a reverse phase 5 µm, PrevailT organic acid HPLC column (15 cm x 4.6 mm) (Alltech). The chromatographic system (Summit Dionex) consisted of P580 pumps (Dionex) connected to an ASI-100 Automated Sample Injector (Dionex Co). The visible absorbance at 220 nm was measured by a PDA-100 Photodiode array variable UV/VIS detector (Dionex). Mobile phase Solution A consisted of potassium phosphate (2.5 mM KH_2PO_4 @ pH 2.5). An isocratic program was used for all the separations with an initial injection volume of 10 μL and a flow rate of 1 ml min^{-1}.

3.3.3 Electron Probe Micro-analysis (EPMA)

Plant samples were prepared by immersing whole sections of shoot in liquid nitrogen after which they were dried under vacuum at –80ºC for 24 hrs to prevent ice crystal formation. Leaves were then fractured to expose the interior of the leaf and pieces were placed on end on a carbon stub. Prior to analysis the samples were sputter coated with carbon and then examined on a JEOL JXA-8600 microprobe (John Hopkins University) with wavelength and energy dispersive detectors (WDS and EDS, respectively). Samples were first scanned manually from 50-300x using back scattered electron (BSE) imaging to find regions of high Ni concentration after which EDS was used to generate elemental maps for O, K, Ca, Fe, Al and Ni.

3.3.4 Computed Micro-Tomography

Chapter 4 describes in detail the synchrotron-based tomographic methods used herein. Briefly, samples for fluorescence tomography were first shock frozen by immersion in liquid nitrogen and then dried frozen prior to analysis to minimize damage and redistribution of Ni. Freeze-drying of samples for fluorescence tomography was necessary to reduce movement associated with dehydration due to the high photon flux of the X-ray beam and the longer data acquisition times. For absorption edge tomography, living plants were brought to the beamline.

3.3.5 ATR-FTIR Standard and Plant Sap Characterization

Attenuated Total Reflectance –Fourier Transform Infrared (ATR-FTIR) Spectroscopy was used to characterize the organic and amino acid standards used in EXAFS PCA-LLSF as well as in characterization of extracted plant sap from *Alyssum murale* grown in Ni enriched soils. A Thermo Electron NEXUS 670 FTIR spectrometer equipped with a PIKE Technologies horizontal attenuated total reflectance (HATR) flow-through accessory and a germanium (Ge) internal reflection element was used for data collection. The organic acids citrate, malate, malonate, oxalate, tartrate, aconitate, and the amino acid histidine, cysteine and glyceine were examined with and without Ni present (at the concentrations described in section 3.36) to verify the type of complex formed. Samples were pipetted directly on to the germanium crystal prior to analysis. 128 co-added scans at 8 cm^{-1} resolution were collected from 650 to 4000cm^{-1} using a mercury cadmium telluride (MCT-A) detector.

3.3.6 XAFS Standard Preparation, Data Collection and Characterization

A total of 12 aqueous organic standards were prepared as follows: Ni-aqueous, 30mM $NiNO_3$; Ni-Aconitate, 50 mM $NiNO_3$ + 150 mM Aconitate; Ni-malate, 30 mM $NiNO_3$ + 300 mM malate; Ni-malonate, 30 mM $NiNO_3$ + 300 mM malonate; Ni-Citrate, 30 mM $NiNO_3$ + 120 mM citrate; Ni-Oxalate, 30 mM $NiNO_3$ + 300 mM Oxalate; Ni-Tartrate, 50 mM $NiNO_3$ + 500 mM tartrate; Ni- Succinate, 30mM $NiNO_3$ + 150 mM Succinate; Ni-histidine, 30 mM $NiNO_3$+ 300 mM histidine; Ni-Glutathione, 30 mM $NiNO_3$ + 300 mM glutathione; Ni-Cystine, 30 $NiNO_3$ + 300 mM cystine; Ni-Glycine, 30 mM $NiNO_3$ + 300 mM glycine. ACS trace metal grade chemicals, acid washed containers and ultra-pure double-deionized (18.2Ω Millipore) water were used to generate all standards.

XAS data for standards were collected on beamline X-11A at the National Synchrotron Light Source (NSLS), Brookhaven National Laboratory, Upton, NY (unless otherwise stated). The electron beam energy was 2.5-2.8 GeV with a maximum beam current of 300 mA. The monochromator consists of two parallel Si (111) crystals with a vertical entrance slit opening of ~0.5 mm. The beam size on the sample was maintained at 2 × 10 mm for all samples and standards. Prior to data collection, the energy was calibrated to the first inflection point on the K absorption edge of a Ni metal foil standard (E_o = 8.333 keV for Ni). Aqueous standards were loaded into individual acrylic sample holders and sealed with Kapton™ tape. A non-adhesive Kapton™ film was placed on the adhesive side of the tape where it covered the sample reservoir to avoid any interaction of the sample with the tape adhesive. The samples were then mounted 45^o to the incident beam and data collected at the Ni K-edge over the energy range 8183-9082 eV in fluorescence mode using a N_2/Ar (95/5%) filled Lytle Cell. To optimize the Ni signal and remove elastically scattered radiation, the fluorescence signal was filter using a Co foil, one to two sheets of Al foil and Soller slits. Harmonic rejection was achieved by detuning the monochromator 20% of I_o. Multiple scans (≥ 3) were collected for each sample to improve the signal-to-noise ratio.

XAS data analyses were performed using WinXAS 3.1 (Ressler 1997). Prior to averaging, the individual spectra were background corrected and normalized. Background subtraction was performed by fitting a linear polynomial to the pre-edge region between 150 and 50 eV below the Ni K-edge. The edge jump was normalized to unity by fitting a linear polynomial between 100 and 500 eV above the Ni K-edge. The threshold energy (E_o) was determined by selecting the root of the second derivative through the absorption edge of the differentiated spectra, and used to convert the spectra from energy to k-space (photoelectron wave vector ($Å^{-1}$)). A cubic spline function with ≤ 7 knots was then used to remove the contribution to the spectrum resulting from atomic absorption in the absence of backscattering contributions. This step generated the XAFS function (χ (k)), which was then weighted by k^3, to compensate for dampening of the XAFS amplitude with increasing k. The $k^3\chi(k)$-spectra were then Fourier transformed using a Bessel window with a smoothing parameter of 3-4 to reduce artifacts due to the finite Fourier filtering range used. This step produced radial structural functions (RSF) which were not corrected for phase shift.

The first two major shells below 3.5 $Å^{-1}$ were individually selected, back-transformed and fit using a non-linear least squares approach and theoretical scattering paths generated using ATOMS and FEFF 7.02 software packages (Zabinsky et al., 1995). The Ni-O and Ni-C (organic acids) phase and amplitude functions were generated using either Nickel acetate tetrahydrate ($Ni(CH)_3COO)_2{\bullet}H_2O$) (Nicolai et al. 1998) or disaguabis(salicyladehydato) nickel ($Ni(sal)_2(H_2O)_2$) (Stewart et al. 1961) and Ni-N (amino acids) paths using Ni – Imidazole $(C_3H_4N_2)_6Ni(NO_3)_2$ (Santoro et al. 1969). The parameters obtained fitting the individual shells were then refined using a multi-shell fit over the entire spectra in k and R spaces. The energy shift parameters (E_o) were set equal for all paths and the root mean square disorders (RMSD (σ^2(Å^2)) or the Debye-Waller factor) and bond distance (R) were set equal for those metals sharing atomic shells. The amplitude reduction factor (S_o^2) was fixed at 0.85. Errors in the bond distance (R) are estimated to be R ± 0.02 Å and R ± 0.05 Å, and errors for the coordination number (CN) are estimated to be CN ± 20% and CN ± 40%, for the first (Ni-O/S/N) and second shells (Ni-Ni/Al/Si/C), respectively. These estimates are based on the fitting results and comparison with previously published XRD and EXAFS data.

3.3.7 μ-SXRF and μ-EXAFS Data Collection and Analysis

Micro-EXAFS and μ-synchrotron based X-ray fluorescence (μ-SXRF) data were collected on beamline 10.3.2 (1.9 GeV and 300 mA) at the Advanced Light Source, Lawrence Berkeley National Lab (Berkeley, CA) (Marcus et al. 2004). Leaves and stems were removed from living plants and mounted directly to a Peltier cold stage using metal-free silicon vacuum grease and rapidly frozen to ~-30°C. The sample stage was then oriented 45^o to the incident X-ray beam. Fluorescence signals were collected using a Ge solid-state multi-element detector. To assess the spatial distribution of Ni and other elements in the samples, fluorescence maps were collected over 1000 μm^2 (coarse map) and 200 μm^2 (fine map) with a beam size of 16 x 7 μm and 5 x 5 μm and using a step size of 20 and 5 μm, respectively and an integration time of 100 ms. For mapping, the beam energy was set to 11 keV to allow the detection of relevant elements including Ni, Fe, Ca, Co, Cu, Zn, and Mn. To determine the Ni speciation at regions of interest in the maps, μ-XAS spectra were collected up to 500 eV above the Ni K-edge. Prior to μ-XAS data collection, the beamline energy was calibrated to the first inflection point of the Ni metal foil standard (E_o = 8.333 keV)

Analysis of the XAFS spectra was done using both conventional non linear least squares fitting (NLLSF) and principal component analysis (PCA). Traditional shell fitting was used as an initial assessment of the coordination environment of Ni. It should be noted that analysis of XAFS spectra collected from multicomponent systems (such as plants) cannot rely on traditional fitting procedures in which atomic shells are individually selected and fit. The difficulty arises because the multiple metals in the system may have overlapping atomic shells making it difficult if not impossible to separate them. Therefore, to determine the species present within a mixed system, a dataset of spectra from multiple spots throughout a sample are analyzed statistically using principal component analysis (PCA) (Wasserman et al. 1999). The PCA technique determines if the data set can be described as weighted sums of a smaller number of components, which would be the case if each spot in the dataset is comprised of a smaller number of distinct compounds. Selection of the number of principal components was made where the empirical indicator (IND) and Eigenvalues were at their minimum (Malinowski 1977). Target transformation (TT) is then used to identify the components by taking a spectrum of a known reference compound and mathematically removing from the spectrum anything that does not look like the principal components identified by PCA. If minimal information has to be removed from the known reference spectrum, then one can conclude it is most likely present in the sample. Reference spectra are evaluated for their "goodness of fit" by the SPOIL value (Malinowski 1978). Generally, numbers < 1.5 are considered excellent, 1.5 to 3 good, 3-4.5 fair, 4.5-6 poor and >6 unacceptable. After the contributing standard phases are identified, linear least squares fitting (LLSF) is used to determine the amount (%) of each standard within the individual sample spectra making up the dataset. The fit is optimized where the normalized sum squared (NSS) value is at a minimum. A reference phase was included in the fit only if it decreased the NSS by 20% or more. The accuracy of this fitting approach is dependent upon the data quality, the completeness of the standards data set, and the range over which the data were fit (Manceau et al. 2002).

3.4 RESULTS AND DISCUSSION

3.4.1 Ion Selective Chromatography

Quantification of all of the amino and organic acids present in A. murale tissue and sap extracts was not possible using the current method. However, in all of the samples, we were able to positively identify oxalate, tartrate, malonate, malate and possibly citrate. There are certainly additional components present in the sap (i.e. unidentified peaks in the IC spectra) whose identification and quantification will be facilitated by a more selective IC column coupled with mass-spectrometry.

3.4.2 Element Distribution and Compartmentalization – EPMA, μ-SXRF and μ-tomography

A variety of methods were used to ascertain the compartmentalization of Ni in the leaves of *A. murale*. Scanning electron microscopy (SEM) was used because it provides detailed images and in addition, it is capable of detecting lighter elements unattainable by X-ray techniques. The scanning electron micrographs for a leaf cross section as well as a magnified cross section through the midrib of the leaf are shown in Figure 3.1 a and b. In both panel a and b, Ni is shown to be isolated in the dermal tissues, vascular bundles, and absent from the mesophyll. Potassium and sulfur are isolated to the mesophyll and are not correlated with Ni. Kupper et al. 2001 and Broadhurst et al (2004) both found Ni to be associated with sulfur in the plant epidermal cells which is opposite the pattern we observed. They concluded that the excess sulfur was probably sulfate acting as a counter-ion to Ni, and possibly an inorganic nickel sulfate species stored in the epidermal vacuoles. In the Kupper et al (2001) study, the excess Ni treatments were supplied to the plants as $NiSO_4$ (up to

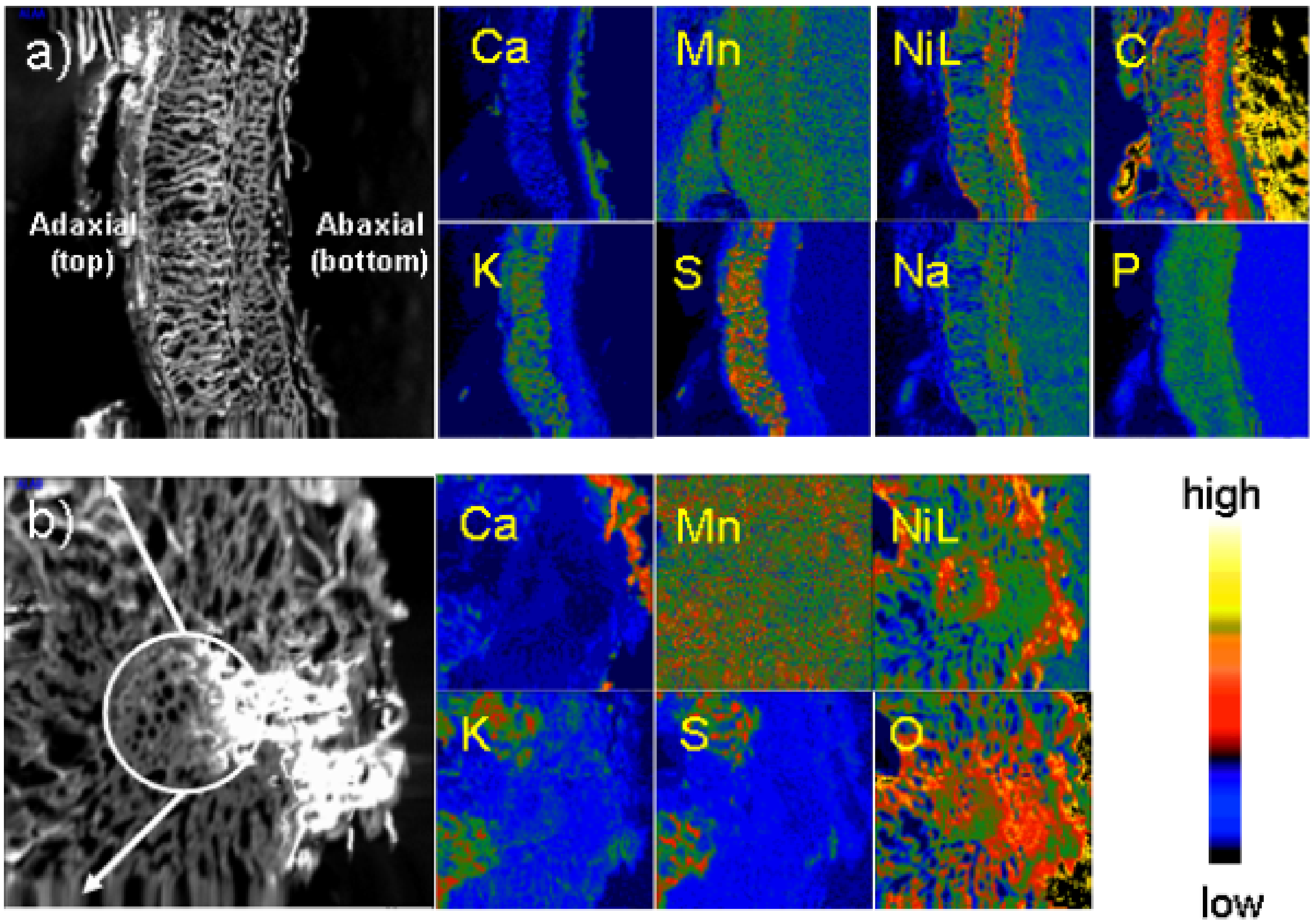

Figure 3.1: Backscatter electron (BSE) image (large) and elemental distribution maps (small) for an *A. murale* leaf cross-section (a), and a cross-section through the midrib of a leaf (b). The circle indicates the vein location and the arrows point in the direction of the leaf margin.

4000mg/kg) which may have induced the observed Ni-S associations. Broadhurst et al (2004) did note that regardless of the sulfate concentration supplied, S concentration in the leaves (on a total S basis) was still elevated; however, they didn't analyze these leaves to assess where the S was located. Again, our analysis, while not as detailed as the previous two, indicates no association of Ni with S. Sulfur is a key constituent, both structural and functional, in proteins, namely cystiene, and the strong antioxidant glutathione. Many of the functions requiring S take place in chloroplasts or the other photosynthetically active tissues of the plant and thus it isn't surprising that the S content of these tissues would be elevated. Interestingly, glutathione, when degraded, forms phytochelatins which have been shown to play a role in the detoxification of excess amounts of metals (e.g. Cd) and oxyanions (e.g. As, Se). There is no evidence to show that phytochelatins play a direct role in metal tolerance or hyperaccumulation in *A. murale* (or any other plants) and the dis-association of Ni with S in the micrographs supports this hypothesis.

Previous work has shown that the leaves of *Alyssum murale* are covered with a thick layer of stellate (star-like) trichomes which are rich in calcium (McNear et al. 2005; Broadhurst et al. 2004). The angle of the leaf in Figure 3.1a is positioned such that the trichomes are not visible; however in the upper right corner of panel b they can be seen. Figure 3.2 shows BSE image and elemental micrographs of a trichome isolate from a leaf. Clearly, the trichome is composed primarily of Ca, with no other metal or elemental associations. Based on the large amount of oxalate detected in the IC analysis of the extracted leaf samples, it is likely that calcium in the trichome is

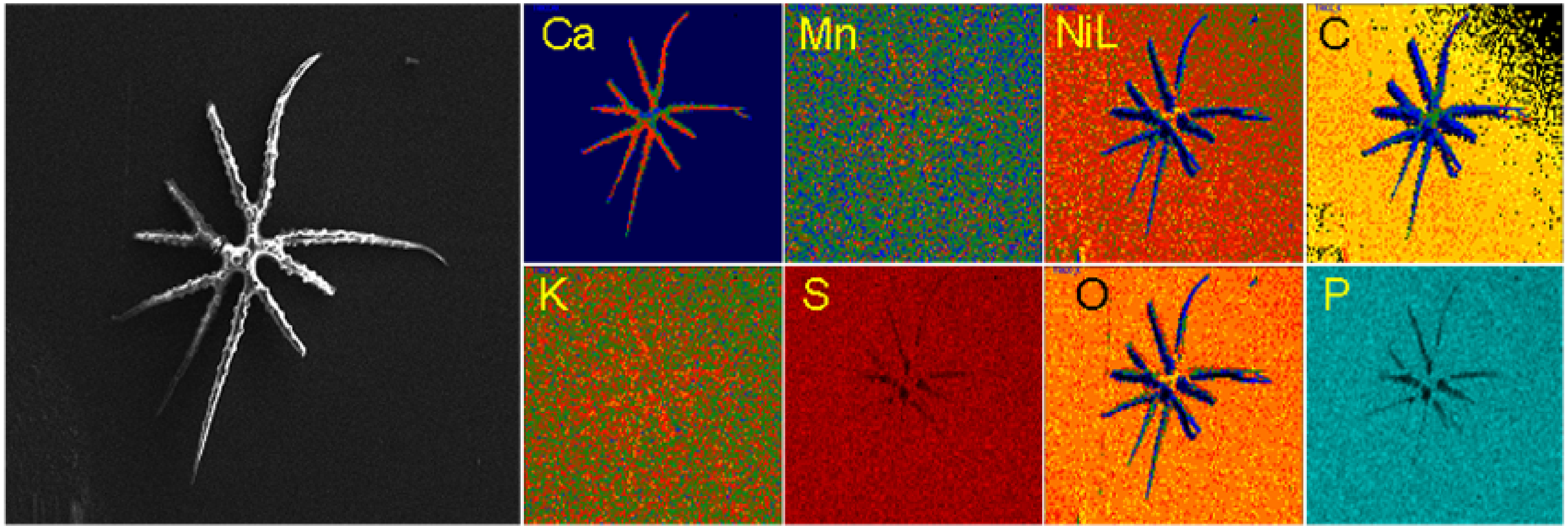

Figure 3.2: Backscatter electron (BSE) image (large) and elemental distribution maps (small) of a trichome isolated from a leaf of *A. murale*

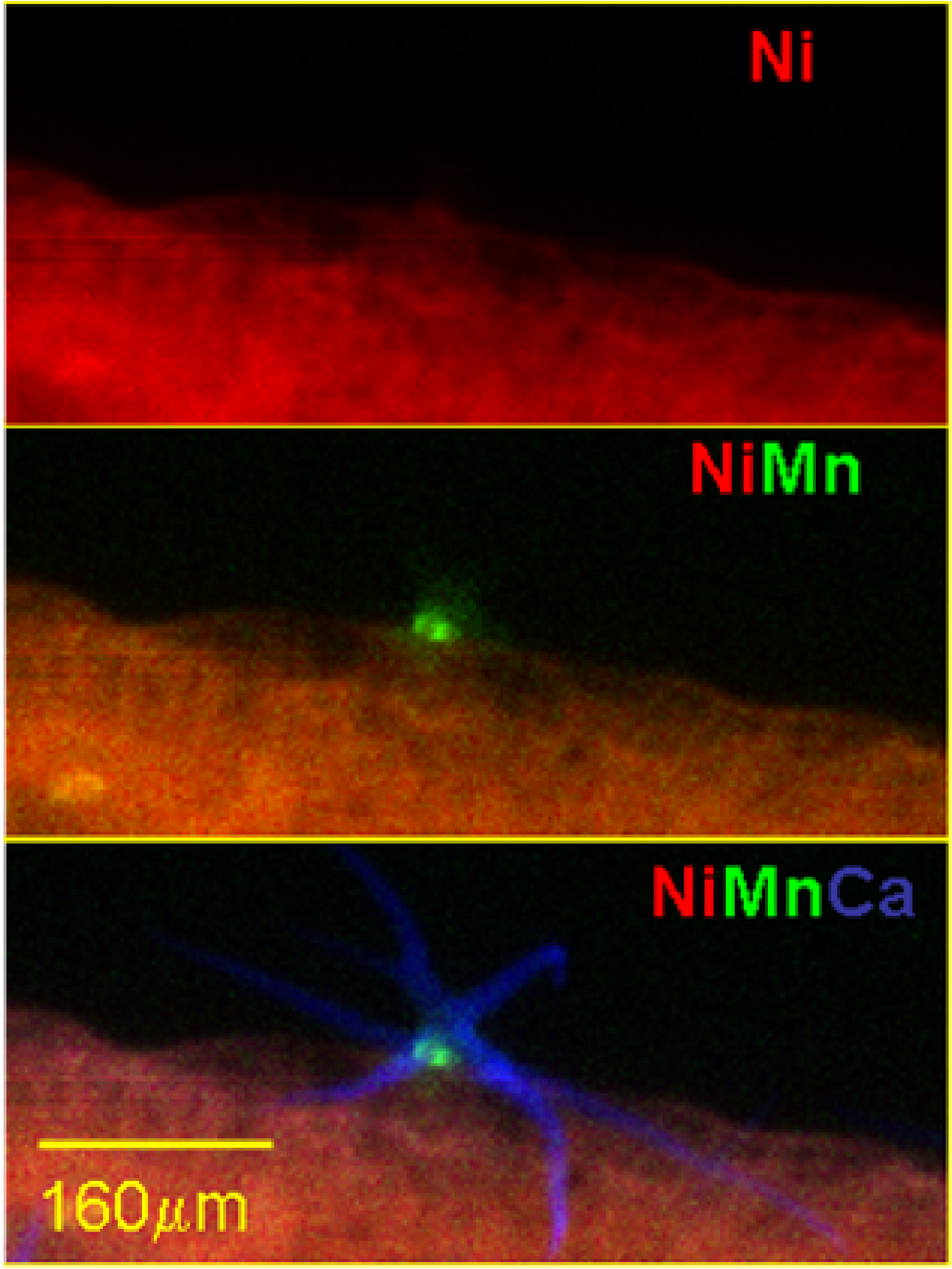

Figure 3.3: m-SXRF maps showing the distribution of Ni (top), Ni and Mn (middle), and Ni, Mn and Ca (bottom) in an *Alyssum murale* leaf edge with a trichome. Notice the "nodule" of Mn at the base of the calcium rich trichome.

primarily calcium oxalate. Broadhurst et al. (2004) found that Ni and Mn were isolated to the basal compartment of the trichomes in *A. murale*. The trichome isolate in Figure 3.2 did not include the pedicle or the basal compartment which is likely why we didn't detect any of these metals. In the μ-SXRF image in Figure 3.3, however, we were able to image a trichome attached to the leaf edge. The top panel shows the distribution of Ni only, the middle Ni and Mn and the bottom all three metals. There is no obvious enrichment of nickel above that in the bulk of the leaf, however, there is clearly a discrete "nodule" of Mn where the trichome attaches to the leaf surface. The Mn- trichome (i.e., Ca) association appears throughout most of the leaves in Figure 3.4, and certainly in Figure 3.5 where the leaves were grown aeroponically with a slightly elevated Mn concentration (15μM compared to 2μM). Broadhurst (2004) as well as Abou Auda et al. 2002) both found that *A. murale* has the unique ability to not only hyperaccumulate Ni, but also Mn, and it appears from our analysis and others that it is primarily stored in the basal compartment of the trichome.

Conclusions about metal compartmentalization from the μ-SXRF maps must be made carefully. The fluorescence from the metals entrained in the plant leaf are collected by the detector from only one direction (i.e. 2-D), and therefore, because the X-ray beam penetrates or passes through the sample, the thickness of the leaf or stem tissue being sampled is important. For example, Ni in the lower dermal tissues and Mn in the upper dermal tissues may appear correlated in the μ-SXRF map; however they are actually separated by the thickness of the leaf. Only by considering the

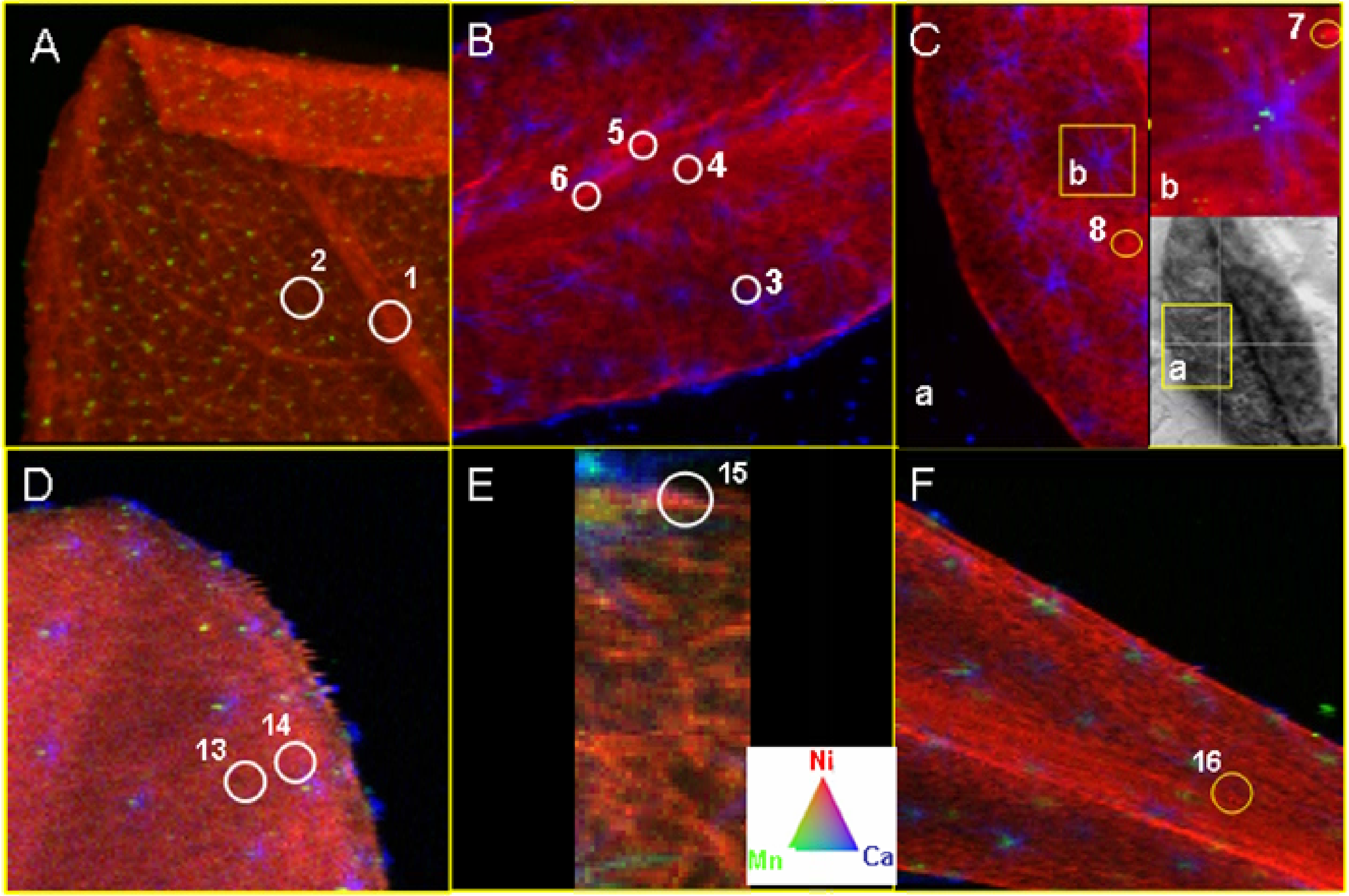

Figure 3.4: μ-SXRF tricolor maps of leaves from soil grown *Alyssum murale* 'Kotodesh'. The numbers indicate where μ-XAFS spectra were collected. Red indicates the distribution of Ni, green of Mn and blue of calcium. The image in the bottom right corner of panel C is a light microscope image of an *A. murale* leaf mounted to a Peltier cold stage during analysis. The yellow box a) is the region mapped in the μ-SXRF image to the left in panel C, and b) a finer map of the leaf surface as seen in the upper right corner of panel C

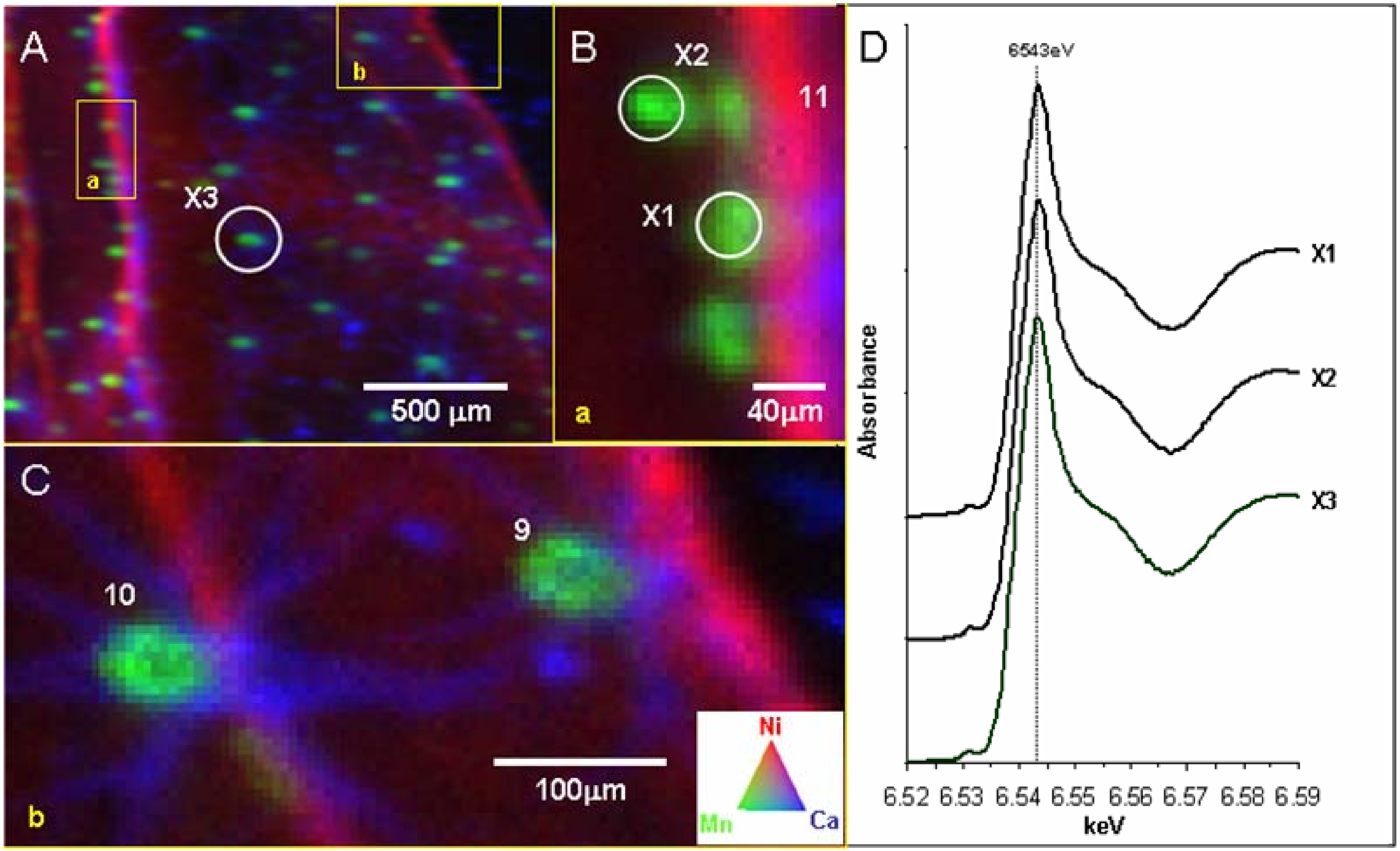

Figure 3.5: µ-SXRF tricolor maps (A-C) of leaves from hydroponically grown *Alyssum murale* 'Kotodesh'. Red indicates the distribution of Ni, green of Mn and blue of calcium. The numbers indicate where µ-XAFS (9, 10, 11) spectra were collected. The circles indicate where the µ-XANES (X1-X3) spectra shown in Panel D were collected. The boxes in panel A indicate where fine maps were collected from a leaf midrib (a; right) and a leaf edge (b;bottom).

findings from both SEM and μ-tomography (Chapter 4), can we confidently interpret the metal distribution found in these images. Ni appears evenly distributed throughout all of the leaves, with obvious enrichment in the vascular tissues (Figure 3.4 Panels A, B, and F), as well as the leaf margins (Figure 3.4 B, C and Figure 3.5 A). Vascular enrichment was seen with both SEM and μ-tomography and is not interpreted as Ni bound to vascular tissues, but simply fixed there upon freezing. The apparent enrichment of the leaf margins results because the X-ray beam traverses a larger volume of dermal tissue (which we found using SEM and μ-tomography to contain the most Ni) at these locations compared to others. Therefore, we find that Ni is evenly distributed throughout the leaf dermal tissues, in the xylem vesicles, and absent from the mesophyll.

3.4.3 ATR-FTIR and XAFS Spectroscopic Characterization of Standards

The ATR-FTIR spectra for citrate, malate, malonate, oxalate, histidine, tartrate, aconitate and cystine with and without Ni can be seen in Figure 3.6. Figure 3.7 shows the raw, $k^3\chi(k)$-spectra and radial structure functions (RSF) for the organic reference phases, and Table 3.1, the results from non-linear least squares fitting. The pH of the aqueous standards was adjusted to match the pH found in typical plant xylem (i.e. pH 6.5-7.0). At these values we would expect all of the carboxyl groups of the organic and amino acids to be fully deprotonated in Ni free solutions. For the Ni-organic/amino acid complexes the ligand was provided in considerable excess (4-10x)

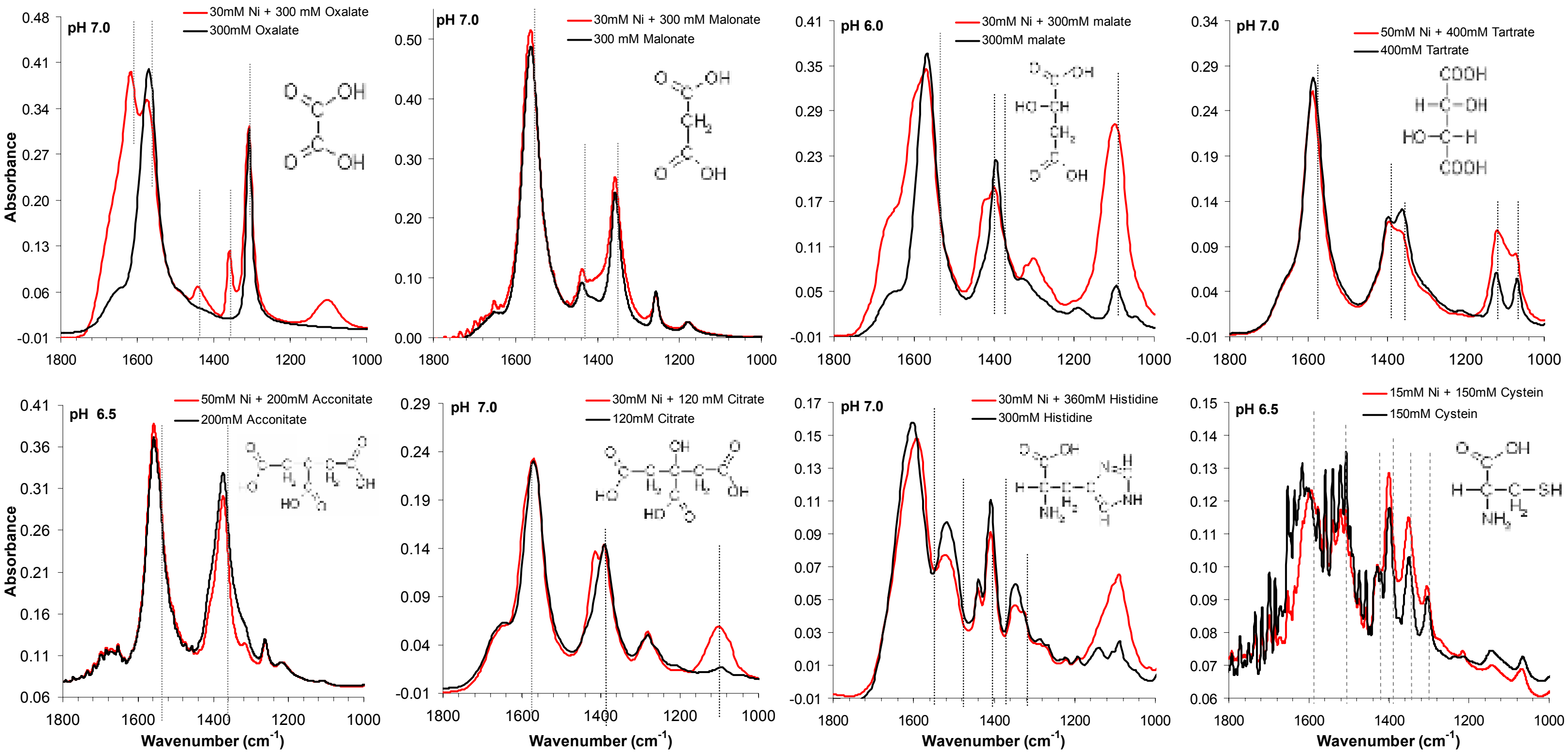

Figure 3.6: Attenuated total reflectance-Fourier transform infrared spectra (ATR-FTIR) of oxalate, malonate, malate, tartrate, aconitate, citrate, histidine, and cystine with (red line) and without (black line) Ni. Dotted lines indicate the primary absorption features in the IR spectra that are diagnostic of the protonation state of the carboxylic (1690 to 1750 cm^{-1} (νC=O) and 1200 to 1300 cm^{-1} (νC-OH)) and alcohol (1000 to 1200 cm^{-1} (νaC-OH)) functional groups.

in order to assure that the standard represented the fully complexed Ni-organic/amino acid species. In the IR spectra, the region between 1000 cm^{-1} and 1800 cm^{-1} (i.e. near-IR region) was isolated because it provides the most information about the coordination environment of the metal – ligand complex. There are two primary absorption features in the IR spectra that are diagnostic for the protonation state of carboxylate functional groups. The features for the protonated carboxylic acid group/s occurring between 1690 and 1750 cm^{-1} are attributed to asymmetric carbonyl stretching (νC=O) and those between 1200 and 1300 cm^{-1}, symmetric C-OH vibrations (νC-OH) (Cabaniss et al. 1998). Upon deprotination, the νC=O shifts to higher energy and the νC-OH to lower. In addition, for the organic and amino acids malate, tartrate, citrate and histidine, absorption bands between 1000 cm^{-1} and 1200 cm^{-1} were observed which may be attributed to the C-O stretching of the intermediary alcohol groups (ν_α(C-OH)) (Cabaniss and McVey 1995).

The $k^3\chi(k)$-spectra of the organic and amino acid standards (Figure 3.7) have distinct features in the second and third oscillations between 3 and 7 Å^{-1} which are indicative of the binding environment of Ni. Strathmann and Myneni 2004) used both FTIR and synchrotron X-ray absorption spectroscopy to characterize the binding environment of Ni with several organic acids. They noted that longer chain organic acids, where the carboxylate functional groups are separated by one or more methylene groups, form weak complexes with Ni and thus have spectra similar to that of the hydrated Ni species. However, those organic or amino acids with shorter chains or closely packed carboxyl (COOH) groups supported by adjacent alcohol (α(C-OH))

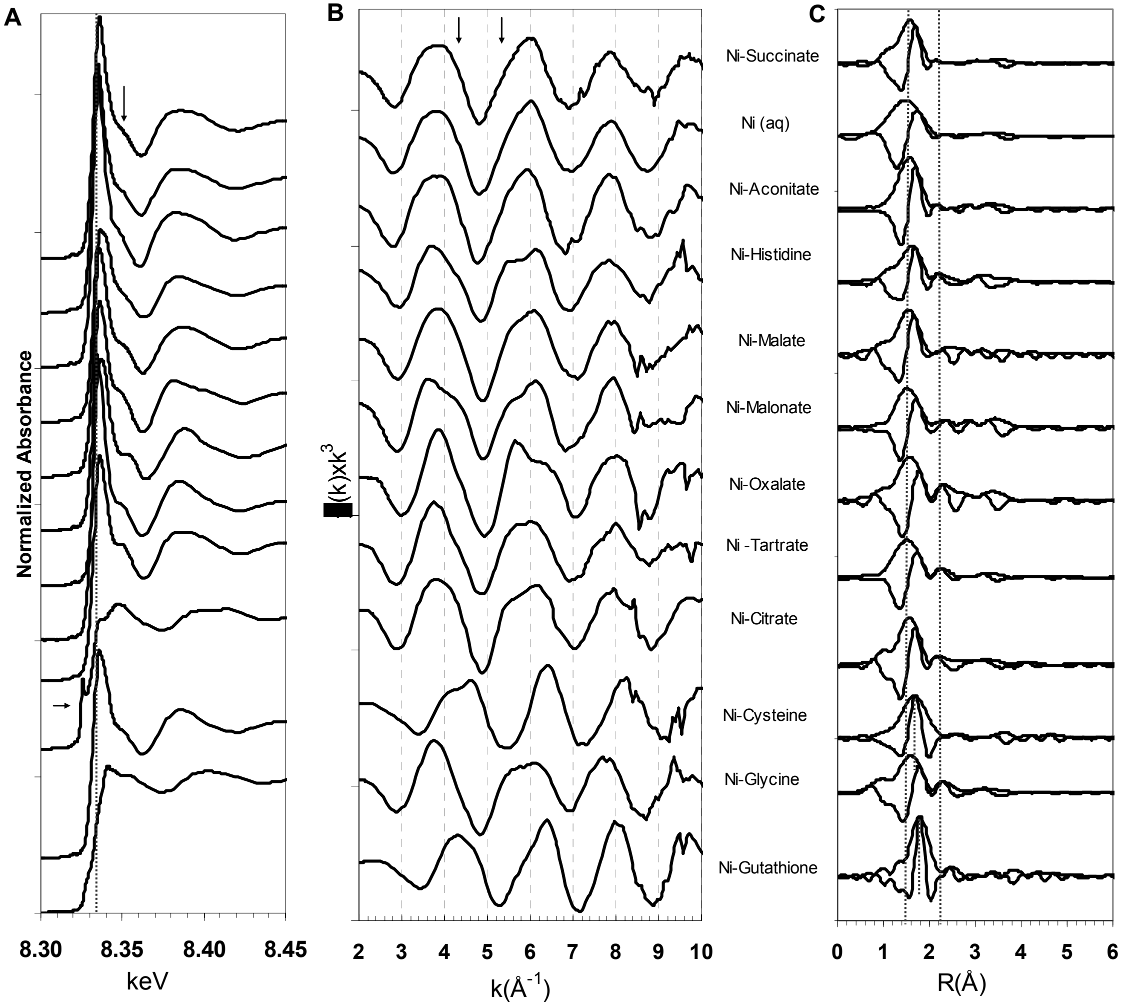

Figure 3.7: Raw (A), $k^3\chi(k)$-spectra (B) and RSF (B) of reference phases used in PCA and LLSF. Arrows indicate areas containing the most diagnostic features in the spectra.

donor groups or ring structures (e.g., the imidizole ring of histidine) form more rigid bonds (i.e., stronger complexes). The rigidity of the resulting structures imparts a pronounced shoulder between 8.34 and 8.35 keV in the raw XANES spectra as well as modification of the oscillations between 3 and 7 $Å^{-1}$ in the $k^3\chi(k)$-spectra. Additionally, the peak at ~2.3 Å (uncorrected for phase shift) in the RSF representing the contribution from second neighbor carbon (see LLSF data in Table 3.1) is more pronounced.

Oxalate forms strong complexes with Ni (and other transition metals) attesting to its use as a chelating agent in many industrial processes. The double *v*C=O and vC-OH absorption bands in the IR spectra occurring at ~1560 and 1620 cm^{-1}, and ~1360 and 1306cm^{-1} indicate that both protonation states are present in the Ni-oxalate standard. In addition, the change in both the *v*C=O and *v*C-OH modes indicates that both carboxyl groups of the oxalate ligand are participating in the complexation of Ni. Non-linear least squares fitting (NLLSF) of the XAFS spectra for Ni-oxalate confirmed these findings, showing that Ni is coordinated with 6 oxygen atoms at R_{Ni-O} = 2.08 Å and 4.25 C atoms at R_{Ni-C} = 2.84 Å. These values are consistent with Ni in a bidentate complex with two oxalate ligands. Sharpening of the peak at ~4$Å^{-1}$ and splitting on the right side of the 6$Å^{-1}$ peak in the $k^3\chi(k)$-spectra, as well as a significant step (~8.5 keV) in the XANES spectra provide further evidence for the strong complex formed between Ni and oxalate.

There is very little change in the Ni and Ni-free malonate IR spectra. There is a slight shift to higher energy in the *v*(C=O) absorption band as well as a slight

Table 3.1: Best fit XAFS parameters obtained from non linear least squares fitting (NLLSF) of the reference spectra used in principal component analysis and linear least squares fitting (PCA-LLSF)

		First shell				Second Shell				
	Atom	CN	R (Å)^a	$\Delta\sigma^2$ (Å^2)	Atom	CN	R (Å)^a	$\Delta\sigma^2$ (Å^2)	ΔE_o (eV)	X^2_{res} %
Aqueous Organic										
Ni-Succinate	**O**	6.00	2.05	0.007	---	---	---	---	-0.12	2.23
Ni (aq)	**O**	6.70	2.05	0.006	---	---	---	---	-4.31	1.47
Ni-Aconitate	**O**	6.50	2.05	0.006	**---**	---	---	---	-0.40	9.97
Ni-Histidine	**N/O**	6.40	2.03	0.005	**C**	5.50	2.92	0.012	-2.23	5.44
Ni-malate	**O**	6.00	2.05	0.002	**C**	3.50	2.82	0.003	1.96	6.48
Ni-malonate	**O**	5.90	2.03	0.004	**C**	3.01	2.87	0.007	-1.40	7.63
Ni-citrate	**O**	6.00	2.03	0.004	**C**	4.30	2.83	0.006	-3.52	6.76
Ni-Oxalate	**O**	6.00	2.05	0.004	**C**	4.25	2.84	0.000	-1.07	6.12
Ni-Tartrate	**O**	6.00	2.05	0.004	**C**	5.50	2.82	0.007	0.61	7.30
Ni-Glutathione	**S**	3.64	2.10	0.001	**C**	1.90	2.87	0.001	6.17	5.54
	N	3.25	2.21	0.008	**---**	**---**	**---**	**---**		
Ni-Cystine	**S**	4.59	2.15	0.007	**C**	5.43	2.93	0.007	-6.38	7.21
Ni-Glycine	**N**	6.80	2.11	0.005	**C**	5.34	2.85	0.006	-0.39	7.14

CN = Coordination Number (±20% (Scheidegger et al., 1997)

R = inter-atomic distance (±0.02 Å for first shell and ± 0.05 Å for the second and third shell (Scheidegger eta al., 1997))

σ^2(Å^2) = Debye Waller factor

ΔE_o = Phase shift

intensity increase in both the *v*C=O and *v*C-OH absorption bands. The most notable change occurs in the 1300-1500 cm^{-1} range with the intensification of the peak at 1440

cm^{-1}. Dobson and McQuillan 1999) attributed the 1440cm^{-1} peak to dipole moment changes resulting from straining of the central $-CH_2$ group as it binds to a variety of solid surfaces. In our case, the formation of a bidentate complex with a single Ni ion may contribute to the enhancement of this feature. NLLSF for Ni-malate confirms these findings. Nickel is coordinated to ~6 O atoms at R_{Ni-O} = 2.03 $Å^{-1}$ indicating it is octahedrally coordinated. The second shell is occupied by 3.01 C atoms at R_{Ni-C} =2.87 Å consistent with Ni in a 1:1 bidentate complex with both carboxyl groups of malonate. In the 3 to 7 $Å^{-1}$ diagnostic region of the $k^3\chi(k)$-spectra, both peaks at ~ 4 and 6$Å^{-1}$ are noticeably flattened.

Structurally, malate and tartrate are similar with the only difference being both the C_2 and C_3 carbons of tartrate have alcohol groups (-OH), compared to only one alcohol on the C_2 of malate. The presence of two –OH groups in tartrate can clearly be seen in the Ni –free IR spectra as two distinct absorption peaks at 1090cm^{-1} and 1120cm^{-1}. The single –OH group of malate appears as a single absorption peak at 1090 cm^{-1}. Upon complexation with Ni, the α(C-OH) absorption bands of tartrate intensify and broaden, the symmetric *v*C-OH vibrational mode at 1360 cm^{-1} is reduced, and there is a slight shift in the *v*C=O vibrational mode. Non-linear least squares fitting for Ni-tartrate were best achieved using 6 O atoms at R_{Ni-O} = 2.05 Å in the first shell and 5.5 C atoms in the second at R_{Ni-C} = 2.82 Å. The IR and XAFS data indicate that both the hydroxyl groups as well as one of the carboxyl groups are participating in the complexation of Ni in tartrate. For malate, there is a significant reduction in the intensity of the νC=O and νC-O absorption peaks (the Ni-malate spectra are enhanced 5x in Figure 3.6 for comparison, however the α(OH) mode remains constant in intensity, but broadens. Best fits were achieved with 6 O in the first coordination shell at $R_{Ni\text{-}O} = 2.05$ Å and 3.5 C at $R_{Ni\text{-}C}= 2.82$ Å. The IR and EXAFS data for malate indicate that the alcohol group and one of the carboxyl groups are participating in the complexation of Ni.

Succinate, a four carbon organic acid resembling malate, but without the C_2 alcohol, has very featureless XANES and $k^3\chi(k)$-spectra; resembling very closely the spectra from the hydrated Ni standard ($Ni(II)(H_2O)_6 \bullet NO_3$). Only first shell oxygen could be accounted for with $CN_{Ni\text{-}O} = 6$ at a distance of $R_{Ni\text{-}O} = 2.05$ Å indicating Ni is in octahedral coordination. As noted earlier, the absence of the supporting alcohol group (as in malate) results in the formation of only weak complexes of Ni with succinate.

Aconitate and citrate are both six carbon tricarboxylic acids with the only difference being the absence of an alcohol adjacent to the carboxyl group on the C_3 carbon in aconitate. The presence of the C_3 alcohol group in citrate is clearly visible in the IR spectra as a peak at ~1090cm^{-1} (ν_α(C-OH)) which is absent in the aconitate spectra. Upon complexation with Ni, there is a significant increase in the ν_α(C-OH) absorption peak of citrate indicating that the alcohol group is participating in the complexation of Ni which is in agreement with the findings of Hedwig et al. 1980). In addition to changes in the ν_{α}(C-OH) region, there is a splitting in the ν(C-O) peak with very little change in the ν(C=O) peaks. Strathmann and Myneni (2004) hypothesized these features result from either non-participation of one of the carboxyl groups in the complexation of Ni or, significant malleability in one or more of the carboxyl linkages. Best fits of the Ni-citrate XAFS spectra were achieved using 6 O atoms in the first shell at $R_{Ni\text{-}O}$ = 2.05 Å and 4.1 C atoms at $R_{Ni\text{-}C}$ = 2.83 Å in the second shell which is consistent with the IR data and indicates Ni is in a 1:1 complex with C (even at this high [L]:[M] ratio). These results are similar to those found by Baker et al. 1983 and Homer et al. 1991. As was seen with Ni-malate, the alcohol group has a significant influence on the strength of the complex that forms. In aconitate, the presence of Ni results in a slight decrease in the intensity and broadening of the ν(C-O) region and a slight increase in the ν(C=O) absorption bands. The lack of significant changes in energy of these absorption peaks indicates only a weak interaction of Ni with the carboxylate groups, which is confirmed in the XAFS fits by the inability to confidently fit C to the second shell. Therefore, much like with succinate, Ni forms weaker, outer-sphere complexes with aconitate.

The IR spectra for histidine is rich with peaks, most resulting from stretching or bending modes of the C-N bonds in the imidazole ring. The most prominent of these features occurs at 1602 cm^{-1} (ring motion) and 1518 cm^{-1} (ring vibration) (Jung 2000). Additional absorption bands between 1000 and 1200 cm^{-1} were assigned to C-N stretching (ν(C-N)). The structural complexity of nickel (with its imidazole ring) also imparts unique features in the XAS spectra. The main peak of the XANES spectum for histidine is broadened and there is a very distinct depression in the oscillation at ~5.6 $Å^{-1}$ in the $k^3\chi(k)$-spectra. Six nitrogen atoms were fit to the first shell at R_{Ni-N} = 2.09 Å and five carbons in the second at R_{Ni-C} = 5.5 Å.

Glycine, cysteine and glutathione are key components of phytochelatins which are suspected to play a role in metal tolerance in some species. While they haven't been implicated in Ni hyperaccumulation, there inclusion was intended to keep the standard dataset as inclusive and objective as possible. The XANES spectra for both cysteine and glutathione are very unique. Cysteine has a prominent pre-edge feature around 8.3 keV. The feature is the result of $1s \rightarrow 3d$ or $1s \rightarrow 4pz$ transitions (i.e. orbital mixing), and is indicative of noncentrosymmetric coordination resulting from either tetrahedral or square pyramidal complexes (Colpas et al. 1991; Feth et al. 2003; Strathmann and Myneni 2004). The LLSF of the XAFS spectra support these observations, with Ni coordinated to CN_{Ni-S} = 4.59 S atoms at R_{Ni-S} = 2.15 Å in the first shell and and CN_{Ni-C} = 5.43 C atoms at R_{Ni-C} = 2.93 Å in the second shell.

Glutatione had a very small edge step in the XANES spectra and a shoulder in the pre-edge region similar to that of cysteine. Glutathione is a tripeptide composed of cysteine, glycine and glutamate and therefore, the fit parameters are intermediary to those of its components. Best fits of the XAFS spectra were achieved by including both S and N in the first coordination shell indicating that the sulfur and nitrogen side chains are taking part in the complexation of Ni. No IR data were collected for glutathione or cysteine because of their already distinct XAFS features.

The IR-spectrum for glycine is very noisy particularly in the region between 1500 and 1700 cm^{-1} for the uncomplexed form. Regardless, the absorption bands at ~1595cm^{-1} and 1518cm^{-1} are indicative of interactions with carboxylate, however, they are significantly dampened (particularly the peak at 1595cm^{-1}), which may have to do with the sulfur donor ligand. The peaks between 1300cm^{-1} and 1500cm^{-1} again, indicate interaction with the carboxyl group. Bell 1977) noted that at pHs between 4 and 9, glycine is present as the zwitterions ($H_3^+NCH_2CO_2^-$), losing a proton from the –NH^{3-} group allowing it to complex with Ni forming a five member ring. These findings are supported by the XAFS LLSF fits where 6.8 N atoms were fit to the first shell at R_{Ni-N} = 2.11Å and 5.34 carbon atoms were fit to the second shell at R_{Ni-C} = 2.85Å.

3.4.4 ATR-FTIR Spectroscopy of Plant Sap

FTIR spectroscopy has been used to investigate a variety of constituents in plants including proteins (Surewicz et al. 1993) and cell wall materials (McCann et al. 1992). No studies have used ATR-FTIR methods to investigate plant sap extracts. This may be due in large part to complexity of the spectra which results from the many IR active materials in plant saps including carbohydrates, proteins, and sugars. This complexity may make conclusions about the sap contents based solely on the IR-spectra difficult; however by interpreting the spectra based on the findings from our other the results may be better constrained. As we saw when characterizing the standards, there are many features in the mid-IR region of the spectra which can

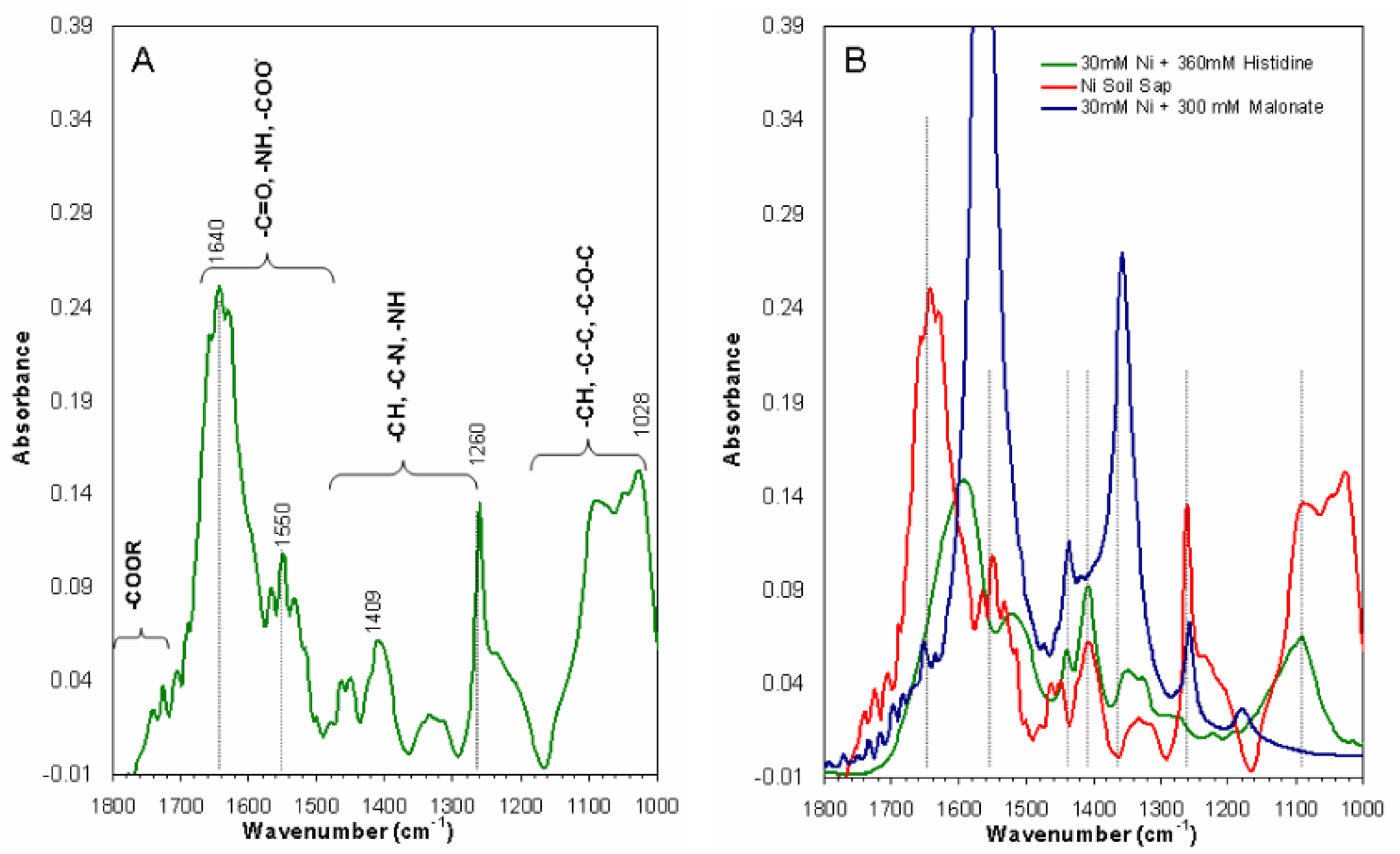

Figure 3.8: Attenuated total reflectance-Fourier transform infrared spectra (ATR-FTIR) of (A) sap extracted from *A. murale* grown in a Ni enriched soil from an area adjacent to a Ni refinery in Port Colborne, Ontario Canada and (B) the ATR-FTIR spectra of the sap and Ni-histidine and Ni-malonate reference spectra. The brackets in panel A indicate the typical functional groups contributing to the spectral features in that region.

provide some insight into how and which ligands Ni is interacting with. Figure 3.8 shows the IR spectra for sap extracted from *A. murale* grown in a Ni enriched mineral soil (panel A) and the plant sap with the malonate and histidine reference IR-spectra overlaid (panel B). The sap was initially compared to all of the IR reference spectra, but malonate and histidine shared the most spectral features with the sap. Most notably are the sharp peak at 1260cm^{-1} shared by malonate and the sap, as well as the multiple, similarly shaped peaks between 1300cm^{-1} and 1500 cm^{-1} shared by histidine and the sap. While not unequivocal, the sharpness of the peak at 1260cm^{-1} makes this feature unique and fairly diagnostic (Cabaniss and McVey 1995) for malonate and, since malonate was also detected in the IC analysis, we can say with some certainty that it is present in the plant sap. Additionally, the uniqueness of the features between 1300cm^{-1} and 1500cm^{-1}, particularly the broad absorption band at 1300-1380cm^{-1} are fairly diagnostic for histidine. A variety of amino acids, including those with and without the imidazole ring, should be tested to verify the uniqueness of these features.

3.4.5 Ni Speciation – Evidence from XAFS

The numbered raw, $k^3\chi(k)$-spectra and RSF in Figure 3.9 correspond to the numbered spots in the μ-SXRF maps in Figures 3.4 and 3.5 and designate where μ-XAFS spectra were collected. The dataset included a total of 19 spectra including bulk XAFS spectra from freeze-dried and ground stem (#16 and 18) and leaf tissue

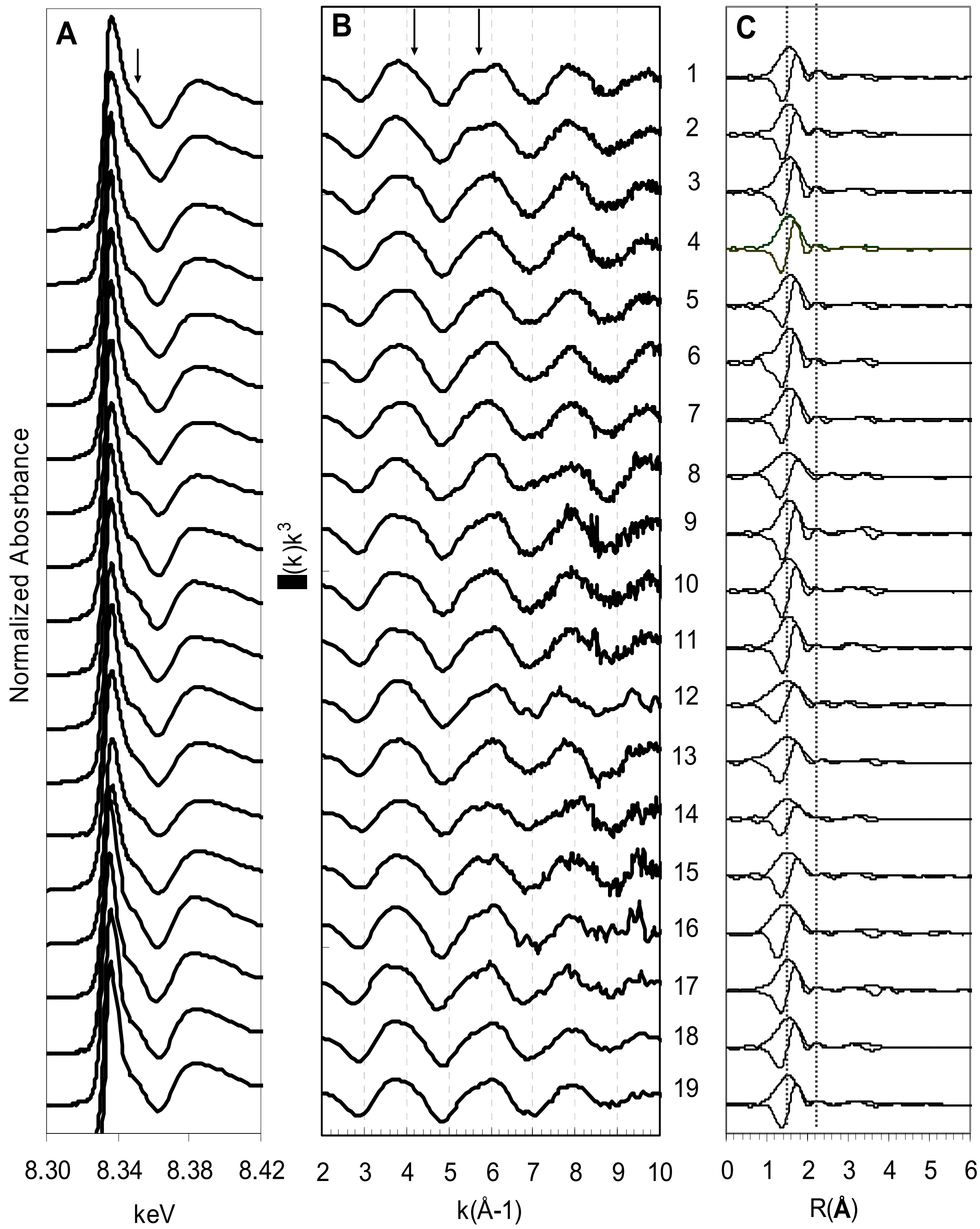

Figure 3.9: (A) Background corrected, (B) $k^3\chi(k)$-spectra, and (C) radial structure functions (RSF) for the μ-XAFS spectra corresponding to the numbered spots in the μ-SXRF maps in Figures 3.4 and 3.5. Spectra 12 and 16-19 are bulk spectra and don't appear on the μ-SXRF maps. Arrows indicate areas containing the most diagnostic features in the spectra.

(#17 and 19) as well as extracted sap (#12). All of the spectra are very similar, however, upon closer inspection, there are subtleties in each that provide an indication of the Ni coordination. The arrows in panels A and B point to regions in the raw and $k^3\chi(k)$-spectra providing the most diagnostic detail. In some of the spectra (e.g. 1 and 2) there is obvious splitting in the peak around 5.8 $Å^{-1}$ which, as we saw from fitting the standards, is indicative of a stronger Ni-ligand complex. The RSF of all spectra show a prominent first shell peak at ~1.6 Å and, in most, another smaller peak at ~ 2.3Å (uncorrected for phase shift).

As an initial assessment of the coordination environment of Ni in the plant tissues, conventional non-linear least squares shell fitting (NLLSF) was carried out. Table 3.2 shows the results from fitting the sample spectra using phase and amplitude functions generated from either $Ni(sal)_2(H_2O)_2$ (Stewart et al. 1961) for Ni-C paths or Ni-Imidazole ($(C_3H_4N_2)_6Ni(NO_3)_2$) for Ni-N paths (Santoro et al. 1969). The first coordination shell in all spectra is occupied by approximately 6 oxygen/nitrogen atoms at $R_{Ni\text{-}O/N} \approx 2.03\text{-}2.06$ Å indicating that Ni is in octahedral coordination. Some spectra had a significant second shell contribution from carbon at $R_{Ni\text{-}C} = 2.76\text{-}2.91$ Å with coordination numbers ranging from $CN_{Ni\text{-}C}$ 1-4.67. It should be noted that coordination numbers less than 2 are outside the error associated with EXAFS second shell coordination number estimates (± 20%). However, each of the fits was performed with carbon and without, and carbon was only included when it significantly improved the fit (based on the % residual error X^2_{res} %). The NLLSF results show that only oxygen donor ligands are participating in the complexation of

Table 3.2: Best fit XAFS parameters from traditional non linear least squares fitting (NLLSF) and species composition determined by principle component analysis (PCA) and linear least squares fitting (LLSF) for the μ-XAFS and bulk XAFS spectra. Numbers correspond to the locations on the leaves of *A. murale* in the m-SXRF maps (Figures 3.4 and 3.5) where spectra were collected (does not apply to bulk XAFS spectra).

Non linear least squares fitting											Linear Least Squares Fitting
		First shell				Second Shell					
Spectra #	Atom	CN	R (Å)	$\Delta\sigma^2$ (Å^2)	Atom	CN	R (Å)	$\Delta\sigma^2$ (Å^2)	?E_o (eV)	X^2_{res} %	Ni-Organic/Amino Acid Composition
1	**N/O**	5.60	2.05	0.005	**C**	4.67	2.91	0.008	-2.19	3.57	40% malate, 35% histidine, 25% malonate
2	**N/O**	6.30	2.04	0.006	**C**	3.00	2.89	0.004	-3.56	13.89	65% malate, 28% malonate
3	**O**	6.80	2.05	0.006	**C**	1.18	2.87	0.001	1.19	2.09	57% malate, 40% aconitate
4	**O**	6.50	2.05	0.005	**C**	1.50	2.86	0.007	0.59	3.01	52% malate, 43% aconitate
5	**O**	6.75	2.06	0.006	**C**	1.00	2.81	0.002	2.07	2.74	52% malate, 35% aconitate
6	**O**	6.53	2.05	0.005	**C**	2.30	2.84	0.009	1.03	6.08	54% malate, 52% Ni(aq)
7	**O**	6.50	2.05	0.005	**C**	1.64	2.78	0.005	1.30	4.53	99% succinate
8	**O**	6.07	2.05	0.005	**C**	---	---	---	1.77	4.98	96% Ni(aq)
9	**O**	6.32	2.04	0.004	**C**	2.30	2.88	0.004	0.44	4.22	101% malate
10	**O**	6.00	2.05	0.005	**C**	2.70	2.88	0.008	2.38	9.02	92% malate
11	**O**	5.21	2.03	0.005	**C**	2.58	2.78	0.003	-0.45	8.17	94% Ni(aq)
Bulk Plant Sap (12)	**O**	4.50	2.03	0.005	**C**	3.00	2.76	0.005	-0.21	3.30	43% tartrate. 24% Ni(aq). 23% histidine
13	**O**	6.20	2.06	0.006	**C**	2.00	2.83	0.005	1.55	2.83	55% malate, 38% histidine
14	**O**	6.24	2.04	0.004	**C**	1.50	2.83	0.005	-0.25	5.00	56% malate, 38% acconitate
15	**O**	6.39	2.04	0.005	**C**	1.93	2.88	0.007	0.64	4.10	93% malate
Bulk Stem Muck (16)	**O**	6.50	2.03	0.004	**C**	---	---	---	-2.60	10.19	67% tartrate, 34% Ni(aq)
Bulk Leaf Muck (17)	**O**	6.00	2.05	0.004	**C**	2.00	2.84	0.006	-0.09	5.72	70% succinate, 27% malonate
Bulk Stem Loam (18)	**O**	6.00	2.04	0.005	**C**	1.50	2.81	0.009	-0.11	9.27	51% succinate, 46% tartrate
Bulk Leaf Loam (19)	**O**	6.00	2.04	0.005	**C**	1.30	2.86	0.004	-0.92	9.95	50% malate, 44% succinate

CN = Coordination Number (±20% (Scheidegger et al., 1997)

R = inter-atomic distance (±0.02 Å for first shell and ± 0.05 Å for the second and third shell (Scheidegger eta al., 1997))

σ^2(Å^2) = Debye Waller factor

ΔE_o = Phase shift

X^2_{res} % = residual

Ni in the tissues of *A. murale*, as none of the fits nor spectral features indicate a contribution from sulfur. The species contributing to these fitting results and the spectral features were determined by principal component analysis (PCA) using all 19 spectra over the k-

range of 2 to 10 Å^{-1}. The weights of the first four components were 140, 21, 18 and 13 with indicator values of 0.0286, 0.0280, 0.0275 and 0.0288, respectively. The total normalized sum of squares values (a "badness" of fit parameter) significantly improved when going from 2 to 3 components (0.0526 to 0.0376), but not four. Therefore, PCA indicates that, while the first component contributes significantly more to the overall fit (i.e. indicating one dominant species), the dataset can best be described by three components. Target transformation (TT) was then done with our characterized references to determine the species represented by the abstract principal components. We used a reference dataset that included both inorganic and organic standards (see Table 2.4, Chapter 2), however, the spoil values for the inorganic standards were large enough (ranging from 6.2 to 25) to exclude them from further consideration. None of the aqueous organic/amino acid reference phases had spoil values in the excellent range, however, Ni(aq) (2.04), Ni-Tartrate (2.43) and Ni-malate (2.73) all had spoil values in the good range and represent the most likely components in the dataset.

Linear least squares fitting (LLSF) of the sample spectra with linear combinations of the identified reference phases was then done to quantify the amount of each of these ligands within the plant tissues The fits resulted in normalized sum squared values (NSS) ranging from 0.0254 to 0.256. The high NSS values indicate that linear combinations of tartrate, malate and Ni(aq) are insufficient to describe all of the spectra in the dataset. For example, the LLSF of spectra #1 (Figure 3.10) using solely malate (as LLSF indicates) doesn't adequately fit the splitting in the peak at 5.8Å^{-1} in the $k^3\chi(k)$-spectra. As was shown earlier, this splitting at 5.8Å^{-1} is fairly diagnostic for Ni bound to a strong ligand and was present in the Ni-malonate, Ni-histidine and Ni-citrate reference spectra. However, the maximum absorbance peak in the histidine XANES spectra is slightly broader than the citrate or malonate standard, a feature also present in sample spectra #1. Linear least squares fitting of spectra 1 found Ni coordinated to 5.6 O/N atoms at $R_{Ni-O/N}$ ≈2.05Å and 4.7 C atoms in the second shell at the slightly longer distance of R_{Ni-C} ≈ 2.91Å. Comparing these fits to those of the standards, it appears that the first spectrum most resembles that of histidine. Not surprisingly, spectra #1 was collected from a spot on the midrib of a leaf (Figure 3.4 panel A) and thus, as our IR data suggests and others have shown, it likely represents Ni complexed with histidine being transported in the xylem for delivery and storage in the leaf.

Based on these findings, PCA alone appears inadequate for describing all of the species within the plant tissues. This may have to do in part with the similarity of the spectra or that malonate and histidine are present in small enough quantities that they go undetected. To overcome these limitations, all of the spectra were evaluated based on the following five criteria: 1) NSS value of the LLSFs, 2) bulk XAFS NLLSF, 3) goodness of the fit to the diagnostic features between 3 and 7 Å^{-1} of the

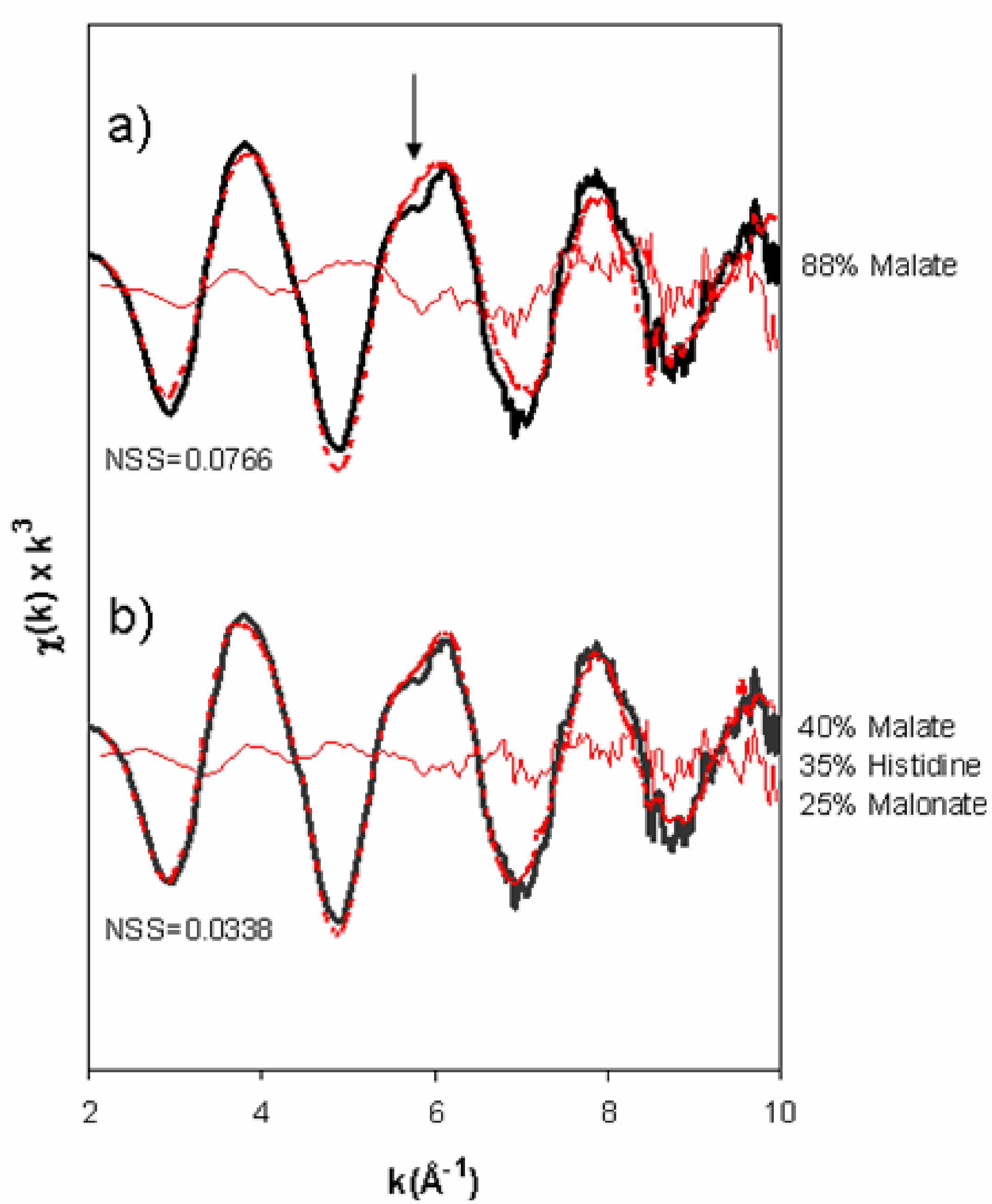

Figure 3.10: Comparison of the linear least squares fit (LLSF) of a) the c(k)k3 m-XAFS spectra from spot #1 based solely on the results from principal component analysis which indicated that Ni-malate was the only component in the spectrum, and b) the fit including Ni-malate, Ni-histidine and Ni-malonate which NLLSF, ATR-FTIR and/or chromatography indicate are in the sample. The black line indicates the raw k3c(k)data, the dotted red line the fit and the solid red line the residual. Notice the improved fit of the feature at 5.8Å-1 which is indicative of Ni-histidine and Ni-malonate.

$k^3\chi(k)$-spectra, 4) Ion chromatography data, 5) ATR-FTIR data and 6) published data on ligands in similar hyperaccumulating plants. For example, fits with a high NSS value were inspected to determine where the data was inadequately fit, paying particular attention to the diagnostic region between 3 and 7Å^{-1}. In addition, the coordination number and atomic distances for the ligand identified by NLLSF, and the LLSF data for the sample spectra were compared to determine if it was appropriate to include the identified ligand in the NLLSF. That is, if the NLLSF indicates that the XAFS spectra are comprised primarily of histidine, there should be a significant second shell carbon contribution in the LLSF of that spectra, as well as splitting in the $k^3\chi(k)$-spectra at 5.8Å^{-1} and broadening of the maximum absorption peak in the XANES spectra.

Using these criteria we find that the average distribution of Ni species from all of the plant tissues to be 38% Ni-malate, 15% Ni(aq), 14% Ni-succinate, 13% Ni-tartrate, 4% Ni-malonate and 4% Ni histidine (Table 3.2) . The low histidine and malonate contributions (4 and 5%, respectively) provide some evidence as to why they were not distinguishable using PCA. Interestingly, the inclusion of Ni-succinate and Ni-aconitate, even though there is no evidence they exist in the plant or play a role in Ni detoxification, was found to significantly improve the fit for some of the spectra. We interpret this improvement in the fit to indicate the presence of a weakly complexing donor ligand instead of solely the hydrated Ni species. Therefore, 58% of the Ni in the plant tissues appears to be complexed by stronger ligands, with the remaining 38% as either weak complexes with non-specific oxygen donor ligands or

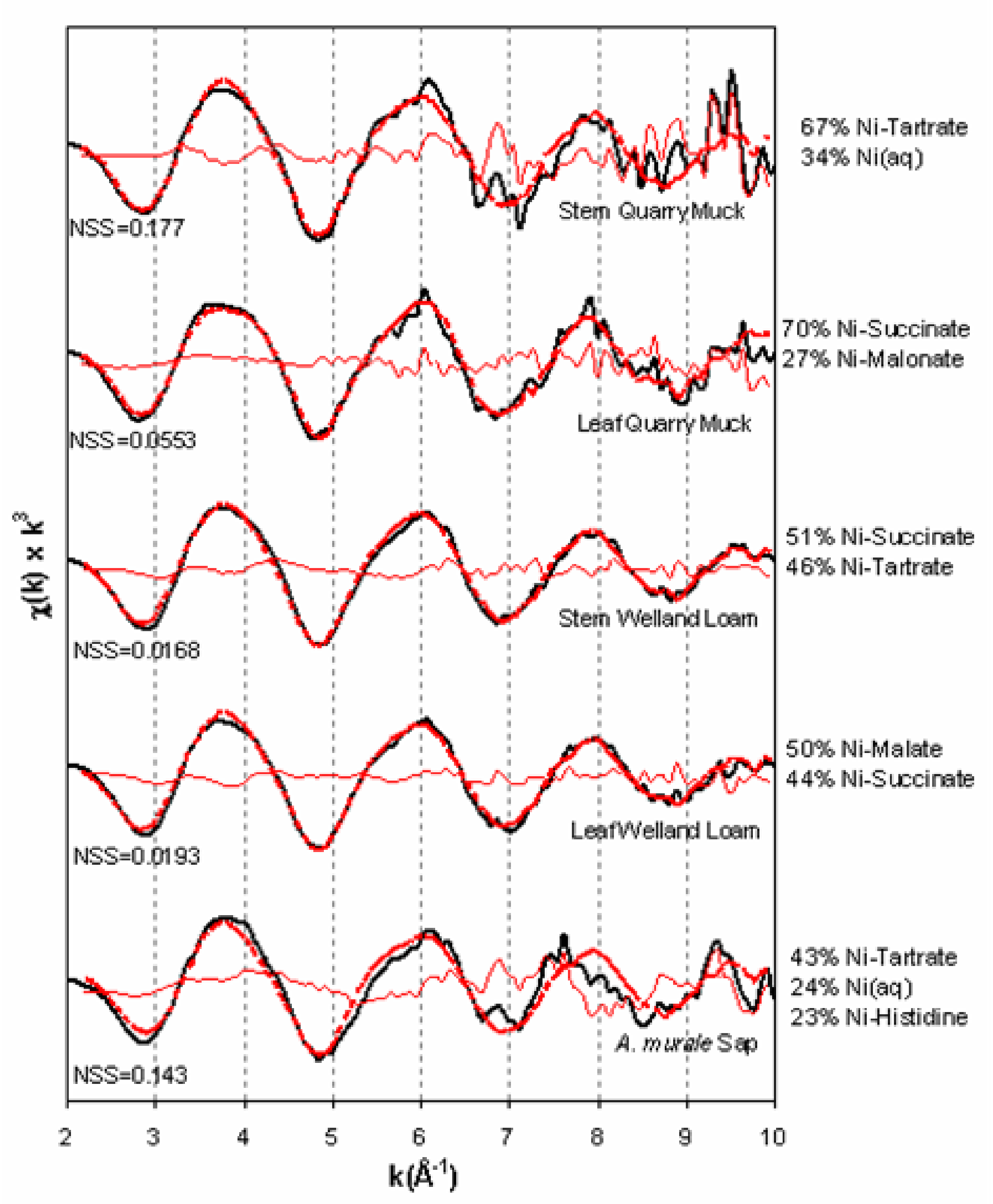

Figure 3.11: Best non-linear least squares fits (NLLSF) of the bulk XAFS spectra from freeze-dried and ground *A.murale* stem and leaf tissues from plants grown in Quarry muck and Welland loam soils from an area adjacent to a Ni refinery in Port Colborne Ontario Canada. Bottom scan is of sap extract. Solid black lines represent the $k^3\chi(k)$-spectra, the doted red lines the best fits and the solid red lines the residual.

present as free hydrated Ni. The fits from the bulk XAFS spectra of leaves and stems grown in Ni enriched soils (Figure 3.11**)** show a similar trend where 50-67% of the Ni is complexed with either malate, malonate or tartrate and the balance with succinate or as Ni(aq). Interestingly, both muck and loam grown plant stems contain tartrate as the primary complexant, while the leaves have malate or malonate. Included in Figure 3.11 is the $k^3\chi(k)$-spectra and LLSF for sap extracted from a soil grown plant. The fit, in addition to tartrate and Ni(aq) includes histidine which was found in previous μ-XAFS spectra of the leaf veins. Not detecting histidine in the bulk leaf and stem tissues most likely has to do with histidine being responsible for Ni transport and delivery and not storage, which is the primary function of the leaf. Therefore, because the vein tissues represents a smaller fraction of the total tissue in the leaf and stem, homogenization of the dried tissues in preparation for bulk-XAFS analysis may have lead to the dilution of this phase. This shows the utility of using microprobe techniques for determining the metal speciation in heterogeneous systems.

3.4.6 Mn and Ni speciation in the trichomes of A. murale

Figure 3.5 shows the μ-SXRF images of a leaf from A. murale grown hydroponically in the presence of slightly elevated Mn concentrations (15μM). Contained in Panel D are the XANES spectra collected from three locations (X1-X3) with elevated Mn concentrations. The position of the maximum absorbance peak at ~6543 eV (indicated by the dotted line) indicates that Mn, at the trichome base, is in the +2 oxidation state (Schulze et al. 1995; Yun et al. 1998). To evaluate the Ni species at these locations, Ni μ-XAFS spectra were also collected from similar locations (Spectra #9 and 10 Figures 3.5 and 3.9). Best LLSF of the spectra from these locations show that Ni is in octahedral coordination with second shell contribution from C. The NLLSF of these spectra indicate that all of the Ni is complexed with malate at these locations. Based on these results, there is no evidence to suggest that Ni and Mn are chemically associated at these locations, but instead co-localized within the tichome basal compartment. Broadhurst et al (2004) found similar results, suggesting that Ni and Mn may be detoxified in different ways, and possibly segregated into separate vacuoles for this purpose. Blamey et al. 1986) found that sunflower, when exposed to elevated concentrations of Mn, accumulated and secreted Mn out of its' glandular trichomes as MnO. While the trichomes of *A. murale* are not glandular, they still may function in a similar way, sequestering Mn as MnO. Alternatively, Mn shares a similar ionic radius with Ca (0.075 nm vs 0.099nm) and therefore it may be substituting or competing with Ca in the during formation of the trichome structure. Additional work is warranted to explore the chemical form of Mn within these cells and to decipher the mechanisms responsible for its detoxification.

3.5 Summary of Ni Speciation and Compartmentalization

Using electron microscopy, μ-SXRF and μ-tomography we found that Ni is evenly distributed throughout the epidermal tissues, entrained in xylem vesicles, and absent from the mesophyll of the leaf. Sulfur was found to be concentrated in the mesophyll where it plays a functional role in several metabolic processes (e g., component of proteins, coenzymes etc.). We found no association of sulfur with Ni, providing additional evidence that S-donor ligands (i.e. phytochelatins) do not play a role in metal detoxification and/or tolerance in A. murale. The trichomes on the leaf surface are highly enriched with Ca which, based on the IC data from the whole leaf extracts, is most likely calcium oxalate. We identified a clear association of Mn with the basal compartment of the trichome and in some cases (but not all) it was co-localized with Ni. The XANES data indicates that Mn is in the +2 oxidation state and not chemically associated with Ni, which we found to be complexed with malate. These findings are consistent with those from Broadhurst et al (2004), who hypothesized different mechanisms of Ni and Mn detoxification within these cells. Interestingly, Mn, unlike Ni, was found concentrated only in the basal compartment of the trichome, and not in the rest of the plant tissues which, as suggested by McNear et al (2005), alludes to these cells having a specific functional role in the detoxification of Mn. Further analysis is necessary to determine the chemical form of Mn at these locations as well as the contribution of the trichome basal compartment to the overall sequestration of Mn in the leaves of *A. murale*.

Determination of Ni organic/amino acid complexes in plant tissues using solely hard X-ray spectroscopic methods is complicated because the lighter, weak backscattering atoms of the complexing ligands (i.e. N or C) provide very little structure to the XAFS spectra. However, by using a thoroughly characterized standard database, multiple statistical data analysis methods and complimentary techniques, definitive detection is possible.

Considering the findings from ATR-FTIR and IC analyses as well as utilizing both LLSF and PCA-NLLSF spectral interpretation methods we can conclude that phytochelatins play no role in the detoxification of Ni in A. murale. Our analyses indicate that the majority of Ni within *A. murale* is complexed with malate, with the remaining fraction either as weak complexes with non-specific oxygen donor ligands, or as free aquo-Ni(II). Malate and/or malonate have been implicated in the complexation of Ni in several Ni hyperaccumulating Alyssum species including *A. bertolonii* (Pelosi et al. 1976) and *A. serpyllifolium* (Brooks et al. 1981). Boominathan and Doran 2003, Tolra et al. 1996 and Shen et al. 1997found OA concentrations to be endogenously higher in several hyperaccumulator plants, finding no specific response (i.e. increased OA production) when the plants were exposed to metals. They all noted that the constitutively high organic acid concentrations were enough to explain the increased Ni concentrations in the plants tested. While we have yet to quantify the organic acid concentrations, it is likely that a similar tolerance mechanism is also functioning in *A. murale*.

In addition to organic acids, we also found Ni complexed with histidine in the XAFS scans taken from leaf veins, as well as the ATR-FTIR spectra of sap extracts. Kramer et al. 1996) showed that exposure of *A. lesbiacum* to 0.3mM Ni in hydroponic cultures resulted in a 36-fold increase in xylem histidine levels. These results indicate that histidine plays a key role in the transport of Ni from the roots to the shoots. The detection of histidine in the leaf veins and xylem in this study is an agreement with these findings, and supports a model where transport in the xylem is facilitated by chelation of Ni by histidine, after which it is transported and stored in the vacuoles of the leaf epidermal cells complexed with organic acids (malate, malonate, tartrate, succinate) or as the free aquo-Ni(II).

3.6 CONCLUSIONS

The findings contained herein contribute to the current understanding of metal tolerance and hyperaccumulation and provide a thorough example of how coupling complimentary techniques at multiple scales can provide a complete and unique picture of metal sequestration and compartmentalization in biological tissues. There are still many questions to be answered concerning the uptake and delivery of metals to the shoots of hyperaccumulating plants. For example, there is little known about how metals, once reaching the leaves, are transported to and into the epidermal vacuoles. On the other end, the mechanisms that plant roots use to mobilize metals from the rhizosphere (e g., organic acid exudation), and how these metals, once mobilized, enter the root and subsequently the xylem are still not understood.

The techniques used in this paper should prove useful in helping to answer some of these questions. However, it is clear that more studies need to be done to ascertain the subtleties in the XAFS spectra arising from single and mixed organic - metal complexes as well as carbohydrates, proteins and other plant sap constituents. The development of micro X-ray beamlines with lower energy resolution as well as focusing optics that enable single cell resolution should aid in this process. Finally, determining the true physiological and biochemical mechanisms responsible for metal transport, tolerance and storage will require not only the use of multiple techniques, but the involvement of scientists across multiple disciplines.

3.7 REFERENCES

Abou Auda MM, Symeonidis L, Hatzistavrou E, Yupsanis T (2002) Nucleolytic activities and appearance of a new DNase in relation to nickel and manganese accumulation in Alyssum murale. Journal of Plant Physiology 159: 1087-1095

Assuncao AGL, Bookum WM, Nelissen HJM, Vooijs R, Schat H, Ernst WHO (2003) Differential metal-specific tolerance and accumulation patterns among *Thlaspi caerulescens* populations originating from different soil types. New Phytologist 159: 411-419

Baker EN, Baker HM, Anderson BF, Reeves RD (1983) Chelation of nickel(II) by citrate. The crystal structure of a nickel-citrate complex, $K_2[Ni(C_6H_5O_7)(H_2O)_2]_{2.4}H_2O$. Inorganica Chimica Acta 78: 281-285

Bell CF (1977) Principles and applications of metal chelation. Oxford University Press, Oxford

Bisessar S (1989) Effects of lime on nickel uptake and toxicity in celery grown on muck soil contaminated by a nickel refinery. The Science of The Total Environment 84: 83-90

Blamey FPC, Joyce DC, Edwards DB, Asher CJ (1986) Role of trichomes in sunflower tolerance to manganese toxicity. Plant and Soil 91: 171-180

Boominathan R, Doran PM (2003) Organic acid complexation, heavy metal distribution and the effect of ATPase inhibition in hairy roots of hyperaccumulator plant species. Journal of Biotechnology 101: 131-146

Broadhurst CL, Chaney RL, Angle JS, Maugel TK, Erbe EF, Murphy CA (2004) Simultaneous hyperaccumulation of nickel, manganese, and calcium in Alyssum leaf trichomes. Environmental Science & Technology 38: 5797-5802

Brooks RR, Shaw S, Marfil AA (1981) The Chemical Form and Physiological-Function of Nickel in Some Iberian Alyssum Species. Physiologia Plantarum 51: 167-170

Cabaniss SE, Leenheer JA, McVey IF (1998) Aqueous infrared carboxylate absorbances: aliphatic di-acids. Spectrochimica Acta Part A 54: 449-458

Cabaniss SE, McVey IF (1995) Aqueous infrared carboxylate absorbances: aliphatic monocarboxylates. Spectrochimica Acta Part A 51: 2385-2395

Colpas GJ, Maroney MJ, Bagyinka C, Kumar M, Willis WS, Suib SL, Baidya N, Mascharak PK (1991) X-ray spectroscopic studies of nickel complexes with application to the structure of nickel sites in hydrogenases. Inorganic Chemistry 30: 920

Dobson KD, McQuillan AJ (1999) In situ infrared spectroscopic analysis of the adsorption of aliphatic carboxylic acids to TiO_2, ZrO_2, Al_2O_3, and Ta_2O_5 from aqueous solutions. Spectrochimica Acta Part A 55: 1395-1405

Ebbs S, Lau I, Ahner B, Kochian L (2002) Phytochelatin synthesis is not responsible for Cd tolerance in the Zn/Cd hyperaccumulator Thlaspi caerulescenes (J. and C. Presl). Planta 214: 635-640

Feth MP, Klein A, Bertagnolli H (2003) Investigation of the ligand exchange behavior of square planar nickel(II) complexes by X-ray absorption spectroscopy and X-ray diffraction. European Journal of Inorganic Chemistry 5: 839-852

Frank R, Stonefield KI, Suda P, Potter JW (1982) Impact of nickel contamination on the production of vegetables on an organic soil, Ontario, Canada, 1980-1981. The Science of The Total Environment 26: 41-65

Hedwig GR, Liddle JR, Reeves RD (1980) Complex formation of nickel(II) ions with citric acid in aqueous solution: A potentiometric and spectroscopic study. Australian Journal of Chemistry 33: 1685-1693

Homer FA, Reeves RD, Brooks RR, Baker AJM (1991) Characterization of the nickel-rich extract from the nickel hyperaccumulator Dichapetalum gelonioides. Phytochemistry 30: 2141-2145

Jung C (2000) Insight into protein structure and protein-ligand recognition by Fourier transform infrared spectroscopy. Journal of Molecular Recognition 13: 325-351

Kramer U, Cotter-Howells JD, Charnock JM, Baker AJM, Smith JAC (1996) Free histidine as a metal chelator in plants that accumulate nickel. Nature 379: 635-638

Kupper H, Lombi E, Zhao FJ, Wieshammer G, McGrath SP (2001) Cellular compartmentation of nickel in the hyperaccumulators *Alyssum lesbiacum*, *Alyssum bertolonii* and *Thlaspi goesingense*. Journal of Experimental Botany 52: 2291-2300

Kupper H, Mijovilovich A, Meyer-Klaucke W, Kroneck PMH (2004) Tissue- and age-dependent differences in the complexation of cadmium and zinc in the cadmium/zinc hyperaccumulator *Thlaspi caerulescens* (Ganges ecotype) revealed by x-ray absorption spectroscopy. Plant Physiology 134: 748-757

Malinowski ER (1977) Determination of the number of factors and the experimental error in a data matrix. Anal Chim Acta 49: 612-617

Malinowski ER (1978) Theory of error for target factor analysis with applications to mass spectrometry and nuclear magnetic resonance spectrometry. Anal Chim Acta 103: 354-359

Manceau A, Marcus MA, Tamura N (2002) Quantitative speciation of heavy metals in soils and sediments by synchrotron X-ray techniques. In: Fenter PA, Rivers ML, Sturchio NC, Sutton SR (ed) Applications of synchrotron radiation in low-temperature geochemistry and environmental sciences, Reviews in Minerology and Geochemistry 49, Minerological Society of America pp 341-428

Marcus MA, MacDowell AA, Celestre R, Manceau A, Miller T, Padmore HA, Sublett RE (2004) Beamline 10.3.2 at ALS: a hard X-ray microprobe for environmental and materials sciences. Journal of Synchrotron Radiation 11: 239-247

McCann MC, Hammouri M, Wilson R, Belton P, Roberts K (1992) Fourier transform infrared microspectroscopy is a new way to look at plant cell wall. Plant Physiol. 100: 1940-1947

McNear DH, Peltier E, Everhart J, Chaney RL, Sutton SR, Newville M, Rivers M, Sparks DL (2005) Application of quantitative fluorescence and absorption-edge computed microtomography to image metal compartmentalization in Alyssum murale. Environ Sci Technol 39: 2210-2218

Nicolai B, Kearley GJ, Johnson MR, Fillaux F, Suard E (1998) Crystal structure and low-temperature methyl-group dynamics of cobalt and nickel acetates. Journal of Chemical Physics 109: 9062-9074

Pelosi P, Fiorentini R, Galoppini C (1976) On the nature of nickel compounds in Alyssum bertolonii. Agr. Biol. Chem 40: 1641-1642

Ressler T (1997) WinXAS: A new software package not only for the analysis of energy-dispersive XAS data. Journal De Physique IV 7: 269-270

Santoro A, Mighell AD, Zocchi M, Reimann CW (1969) The crystal and molecular structure of hexakis(imidazole)nickel(II) nitrate, $(C_3H_4N_2)_6Ni(NO_3)_2$. Acta Crystallographica Section B 25: 842-847

Schat H, Llugany M, Vooijs R, Hartley-Whitaker J, Bleeker PM (2002) The role of phytochelatins in constitutive and adaptive heavy metal tolerances in hyperaccumulator and non-hyperaccumulator metallophytes. Journal of Experimental Botany 53: 2381-2392

Schulze DG, Sutton SR, Bait S (1995) Determining manganese oxidation state in soils using X-ray absorption near-edge structure (XANES) spectroscopy. Soil Science Society of America Journal 59: 1540-1548

Shen ZG, Zhao FJ, McGrath SP (1997) Uptake and transport of zinc in the hyperaccumulator Thlaspi caerulescens and the non-hyperaccumulator Thlaspi ochroleucum. Plant Cell and Environment 20: 898-906

Stewart JM, Lingafelter EC, Breazeale JD (1961) The crystal structue of Disaguabis(salicylaldehydato) nickel. Acta Cryst 14: 888

Strathmann TJ, Myneni SCB (2004) Speciation of aqueous Ni(II)-carboxylate and Ni(II)-fulvic acid solutions: Combined ATR-FTIR and XAFS analysis. Geochimica et Cosmochimica Acta 68: 3441-3458

Surewicz WK, Mantsch HH, Capman D (1993) Determination of protein secondary structure by Fourier transform infrared spectroscopy: a critical assessment. Biochemistry 32: 389-394

Temple PJ, Bisessar S (1981) Uptake and toxicity of nickel and other metals in crops grown on soil contaminated by a nickel refinery. Journal of Plant Nutrition 3: 473-482

Tolra RP, Poschenrieder C, Barcelo J (1996) Zinc hyperaccumulation in Thlaspi caerulescens 2: Influence on organic acids. Journal of Plant Nutrition 19: 1541-1550

Wasserman SR, Allen PG, Shuh DK, Bucher JJ, Edelstein NM (1999) EXAFS and principal component analysis: A new shell game. Journal of Synchrotron Radiation 6: 284-286

Yun W, Pratt ST, Miller RM, Cai Z, Hunter DB, Jarstfer AG, Kemner KM, Lai B, Lee H-R, Legnini DG, Rodrigues W, Smith CI (1998) X-ray Imaging and Microspectroscopy of Plants and Fungi. Journal of Synchrotron Radiation 5: 1390-1395

Zhang WH, Cai Y (2003) Purification and characterization of thiols in an arsenic hyperaccumulator under arsenic exposure. Analytical Chemistry 75: 7030-7035

Chapter 4

THE APPLICATION OF QUANTITATIVE FLUORESCNECE AND ABSORPTION EDGE COMPUTED MICROTOMOGRAPHY TO IMAGE METAL COMPARTMENTALIZATION IN ALYSSUM MURALE

4.1 ABSTRACT

This paper shows that synchrotron based fluorescence and absorption edge computed microtomographies (CMT) are well suited for determining the compartmentalization and concentration of metals in hyperaccumulating plant tissues. Fluorescence CMT of in-tact leaf, stem and root samples revealed that Ni concentrated in stem and leaf dermal tissues and, together with Mn, in distinct concentrations associated with the Ca rich trichomes on the leaf surface of the nickel hyperaccumulator *Alyssum murale* ‘Kotodesh’. Metal enrichment was also observed within the vascular system of the finer roots, stem and leaves, but absent from the coarser root, which had a well correlated metal coating. Absorption edge CMT showed the three-dimensional distribution of the highest metal concentrations and verified that epidermal localization and Ni and Mn co-localization at the trichome base are phenomena that occurred throughout the entire leaf and may contribute significantly to metal detoxification and storage. Ni was also observed in the leaf tips,

possibly resulting from release of excess Ni with guttation fluids. These results are consistent with a transport model where Ni is removed from the soil by the finer roots, carried to the leaves through the stem xylem, distributed throughout the leaf by the veins to the dermal tissues, trichome bases and in some cases the leaf tips.

4.2 INTRODUCTION

The search for an economically viable alternative to conventional remediation of heavy metal enriched soils has led to the use of specialized metal accumulating plants (Banuelos et al. 1997; Chaney et al. 1997; Tu et al. 2002; Li et al. 2003) . Metal hyperaccumulators have long been identified (Brooks et al. 1977), but only recently have attempts been made to elucidate the physiological and biochemical mechanisms these plants use to accumulate and compartmentalize excess metals (Kramer et al. 1996; Salt et al. 1999; Lombi et al. 2001; Kerkeb and Kramer 2003). A greater understanding of these processes could aid in increasing the efficiency of natural metal accumulators or in the engineering of specialized crops, capable of impeding or accelerating metal uptake. Deciphering which plant tissues store metals is one step in understanding the sequestration mechanism(s). Current approaches for determining the compartmental-ization of metals in plant tissues are limited by the use of techniques with low sensitivity, insufficient tissue specificity, or considerable sample handling and pretreatment requirements, the latter potentially altering the metal allocation (Kramer et al. 1997; Kupper et al. 2000; Pickering et al. 2000; Liu and Kottke 2003). A tool that compliments the current methods, but can overcome some of their drawbacks, would be valuable in elucidating the mechanisms involved in metal hyperaccumulation by plants.

A majority of the previous studies on plant metal compartmentalization use scanning electron microscopy with energy dispersive x-ray analysis (SEM-EDX) to decipher metal locations within plant tissues. SEM-EDX is very effective at resolving the cellular structures within plant tissues, and when coupled with energy dispersive analysis can provide relative cellular elemental distributions including lighter elements (K, P, C, O) unattainable by other techniques. However, there are limitations involving sample preparation (e.g. freeze-drying, carbon coating etc.) and, because SEM is a surface imaging tool, the need to section the tissues in order to get cross-sectional elemental distributions. These treatments have the potential to alter the chemical and physical elemental distribution of the metal within the plant tissues. In addition, the detection limits of SEM are quite high (~1000 $\mu g\ g^{-1}$) which, while not as important for hyperaccumulating plants with typical dry matter metal concentrations well over 1000 $\mu g\ g^{-1}$, may limit the identification of smaller but potentially relevant localizations.

Synchrotron x-ray fluorescence (SXRF) spectroscopy can overcome many of these limitations by providing in-situ, highly sensitive and well resolved 2D elemental maps and, when coupled with x-ray absorption spectroscopy (XAS), the ability to determine the elemental species (Pickering et al. 2000; Howe et al. 2003; Scheckel et al. 2004). However, because SXRF is two-dimensional and the beam penetrates into or through the sample, the resulting SXRF image is actually a projection showing all of the entrained metals from one specific direction. Therefore, it may be difficult to tell exactly which compartment or specific tissue contains an observed metal-rich region. For instance, a face-on view of a leaf will show metals on both surfaces (top and bottom epidermal tissues) as well as those in the interior. Thus, a metal could be entrained in the top as well as the bottom dermal tissues, which would appear associated in the SXRF image, but are instead separated by the thickness of the leaf. Therefore, because of these “thickness” effects, determining the compartmentalization of metals using SXRF should be done with caution and if possible, verified using another technique.

Synchrotron based x-ray computed microtomography (CMT) can compensate for some of the drawbacks associated with using SXRF and SEM for imaging metal compartmentalization in plant tissues. Synchrotron based x-ray absorption edge and fluorescence CMT are techniques that utilize a high intensity, tunable x-ray beam to nondestructively interrogate a sample as it is translated and/or rotated within the beam. The result, after computational reconstruction, is the cross-sectional two and three dimensional distributions of specific elements within the sample. Unlike conventional x-ray CMT instruments, synchrotron based fluorescence CMT can provide a highly resolved picture of the multi-elemental distribution through a virtual slice of the sample at concentrations down to approximately 1 $\mu g\ g^{-1}$ (element dependent). Absorption edge CMT provides a fully three-dimensional image of the metal distribution, albeit, with some loss of resolution and sensitivity.

Application of these techniques has included imaging of various phenomena in earth and material sciences. For example, McLain et al. (2002) used absorption edge CMT to explore the association between cation sorption sites in alluvial soils and Fe and pore space distributions. They were able to do so by exposing the soils to a CsCl solution and then obtaining absorption edge CMT images for Cs which revealed the location of the sorption sites. Absorption edge CMT images of Fe then revealed the relation between sorption site, Fe and pore space distributions. In another application, Flynn et al. (2000) used fluorescent CMT to investigate interplanetary dust collected from the Earth's stratosphere. They determined that the volatile elements Zn and Br were present not only on the surface but also in the core of the particle, indicating that the observed enrichments in these elements are indigenous rather than contaminants from the atmosphere. These studies highlight the utility of CMT techniques for deciphering elemental distributions in structurally sensitive samples.

The closest application of synchrotron tomographic techniques to biological systems relevant to this study were by Hansel and Fendorf (2001) and Hansel et al. (2002) who used fluorescence CMT to help characterize Fe plaques and associated metals on the surface of roots from the aquatic plants *Phalaris arundinacea* (Reed canarygrass) and *Typha latifolia* (cattail). Using this technique, they were able to determine that Pb and Fe accumulated on the surface of the root in a similar pattern, forming a covering on the root surface while As was isolated to distinct regions on the exterior and interior of the root. Similarly, Keon-Blute et al. (2004) used fluorescence CMT to reveal that As was sequestered by Fe(III) oxyhydroxides within cattail root plaques from a contaminated wetland. However, these studies, because of the aquatic and metal excluding nature of the plants, were limited to the roots only. Additionally, no absorption edge CMT technique was utilized to see if this characteristic was observed over the entire root length, or just over the section chosen for analysis.

Therefore, the objective of this study was show that synchrotron based computed microtomographic techniques, including the novel application of synchrotron absorption edge CMT, are effective at determining the metal compartmentalization and concentration throughout plant tissues, and to do so by exploring the metal partitioning behavior of Ni within the shoots and roots of the Ni hyperaccumulator *Alyssum murale* “Kotodesh”.

4.3 MATERIALS AND METHODS

4.3.1 Plant sample preparation

The soils and plants used in this study have been described and characterized elsewhere (Kukier and Chaney 2001). Briefly, the Kotodesh cultivar of the known Ni hyperaccumulator *Alyssum murale* (common name yellowtuft) is an herbaceous perennial with upright growth habit from the Brassicaceae family and is native to serpentine soils throughout Mediterranean Southern Europe. This ecotype has been proven to be an effective Ni hyperaccumulator through greenhouse and field trials and has been developed into a commercial crop for phytoremediation or phytomining (Chaney et al. 1999; Li et al. 2003; Li et al. 2003). *Alyssum murale* used in this study was grown in a greenhouse using natural and artificial light, in Ni enriched loam soils

(Welland soil, Typic Epiaquoll; Canadian classification, Terric Mesisol) collected from an area surrounding an historic Ni refinery in Port Colborne, Ontario Canada. The soils containing approximately 100 mg kg $^{-1}$ (FCMT) and 2000 mg kg^{-1} Ni (AECMT) were sieved wet, mixed thoroughly, placed in 1.5 liter plastic pots and allowed to equilibrate with fertilizers for one week. Seeds of *A. murale* were first germinated in Promix® before being transplanted into the 1.5 liter soil pots. Plants were harvested after approximately 120 – 180 days of growth. The roots used for analysis were removed from the pots and lightly washed with double deionized water to removed attached soil particles. Roots were examined under a light microscope to verify cleanliness.

Attempts were made to image "fresh" plant tissues using fluorescent CMT, however, it was found that shock freezing and partial drying was required because the high power density of the microfocused x-ray beam caused motion associated with dehydration in "live" Alyssum plant tissue which compromised reconstruction of the tomograms. As such, whole shoot sections were excised from the plant and immediately immersed in liquid nitrogen and dried under vacuum at –180ºC for 24 hrs to prevent ice crystal formation. Shoots and roots were then taken to the beamline at which point the leaves were separated from the steam and attached to a wooden shafts using epoxy resin. The wooden shaft was then cut to ~5mm in length and the cut end inserted into the rotation axis of an x-y-theta stepping sample stage for imaging. The roots were mounted in a similar way, however, the stems, because of their inherent rigidity, were simply inserted into a bead of modeling clay and attached to the stage.

For absorption edge CMT, living plants were transported to the beamline and a leaf was removed just prior to analysis and mounted directly to the x-y-theta stage by placing the proximal (bottom) portion of the leaf into a bead of modeling clay.

4.3.2 Scanning Electron Microscopy (SEM)

Scanning electron microscopy was used in an effort to obtain highly resolved cross-sectional images for correlating the metal compartmentalization observed in fluorescence CMT with specific plant tissues. Scanning electron micrographs were recorded using a Hitachi 4700 FESEM. Leaves from *A. murale* were freeze dried as described above and then re-suspended in liquid nitrogen where they were fractured using forceps to acquire representative cross sections. Samples were then mounted on a conductive carbon stub and sputter coated with carbon prior to analysis. Samples were scanned manually at magnifications of 85-300x.

4.3.3 X-ray fluorescence CMT

Thorough discussions on the fundamentals of tomographic instrumentation and techniques can be found elsewhere (Flannery et al. 1987; Kinney et al. 1994; Rivers et al. 1999; Sutton et al. 2002) and only a brief instrumental description is provided here. Samples were analyzed at the GeoSoilEnviroCARS (GSECARS) beamline at the Advanced Photon Source, Argonne National Laboratory (APS-ANL), Chicago, Ill. For fluorescence CMT, the APS undulator (13-ID-C) source was used in conjunction with a cryogenically cooled, Si double-crystal monochromator, and Kirkpatrick-Baez microfocusing mirrors (Kirkpatrick and Baez 1948; Eng et al. 1995; Eng et al. 1998) to produce a 5 μm x-ray beam. X-ray fluorescence spectra were collected with a 16-element Ge array detector (Canberra Industries, Inc.) coupled with digital signal processing electronics (XIA, Inc.). Transmission tomograms were recorded simultaneously, resulting in a density profile of the leaf tissue which provides an image of the plant tissue structure. Fluorescence microtomography data collection consisted of mounting the specimen on a rotation-translation stage, collecting XRF intensities as the specimen is translated through the x-ray beam, rotating by a small angle, repeating the translation-XRF collection, and continuing this process to encompass a total rotation of 180 degrees. Typical datasets were collected with 5 μm translation steps over 1.5 mm, 3 degree angular steps and dwell times of 1 second resulting in 2-D "sinograms" (intensity on a "position-angle" plot) for each element with total collection times of ~ 5 hours. 2-D element images were then computationally reconstructed using FFT-based Gridrec software developed by Brookhaven National Laboratory (Dowd et al. 1999), which was controlled by the IDL programming language (Research Systems Inc.) yielding images of the cross-sectional internal metal distributions.

Absorption by the object of incoming x-rays and outgoing fluorescence x-rays can affect the reconstructed images thereby limiting the size of objects that can be imaged. The absorption is given by

$$\frac{I}{I_o} = e^{-\mu x} \qquad (1)$$

where I_o is the initial x-ray intensity, I is the intensity after passing a distance x (cm) through material of linear absorption coefficient μ (cm^{-1}). The coefficient μ depends on the composition of the material and the x-ray energy. In a fluorescence microtomography measurement, the incident energy is chosen to be well above the absorption edge energies of the elements of interest, in order to excite the fluorescence from all elements of interest simultaneously. Consequently, absorption effects typically result from the absorption of the fluorescence x-rays (at lower energies than the incident energy) traversing the object on their way to the detector. Using the equation above, the absorption of fluorescence x-rays of interest can be determined. A useful "rule of thumb" for the upper limit of "correctable" absorption is the factor e (= 2.7), a "characteristic absorption value".

Using the transmission tomograms collected simultaneously with the fluorescence tomograms for our partially-dried samples and assuming the major sample composition was approximately cellulose (CH_2O, $\mu = 3.0$ cm^{-1} for 11 keV), the characteristic absorption length (length for an absorption factor of "e") for the 11 keV incident x-rays is ~5 mm. The characteristic lengths for the fluorescence x-rays, Ca K_α (3.7 keV), Mn K_α (5.9 keV), Fe K_α (6.4 keV), Ni K_α (7.5 keV) and Zn K_α (8.6 keV), were 0.2, 0.7, 0.9, 1.5, and 2.3 mm, respectively. Thus, the practical size limit for Ni K_α fluorescence tomograms was about 1 mm. The maximum size of objects imaged was ~1 mm, i.e., near this limit.

Various algorithms have been or are being developed for correcting fluorescence microtomography data for absorption artifacts (e.g. Hogan et al. 1991;

Golosio et al. 2003; La Riviere and Billmire 2004). In the present work, approximate absorption corrections were applied to fluorescence sinograms by using the transmission sinograms collected simultaneously to empirically determine the linear absorption coefficient μ of the absorbing material. Each sinogram is a plot of intensity (fluorescence or absorption) versus translation position and rotation angle. Each row (rotation angle) in the fluorescence sinogram was treated separately in the following way. First, the pixel representing the detector facing edge of the object was identified and defined as a reference point (X_0). At other pixels (translation position) in the row (X), the intensity $I_{f,0}$ was corrected to "no absorption" intensity $I_{f,x}$ by multiplying by an absorption factor ϕ_x. ϕ_x was calculated by first determining the average absorption $\overline{I_{t,x}}$ in the transmission sinogram (values of $I_t/I_{t,0}$) over the pixels between X and X_0. The linear absorption coefficient at incident energy Eo, $\mu_{x,Eo}$ (cm^{-1}) was then

$$\mu_{x,Eo} = -\ln(\overline{I_t})/L_x \tag{2}$$

where L_x is the width of the object in the orthogonal direction (determined from the transmission sinogram). The linear absorption coefficient for a fluorescence x-ray E_f was determined from

$$\mu_{x,Ef} = \mu_{x,Eo}\left[\frac{\mu_{cellulose,Ef}}{\mu_{cellulose,Eo}}\right] \tag{3}$$

where the cellulose coefficients were computed theoretically assuming a composition of CH_2O. Finally, the corrected intensity at pixel X is

$$I_{f,x} = \varphi_x\left(I_{f,0}\right) = I_{f,0}e^{\left(\mu_{x,Ef}*\Delta X\right)} \qquad (4)$$

where $\Delta X = X - X_0$. In this way, absorption corrections were applied to each pixel in each fluorescence sinogram and then reconstruction was performed on the corrected dataset. Figure 4.1 shows the result of applying this absorption correction algorithm to the Ni fluorescence tomogram of an *A. murale* stem.

The density ρ_x of the material absorbing fluorescence x-rays from each pixel at translation position X was approximated by using the mass absorption coefficient for cellulose (CH_2O, $\mu/\rho = 3.0\ cm^2\ g^{-1}$ *for 11 keV)* in which case

$$\rho_x = \mu_{x,Eo} / \left(\mu/\rho\right)_{cellulose,Eo} \qquad (5)$$

The average of these density values was defined to be the object density ρ_{obj}.

Element concentrations were calculated for the fluorescence microtomograms by using measurements of the SRM1832/33 (NIST) thin film standards to obtain sensitivities (counts per second per $\mu g\ cm^{-2}$) for Ca, Mn, Fe, Cu, and Zn. The Fe and Cu sensitivities (different by a factor of two) were then interpolated by atomic number

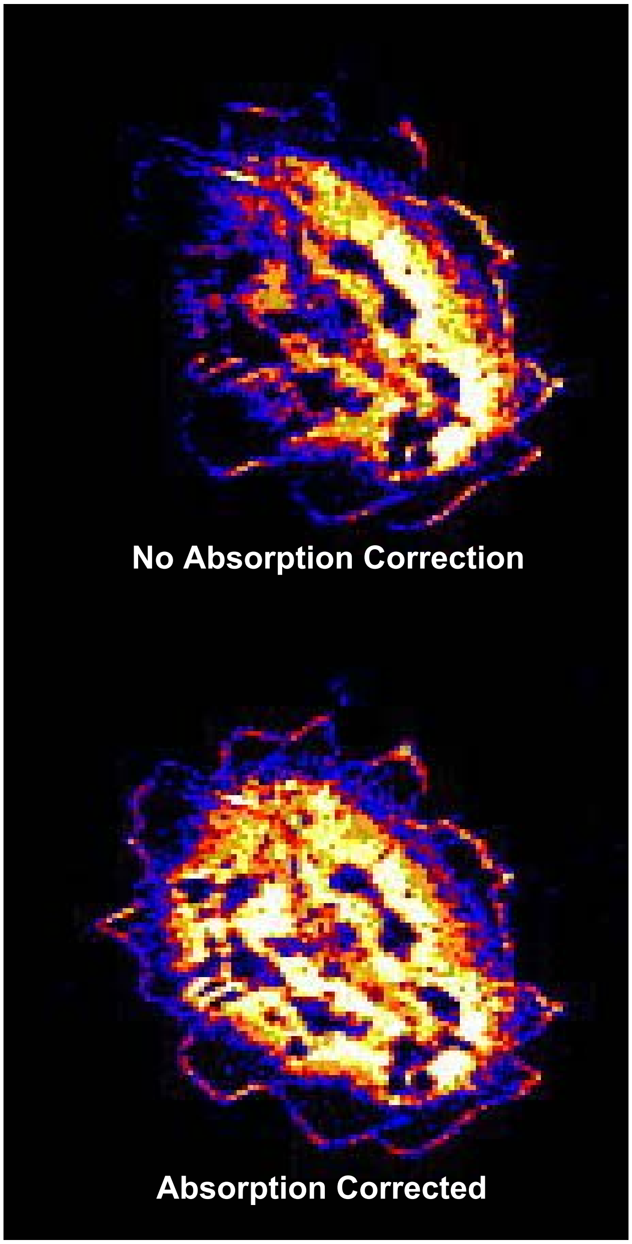

FIGURE 4.1: Nickel fluorescence microtomograms of the stem showing the result of absorption correcting the data. Top tomogram is uncorrected for absorption effects, while the bottom tomogram results from absorption correcting the fluorescent intensity. The x-ray fluorescence detector is located to the right in both cases.

to infer Ni sensitivity. This approach yielded mass per unit area (μg cm^{-2}) for a specific element at each pixel in the fluorescence microtomogram which, when divided by the beam size (5 μm), gave the element density at each *(i,j)* pixel $\rho_{el,obj}(i,j)$. Element concentrations (weight fraction) $C_{el,obj}(i,j)$ were calculated using the object density ρ_{obj} (0.4, 1.3 and 0.6 g cm^{-3} for the leaf, stem and root, respectively) where

$$C_{el,obj}(i,j) = \rho_{el,obj}(i,j) / \rho_{obj} \tag{6}$$

For the leaf Ca microtomogram, a value of 2.5 g cm^{-3} was used for object density (ρ_{obj}), based on the expectation that Ca resides in trichomes composed of calcite and/or calcium oxalate (average density of the two utilized). The concentrations determined in this way may be interpreted as dry tissue concentrations (μg g^{-1}). The concentration precision is typically ±15% and ±10% (1σ), for individual and mean values, respectively.

4.3.4 Absorption edge CMT

The GSECARS bending magnet source (13-BM-D) provided a wide fan x-ray beam for flood field applications used in absorption edge CMT (*Rivers et al. 1999; Rivers et al. 2004*). The monochromator was a narrow gap, Si(111) double crystal instrument. The transmitted x-rays were converted to visible light with a single crystal

YAG scintillator and the scintillator was imaged with a microscope objective (10X) projected onto a 1300x1030 pixel fast charge-coupled device (CCD) x-ray area detector (MicroMax) resulting in a field of view 2.15 x 1.7 mm and an optical resolution of 3.3 µm. Typical 3D datasets were collected with 0.5 degree steps over 180 degrees and dwell times of 10 seconds. One tomogram was collected with the x-ray beam energy at 8300 eV, i.e., ~30 eV below the Ni K absorption edge (8333 eV) and a second tomogram was acquired above the Ni K edge. To enhance absorption contrast, the above-edge energy was selected to coincide with the XANES white line for the Ni in the plant tissue (8350 eV). This energy was determined empirically by viewing the absorption radiograph in real time as the monochromator energy was scanned manually until the energy of maximum absorption was found. These two sinograms (above edge and below edge) were then subtracted, the difference matrix reconstructed using the Gridrec-based software (*Dowd et al. 1999*) and the resulting images then stacked and viewed sequentially resulting in a movie depicting the metal distribution from the top (distal) to the bottom (proximal) end of the leaf. Typical image acquisition times with these settings were 45 min. to 1.5 hours.

The phase contrast in the transmission microtomography images is negligible. The region *r* in the sample that contributes to a point at the detector is given by (*Cloetens et al. 2001)*

$$r = \sqrt{\lambda D} \tag{7}$$

where λ is the x-ray wavelength and D is the sample to detector distance. In our setup, D is ~ 0.1 m and λ is ~ 1 Å (10^{-10} m). Thus, r is ~ 3 μm, i.e., comparable to our empirically-determined resolution of 3.3 μm, suggesting that the phase contrast content of the transmission images is minimal. Furthermore, any phase contrast present in these images will cancel out during the image subtraction procedure since the difference in λ between the two images (corresponding to an energy difference of 50 eV out of 8300 eV) results in a change in r of < 1%.

The Ni concentrations in the absorption edge microtomograms were quantified by comparison with a theoretical absorption coefficient μ_0 (cellulose containing Ni at concentration C_0; 1.1 g/cm^3; 8.35 keV) with the measured absorption coefficients where the Ni concentration at pixel *(i,j)* is

$$C(i,j) = C_0\left(\frac{\mu(i,j)}{\mu_0}\right) \tag{8}$$

μ_0 includes an absorption coefficient enhancement factor (2.1) resulting from collecting the above-edge tomogram with the incident energy on the Ni K absorption edge white line. This factor was determined empirically from a XANES spectrum collected on a similar Ni-accumulated Alyssum leaf. The Ni concentrations determined in this way are wet-tissue values (μg g^{-1} wet tissue). The concentration precision is typically ± 10% and ± 5% (1σ), for individual and mean values, respectively.

The Ni detection limit was calculated by taking the standard deviation of values in a relatively uniform, Ni-free, part of the difference image and comparing that absorption value (2 σ) with the absorption expected from water containing 3% Ni (to convert to concentration). This resulted in a calculated Ni detection limit of about 0.5 % or 5000 μg g^{-1} wet tissue weight. In order to compare the wet weight with the dry weight values calculated by fluorescence CMT, a correction must be made to make up for the presence of water within the sample. The density value for the dry leaf tissue was calculated to be 0.4 g cm^{-3} compared to the 1.1 g cm^{-3} used for the wet leaf; roughly a difference of 3. Therefore, in order to equate the absorption edge to the fluorescence CMT concentrations, the absorption edge values were multiplied by a factor of 3.

4.4 RESULTS AND DISCUSSION

4.4.1 Leaf Metal Compartmentalization

Tabulated in table 4.1 are the leaf, stem and root metal concentrations (μg g^{-1}) calculated from the fluorescent tomograms in figure 4.2. The mean Ca, Ni, Mn and Zn concentrations in our leaf sample are ~ 90,000, 500, 200 and 100 μg g^{-1} dry weights respectively. In whole leaves of *A murale* "Kotodesh" plants grown in similarly enriched soils, Broadhurst et al.(*Broadhurst et al. 2004*) found Ca, Ni, Mn and Zn concentrations of ~40,000, 2000, 125 and 140 μg g^{-1} dry weight respectively. The concentrations of Mn and Zn in the two studies are very similar, however, there is a slight difference in the Ni and Ca concentrations. These small differences most likely resulted from variations in the way the plants were grown, soil metal content, the age of the leaf and/or differences in the mass of tissue sampled. The latter of these is of particular importance, because the metal concentrations detected by fluorescence CMT will be sensitive to the exact 5μm slice chosen for analysis. For example, the Ca concentration will be highly influenced by how many Ca rich trichomes the tomogram intersects. Nonetheless, the agreement

Table 4.1: Leaf, stem and root metal concentrations (μg g^{-1}) calculated for the fluorescent tomograms in Figures 4.2 and 4.4

	Dried Tissue Density	Element	Max Conc.	Mean Conc.	MDL[a]
	g cm^{-3}		μg g^{-1}		
Leaf	0.4	Ni	2700	500	18
		Fe	642	150	18
		Zn	464	95	18
		Ca	571000	88000	1900
		Mn	1250	200	18
Stem	1.3	Ni	1320	440	37
		Fe	37	11	5
		Zn	337	51	37
Roots	0.6	Ni	19000(2500)[b]	670	33
		Fe	110000(9000)[b]	3300	333
		Zn	1700(670)[b]	230	33

[a] Minimum detection limit is defined to be the two standard deviation variability of the image background in each case. [b] Values in parenthesis represent the Ni concentrations in the finer root shown in the inset of the root tomogram in Figure 4.4

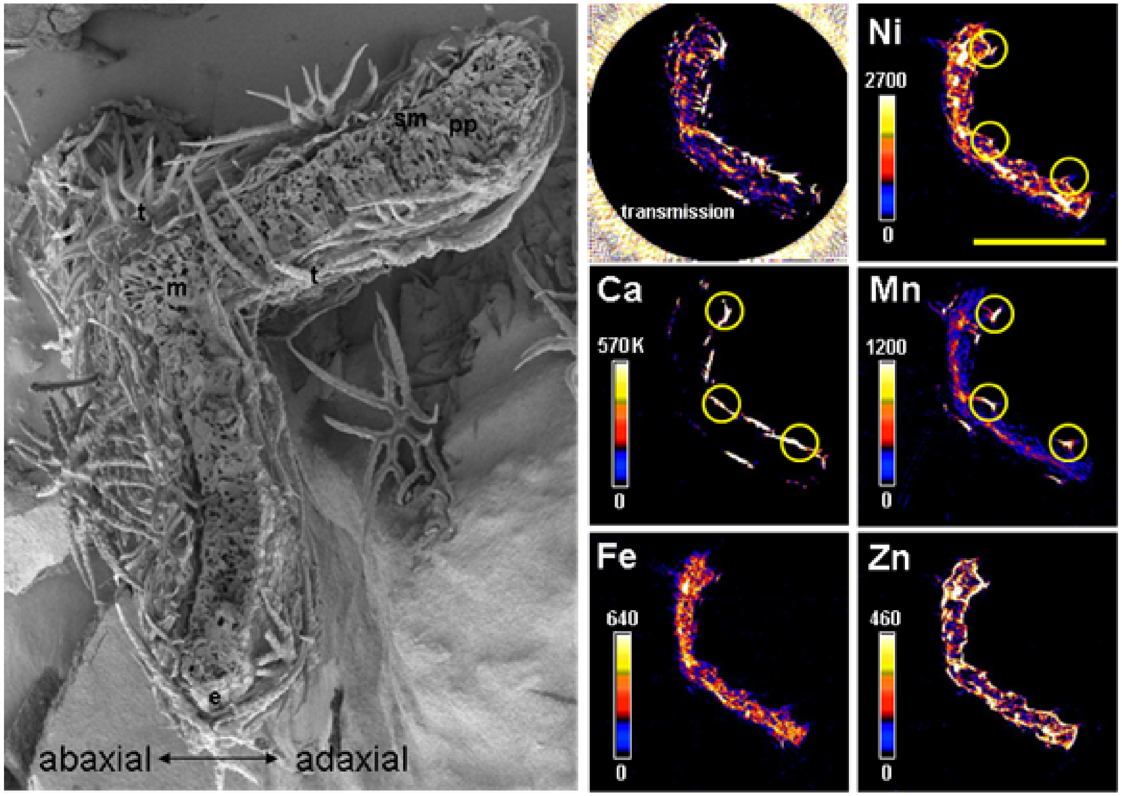

FIGURE 4.2: Fluorescent computed microtomography images showing the Ni, Ca, Mn, Fe and Zn distributions in an *Alyssum murale* 'Kotodesh' leaf cross-section. An SEM image showing a cross-section of an *A. murale* leaf is provided to highlight the internal architecture of the leaf and to aid in correlating the metal distribution in the fluorescent CMT images with specific leaf tissues (**m**-midrib, **t**=trichome, **sm**= spongy mesophyll, **pp**= pallisade parenchyma, **e**=epidermis). The colorimetric scale maps region-specific relative metal concentrations (µg g^{-1}) for each element, with brighter colors indicating areas of higher enrichment. The lower thresholds for the tomograms were adjusted up slightly to suppress background noise and thereby improve image quality. In the transmission tomogram, brighter regions indicate tissues of higher density. Note that the Ca concentrations are in thousands. Yellow scale bar represents ~500 µm.

between the two studies is a good indication that our calculated values provide a reasonable estimate of the average metal concentrations within *A. murale* tissues. Moreover, the tomograms have the added advantage of revealing the concentrations in specific tissues, crucial information in trying to understanding the mechanisms of metal compartmentalization and tolerance.

The highest Ni concentrations (Figure 4.2 and 4.3) are within the epidermal (upper and lower) and vascular tissues (up to ~2700 $\mu g\ g^{-1}$) with relatively little enrichment within the ground tissues (spongy mesophyll and palisade parenchyma; < 680 $\mu g\ g^{-1}$). Epidermal localization of metals in hyperaccumulating plants is commonly attributed to compartmentation of organic acid complexed metals within the vacuoles of epidermal cells (Heath et al. 1997; Kupper et al. 1999; Kupper et al. 2000; Kupper et al. 2001). The mechanism for the exclusion of excess Ni from the mesophyll and concentration in the epidermal vacuoles is still not clearly understood, however it may be both a physiological and/or defense-related responses. In higher plants, a majority of the photosynthetic activity takes place within the mesophyll of the leaf (Taiz and Zeiger 2002), and as such, segregation of Ni from these tissues is essential to prohibit disruption of the metal sensitive photosynthetic apparatus (Prasad and Strzalka 2004). Alternatively, Jhee et al. (1999) suggested that hyperaccumulation may have evolved from selective pressure of insect herbivores and as such hypothesize that the plants are excluding Ni to the dermal tissues of the leaf to avoid insect damage. However, there is still little consensus as to the role of metals in preventing insect herbivory (Pollard and Baker 1997; Boyd and Moar 1999; Davis and

Boyd 2000; Boyd et al. 2002). Regardless, studies on several Ni hyperaccumulators have identified histidine (Kramer et al. 1996) and citrate (Lee et al. 1978; Kersten et al. 1980; Sagner et al. 1998) as the primary complexing ligand and therefore, it is likely that they are playing the main role in the detoxification and compartmentalization of Ni in *A. murale*.

The vascular tissues also exhibit high Ni concentrations, which can be seen in figure 4.2 as discrete white/yellow areas within the interior of the leaf. Few studies have observed notable enrichment of the vascular bundles as was observed here. The presence of nickel within the vascular system (as well as Fe and Zn) is expected because the plant veins (xylem) are the primary mode of transport and delivery of metals to the leaves. We interpret the association of Ni with the vascular system as being due to entrainment during fixation, as opposed to tissue loading. Detection of entrained metals may have been facilitated by the analysis of in-tact versus sectioned and/or carbon coated specimens. Admittedly, the resolution is only sufficient to elucidate enrichment of the vascular bundle, and not the constituent tissues (tracheid or sieve cells, bundle sheath etc.). However, there is little, if any, evidence as to the redistribution of Ni via phloem loading and, as such, it is more likely that Ni is being transported in the xylem, bound to organic ligands (histidine, citrate) and as hydrated Ni, from which it is then offloaded into the epidermal vacuoles for storage.

As can be seen in the SEM image (Figure 4.2), the abaxial and adaxial surfaces of the *A. murale "Kotodesh"* leaves are densely carpeted with stellate (star-like) trichomes. The trichomes are unicellular and comprised of a basal compartment, pedicle and rays. Trichomes function to prevent water loss and potentially as a defense against insect herbivory (Levin 1973). They are predominantly made of calcium oxalate or calcite (Lanning 1961) and as such show up quite clearly in the calcium tomograms as bright spots on the surface of the leaf (figure 4.2). The mean Ca concentration is ~ 90,000 μg g^{-1} (or 9%) with concentrations exceeding 500,000 μg g^{-1} dry tissue (or 50%) in select pixels. Mn is absent or below detection throughout the bulk of the epidermal tissues, with the exception of highly concentrated spots that coincide with Ca (trichome) and possibly Ni on the leaf surface (circles in figure 4.2). There is still no clear consensus as to whether trichomes on the surface of hyperaccumulating plants serve as a repository for metals (Blamey et al. 1986; Kramer et al. 1997; Kupper et al. 2000; Psaras et al. 2000; Kupper et al. 2001). Our tomograms are consistent with the results of a recent study by Broadhurst et al. (Broadhurst et al. 2004) who demonstrated that the trichome pedicle, trichome basal compartment and the epidermal cells adjacent to the trichomes of *A. murale* "Kotodesh" were significantly enriched with both Ni and Mn, while the rays were only enriched in Ca. An x-ray bit map showed that the Ni and Mn were co-localized but they were stored in distinctly different regions, indicating that the plant may detoxify these metals in metabolically different ways. Sunflower is one of the few plants known to accumulate Mn, storing and secreting the metal out of its glandular trichomes as MnO (Blamey et al. 1986). Although the trichomes on the surface of *A. murale* are non-glandular and secretion is not possible, accumulation within the cells associated with these structures suggested that they may still have a functional role in metal storage and detoxification.

To determine if the patterns of Ni distribution observed in the fluorescent CMT images were consistent throughout the entire leaf, absorption edge CMT was used. Movie 1 (see supporting information) and Figure 4.3a-f show that there are three distinct occurrences of Ni. First, as was seen in the fluorescence CMT images, enrichment of Ni occurs within the epidermal layers evidenced as a thin, brighter outline (more evident in Movie 1, supporting information) surrounding the central tissues. Second, there are small, highly concentrated regions of Ni within the epidermal tissues of the entire leaf, appearing as bright white spots in the reconstructed leaf cross-section (black arrows figure 4.3f). These Ni enrichments most likely correspond with Mn at the base of the calcium rich trichomes (circles Figure 4.2, Ca, Mn, Ni) as was observed in the fluorescent CMT images. Third, Ni enrichments occur in isolated regions within the interior of the leaf, possibly associated with the vascular system (white arrows figure 4.3d and f and Movie 1). However, the omnipresent pattern of Ni enrichment associated with the vascular tissues seen in the fluorescence tomograms (figure 4.2) is less evident in the absorption edge series (Figure 4.3 and Movie 1) resulting because the Ni concentration in the majority of this material is below the detection limit of absorption edge CMT (~5000μg g^{-1}). Thus, only the most concentrated regions of Ni enrichment within the vascular system were resolved in the absorption edge images. The leaf used in the absorption edge measurement contained on average 0.8% Ni, with a maximum of

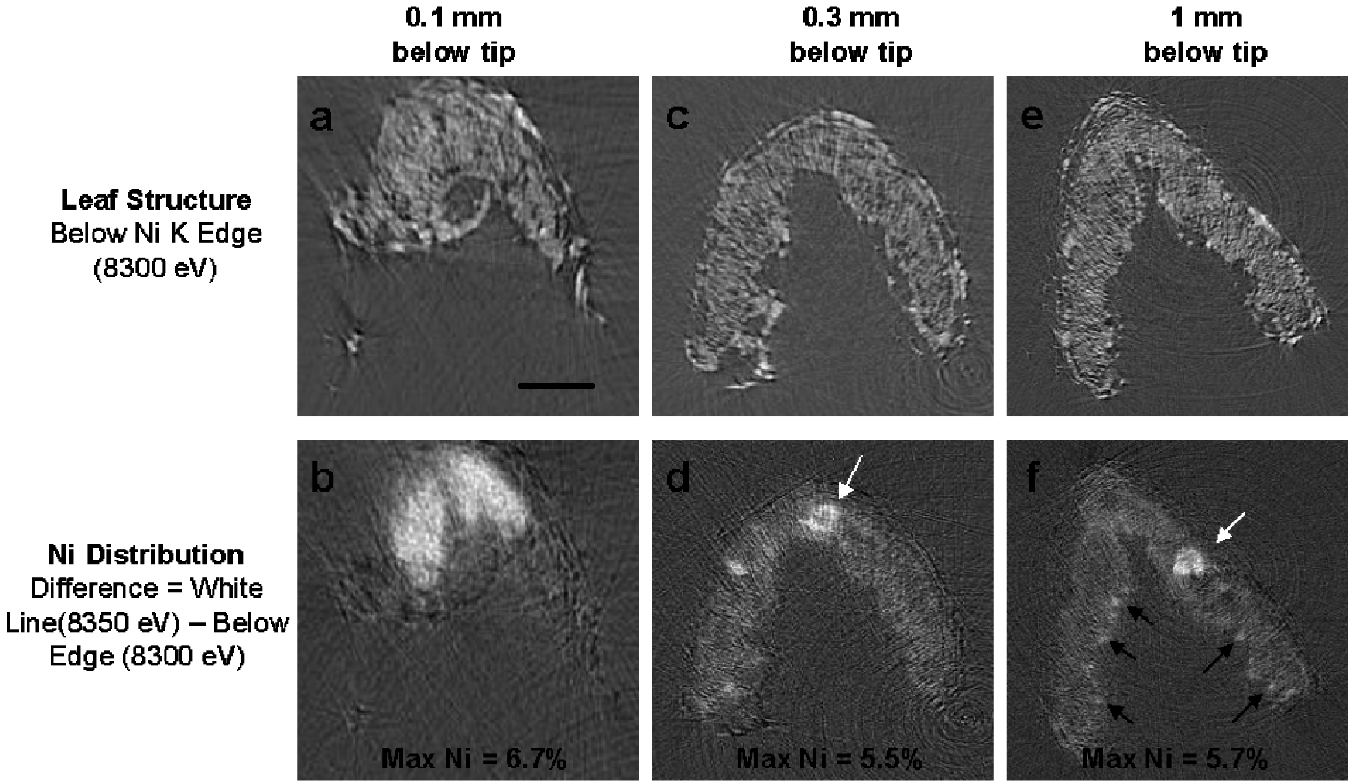

FIGURE 4.3a-f: Stop frames from the absorption edge projection series showing the below edge images depicting the leaf structure (a, c and e) and the subtracted (above (8350eV) –below (8300eV)) images showing the Ni distribution (b, d and f) from 0.1 (a and b), 0.3 (c and d) and 1 (e and f) millimeter below the *Alyssum murale* 'Kotodesh' leaf tip. Maximum Ni concentrations in the 0.1, 0.3 and 1mm sections are 6.7, 5.5 and 5.7 wt% respectively. Black arrows indicate regions of Ni enrichment on the leaf surface while white arrows indicate Ni concentrations within the veins. Scale bar represents ~250 μm.

~8%, corresponding to 2.4% and 24% dry weight respectively (see methods for wet wt conversion), and are some of the highest Ni concentrations reported in “fresh” plant tissues (Sagner et al. 1998; Broadhurst et al. 2004). These values are higher than those for the leaf used in the fluorescence tomograms (~500μg g^{-1}), reflecting the difference in the soil Ni concentrations used in growing the plants.

In addition to vascular enrichment, accumulation of Ni within the tip of selected leaves was observed (Figure 4.3b). Nickel accumulation in the tip most likely results from a combination of both transport and storage mechanisms. The transport and delivery of Ni to the leaves probably occurs as mass flow through the xylem, driven by transpiration. Evidence for this is the presence of Ni within the xylem vesicles of the stem (Figure 4.4). Transpirational flow has been similarly implicated in the transport of Cd to the shoots of Indian mustartd (*Brassica juncea*) (Salt et al. 1995) and for several other elements including B, Ca, Mn and Si (Marschner 1995). As discussed previously, once Ni enters the leaves it is sequestered into the epidermal vacuoles, away from the mesophyll (as seen in figure 4.2). However, the vacuoles are a finite reservoir and, if transpirational delivery of Ni is unceasing, could reach capacity. The mechanisms for coping with excess (i.e. beyond which even a hyperaccumulator can tolerate) leaf Ni are unclear. One possibility is that excess Ni escapes the leaves via leaf venation terminals (hydathodes) in guttation fluids. Mizuno et al. (2002) examined the guttation fluid of several plant species growing in ultramafic soils and found elevated levels of both Ni and Mn. They suggested that guttation acts as a method of expelling elements carried in the transpiration stream that are in excess of plant requirements. This would explain the abundance of Ni on/in *A. murale* leaf tips observed in this study. Since Ni delivery to the leaves is dependent upon transpiration, factors affecting transpiration (i.e. full sun or shade) would have an impact on the total metal content and could explain why we found enrichment of Ni in some leaf tips and not others. However, Kovacheva et al. (2000) pointed out that there are several factors such as biological variety, seasonal and climatic changes, age and height of sampling, and soil conditions that can influence the distribution of metals and nutrients within plant organs. Boyd et al. (*1999*) and more recently Kupper et al. (*2004*) also found age dependent changes in metal concentrations, generally with older leaves exhibiting higher, and more segregated metal concentrations than younger.

Further analysis is necessary to evaluate the role of transpiration and guttation in controlling the compartmentalization of Ni within the leaves of *A. murale*. In addition, the contribution of the regions of highest Ni enrichment (leaf tip, trichome) to the overall distribution of Ni within the leave should be assessed to explore their significance as a mechanism for Ni tolerance.

4.4.2 Metal Compartmentalization in Stems and Roots

We also used fluorescence microtomography to explore the distribution of metals in the stem and root tissues of *A. murale* “Kotodesh” as shown in Figure 4.4. The epidermis of the stem has pulled away from the cortex, most likely as a result of the drying process, and can be seen as a thin jagged line enriched in Ni. Nickel is also concentrated in the xylem (black arrow Figure 4.4), and absent from the phloem (gray arrow, Figure 4.4) and cortex. In the roots of *A. murale*, Ni is isolated in the stele or vascular tissues of the finer root (Figure 4.4 inset in root tomogram), with very little metals on the exterior. The opposite pattern is seen for the coarser root, which is devoid of metals on the interior, but covered in a “coating” of well correlated Fe, Zn and Ni. The presence of these metals on/in the exterior of the root could have resulted from numerous processes including sorption, precipitation, microbial activity or inadequate washing. Further analysis is under way to verify the relationship (if any) between root coatings and the uptake of Ni from the surrounding environment, especially since no coating were found on the finer roots possessing vascular enrichment.

This research clearly highlights the applicability of synchrotron based tomographic techniques to the study of metal partitioning within hyperaccumulating plant tissues. Synchrotron fluorescence microtomography provided highly-sensitive, quantitative, multi-element, tissue specific images of the metal distributions in leaf, stem and root tissues. Absorption edge CMT allowed us, for the first time, to resolve the *in-vivo* metal distributions three-dimensionally, highlighting the variability of the highest metal concentrations. The results are consistent with a transport model involving uptake of Ni by roots, transport through the stem xylem to the shoots where it is then distributed through the veins to the dermal tissues, and in some cases leaf tips. Verification of these findings with additional analysis is required, particularly to explore further how factors affecting transpiration and guttation may control the

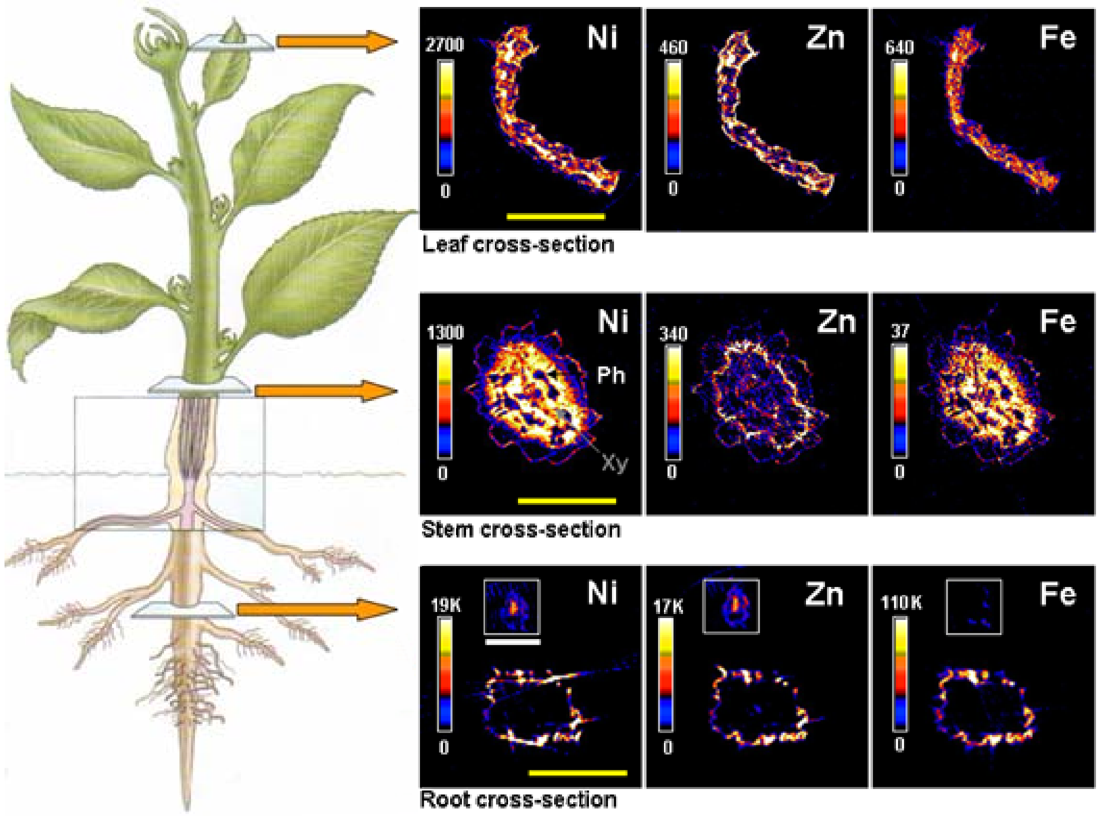

FIGURE 4.4: Ni, Fe and Zn fluorescence CMT images of a leaf, stem, coarse and fine root cross-sections from *Alyssum murale* 'Kotodesh'. Inset in root tomogram is of a finer root. The colorimetric scale maps region-specific relative metal concentrations (μg g^{-1}) for each element, with brighter colors indicating areas of higher enrichment. The slight streakiness of the coarser root Ni image is most likely due to beam hardening by very high Ni spots on the root surface. The lower thresholds for the tomograms were adjusted up slightly to suppress background noise and thereby improve image quality. Yellow scale bar represents ~500 μm, white scale bar (root inset) represents ~ 100μm. Plant figure adapted from Plant Physiology, 3rd edition, Tiaz and Zeiger (Ed) with permission from Sinauer Associates, Inc. Publishers.

distribution of Ni (and possibly other metals) in/on the tips of *A. murale* leaves. Furthermore, examination of more extensive sections of roots from both soil and hydroponic mediums should be done to help identify the section/s of the root that are the most transport active with respect to Ni as well as the ubiquity or uniformity of the mixed metal "coatings" observed in/on the coarser roots. It is clear, even from this small data set, that the variability of metal distributions within plant tissues can differ, not only between the roots, stems and shoots, but also within individual organs. Understanding this variability is important in elucidating how hyperaccumulating plants cope with foliar metal concentrations grossly beyond the physiological needs of most plants. Together, fluorescence and absorption edge CMT provide a valuable method for exploring this variability and are uniquely suited for elucidating and quantifying the microdsitributions of multiple metals, and determining the ubiquity of these distributions, within specific tissues of intact hyperaccumulating plant tissues.

4.4.3 Supporting Information Available

An absorption edge CMT movie showing the Ni distribution/concentration as a sequence of projections from the tip to the proximal end in a "fresh" Alyssum murale 'Kotodesh' leaf with brighter regions indicating higher (>5000μg g-1) Ni enrichment, the maximum of which was 7.9% wet weight (~40% dry wt.) can be viewed, free of charge, via the internet at http://pubs.acs.org.

4.5 REFERENCES

Banuelos GS, Ajwa HA, Terry N, Zayed A (1997) Phytoremediation of selenium laden soils: A new technology. Journal of Soil and Water Conservation 52: 426-430

Blamey FPC, Joyce DC, Edwards DB, Asher CJ (1986) Role of trichomes in sunflower tolerance to manganese toxicity. Plant and Soil 91: 171-180

Boyd RS, Davis MA, Wall MA, Balkwill K (2002) Nickel defends the South African hyperaccumulator *Senecio coronatus* (Asteraceae) against *Helix aspersa* (Mollusca : Pulmonidae). Chemoecology 12: 91-97

Boyd RS, Jaffre T, Odom JW (1999) Variation in nickel content in the nickel hyperaccumulating shrub *Psychotria douarrei* (Rubiaceae) from New Caledonia. Biotropica 31: 403-410

Boyd RS, Moar WJ (1999) The defensive function of Ni in plants: response of the polyphagous herbivore *Spodoptera exigua* (Lepidoptera : Noctuidae) to hyperaccumulator and accumulator species of *Streptanthus* (Brassicaceae). Oecologia 118: 218-224

Broadhurst C, Chaney R, Angle JS, Maugel T, Erbe E, Murphy C (2004) Simultaneous hyperaccumulation of Nickel, Manganese, and Calcium in *Alyssum* leaf trichomes. Environmental Science & Technology 38: 5797

Brooks RR, Lee J, Reeves RD, Jaffre T (1977) Detection of nickeliferous rocks by analysis of herbarium specimens of indicator plants. J. Geochem. Explor. 7: 49-57

Chaney R, Angle J, Baker A, Li Y (1999) Method for phytomining of nickel, cobalt, and other metals from soil. US Patent No. 5,944,872 issued Aug 31, 1999 (Continuation in part of US Patent 5,711,784), issued Jan. 27, 1998

Chaney RL, Malik M, Li YM, Brown SL, Brewer EP, Angle JS, Baker AJ (1997) Phytoremediation of soil metals. Current Opinion in Biotechnology 8: 279-284

Cloetens P, Boller E, Ludwig W, Baruchel J, Schlenker M (2001) Absorption and phase imaging with synchrotron radiation. Europhysics News 32

Davis MA, Boyd RS (2000) Dynamics of Ni-based defense and organic defenses in the Ni hyperaccumulator, *Streptanthus polygaloides* (Brassicaceae). New Phytologist 146: 211-217

Dowd BA, Campbell GH, Marr RB, Nagarkar VV, Tipnis SV, Axe L, Siddons DP (1999). Developments in synchrotron x-ray computed microtomography at the National Synchrotron Light Source. Developments in X-Ray Tomography II, Denver, CO, U.S.A.

Eng PJ, Newville M, Rivers ML, Sutton SR (1998). Dynamically figured Kirkpatrick Baez micro-focusing optics. SPIE Proc., San Diego, CA, U.S.A.

Eng PJ, Rivers M, Yang BX, Schildkamp W (1995). Micro-focusing 4keV to 65keV x-rays with bent Kirkpatrick-Baez mirrors. SPIE Proc., San Diego, CA, U.S.A.

Flannery BP, Deckman HW, Roberge WG, D'Amico KL (1987) Three-dimensional x ray microtomography. Science 237: 1439-1444

Flynn GF, Rivers ML, Sutton SR, Eng P, Klock W (2000) X-Ray computed microtomography (CMT): a non-invasive screening tool for characterization of returned rock cores from mars and other solar system bodies. Lunar and Planetary Science XXXI LP1 #1893: Houston, TX 2000

Golosio B, Simionovici A, Somogyi A, Lemelle L, Chukalina M, Brunetti A (2003) Internal elemental microanalysis combining x-ray fluorescence, Compton and transmission tomography. J. Appl. Phys. 94: 145-157

Hansel CM, Fendorf S (2001) Characterization of Fe plaque and associated metals on the roots of mine-waste impacted aquatic plants. Environmental Science & Technology 35: 3863-3868

Hansel CM, LaForce MJ, Fendorf S, Sutton S (2002) Spatial and temporal association of As and Fe species on aquatic plant roots. Environmental Science & Technology 36: 1988-1994

Heath SM, Southworth D, Dallura JA (1997) Localization of nickel in epidermal subsidiary cells of leaves of *Thlaspi montanum* var siskiyouense (Brassicaceae) using energy-dispersive x-ray microanalysis. Int. J. Plant Sci. 158: 184-188

Hogan JP, Gonsalves RA, Krieger AS (1991) Fluorescent computer tomography: a model for correction of x-ray absorption. IEEE Trans. Nucl. Sci 36: 1721-1727

Howe JA, Loeppert RH, Derose VJ, Hunter DB, Bertsch PM (2003) Localization and speciation of chromium in subterranean clover using XRF, XANES, and EPR spectroscopy. Environmental Science & Technology 37: 4091-4097

Jhee EM, Dandridge KL, Christy Jr. AM, Pollard JA (1999) Selective herbivory on low-zinc phenotypes of the hyperaccumulator *Thlaspi caerulescens* (Brassicaceae). Chemoecology 9: 93-95

Keon-Blute N, Brabander DJ, Hemond HF, Sutton SR, Newville M, Rivers M (2004) Arsenic sequestration by ferric iron plaque on cattail roots. Environmental Science & Technology 38: 6074-6077

Kerkeb L, Kramer U (2003) The role of free histidine in xylem loading of nickel in *Alyssum lesbiacum* and *Brassica juncea*. Plant Physiology 131: 716-724

Kersten WJ, Brooks RR, Reeves RD, Jaffre T (1980) Nature of nickel-complexes in *Psychotria douarrei* and other nickel-accumulating plants. Phytochemistry 19: 1963-1965

Kinney JH, Haupt DL, Nichols MC, Breunig TM, Jr. GWM, Marshall SJ (1994) The x-ray tomographic microscope: three-dimensional perspectives of evolving microstructures. Nucl. Instrum. Methods Phys. Res., Sect. A 347: 480-486

Kirkpatrick P, Baez AV (1948) Formation of optical images by x-rays. J Opt Soc Am 38: 766

Kovacheva P, Rumiana D, Ivelin K (2000) On the representative sampling of plants for multielement analysis. Phytologia balcanica 6: 91-102

Kramer U, Cotter-Howells JD, Charnock JM, Baker AJM, Smith JAC (1996) Free histidine as a metal chelator in plants that accumulate nickel. Nature 379: 635 638

Kramer U, Grime GW, Smith JAC, Hawes CR, Baker AJM (1997) Micro-PIXE as a technique for studying nickel localization in leaves of the hyperaccumulator plant *Alyssum lesbiacum*. Nucl. Instrum. Methods Phys. Res., Sect. B 130: 346-350

Kukier U, Chaney RL (2001) Amelioration of nickel phytotoxicity in muck and mineral soils. Journal of Environmental Quality 30: 1949-1960

Kupper H, Lombi E, Zhao FJ, McGrath SP (2000) Cellular compartmentation of cadmium and zinc in relation to other elements in the hyperaccumulator *Arabidopsis halleri*. Planta 212: 75-84

Kupper H, Lombi E, Zhao FJ, Wieshammer G, McGrath SP (2001) Cellular compartmentation of nickel in the hyperaccumulators *Alyssum lesbiacum*, *Alyssum bertolonii* and *Thlaspi goesingense*. Journal of Experimental Botany 52: 2291-2300

Kupper H, Mijovilovich A, Meyer-Klaucke W, Kroneck PMH (2004) Tissue- and age dependent differences in the complexation of cadmium and zinc in the cadmium/zinc hyperaccumulator *Thlaspi caerulescens* (Ganges ecotype) revealed by x-ray absorption spectroscopy. Plant Physiology 134: 748-757

Kupper H, Zhao FJ, McGrath SP (1999) Cellular compartmentation of zinc in leaves of the hyperaccumulator *Thlaspi caerulescens*. Plant Physiology 119: 305-311

La Riviere PJ, Billmire DM (2004). Penalized-likelihood image reconstruction for x ray fluorescence computed tomography with unknown fluorescence attenuation maps. Developments in X-Ray Tomography IV, Denver, CO, U.S.A, Geochemical and Minerological Society of America.

Lanning FC (1961) Calcite in *Lesquerella ovalifolia* trichomes. Science 133: 380

Lee J, Reeves RD, Brooks RR, Jaffre T (1978) Relation between Nickel and Citric Acid in Some Nickel-Accumulating Plants. Phytochemistry 17: 1033-1035

Levin DA (1973) The role of trichomes in plant defense. Quart. Rev. Biol. 48: 3-15

Li Y-M, Chaney RL, Brewer EP, Angle JS, Nelkin J (2003) Phytoextraction of nickel and cobalt by hyperaccumulator *Alyssum* species grown on nickel contaminated soils. Environ. Sci. Technol. 37: 1463-1468

Li Y-M, Chaney RL, Brewer EP, Roseberg R, Angle JS, Baker AJM, Reeves R, Nelkin J (2003) Development of a technology for commercial phytoextraction of nickel: economic and technical considerations. Plant and Soil 249: 107-115

Liu DH, Kottke I (2003) Subcellular localization of Cd in the root cells of *Allium sativum* by electron energy loss spectroscopy. Journal of Biosciences 28: 471 478

Lombi E, Zhao FJ, McGrath SP, Young SD, Sacchi GA (2001) Physiological evidence for a high-affinity cadmium transporter highly expressed in a *Thlaspi caerulescens* ecotype. New Phytologist 149: 53-60

Marschner H (1995) Mineral Nutrition of Higher Plants. Second. Academic Press, San Diego, CA, U.S.A.

McLain AA, Altman SA, Rivers ML, Cygab RT. Use of computerized microtomography to examine the relationships of sorption sites in alluvial soils to iron and pore space distributions 2002. US Nuclear Regulatory Commission, Washington, DC July 2002

Mizuno N, Takahashi A, Wagatsuma T, Mizuno T, Obata H (2002) Chemical composition of guttation fluid and leaves of Petasites japonicus v. giganteus and Polygonum cuspidatum growing on ultramafic soil. Soil Science and Plant Nutrition 48: 451-453

Pickering IJ, Prince RC, Salt DE, George GN (2000) Quantitative, chemically specific imaging of selenium transformation in plants. Proc. Natl. Acad. Sci. U.S.A. 97: 10717-22

Pollard AJ, Baker AJM (1997) Deterrence of herbivory by zinc hyperaccumulation in *Thlaspi caerulescens* (Brassicaceae). New Phytologist 135: 655-658

Prasad MNV, Strzalka K (2004) Heavy Metal Stress in Plants: From Molecules to Ecosystems. 2. Springer, Berlin

Psaras GK, Constantinidis T, Cotsopoulos B, Manetas Y (2000) Relative abundance of nickel in the leaf epidermis of eight hyperaccumulators: evidence that the metal is excluded from both guard cells and trichomes. Ann. Bot. 86: 73-78

Rivers M, Wang Y, Uchida T (2004). Microtomography at GeoSoilEnvironCARS. Developments in x-ray tomography IV.

Rivers ML, Sutton SR, Eng P (1999). Geoscience applications of x-ray computed microtomography. Developments in x-ray tomography II, Denver, CO, U.S.A.

Sagner S, Kneer R, Wanner G, Cosson JP, Deus-Neumann B, Zenk MH (1998) Hyperaccumulation, complexation and distribution of nickel in *Sebertia acuminata*. Phytochemistry 47: 339-347

Salt DE, Prince RC, Baker AJM, Raskin I, Pickering IJ (1999) Zinc ligands in the metal hyperaccumulator *Thlaspi caerulescens* as determined using x-ray absorption spectroscopy. Environmental Science & Technology 33: 713-717

Salt DE, Prince RC, Pickering IJ, Raskin I (1995) Mechanisms of cadmium mobility and accumulation in Indian Mustard. Plant Physiology 109: 1427-1433

Scheckel KG, Lombi E, Rock SA, McLaughlin NJ (2004) In vivo synchrotron study of thallium speciation and compartmentation in *lberis intermedia*. Environmental Science & Technology 38: 5095-5100

Sutton SR, Bertsch PM, Newville M, Rivers M, Lanzirotti A, Eng P (2002). Microfluorescence and microtomography analyses of heterogeneous earth and environmental materials. Applications of Synchrotron Radiation in Low Temperature & Environmental Science, Monterey, CA, U.S.A.

Taiz L, Zeiger E (2002) Plant Physiology. Third. Sinauer Associates, Inc., Sunderland, Massachusetts

Tu C, Ma LQ, Bondada B (2002) Arsenic accumulation in the hyperaccumulator Chinese brake and its utilization potential for phytoremediation. Journal of Environmental Quality 31: 1671-1675

Chapter 5

SUMMARY AND RESEARCH NEEDS

The objectives of this research focused on elucidating the speciation and distribution of metals in complex, heterogeneous, organic and inorganic natural materials. The first objective was to assess the affect of soil type (muck vs. mineral) and in-situ chemical treatment (dolomitic limestone) on the speciation of Ni in soils contaminated with aerial deposition from a Ni refinery in Port Colborne, Ontario, Canada. The second objective was to examine the biochemical mechanisms of Ni transport and storage in the Kotodesh cultivar of the Ni hyperaccumulator *Alyssum murale* in an effort to improve our understanding of metal hyperaccumulation in this alternative remediation technique. The third objective was to demonstrate how synchrotron based computed microtomographic techniques can be used to determine the location and concentration of Ni in *A. murale* tissues. Meeting these objectives required a multi-disciplinary, multi-technique approach.

The research findings presented in Chapter 2 showed for the first time that Ni-Al LDH phases can form in anthropogenically enriched mineral field soils at circumneutral pH, and that liming can promote the formation of neoformed-phyllosilicate phases. Principal component analysis and target transformation indicated that the spectral dataset for both the treated and untreated mineral soils could best be described by fresh and aged Ni Al LDH phases, Ni-phyllosilicate and NiO. Linear least squares fitting of the bulk XAFS spectra showed that the LDH phases comprised >60% of the total Ni within both limed and unlimed mineral soils. The remaining portion is present as distinctly spherical, 10-50 μM NiO or Ni-metal particles. Monitoring the dissolution of Ni from both treated and untreated mineral soils by pH 4 HNO_3 using a stirred-flow technique showed that the release of Ni, while small (~2%), was reduced in the lime treated soil compared to the unlimed. Dissolution studies using the pure end member phases showed that NiO was insoluble in pH 4 HNO_3 while the *fresh* Ni-Al LDH phase was characterized by an initial rapid release of Ni followed by a steady release throughout the 8 hour experiment (~60% remaining after 8hrs) indicating that the LDH phase formed in the soil is more stable than the freshly precipitated, lab-generated standard. These results are contrary to those of Nachtegaal et al (2005) who found that the Zn-LDH phases formed in a Zn smelter enriched soil were not stable with decreasing pH. These results indicate that that the type of metal forming the LDH phases has a significant influence on the precipitate solubility. To verify the influence of metal identity on LDH phase solubility, dissolution studies should be performed with a variety of mixed metal LDH phases (e.g. Co, Zn, Ni etc). Aging time and the type of interlayer anion of each of the metal precipitates should also be varied, which have been shown by Peltier et al (in press) to significantly influence the stability of the precipitate phase formed. Regardless, these results (as those with Zn) show that secondary mixed-metal precipitate phases can comprise a significant portion of the total metal in near-neutral contaminated mineral field soils, and therefore, should be include in surface complexation and transport models in order to accurately predict metal mobility and bioavailability.

In the highly organic soils, no precipitate phases were found, but instead, PCA identified Ni-fulvic acid and NiO as the primary Ni species. Excluding the Ni-soil fulvic acid standard from the PCA routine resulted in the identification of the di- and tricarboxylic acids malate and citrate which likely serve as proxies for the different coordination environments of Ni in the highly organic muck soils. The limed muck soil had a higher proportion of the more stable Ni-citrate like complexes compared to the unlimed muck soil which had more of the weaker Ni-malate type Ni complexes which explains the reduction in Ni dissolution from the limed soils by pH 4 HNO_3 using the stirred-flow technique. Additional research into the metal coordination with soil organic fractions (i.e. humic and fulvic acids) as affected by pH should be further explored. These studies could be facilitated by the use of novel *soft* spectromicrospy and C1s NEXAFS techniques as first demonstrated by Nachtegaal et al (PhD dissertation).

Chapter 2 also showed that conventional sequential chemical extractions alone were ineffective at accurately predicting the Ni speciation within the field and forested soils around the Ni refinery. This is an important finding because not everyone has access to synchrotron facilities to directly assess metal speciation in soils and therefore, they rely on sequential extracitons to predict metal speciation and make remediation decisions based on these findings. Our results demonstrate that in order to accurately determine the speciation of metals in soils, sequential extractions should be coupled with more direct measures of Ni speciation (i.e. SEM, FTIR and if possible XAFS). For example, the sequential extraction of the filed and muck soils indicated a large amount of carbonate associated Ni which, based on the XAFS and SEM data, was more likely either specifically sorbed Ni, or the result of partial dissolution of the Ni Al LDH or NiO particles. There have been many efforts to standardized sequential extraction methods so that results could be compared more easily from one contaminated site to the next. Results are highly dependent on the extraction reagents used, the order in which they are implemented, soil type, total metal content, and solubility of the metal phases. In order for sequential extractions to be more effective at predicting metal speciation, efforts need to be made to standardize and better characterize the current sequential extraction methodologies. One approach could be to use a standardized materials (i.e. soils in which the various metal fractions are have been verified) and run them through a variety of SE schemes, assessing each using direct speciation methods (i.e. XAFS) for their ability to remove the targeted phases. A variety of soil types and metal species could be assessed to get an idea of the accuracy of each of the sequential extraction steps.

In chapter 3 and 4, we used a variety of microscopic and spectroscopic tools to determine the distribution and speciation of Ni in the tissues of the Kotodesh cultivar of the Ni hyperaccumulator *Alyssum murale*. Identifying the Ni species within *A. murale* tissues using bulk and μ-XAFS alone was difficult because of the week backscattering of the light second neighbor carbon atoms. Therefore, we relied on a variety of methods including ATR-FTIR and ion chromatography to verify the Ni speciation determined using XAFS. We found a majority of the Ni in *A. murale* complexed with stronger ligands such as malate and histidine, with the balance either complexed with non-specific oxygen donor ligands or present as free, hydrated Ni. We also found that manganese (Mn(II)) preferentially localized in the basal compartment of the leaf trichomes. The function of manganese within the trichome basal compartment, or the significance of Mn storage at this location as a specific mechanism for Mn detoxification is still not known. Using synchrotron based fluorescence computed microtography (F-CMT) we demonstrated how synchrotron based microtomography could be used to ascertain the location and concentration of metals in and throughout plant tissues. It is likely, based on the relative insolubility of NiO in the Port Colborne Soils that phytoremediation alone would not be an effective strategy to reduce Ni concentrations below the Canadian Ministry of the Environment standard of 200 ppm. However, coupling soil calcification with occasional rotations of *A. murale* should suffice to alleviate any concern of Ni toxicity, mobility and bioavailability in these soils.

There are still many unanswered questions concerning the accumulation of metals in hyperaccumulating plants. For example, it is still not know how *A. murale* (and other metal hyperaccumulators for that matter) acquires Ni from the rhizosphere, or what influence Ni species has on the removal. Rhizosphere acidification, or the release of organic root exudates to solubilized and complex metals for uptake are hypotheses currently under investigation. Additionally, in the shoots of the plant, the physiology and biochemistry behind metal delivery from the xylem and preferential accumulation in the epidermal vacuoles is still not understood. The development of micro synchrotron X-ray beams capable of examining lighter elements (e.g. S, C) together with improved focusing optics for single cell resolution, and in collaboration with individuals across multiple disciplines should help answer these questions.